Development of a Computational Model of Skin Damage under Blunt Impact to Investigate Skin Failure Threshold

A Dissertation

Presented to

the faculty of the School of Engineering and Applied Science

University of Virginia

in partial fulfillment
of the requirements for the degree

Doctor of Philosophy

by

Kevin Sien Yew Kong

December 2020

APPROVAL SHEET

This Dissertation

is submitted in partial fulfillment of the requirements for the degree of

Doctor of Philosophy

Author Signature: ____________________

This Dissertation has been read and approved by the examining committee:

Advisor: Matthew B. Panzer

Committee Member: Jason R. Kerrigan

Committee Member: Robert S. Salzar

Committee Member: Gregory J. Gerling

Committee Member: Michael J. Danilich

Committee Member: ____________________

Accepted for the School of Engineering and Applied Science:

Craig H. Benson, School of Engineering and Applied Science

December 2020

ABSTRACT

Skin injury is one of the most common wounds experienced by individuals, and these injuries can compromise the skin's ability to protect the body from external pathogens. Skin wounds can become chronic, and lead to infections that are estimated to affect 4.5 million people per year in the United States, at an annual cost ranging from $28 to $97 billion. Therefore, it is important that we understand how skin injuries occur so that we can identify and design countermeasures to prevent skin injuries in circumstances that involved human body impact, and to ensure that devices such as less-than-lethal blunt projectiles are designed to not penetrate the skin. However, research on the mechanical characteristics of human skin to failure is limited, and we do not have the knowledge necessary to develop biofidelic skin surrogates and computational models that can be used to study open skin injury. Therefore, the goals of this dissertation were to characterize the mechanical properties of human skin in dynamic loading and failure and use this knowledge to develop an advanced computational model for studying skin injury. In particular, this work focuses on understanding the skin mechanics related to impact from blunt objects and investigating the sensitivity of skin injury tolerance to a variety of underlying tissues, impactor types, and skin properties.

A comprehensive test protocol for human skin was performed to characterize the mechanical properties of the tissue in loading modes that include uniaxial tension, compression, and stress relaxation tests to gain an understanding of skin characteristics at dynamic loading rates. The dynamic tensile tests and stress relaxation tests demonstrated the skin's viscoelastic and nonlinear mechanical response. The skin was observed to be anisotropic at a lower loading rate (1/s), but isotropic at a higher loading rate (180/s). For the application of blunt impact, the experimental results informed the development of an isotropic, hyper-viscoelastic constitutive

model, coupled with a damage function to capture the skin's failure response. Three sets of skin material parameters were generated that represented the average, upper bound, and lower bound of the measured skin properties to demonstrate the biological variations as observed in the dataset. An independent set of destructive dynamic indentation tests of human skin were performed to provide response data for model validation. The damage constitutive model was implemented into a finite element analysis software as a user-defined material, which was verified by simulating the experimental tensile tests and validated against the dynamic indentation tests. Overall, the newly developed skin model simulated the uniaxial tensile response successfully but underpredicted the dynamic indentation failure response. It was found the skin's through-thickness compression properties were an important factor in capturing the biofidelity of the skin during dynamic indentation. Therefore, a transversely isotropic material model for the skin tissue was recommended for future improvement.

A sub-system model that included skin, adipose tissue, and muscle was developed to investigate the skin failure threshold under various types of blunt impact. Both adipose and muscle models were obtained and calibrated from recent experimental data. Using independent stress relaxation and impact test data, the sub-system model was verified and validated. Lastly, a simulation matrix was designed to include the range of masses and velocities of less-than-lethal blunt projectiles that are used by law enforcement. Six sub-system models representing different body regions, skin properties, and impactor geometry were used to investigate the skin failure threshold. This investigation demonstrated that impactor geometry and the skin properties on the skin failure threshold was negligible except for the body regions where the boundary condition is different due to different amount of underlying tissues.

This dissertation delivers a comprehensive skin failure dataset and a skin computational model with the capability to simulate skin failure responses which are crucial to open skin injury research. The skin model facilitates the development of an engineering tool that can be used to predict skin failure in human body models or with physical skin simulants, which will allow engineers to develop and evaluate the effectiveness of protective systems and the safety of less-lethal blunt projectiles.

Contents

LIST OF FIGURES

LIST OF TABLES

ACKNOWLEDGEMENTS

I would like to express my sincere gratitude to my advisor Dr. Matthew B. Panzer for his unwavering support on this dissertation and throughout my Ph.D. journey. I respect his extraordinary experience and a great sense of humor and it has been a pleasure working with him. I am also grateful to my advisory committee, Dr. Robert S. Salzar, Dr. Jason R. Kerrigan, Dr. Gregory J. Gerling, and Dr. Michael Danilich, for their valuable and countless advice on making this dissertation more comprehensive.

I am grateful for the opportunity to be able to immerse myself in the field of injury biomechanics at the Center for Applied Biomechanics (CAB), UVA, and be around so many talented and friendly people. I want to thank Daniel Perez-Rapela and Zhaonan Sun for always being available for technical discussions and for providing insights into my research. I want to thank Adrian Caudillo and Sayak Mukherjee for their expertise and patience with my modeling issues; Brandon Perry and Jacek Toczyski for their thoughtful inputs to my experimental testing design; Sebastian Giudice, Ahmed Alshareef, Taotao Wu, Hongnan Lin, Deepak Kosanam, Carolyn Roberts, Kristen Reynier, Daniel Shedd, Hamed Joodaki, and John Paul Donlon for their guidance throughout my time in CAB; Brian Overby, Joey White, Sara Sochor and Kevin Kopp for their extensive support that made the testing process successful.

Finally, I would like to thank my family and friends for being so supportive throughout my time in graduate school, without their encouragement and care I would not be where I am today.

CHAPTER 1 - Introduction

1.1 Statement of Problem

Open skin injury is one of the most common wounds experienced by individuals, and this type of injury spans a wide range in severity and mechanism. Minor open skin injuries, such as superficial abrasion and skin tears, are often self-treated and heal easily without complication. However, severe open skin injuries such as lacerations, avulsions, and punctures can potentially cause severe blood loss that can lead to fatality. The disruption and damage to the skin can also cause infections and chronic wounds, which are estimated to affect 4.5 million people per year in the United States (Frykberg & Banks, 2015; Jones et al., 2018) and cost between $28.1 billion to $96.8 billion for treatment annually according to Medicare spending estimates (Nussbaum et al., 2018). While most chronic skin wounds result from underlying health conditions such as obesity and diabetes, other prominent factors associated with open skin injuries during an impact event include skin laceration from interactions with the seat belt during the automotive crash, and skin penetration or avulsion stemming from violent incidents.

To prevent unintended open skin injuries, there is growing interest from the healthcare industry and law enforcement to understand the mechanical properties of human skin and its failure threshold. More knowledge on this topic will help improve the design of medical incision devices for surgical procedures, increase the efficacy of protective body armor, and reduce the risk of injury from blunt less-lethal weapons. Historically, test and evaluation procedures of a potentially new device require a physical skin simulant that exhibits a repeatable and biomechanically-consistent response to human skin tissue, although progress in this area is limited (Bir et al., 2012; Papy et al., 2012). The skin of physical anthropomorphic test dummies (ATDs) used in automotive and military testing is rubber-like and very durable, but it does not represent the mechanics and injury response of human skin tissue. Various ballistic injury surrogates have been constructed using gelatin or clay, and although many of these materials can be used to determine energy transfer from the munition to the tissue surrogate, they lack the viscoelastic nature of human tissue. The limitations of the biofidelity of the skin tissue of existing physical surrogates prevent a deeper study into the mechanisms and tolerances of skin injuries during high rate impact situations.

An alternative approach to physical surrogates for studying injury is using computational human body models (HBMs) to investigate tissue mechanisms. These tools are commonly used in the military and automotive fields to study the biomechanics of impact and the effects of injury countermeasures. However, the current state-of-the-art HBMs have mainly established confidence within the biomechanics field for predicting body kinematics and skeletal injuries. Modeling the mechanics of soft tissues (such as skin) and predicting the failure of these tissues during high rate impact, with good confidence, is a limited capability that needs the support of more research on skin biomechanics.

1.2 Motivation

1.2.1 Experimental Studies of Skin Failure

There is limited biomechanical data on the mechanical properties and injury mechanisms of human skin, particularly for loading conditions consistent with high-rate blunt impact. Several biomedical studies have investigated the mechanics of surgical procedures which focused on the piercing mechanism and threshold of human skin. Micromechanical models developed by Shergold & Fleck (2004) for deep penetration of soft solids have been used to investigate needle cutting tissues (Barnett et al., 2015; Khadem et al., 2016). The study was targeted at surgical applications where sharp penetrators are required to reach a precise target location at a low controlled insertion speed (1-80mm/s). The skin research also led to the development of advanced needle instruments that reduce needle vibration while inserting into skin tissue (Barnett et al., 2016). Besides, research was also performed on post injured skin to study the wound development which is beneficial to surgical planning and wound closure technique (Chanda & Upchurch, 2018).

On the other hand, human skin assessment during high-rate impact is rarely studied and impact studies tend to focus on investigating ribcage or internal organ damage (Bir & Viano, 2004). Skin damage assessments using post-mortem human surrogates (PMHS) have been performed using blunt impactors, and the average energy density (kinetic energy/ impactor cross-sectional area) required to cause skin failure at different body regions were identified (Bir et al., 2005). While Bir's study did not specifically investigate the mechanics of the skin, it helped inform the development of a physical skin penetration surrogate that was calibrated to the response of the anterior thoracic region of the human body for assessing kinetic energy munitions (Bir et al., 2012). A literature review by Breeze & Clasper (2013) examining skin damage in the human thigh region found a correlation between metallic impactor's sectional density (mass/impactor cross-sectional area) and impact velocity. All these studies were conducted at high ballistic impact speed (60m/s to 200m/s) using both sharp and blunt nose impactors.

In terms of material level testing, several *ex vivo* human skin experimental tests to failure have been performed (Jacquemoud et al., 2007; Gallagher et al., 2012; Ní Annaidh, 2012). Unfortunately, each study only focused on one aspect of the skin mechanical properties, such as rate sensitivity (quasi-static and dynamic loading rate) or anisotropy (with respect to Langer line orientations), making it difficult to formulate a general mechanical model for the skin. Uniaxial tensile tests of skin conducted by Ottenio et al., (2015) have provided the first comprehensive dataset regarding mechanical failure properties of human skin by considering anisotropy, strain-rate effect (0.06/s-167/s), and skin failure, but this study was limited to only one PMHS. Although rate sensitivity has been observed from the *ex vivo* tests, experimental work to obtain viscoelastic data from isolated human skin has not yet been conducted.

In summary, the most comprehensive destructive testing of human skin was conducted using a single PMHS which also limits the development of different stiffness of skin models when considering biological variation among human populations which is common in biological tissues. Besides, there is a lack of experimental data to determine the skin's viscoelastic characteristic at a larger stretch ratio without the influence of surrounding tissues. This hinders the development of a strain-rate dependent constitutive damage model of skin.

1.2.2 Skin Constitutive and Computational Modeling

Various constitutive models have been used to represent the skin's response from the experimental tests. Hyperelastic models such as the Neo-Hookean, Mooney-Rivlin, and Ogden models have been previously used for human skin (Shergold et al., 2006b; Delalleau et al., 2008; Lapeer et al., 2010) and showed promising results in simulating skin's nonlinearity. These hyperelastic models are natively isotropic and elastic, and are unable to capture the anisotropy and strain-rate dependency previously observed in skin tissue. To include the strain-rate effect on skin response, a hyper-viscoelastic model that combines a hyperelastic constitutive model with a viscoelastic model was used successfully to capture the stress relaxation response of mice skin at different compressive rates (Wang et al., 2015). Gasser-Ogden-Holzapfel (GOH) model which uses both constitutive and structural parameters is capable of simulating skin's response along and across Langer line orientations (Ní Annaidh et al., 2012) but requires additional work such as determining the fiber dispersion factor through histological analysis. In terms of skin damage modeling, an invariant-based damage constitutive model built based on the GOH model has been developed by Li & Luo, (2016). Researchers claimed this model was the first skin damage constitutive model developed and validated using past human and animal skin test data.

Despite frequent usage of constitutive models for skin tissue, analytical models are often developed for simplified loading conditions and this limits its usage for predicting skin failure under complex scenarios such as blunt impact which can be achieved through computational modeling. Skin computational models have been developed to study skin response by incorporating the constitutive laws (Flynn & McCormack, 2008; Flynn et al., 2011; Groves et al., 2013) but these models are unable to simulate skin failure. In contrast, Ní Annaidh et al., (2013) have validated a finite element (FE) model of skin to simulate skin tearing in a quasi-static stab-penetration event. However, the researchers indicated that the hyperelastic FE model cannot predict the rate effect on skin behavior. A multi-layered skin FE model was also developed to study skin penetration under micro penetrators at quasi-static rate for surgical applications (Meliga et al., 2017). To date, in the automobile field where extensive research has been conducted on the development of modern HBMs, skin failure has not yet been implemented and there is a lack of skin FE damage models that can be utilized for ballistic impact.

In summary, the implementation of the viscoelastic damage model into the computational environment is yet to be performed. The current approach to model skin failure in the FE model (Ní Annaidh et al., 2013) was performed by using element erosion (brittle failure) after reaching a failure threshold (e.g., Von Mises stress). The drawback of this approach is that it does not consider material softening where there will be a damage initiation stage and the skin damage starts to develop before reaching final skin separation. Ultimately, there is a need for a skin injury assessment computational tool that can be used to evaluate skin tolerance, especially in high rate impact conditions. The computational model can serve as an alternative tool to physical surrogates to study skin tolerance from different perspectives such as impactor types and skin material sensitivity based on various skin stiffness among the population.

1.3 Scope of Research

1.3.1 Hypothesis and Specific Aims

The current skin injury research gaps lead to the goals of this dissertation which are to characterize the mechanical and failure properties of human skin in dynamic loading rate and to develop a skin FE damage model to investigate and predict skin failure threshold under the ballistic blunt impact. The overarching hypothesis of this dissertation is that the human skin failure threshold, when subjected to high-rate blunt impact, is dependent on the stiffness of the skin, the mass and shape of the impactor, and the composition of the underlying subcutaneous soft tissues. This dissertation is divided into three phases to develop the knowledge and tools necessary to test this hypothesis. The first phase of this dissertation is to expand the field of knowledge on skin biomechanics by performing a comprehensive experimental test series characterizing the nonlinear, anisotropic, and viscoelastic response of human skin. Further, this test series will characterize the onset of skin damage, and ultimately the tensile failure threshold of skin. Second, these experimental results will be used to formulate a new constitutive equation for skin that will analytically describe the observed behavior of the skin material. This constitutive model will be the basis for the development of a FE model of human skin damage that can be used to improve the capability of current HBMs for predicting skin injury from blunt impact. The third and final phase of this work will be to use the developed skin damage model to explore the effect of skin stiffness, different blunt impactor types on skin injury tolerance, and to predict how skin injury tolerance may change depending on the composition of the underlying subcutaneous soft tissues seen in different body regions.

Aligned with the phases of this dissertation, the specific aims of this research are as follows:

Aim 1: Experimentally characterize human skin tissue to investigate the mechanical response under large strain, high-rate deformation, loading directionality, and failure during blunt impacts.

Aim 2: Develop a constitutive of skin tissue that represents the phenomenological responses observed in the experiment, and adapt this model for FE implementation.

Aim 3: Computationally investigate the injury tolerance to skin subject to different skin stiffnesses and various intrinsic and extrinsic boundary conditions, including blunt impact type and subcutaneous soft tissue composition.

1.3.2 Dissertation Overview

As illustrated in Figure 1-1, after a literature review of human skin research as presented in Chapter 2, the specific aims were accomplished through six tasks, each presented in an individual chapter. Phase 1 consists of two experimental tasks to support the goals of Aim 1: Chapter 3 focuses on performing tensile, compressive, and stress relaxation tests of human skin to investigate the phenomenological response of the tissue to various loading conditions considered important during blunt impact. Chapter 4 focuses on another experimental protocol measuring the mechanical response and failure of skin subjected to a hemispherical indenter. Phase 2 consists of modeling tasks that are designed to mathematically predict the responses observed in Phase 1 and support the goals of Aim 2: Chapter 5 focuses on the development of an analytical model of human skin response, including damage, and ultimately develops models that represent the lower bound (LB), average, and upper bound (UB) skin responses observed in Chapter 3. Chapter 6 advances the work performed in Chapter 5 by implementing the constitutive model into LS-DYNA (a commonly used FE solver for human injury simulation) as a user-defined material (UMAT) which was verified and validated based on the experimental data obtained in Phase 1. Phase 3 applies the knowledge gained in Phase 1 and 2 to explore different intrinsic and extrinsic factors that may affect skin injury threshold, and supports the goals of Aim 3: Chapter 7 develops and validates a multi-layered flesh model consisting of skin, adipose, and muscle tissues with different tissue thicknesses to represent different human body regions. The sub-tissues models were also verified and validated using datasets developed independently from this current dissertation work. Chapter 8 utilizes the validated multi-layered flesh model to investigate the variations of skin failure threshold based on changes to the skin material, underlying tissues, and impactor characteristics.

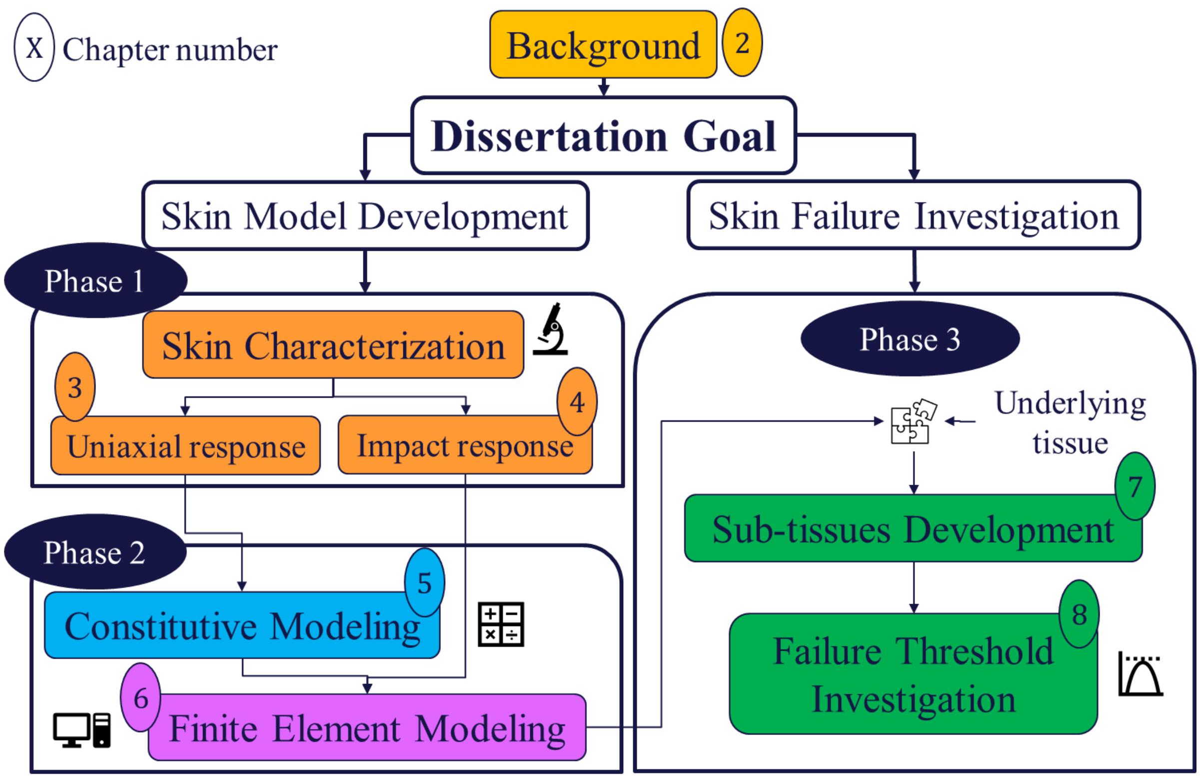

Figure 1-1: Overview of the dissertation.

CHAPTER 2 - Background

2.1 Human Skin Anatomy

Human skin is the largest organ of the human body which covers the entire body with a surface area of 2 m^2 (Gallo, 2017) and occupies 15% body weight (James et al. 2006) of an average adult. The skin serves as the primary protective barrier against pathogens and prevents injuries from the external environment. Moreover, the nerve endings within the skin help to sense aspects of the external environment such as temperature and pressure. The skin acts as a heat regulator and controls fluid evaporation and absorption to stabilize the human body temperature.

The total thickness of skin varies across human body regions, ranging from thin skin of the eyelids to the thick skin found on the breast and foot. Skin thickness ranges from 1.5 mm and 6 mm, which can vary based on age, sex, and ethnic origin (Escoffier et al., 1989; Laurent et al., 2007; Oltulu et al., 2018). There are mainly three layers distributed within the skin namely epidermis, dermis, and hypodermis (Figure 2-1). The epidermis layer is the thinnest (0.5-1.5 mm) while the dermis layer is relatively thicker (0.6-3 mm). The hypodermis is the deepest tissue layer and its thickness varies depending on the adipose content of the individual.

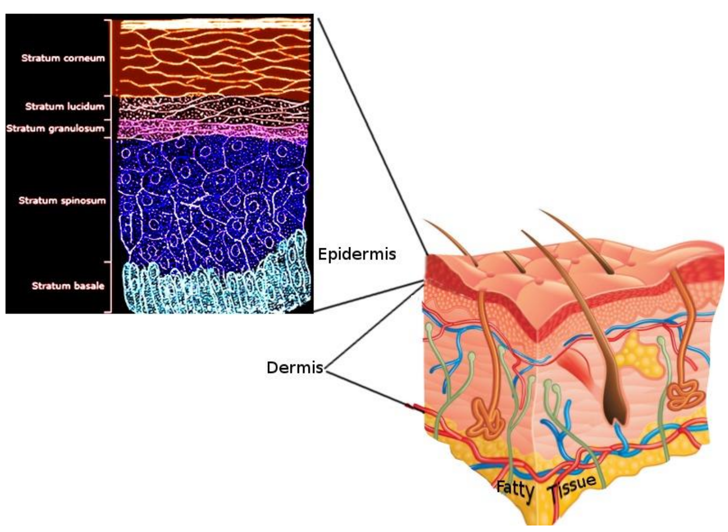

Figure 2-1:Human skin anatomy. (Source: Histology, Skin. 2020)

The outermost layer is called the epidermis and it consists of 5 layers of epithelial cells which are stratum basale, stratum spinosum, stratum granulosum, stratum lucidum, and stratum corneum. Each stratum layer contains a different number of cell layers and cell shapes as the cells travel to the superficial layer of the skin. Overall, there are four types of cells in the epidermis layers which are Keratinocytes, Melanocytes, Langerhans, and Merkel, providing different skin features. Keratinocytes are the majority cells formed at the bottommost stratum basale level with nutrients diffused from the dermis. Keratinocytes move upward towards the stratum corneum while providing protein keratin which is responsible for forming a water barrier and aids the formation of Vitamin D under ultraviolet light. Merkel cells are also found in stratum basale and they provide sensing to human skin and are mostly found at the fingertips. Melanocytes produce melanin which causes different skin tones among humans. Langerhans cells are believed to form a skin protective system with its antigen presentation (Rajesh et al., 2019; Yousef et al., 2020).

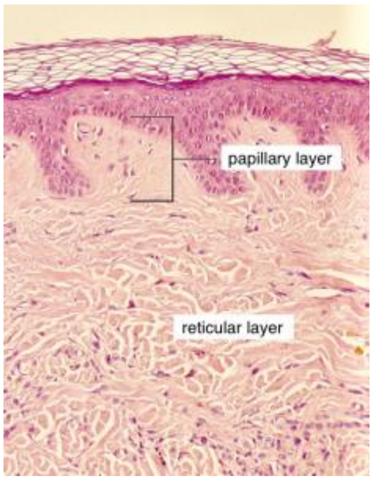

Figure 2-2: Dermis layer. (Source: VirtualMicroscopyDatabase.org)

Underneath the epidermis is a basement membrane that connects to the dermis layer. With no distinct division, the dermis layer has two different areas of connective tissues namely the papillary layer and reticular layer (Figure 2-2). The connective tissues mainly consist of collagen and elastin fibers along with an extracellular matrix. The fibers distribution density differentiates the two layers where the papillary contains loose fiber mesh while denser fiber distribution is found in the reticular layer. The collagen fibers, which makes up most of the dry mass (70-80%) (James et al., 2006; Meyer et al., 2007) and volume (30%) of the dermis layer (Ebling et al., 1992; Van den Berg, 2012) provide structural tensile strength and make the dermis layer become a stress cushion when subjected to an external load. The elastin fiber which is the secondary protein fiber provides little elasticity and only contributes to the strength during initial loading (Oxlund et al., 1988), therefore preventing the skin from getting permanent deformation. The natural orientation of the collagen fibers is also referred to as Langer's line or Cleavage line which was first discovered by Karl Langer in 1861 (Figure 2-3). These Langer's lines, which evolve through aging and is different between sex (Cox, 1941), illustrate how the skin is naturally stretched and has been used to minimize scar formation and better wound recovery in the surgical application when the incision is made along the Langer's line (Lemperle et al., 2019).

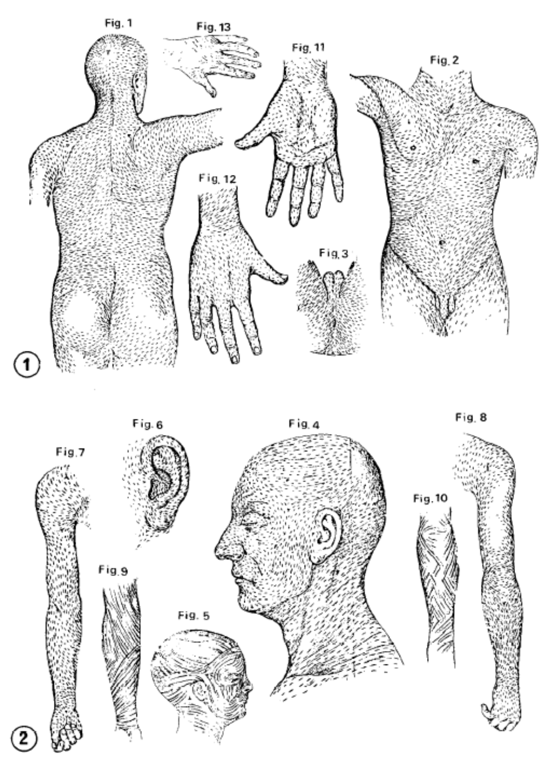

Figure 2-3: Human skin Langer's line distribution. (Source: K. Langer, 1978)

The third layer is the hypodermis which is mainly made up of loose connective tissues and adipose cells that connect to muscles and bones. The hypodermis is a transition area where skin tissue is connected to the subcutaneous tissue. The hypodermis layer acts as a body temperature regulator to prevent unnecessary heat loss and reserve energy. It also helps to protect from minor impacts by acting as an energy absorber.

2.2 Skin Injury

Skin injuries are classified based on how they physically appear and how they occur. At the highest level, skin injuries are divided into open and closed wounds. Closed wounds usually do not involve skin breaking or exposure to underlying soft tissues such as muscle or bone, therefore these wounds have less infection risk and faster tissue healing and recovery. Injuries that are considered closed include hematomas and contusions which can result from mild blunt impact onto the skin during sports contacts or accidental falls. These types of closed wounds primarily involve damage of blood vessels and capillaries underneath the epidermis layer which causes blood pooling and swelling around the injured area (Langlois, 2007; Kostadinova-Petrova et al., 2017). Other closed wounds are blisters and seroma which are caused by repetitive friction movements or extensive surgery taken place on the skin and result in fluid-filled pockets formed underneath the skin as part of the swelling process. The fluids are usually serum or plasma but can be blood if the underlying blood vessels are damaged.

In contrast, open skin wounds such as abrasions, lacerations, punctures, and ulcers involve the physical disruption of the skin tissue, exposing the underlying tissues to the environment. Abrasions occur when the skin’s superficial layer (epidermis) is removed through acute contact such as sliding along a rough surface (van den Eijnde et al., 2014). This results in irregular exposure of the upper dermis along with punctate bleeding and can be easily treated (Basler et al., 2001). Skin puncture is mainly caused by a sharp object that penetrates through the skin and creates deep tissue damage. The puncture creates a small opening on the skin and both the epidermis and dermis layer can be damaged depending on the penetration depth. Two main forces were determined when creating skin puncture i.e. tearing force and spreading force (Barnett et al., 2015). The tearing force is developed at the tip of the sharp object which acts as a pushing force to penetrate the skin while the spreading force acts as a secondary force that enlarges the wounded area as the sharp object continues the penetration. Due to an extremely small contact area between the sharp tip and the skin, this yields a high-stress concentration on the skin that leads to an open crack. The sharp object usually remains in the wounded area which could lead to infection and blood loss and extreme precaution needs to be taken in a reasonable time manner. Another open skin injury called skin ulcer occurs when blood circulation is affected by diabetes or when long-term pressure is applied to the skin and eventually causes the skin to break down. Laceration is the most common open skin injury as it can happen in daily incidents such as door pinch that leads to irregular skin tears and underlying soft tissue injuries (Ito et al., 2017). Unlike skin puncture, skin laceration is usually caused by loading from blunt edges. Therefore, there is no stress concentration as observed in skin puncture while the skin is deformed upon loading by accommodating the impactor. This deformation allows the skin to be elongated in tension until reaching its failure threshold. Similar to skin puncture, both dermis and epidermis can be damaged in skin laceration depending on the loading severity. Although not as severe as skin puncture, skin laceration also requires careful treatment to minimize pain which can affect daily activities. As a result, this dissertation will focus on modeling open skin injuries, particularly in skin laceration due to its commonality as a result of blunt impact.

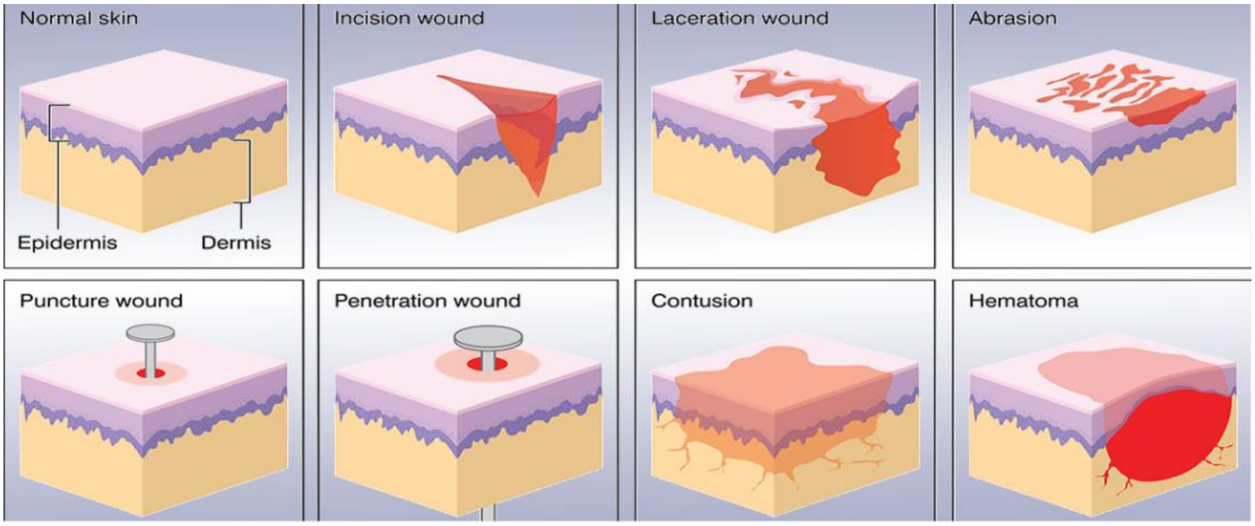

Figure 2-4: Skin injury types. (Source: biodermis)

2.3 Skin Mechanical Properties

As described in human skin anatomy, type I collagen fibers are the predominant content in the dermis layer and are responsible for providing the structural strength of the skin. The collagen fibers are effective in resisting tensile loading but tend to buckle under compression when the load is applied along with the fiber orientation (Ferruzzi et al., 2019). Under natural stress state, the collagen fibers are curved and aligned in the plane of the skin. When impacted by a blunt object, the skin is compressed and starts to accommodate the impactor, the load is mostly applied on the extracellular matrix at this stage, and deformation on the collagen fibers is negligible. As the deformation continues, the skin will be fully engaged at some point, resulting in a tensile loading on the skin membrane. The force will be transmitted to the collagen fibers, causing fiber elongation and eventually lead to skin failure (Figure 2-5). Hence, it is believed that the primary skin failure mode under blunt impact is related to tension.

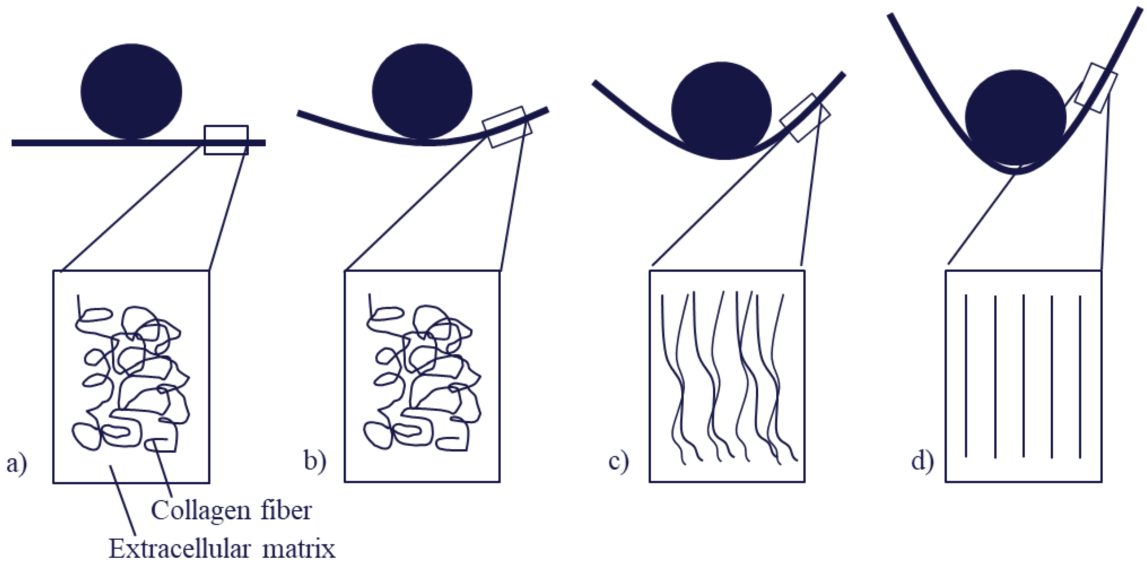

Figure 2-5: Collagen fiber deformation under the blunt impact. a) Curved collagen fibers within the extracellular matrix before impact. b) Negligible force transmitted to collagen fiber during the initial impact, no collagen fiber deformation. c) Tensile force transmitted to the collagen fibers to make them straightened once the skin membrane is engaged. d) Collagen fibers are fully straightened and elongation continues until rupture.

2.3.1 Nonlinear stress-strain response

Based on images obtained from the Scanning Electron Microscope (SEM), the evolution of collagen fibers under tensile loading until failure can be described in 4 stages. First, curved collagen fibrils are orientated and rotated towards the direction of the applied load. Second, the straightening of the collagen fibrils starts to take place while additional fibrils are re-orientated towards the tensile direction. Third, once the collagen fibrils are fully engaged and straightened, sliding, and delamination between fibers occur. Lastly, skin failure (open skin injury) happens as the fibrils fracture and curl back (Yang et al., 2015; Aziz et al., 2016). The 4 stages of collagen fiber deformation provide the skin with a nonlinear stress-strain relationship under tension (Figure 2-6). Although it is known that gradual breaking of the collagen fibers occurs when the fibers are fully engaged, estimation of the strain level at which the breaking starts (i.e., sub failure) is yet to be determined. It is also observed that initial damage that happens on the skin tissues does not lead to instant separation (brittle failure) as observed in bony material. The crack caused by the initial damage continues to grow under the applied load until the skin is completely separated (Yang et al., 2015).

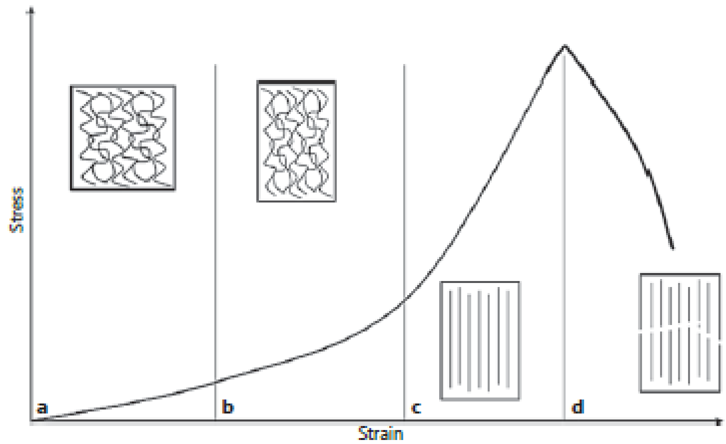

Figure 2-6: Stress-strain curve of skin. (Source: Aziz et al., 2016)

2.3.2 Anisotropy

Skin is anisotropic, which means it will respond differently under different loading directions (Ní Annaidh et al., 2012). The anisotropy property is due to a naturally preferred alignment of the collagen fibers within the skin at various regions of the body. The variation of this preferred direction of collagen gives rise to the descriptions made by Langer and the patterns of Langer's lines. The collagen fiber's resistance to the extension when subjected to loading yields higher reaction force and less elongation on the skin. Hence, the skin is stiffer when loaded along the Langer's line but withstands a shorter stretch before failure occurs compared to cross fiber samples. Figure 2-7 illustrates an example of the human skin anisotropy in terms of material stiffness under the *ex-vivo* tensile test. Both skin samples share similar stiffness during initial loading and the parallel sample reaches maximum stiffness at a lower stretch ratio compared to the perpendicular sample.

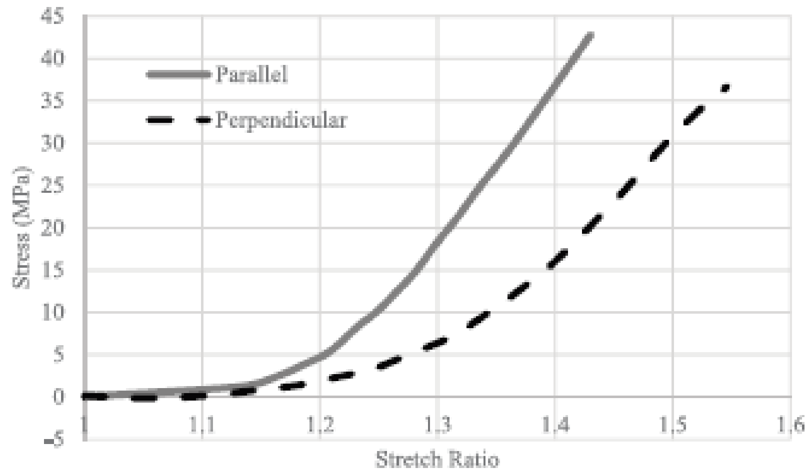

Figure 2-7: Skin's anisotropy effect. (Source: Joodaki & Panzer, 2018)

2.3.3 Viscoelasticity

Skin also exhibits viscoelastic characteristics, meaning that the mechanical response of skin is strain-rate dependent. This has been demonstrated previously using animal skin tissue. Shergold et al., (2006) conducted compression tests of pig skin tissues at strain rates between 0.004/s to 4000/s and observed skin stiffness variation between different applied strain rates. The skin tissues exhibit the highest stiffness response at the highest strain rate and vice versa at the lowest strain rate. In another study, Karimi et al., (2016) performed stress relaxation tests using rat skin tissues. (Figure 2-8). In the stress relaxation test, an instantaneous stress jump profile indicates the elastic portion of the skin, followed by stress decay which characterizes the viscosity part of the skin. The relaxation profile also correlates to the initial stretch level which is dependent on the loading rate of the test.

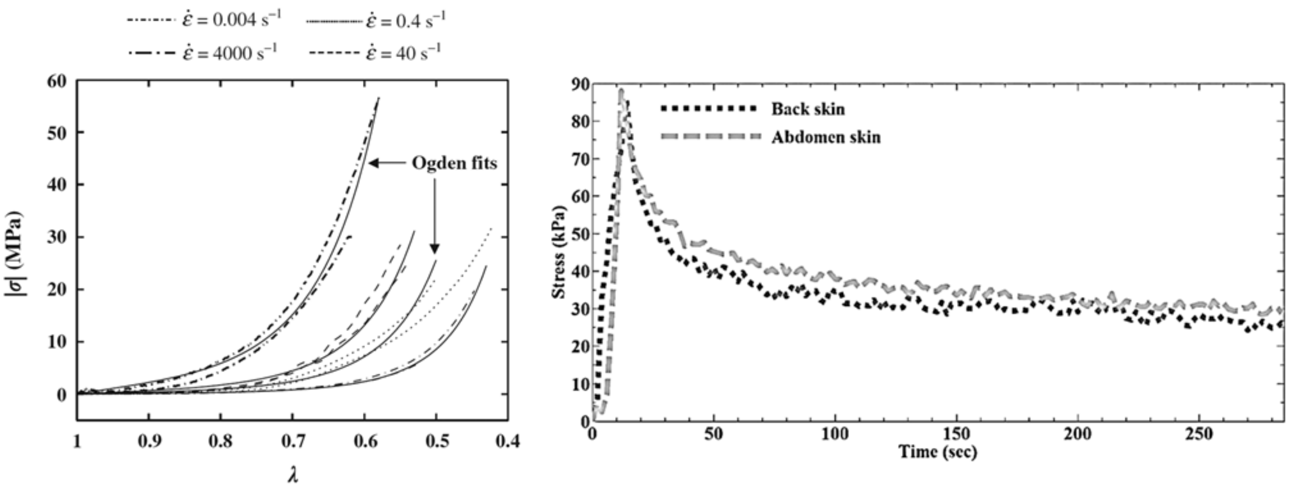

Figure 2-8: (Left) Strain-rate effect on pig skin; (Right) Stress relaxation profile of rat skin. (Source: Shergold et al., 2006; Karimi et al., 2016)

2.3.4 Aging Effects

Age is also an important factor that influences the skin's mechanical properties, especially its stiffness and elasticity. It is believed that skin becomes stiffer and with less extensibility due to calcification of elastin fibers and less crimped collagen fibers as maturation progresses (Sherratt, 2013). Escoffier et al. (1989) conducted 123 human tests with volunteers aged between 8 and 98 years old by applying torsion on their ventral forearm skin and concluded that skin's extensibility decreases while the stiffness increases with age. This agrees with previous findings by Grahame and Holt (1969), but disagree with Sanders (1973) where skin stiffness was reported to decrease with age after applying torque on the dorsal forearm skin of 19 human volunteers ages 6 to 61 years old. Escoffier et al. (1989) believed that this difference was likely due to different tested body regions where some locations may offer more skin flexibility than the others and therefore, recorded elasticity of skin-adipose tissues rather than the skin itself. Other studies reported that skin tissue in children and young adults was more compliant than a fully grown adult, and skin stiffness starts occurring around 15-25 years old (Alexander & Cook, 1976) or 30 years old (Agache et al., 1980). Diridollou et al. (2000) tested 206 human volunteers from 6 months old to

90 years old by conducting *in vivo* suction on their volar forearm skins and concluded skin's Young's modulus increases linearly with age. Boyer et al. (2009) pointed out the conflict of Young's modulus-age relationship could be due to the type of mechanical test performed. Boyer reported a decrement of Young's modulus with age under the indentation test after testing 46 female volunteers between 18 and 70 years old and stated that the unconfined test environment without using a guard ring measures the natural state of human skin. However, this is contrary to the results presented by Dulińska-Molak et al. (2014) who performed indentation tests on skin slices obtained from humans aged between 30 and 60 years old found the skin's Young's modulus increases with age. Furthermore, after performing bulge tests on 6 PMHS, Tonge et al. (2013) observed younger donors (43-59 years) exhibited stiffer responses than older donors (61-83 years).

2.4 Skin Experimental Techniques

Different mechanical test types such as indentation, suction, torsion, tension, and compression tests have been conducted on human skin using the *in vivo* or *ex vivo* approach. *In vivo* approach studies skin responses in its natural state where the skin is attached to underlying tissues on living organisms. This approach accounts for realistic physiological effects but makes it difficult to separate the influence of underlying tissues such as adipose and muscle based on test type. Furthermore, the *in vivo* study limits extreme testing conditions on the skin which can be intrusive and harmful to test subjects. Nevertheless, the *in vivo* approach provides the advantage of repetitive testing on living patients which can be beneficial to the healthcare industry. *The ex vivo* study, on the other hand, provides testing flexibility where the skin is completely excised from living organisms and therefore, allows skin failure testing to determine skin failure properties. Removal of the skin also provides a simpler testing environment where boundary condition is clearly defined, and isolated skin response can be tested. The challenges of *ex vivo* testing include the chance that skin properties might be altered since detachment from the body and may cause loss of nutrients and moisture. Because of this risk, extra precautions must be taken between the excision of the tissue and testing. A common practice to preserve the soft tissues is to place the tissue in saline solution and/or freeze the tissue if immediate testing is not performed. However, the effect of freezing on the mechanical properties of soft tissues has been inconsistent based on multiple studies (Clavert et al., 2001; Ng and Chou, 2003; Giannini et al., 2008; Huang et al., 2011; Jung et al., 2011; Ren et al., 2012; Arnout et al., 2013). Besides, *ex vivo* testing of the skin involves handling and inserting skin samples into test fixtures, without causing permanent deformation before testing or slippage during testing, can be challenging.

2.4.1. Tensile tests

Both *in vivo* and *ex vivo* approaches have been used on the tensile testing of human skin. The *in vivo* tensile tests place two tabs on the skin which are bonded with adhesives and displacement is prescribed to pull along the skin surface (Wan Abas & Barbenel, 1982; Manschot & Brakkee, 1986; Lim et al., 2008). The strain can be measured based on the distance between the tabs. Compared to other test types, the tensile failure test of human skin is the most common type performed *ex vivo*. Dogbone shaped or rectangular skin samples are normally prepared for uniaxial tensile tests. Quasi-static (0.0012/s) tensile tests have been performed using human back skin for different Langer line orientations to investigate its anisotropic property while dynamic tests (0.06-167/s) on human skin were also performed, looking into strain-rate effect on skin mechanical properties (Jacquemoud et al., 2007; Gallagher et al., 2012; Ní Annaidh., 2012; Ottenio et al., 2015). These tests defined key skin properties such as Young’s modulus, failure stretch, strain energy, initial stiffness, and ultimate tensile strength (UTS) which will be further discussed in Chapter 3. In addition to uniaxial tension, biaxial tensile tests on human skin were also conducted where square samples are made and loaded on test fixtures using hooks and strings to prevent any unwanted shearing effect (Lanir & Fung, 1974; Martin., 2000). The benefit of biaxial testing is the skin's anisotropy property can be examined since different stretch directions can be applied simultaneously, mimicking the stretch state similar to the living body. However, the use of hooks and strings for sample fixation can easily cause edge tearing and this limits its usage in dynamic tests.

2.4.2 Indentation tests

In indentation tests, different geometric probes, such as cylinder or sphere, are applied where the probe is perpendicularly pressed onto a small area of the skin surface and the reaction force and indented displacement are measured. It has been reported that experimental parameters such as probe size, shape, and indentation depths can affect the measurement of Young's modulus (Groves, 2012; Kuilenburg et al., 2013). Kuilenburg observed the skin's stiffness decreases when indented in micron level but increases when indented in macro-scale (in millimeters). In terms of the probe's geometrical effect, skin stiffness increases with indentation depth when using a cylindrical probe, while a spherical probe does not affect the stiffness after reaching a certain indentation depth (Jia, 2009; Grove, 2012). To explain this effect, a study conducted by Pailler-Mattei et al. (2008) determined the apparent Young's modulus only increases with increasing indentation depth for a ratio of contact radius to skin thickness larger than 0.5. To calculate Young's modulus, by assuming linear elastic response of the skin, Hertzian contact can be used to deduce relevant strain and stress from indentation depth and measured force, respectively (Johnson, 1985; Lin et al., 2009; Crichton et al., 2011). The same principles can also be applied to elastic-viscoelastic material where Young's modulus is measured as a function of time (Lee & Radok, 1960; Mattice et al., 2006).

The indentation tests conducted on human skin are usually *in vivo* and non-destructive. To understand the skin-piercing mechanism, the tissue fracture mechanics model developed by Shergold & Fleck, (2004) for deep penetration of soft solids has been used to investigate the relationship between insertion speed and resultant force on porcine skin (Barnett et al., 2015). The study was targeted at the surgical application where sharp penetrators are required to reach a precise target location at low insertion speed (~1-80 mm/s). Human skin failure under high rate indentation is rarely studied where studies tend to focus on investigating internal organ damage. With increasing interest in preventing unnecessary skin injuries from law enforcement personnel, high rate indentation tests on human skin using ballistic munitions have been performed to determine the human skin failure threshold (Bir et al., 2005; Kapeles & Bir, 2019).

2.4.3 Torsion tests

Torsion tests of the skin have been performed *in vivo* by applying a small torque on the skin surface using a circular disk and measuring the corresponding rotation (Sanders, 1973; Agache et al., 1980; Leveque et al., 1980; Grebeniuk & Uten'kin, 1994). The applied torque brings an immediate elastic deformation followed by time-dependent creep deformation. The torsion tests allow the calculation of Young's modulus based on the applied torque, skin thickness, disc radius, and measured rotation. Most of the applied torques range from 0.8 mN-m to 28.6 mN-m depending on the size of the circular disk with a corresponding rotation angle between 2 to 10 degrees and Young's modulus is determined between 0.02 MPa and 1.33 MPa. The measured Young's modulus is based on the is believed to be contributed by the epidermis layer of the skin tissue and the dermis layer is not tested due to the nature of the test.

2.4.4 Suction tests

In vivo suction tests involve elevation of skin under a vacuum using a circular dome-like apparatus. Early suction tests focus on superficial skin (i.e., stratum corneum) (Grahame & Holt, 1969; Alexander & Cook, 1977) and have evolved into commercial deep tissue testing to account for anisotropy using optical systems such as Dermaflex (Jemec et al., 1996; Gniadecka & Serup, 2006) and Cutometer (Barel et al., 1995). An empirical equation was developed by Diridollou et al. (2000) to estimate skin's Young's modulus based on the applied pressures, skin thickness, the radius of the probe, and elevation of the dome from the suction test that is based on an ultrasound device. In general, the applied pressure by the suction devices are less than 500 mbar and the measured Young's modulus lies between 56 kPa and 260 kPa.

2.5 Constitutive Models

The constitutive model employs an analytical equation to describe a material's stress-strain relationship. Different constitutive models have been used to describe the skin's response as observed in the experiment. The simplest constitutive model used is Hooke's Law where the skin is modeled as linear elastic solid, defined by Young's modulus. Although incapable of capturing the nonlinearity, anisotropy, and viscoelasticity, the linear elastic model is frequently used to describe *in vivo* experimental data where the skin is usually loaded at a small strain level and only the epidermis is characterized.

To capture the nonlinear stress-strain relationship, there are two models used: the bi-linear elastic model and the hyperelastic model. The concept of the bi-linear elastic model is an extension of Hooke's law where two Young's moduli are determined by separating the response into two rough straight lines at a certain strain threshold (Delalleau et al., 2008). However, the subjective choice of the strain threshold may result in different stiffness being obtained. To capture the continuity of the load curve, many hyperelastic models such as the Mooney-Rivlin (Mooney, 1940) and Ogden (Ogden & Hill, 1972) models have been used to model skin response and showed promising results. However, these constitutive models are isotropic and elastic and are unable to capture anisotropy and viscoelasticity without modification to their formulation (Shergold et al., 2006).

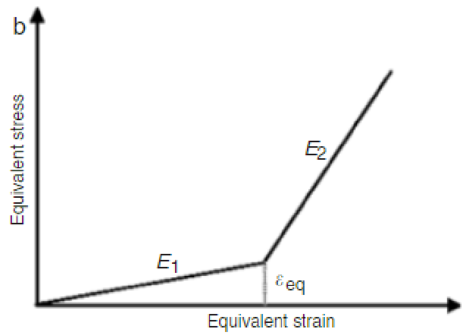

Figure 2-9: Bi-linear elastic modeling where E_1 is initial stiffness and E_2 is stiffness at fully engaged collagen fibers (Source: Delalleau et al., 2008)

Hyperelastic models are derived from the basis of a strain energy density function. The strain energy density function associates the internal strain energy of a material with some metric that describes the amount of deformation of material relative to its reference (no stress) configuration. For example, the Mooney-Rivlin model has a strain energy density function defined as $W = C_1(I_1 + 3) + C_2(I_2 + 3)$ where C_1 and C_2 are material parameters, and I_1 and I_2 are strain invariants. Łagan and Liber-Kneć, (2017), inspired by Martins et al. (2006), studied the effectiveness of 7 constitutive models on swine skin tissues under uniaxial tensile tests. The constitutive models examined were the Neo-Hookean model, the Mooney-Rivlin model, the Yeoh model (Yeoh, 1993), the Ogden model, the Humphrey model (Humphrey & Yin, 1987), the Martin model (Martins et al., 1998), and the Veronda-Westmann model (Veronda & Westmann, 1970). They concluded the Neo-Hookean model failed to capture the skin response and exhibited only a linear stress-strain response while the others were capable of simulating the full nonlinearity of the deformation (Figure 2-10). The study also reported the model's strain energy density function with exponential function and more than two material parameters had better fitting results than the polynomial function.

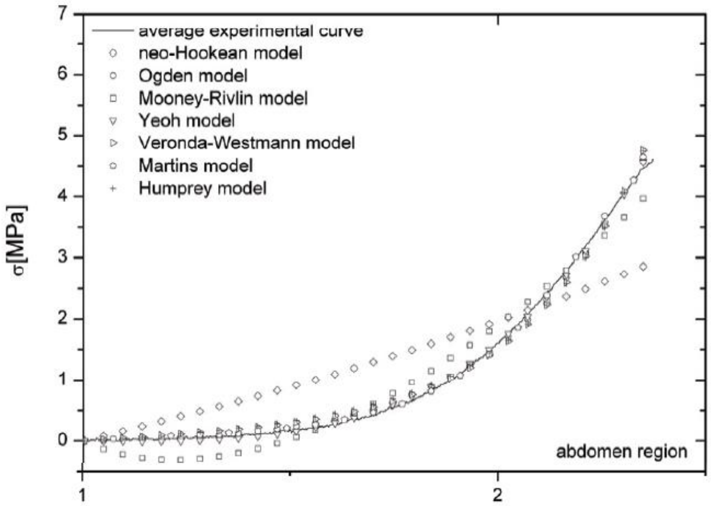

Figure 2-10: Hyperelastic models fitting comparison using swine skin tissue at the abdominal area (Source: Łagan & Liber-Kneć, 2017)

To account for the viscoelastic phenomenon along with the nonlinearity elasticity, a hyper-viscoelastic model using Quasi-Linear Viscoelastic (QLV) formulation (Fung, 1972) has been utilized for the skin. The QLV model simulates the viscosity and elasticity of the skin separately where the elastic response can be modeled using various hyperelastic models. For example, the Yeoh, Ogden, and exponential formulations for hyperelasticity have been used along with the QLV framework to simulate skin response (Liu et al., 2015; Wang et al., 2015). Details of the QLV model coupled with damage modeling will be discussed in Chapter 5.

For the skin anisotropy, the Gasser-Ogden-Holzapfel (GOH) model (Holzapfel & Gasser, 2001; Gasser et al., 2006), which uses both constitutive and structural parameters, is capable of simulating skin's response along and across Langer line orientations (Ní Annaidh et al. 2012) but requires additional work such as determining fiber dispersion factor and fiber preferred orientation angle through histological analysis. The GOH model adds in a fiber term to the existing ground substances' strain energy density function (i.e., Neo-Hookean) which involves the use of the invariant I_4, referred to as the square of fiber stretch. The additional fiber term provides the GOH model the capability to model the fiber response individually. To date, damage modeling of skin tissue has been rarely studied, by adding damage terms to the GOH model, Li and Luo (2016) claimed to be the first to model skin tissue damage under tension. The damage GOH model related ground substances and fiber damage with four additional parameters, which were optimized to control the curve sharpness upon damage occurring. Their damage model usability has been demonstrated using most of the human and animal skin experimental data conducted in the past. The author also concluded that the fiber stretch is an important parameter to model the fiber failure limit.

Table 1. Summary of skin constitutive models

Reference	Sample	Test type	Constitutive model	Model feature
Shergold et al., 2006	Pig skin	Skin	Mooney-Rivlin	Nonlinearity
	Pig skin	compression	Ogden	
Delalleau et al., 2008	Human skin	suction	Neo-Hookean	
Lapeer et al., 2010	Human skin	tension	Ogden	
Łagan & Liber-Kneć, 2017	Swine skin	tension	*See note**	
Ní Annaidh et al., 2012	Human skin	tension	GOH	Nonlinearity/ Anisotropy
Groves et al., 2013	Murine skin	tension	Veronda-Westmann**	
Liu et al., 2015	Pig skin	tension	QLV	Nonlinearity/ Viscoelasticity
Wang et al., 2015	Mouse skin	compression		
Li & Luo, 2016	Human/animal skin	tension	GOH with damage	Nonlinearity/ Anisotropy/ Damage

* 7 hyperelastic models were used for comparison in this study.
** Additional fiber strain energy density function is added to the Veronda-Westmann model to include anisotropy.

2.6 Finite Element (FE) Models

Finite Element (FE) models have been an alternative tool to investigate human body response through its high usability for different loading conditions. To develop a FE model, the constitutive model needs to be implemented to simulate a material's response. Although extensive research has been carried out in skin constitutive modeling, the transition from the analytical method to numerical implementation has been limited. At a non-destructive level, Flynn and McCormack (2008) have developed a three-layer skin model representing stratum corneum, dermis, and hypodermis layers to simulate wrinkling of human forearm skin by moving tabs along the skin surface towards each other. Each layer was modeled using different constitutive models including Neo-Hookean for stratum corneum, two QLV models using two different hyperelastic functions (i.e., an anisotropic hyperelastic) (Bischoff et al., 2002) for the dermis layer, and the Yeoh model for hypodermis layer. A similar FE model was also developed based on *in vivo* indentation tests carried out on different human skin areas (Flynn et al., 2011) by employing the Ogden-based QLV model to simulate skin hysteresis subjected to loading and unloading cycle. Groves et al. (2013) on the other hand, developed three individual skin FE models to represent skin anisotropy to different Langer's line directions by employing the Veronda-Westmann constitutive model with an additional fiber term (Weiss et al., 1996). The fiber term describes strain energy density functions including fiber under compression, crimped fiber, and straightened fiber.

In terms of skin injury modeling, Ní Annaidh et al. (2013) investigated the required skin failure force under stab penetration with a variation of blade sharpness using a skin FE model. The FE model which employs the GOH constitutive model can capture the force-displacement response of human skin under the stab penetration experimental data at a quasi-static rate

(100mm/min). The validated FE model was believed to be the first numerical model to simulate skin failure despite the skin's viscoelasticity not being considered in the model. Furthermore, Chanda and Upchurch (2018) employed a combined experimental-numerical method to simulate skin wound geometry and its evolution under the tensile test. In the study, a 'wounded' skin FE model, modeled with Veronda-Westmann constitutive model was constructed by creating a hollow wound where its dimension was obtained from physical skin simulant under a microscope. The FE model has been validated to study the effect of wound geometry on local straining as a result of skin surgeries. The authors claim the FE model was the first attempt to model post-injured skin. Lastly, the skin FE model in modern HBMs (e.g., GHBMC, v5.0) was modeled using the viscoelastic model with a single time constant and no failure criteria were included. Simplification of the skin FE model in HBMs on skin response under blunt impact has yet to be investigated.

2.7 Summary

In summary, the current state of the art and research gap of human skin injury is listed below:

- Skin laceration is the most common open skin injury which results in irregular skin tears.
- In-plane collagen fiber is the predominant load bearing of skin that resists tensile load, therefore, making tensile failure the primary failure mode of skin upon blunt impact. Under tension, the skin is nonlinear, viscoelastic, and anisotropy.
- An *ex vivo* uniaxial tensile test is the most frequent test carried out on human skin to obtain failure properties. The most up to date human skin failure dataset considered skin's viscoelasticity and anisotropy despite only studying one PMHS. Further, there is a lack of stress relaxation test datasets of human skin.

- Constitutive models derived from strain energy density function accurately simulates skin experimental data. QLV and GOH models are capable of capturing the skin's viscoelasticity and anisotropy, respectively. To date, there is only one analytical study focusing on modeling skin damage using the GOH damage model, but the numerical implementation has yet to be performed.
- The numerical implementation of human skin to study skin injury is limited. Numerical model applications of skin models include skin wrinkles, wounded skin progression, and skin failure under knife stab-penetration. However, there is a lack of skin FE damage models that can be utilized to model open skin injuries subjected to ballistic blunt impact.

CHAPTER 3 - Human Skin Characterization for Constitutive Modeling

Human skin mechanical data is essential for developing constitutive models that can describe skin responses. Hence, experimental characterization of human skin is presented in this chapter. Experimental work in this chapter consists of multiple tests, including uniaxial tensile tests to obtain tensile failure properties, stress relaxation tests to obtain viscoelastic property, and compression tests to determine human skin through-thickness compressive properties. The data collected were analyzed and used to inform the selection of an appropriate constitutive model. The goal of this chapter is to contribute to the current human skin tensile database by adding a failure data corridor and stress relaxation dataset. Portions of this chapter were prepared for a journal article titled "Combined destructive and viscoelastic characterization of human skin for constitutive modeling" intended for the *Journal of Mechanical Behavior of Biomedical Materials*.

3.1 Introduction

Human skin exhibits nonlinearity, anisotropy, and viscoelasticity based on recent extensive skin properties reviewed by Kalra et al. (2016) and Joodaki and Panzer (2018). In the past, these properties have been determined through *in vivo* and *ex vivo* tests. While human skin properties such as Young's modulus is often characterized in these *in vivo* tests within physiological loading range and rate, skin's viscoelasticity has also been examined through oscillatory loading to determine its complex modulus. One major drawback of oscillatory loading is that the resultant complex modulus is frequency-dependent and frequency sweep is often necessary to provide the entire spectrum of human skin's viscoelasticity. To overcome the drawback, one approach is to carry out ramp-hold tests such as relaxation or creep test which can separate the skin's elastic and viscous response in a time domain. Several ramp-hold tests have been conducted on *in vivo* human skin (Khatyr et al., 2004; Piérard et al., 2013) through suction. However, these *in vivo* studies do not allow viscoelastic information at higher stretch levels to be determined and effects from surrounding tissues cannot be eliminated as well. *Ex vivo* testing has been conducted on animal skins through tension and compression to determine their viscoelasticity (Xu et al., 2008; Liu & Yeung, 2008; Wang et al., 2015; Karimi et al., 2016), but this has yet to be performed on *ex vivo* human skin. In terms of destructive testing on human skin, Ní Annaidh et al. (2012) and Gallagher et al. (2012) conducted a quasi-static (0.01/s) and a dynamic (2 m/s) failure test of human back skin respectively by considering skin's anisotropy. Jacquemoud et al. (2007) also conducted uniaxial tensile tests on human forehead skin at a dynamic rate (55/s) which was reported to have occurred at automotive collisions. To date, only Ottenio et al. (2015) have performed destructive uniaxial tensile tests using multiple strain rates (0.06- 167/s) and considered anisotropy on human back skin although only one single PMHS was studied in the test. There remains a lack of data to fully represent human skin tensile failure by considering skin's anisotropy and rate dependency, especially at loading rates up to those experienced in ballistic blunt impacts. These data can contribute to the development of constitutive damage modeling of human skin as well as providing a feasible range of skin properties for developing future physical skin simulants. Therefore, the purpose of this chapter is to characterize human skin tensile failure and viscoelastic properties by considering inter-subject variation with strain rate that is applicable in between automotive crashes and ballistic impact events. The *ex vivo* viscoelastic dataset is expected to inform the selection of an appropriate constitutive model that can be used to model human skin tensile response. The destructive tensile test series provides a stress-stretch relationship of human skin that can be used in conjunction with the viscoelastic data to aid in the development of a human skin viscoelastic damage model.

3.2 Methods

3.2.1 Strain Rate Calculations

As part of test matrix development, test data should reflect skin properties under a range of target loading rates due to its viscoelasticity, however, the magnitude of strain rate in cases of the ballistic blunt impact remains unknown. To estimate an approximate range of strain rate, a HBM (i.e., GHBMC-O v5.0 model) which is frequently used in the automotive industry to study human response under car crashes was chosen to simulate blunt impact conditions. A list of kinetic energy-based less lethal munitions that are available commercially in the current market was identified and details of these munitions are presented in Chapter 8. Among all the less-lethal munitions, a 0.68 caliber (8.636mm in radius) rubber ball (3 grams) was chosen as the impactor for the blunt impact simulation. The rubber ball was modeled as a rigid body with an initial travel velocity of 100 m/s. The 100 m/s was chosen as it was the most common muzzle velocity of the available less lethal munitions. For the impact locations, the two muscle locations of the pectoralis major and rectus abdominis region were chosen to investigate potential strain rate discrepancy due to different boundary conditions (Figure 3-1).

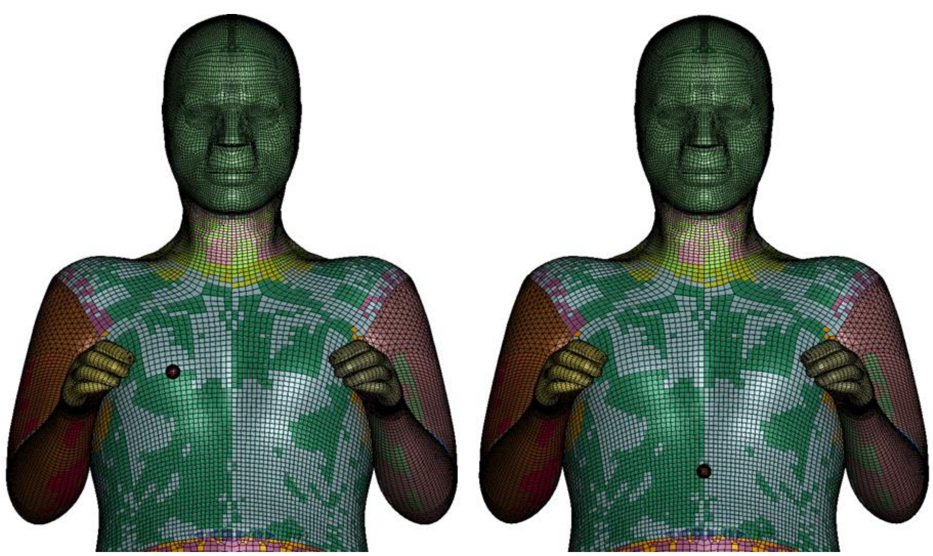

Figure 3-1: Impact location of GHBMC-O v5.0. (Left) pectoralis major. (Right) rectus abdominis.

The simulation data was output every 0.1 ms and terminated at 2 ms because only strain rates during the initial impact were of interest. Using the impactor center as the center of the impacted area, a square region approximately 35 x 35 mm^2 was defined (35 mm being two times the diameter of the impactor). Each element within the impacted area was chosen for extracting infinitesimal strain, in particular, the 1st principal strain was chosen because it represents tensile strain for calculating relevant strain rates (Figure 3-2). An average strain-time history was obtained from the elements within the impacted area. Based on the average strain-time history, a strain rate-time history can be calculated by dividing the strain at each time step by its current time. As a result, it was seen that strain rates up to 200/s and 350/s occurred at the abdominal and pectoral regions respectively (Figure 3-3). Therefore, dynamic skin characterization tests were intended to test at strain rates of similar magnitude. It should be noted that there were a couple of assumptions and limitations with the GHBMC HBM that may affect this preliminary assessment. First, the skin material in the GHBMC model is generally known to be stiffer than human skin to maintain model stability, and therefore the strain rate calculated in this preliminary analysis could be underestimated. Second, the skin material in the GHBMC v5.0 was modeled with a single viscoelastic time-constant, which may misrepresent actual skin response for the impacts assessed. Third, the impact locations were chosen subjectively, and any constitutive model misrepresentation of underlying tissues may also affect the skin response. Nevertheless, this was deemed to be the most suitable numerical approach to identify a target strain rate, and further study regarding re-assessment of the strain rate with an improved skin material model is necessary.

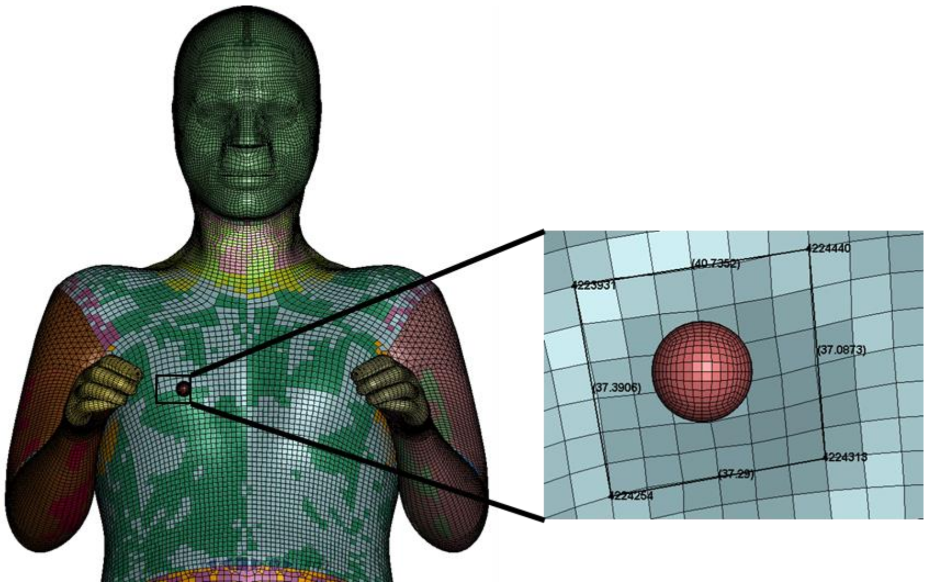

Figure 3-2: Area of interest to acquire the strain-time history of the ballistic blunt impact simulation.

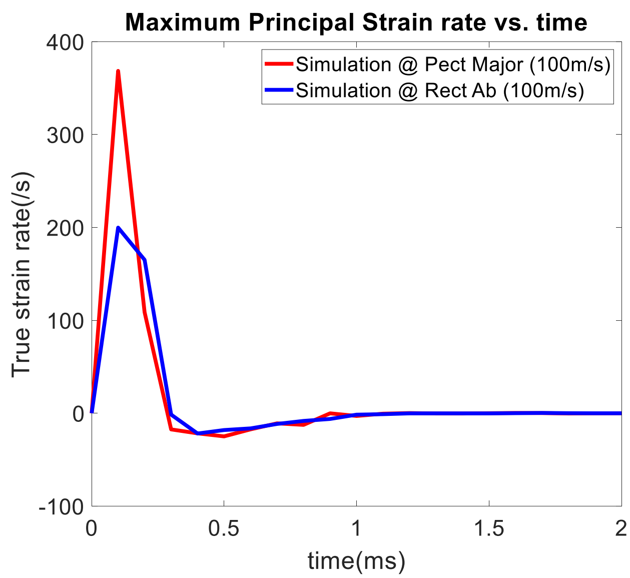

Figure 3-3: Strain rate-time history upon ballistic blunt impact at 100m/s.

3.2.2 Test Matrix Development

Three types of experimental tests were designed to determine the nonlinearity, anisotropy, and viscoelasticity of human skin. The first test was the uniaxial tensile test to determine the tensile failure properties of the human skin. Within the tensile test, three discrete strain rates were planned on two types of skin samples (i.e. parallel (0°) and perpendicular (90°) to the Langer's line orientation) which help to test the skin's anisotropy and strain rate dependency. The highest strain rate applied should be around a similar order of magnitude as the strain rate determined previously under the ballistic blunt impact simulations. After running pilot experimental tests on human skin, 180/s was chosen as the highest end of the applicable strain rate that was obtainable from the test rig while 75/s and 1/s were chosen as the lower magnitude of the loading rate.

In the stress relaxation test, an infinite fast loading rate, followed by some amount of holding period on the skin was desired to distinctly inform the elastic and viscous response. The step-hold profile was designed to include five consecutive strain levels up to 30% strain by assuming no skin damage occurs at these loading levels. However, the theoretical infinite loading rate cannot be physically carried out on mechanical devices, and the skin was uniaxially loaded as quickly as possible to minimize any relaxation response during loading. For the holding period, studies have shown approximately 70% of stress was dissipated on pig skin during the first 60 seconds of the holding period (Xu et al., 2008), while others have shown similar dissipation in less than 1 second on mouse skin under compression (Wang et al., 2015) and 90% dissipation within 60 seconds on rat skin (Karimi et al., 2016). These studies also show that no significant stress relaxation occurred after the rapid decay. Hence, a dwell period of 60 seconds was chosen for the stress relaxation test and preliminary results show a 50% to 70% stress relaxation between the five strain levels.

In addition to the tensile tests, a quasi-static non-failure compression test of human skin at low strain level (30%) was also planned to provide skin characteristic information which was perpendicular to the direction of loading that excludes the influence of the collagen fibers.

The approach was to maximize the number of skin samples within individual PMHS specimens for each test type, and Table 2 summarizes the test matrix designed for each PMHS specimen to capture the skin properties as mentioned.

Table 2: Summary of the test matrix. (Y=Yes, N=No)

Tests	**Stress Relaxation**		**Tensile**						**Compression**
Test rate	2 /s		1/s		75/s		180/s		0.01/s
Langer's line orientation	0 °	90 °	0 °	90 °	0 °	90 °	0 °	90 °	N/A
Sample #	2	2	2	2	2	2	2	2	3
Failure test	N	N	Y	Y	Y	Y	Y	Y	N

3.2.2 Skin Sample Preparation

Skin samples were excised from the back of six adult male post-mortem human surrogates (PMHS). All test procedures were approved by the UVA Institutional Review Board before any testing and the PMHS were screened for pre-existing pathologies to avoid skin diseases that may have affected skin quality. The PMHS represent an average of 57±11 years old, 178.6±3.8 cm in height, and 88.4±19.8 kg in weight (Table 3). Neither age nor sex factor was considered when selecting the specimen since this study aimed at providing a general human skin dataset corridor.

Table 3: PMHS information.

Specimen ID	**Age (years)**	**Height (cm)**	**Weight(kg)**
795	60	175.3	83.9
757	49	185.4	122
702	42	178	86
733	74	180.3	78.9
919	59	177.8	96.6
680	58	175	63

All PMHS were thawed for three consecutive days in a room temperature environment before skin excision took place. The orientation of the skin sample was determined with reference to anatomy illustration of the Langer's line (Langer, 1978), and both parallel (0°) and perpendicular (90°) samples with respect to the Langer's line were excised (Figure 3-4a). Custom printed stencils and sharpie markers were used to mark the contour and *in vivo* dimension of the skin samples prior to excision (Figure 3-4b). For the compression samples, three 1" x 1" skin samples were excised from the remaining available space. After marking, a surgical scalpel was used to excise the skin samples along the marked contour and excessive adipose tissues were carefully scraped off to avoid any permanent deformation developed on the skin (Figure 3-4c). This completed the skin excision process and each skin sample was wrapped in saline dampened gauze pad to prevent moisture loss and refrigerated at 4°C until testing, which occurred within 48 hours.

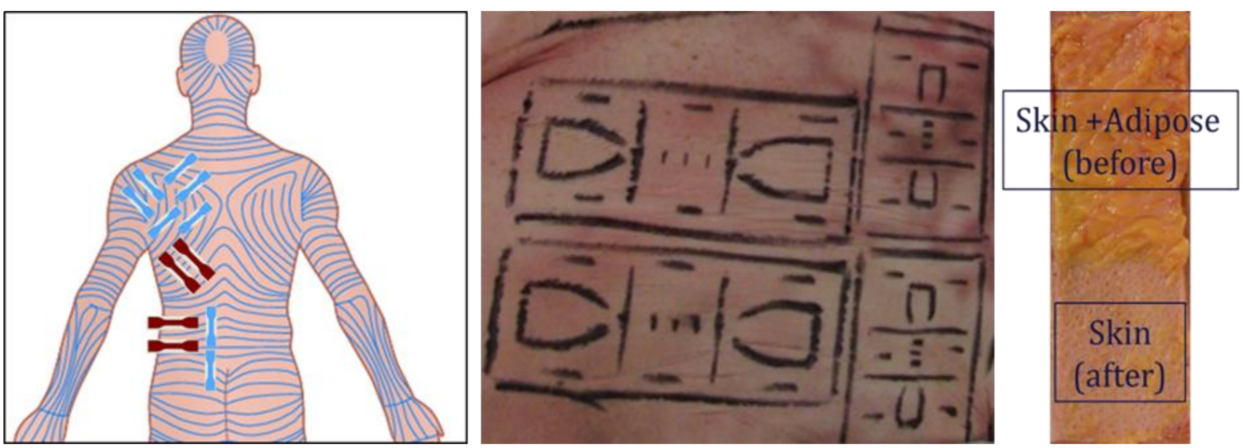

Figure 3-4: (a) Left: Locations of skin samples excised on the left side of the human back (blue – ST samples (n=4) and SR samples (n=4), red – DT samples (n=4)). (b) Middle: Marked in-vivo state of human skin before excision. (c) Right: Skin samples with underlying adipose tissue (before) versus isolated skin samples without the adipose tissue (after).

For each PMHS, 2 different sizes of skin samples were excised on the left side of the back of the PMHS (Figure 3-4a) for the tensile tests and the stress relaxation tests, the contralateral side of the back skin was reserved for the dynamic indentation test which will be covered in Chapter 4. An additional cutting step was performed during the day of testing where the excised skin was cut into a dogbone shape using a custom made hardened steel cutter based on ASTM D412 standard (Figure 3-5a) for dynamic tensile (DT) test while a scaled version (Figure 3-5b) of the standard was used for static tensile (ST) and stress relaxation (SR) test. The DT test refers to the 75/s and 180/s test cases while the ST test refers to the 1/s test case. Overall, a total of 90 (48 tensile test samples [24 DT and 24 ST], 24 SR test samples, and 18 compression samples) skin samples were collected from the six PMHS. Each skin sample's thickness was measured at three different locations within the sample gauge length using a digital caliper prior to testing and the measured mean thickness of all the tensile samples was 3.33±0.87 mm while the compression samples had a mean average thickness of 2.98±0.66 mm.

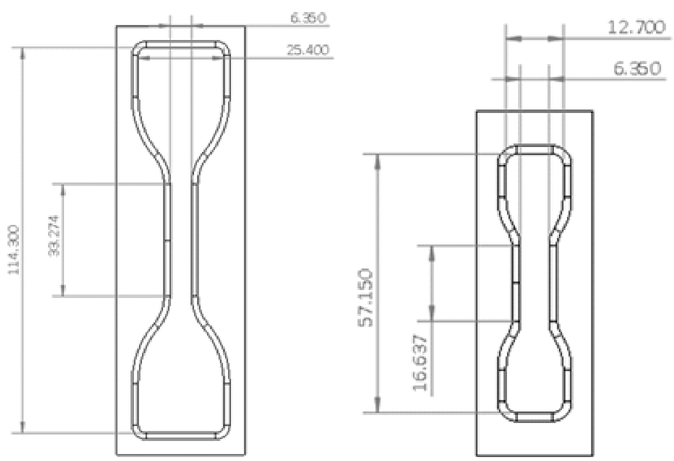

Figure 3-5: (a) Left: DT skin sample dimensions (mm). (b) Right: ST/SR skin sample dimensions (mm).

3.2.3 Test Fixture Design & Data Acquisition

To achieve the test rates for the tensile test series, two devices were used for different loading rates. The ST test case was performed using the Instron Model 8874 servohydraulic actuated test machine (Instron, Canton, MA) while the DT test cases were conducted on a custom-built gravity-based drop tower. In the ST tests, 3D printed carbon fiber reinforced plastic fixtures which consist of two sets of mounting holders and holding plates were used to sandwich the skin samples on both ends. One of the fixtures was connected to the top end of the Instron machine through swivels and connecting rods, this provides flexibility which helps to prevent unnecessary in-plane shear developing on the skin during testing. The other end of the fixture was connected to a 1000 lbf (4.4kN) Honeywell model 31 piezoresistive one axis load cell (Honeywell, Charlotte, NC) that was fixed on the Instron base. The ST tests were initiated by moving the crosshead of the Instron machine at 16 mm/min until skin failure occurred.

A similar concept utilizing mounting holders and holding plates were used to sandwich skin samples in the DT tests where the top part of the fixture was connected to the load cell. The load cell was attached to the frame of the test rig which was bolted to the base of the drop tower. The bottom fixture was attached to sliding rods which extended upwards connecting to an aluminum plate. The aluminum impactor was allowed to drop at two different heights, creating approximate travel velocities of 2.5 m/s and 6 m/s which were measured by a velocity gate right before the impact occurred. Upon impacting the aluminum plate, the kinetic energy pushes the sliding rods and that creates tensile deformation on the skin samples until failure. A rubber pad was placed on top of the aluminum plate to avoid excessive damage and vibration from occurring between the two metallic materials. A travel distance of 3 times the gauge length of the skin sample was allowed before the aluminum plate hit a honeycomb which acts as deceleration to end the impact process. An overview of the test fixture design for both test series is illustrated in Figure 3-6.

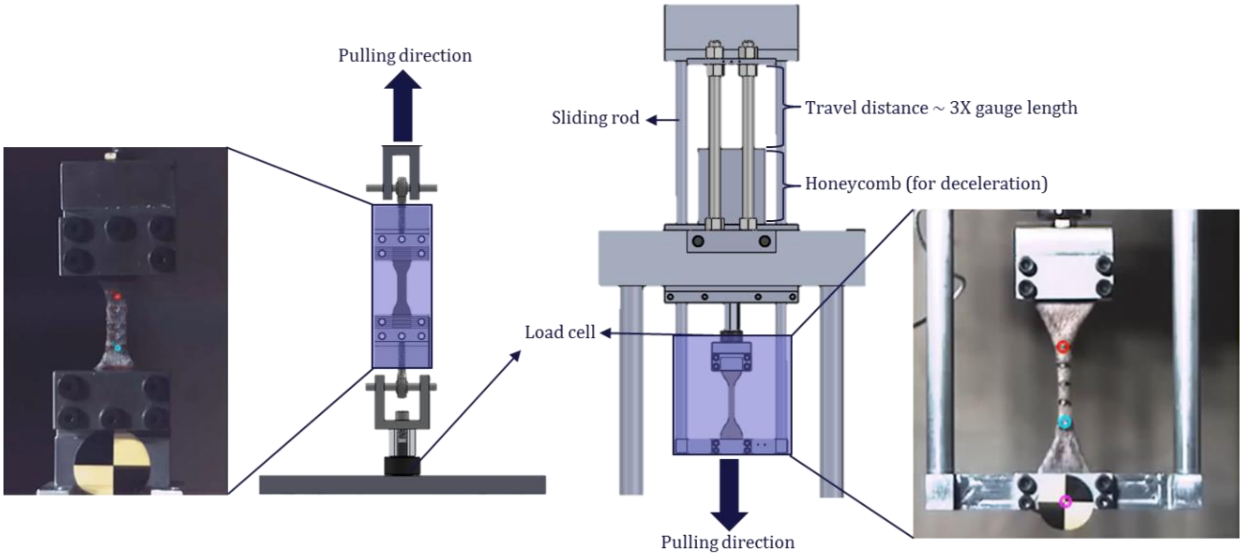

Figure 3-6: (Left) Uniaxial ST test setup. (Right) Uniaxial DT test setup.

The dogbone sample was clamped with an additional 80 grit sandpaper at both ends of the test fixture to avoid slippage during testing. After clamping, the skin sample was loaded until reaching its in-vivo length by comparing it to an in-vivo reference length rod (Figure 3-7) before initiating the test. Data acquisitions include data sampling rates of 1000 and 10,000 Hz and a Memrecam GX-1 high-speed camera (NAC Image Technology, Simi Valley, CA) was used to record test videos at 1000 and 10,000 fps for ST and DT tests, respectively. Sharpie markers within the skin gauge length which were predetermined on the back of PMHS before skin excision were used for determining deformation history through video tracking software (Tracker, ver. 4.11.0). A trigger box was utilized to activate data acquisition of the load cell and video recording simultaneously when the test was initiated.

Figure 3-7: Skin sample loaded to in-vivo length by comparing with a reference length rod prior to testing.

Stress relaxation (SR) tests and compression tests were performed using the Bose ElectroForce Testing Machine (TA Instruments, New Castle, DE). A similar test fixture and sample setup as mentioned in the ST test was also employed for the SR test. A series of displacement-controlled step-hold profile was used by subjecting the skin samples to approximately 10%, 15%, 20%, and 30% engineering strain at the fastest loading rate (i.e. 0.3 m/s) achievable by the test machine without overshooting the programmed profile to obtain the instantaneous elastic response, each step was followed by a 60 seconds dwell period to collect the relaxation response. The experimental force was measured using a 50 lbf (222.41 N) Bose model WMC-50-456 one axis load cell (TA Instruments, New Castle, DE) at a data sampling rate of 5000 Hz and gauge length deformation were determined through video analysis as described in the tensile test series.

Unconfined compression test was performed by subjecting the skin sample to 2" diameter platens and the test was initiated after applying a 0.2 N pre-load on the samples. While the base platen was fixed in motion, the top platen, programmed to move uniaxially at an average speed of

1.8 mm/min compresses the skin to its 30% strain. The compressive strain of the skin samples was calculated based on the machine crosshead displacement history. Since thickness varies between each skin sample and having 0.01/s as the target loading rate, the travel velocity of top platen was programmed differently for each skin sample by multiplying the strain rate by 30% of the measured skin thickness.

3.2.4 Parameters of Interest & Data Processing

From the measured force and the video tracked displacement, engineering stress-stretch curves of the skin samples are constructed. The engineering stress was calculated by dividing the measured force by the initial undeformed cross-section area. The stretch ratio was defined as the ratio between the current gauge length and the original gauge length. An example of the experimental engineering stress-stretch curve is plotted (Figure 3-8), showing 5 skin parameters that were of interest to represent skin properties. The definition of each parameter is explained as follow:

- Ultimate tensile strength (UTS): Maximum force divided by the original cross-section gauge area.
- Strain energy: Area underneath the engineering stress-stretch curve.
- Initial Young's modulus (E_1): Slope of the stress-stretch curve taken at the initial 5% of the UTS.
- Young's modulus (E_2): Slope of the stress-stretch curve taken in between 30% and 70% of the UTS.
- UTS stretch (λ_{UTS}): stretch ratio at UTS.
- Failure stretch (λ_f): stretch ratio at superficial damage occurs.

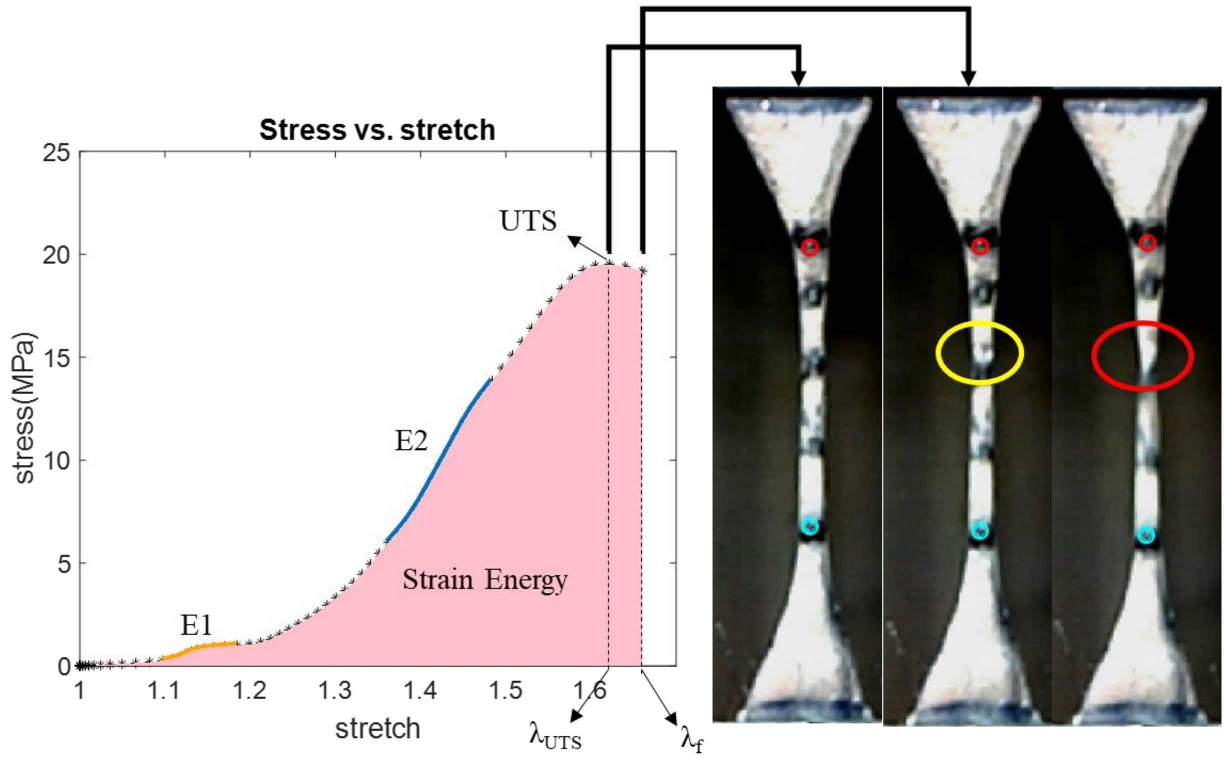

Figure 3-8: Example of engineering stress-stretch curve of human skin under uniaxial tensile test. The yellow circle shows superficial damage. The red circle shows further skin separation which is not shown in the graph.

Pre and post-test experimental data history were recorded and a range of data of interest was determined through video analysis and force measurement data. The initial data point was determined from video analysis by tracking the movement initiation of the marker within the sample gauge length. The reason to use the video analysis technique was to make sure the deformation history of the sample was captured (i.e. initial elongation with very little force) as opposed to relying on the displacement of the clamps. The end data point where the failure occurred was determined when a superficial tear was observed from the experimental footage. The raw data was filtered using the SAE J211 standard with channel frequency class (CFC) 600 (1000Hz cut-off frequency).

To calculate mean and standard deviation responses of each test configuration (e.g., all 0 ° samples tested at 1/s case) within the tensile test series where different failure stretches occurred, an arc length normalization approach (Figure 3-9) was adopted:

1. A pivot point (indicated as a blue asterisk in Figure 3-9) is chosen based on the UTS of each stress-stretch curve which separates the curves into two groups: pre-pivot curve and post-pivot curve.
2. Arc lengths of each pre-pivot curve and post-pivot curve are calculated separately and used as normalization parameter to compute respective normalized arc length.
3. Average and standard deviation of interested parameters i.e. stretch ratio and stress are calculated in the normalized domain.
4. The average response is constructed by coupling the average pre-pivot and the average post pivot curves. To develop the data corridor, two additional stress-stretch curves which represent the upper (stiffer) and lower (softer) bound of the skin's response are also developed using the above steps with a slightly different approach. The upper bound (UB) curve is constructed by taking the lower limit of the stretch ratio and upper limit of the stress values while vice versa for the lower bound (LB) curve.

Mann-Whitney U-tests (a non-parametric equivalent of two-sample t-tests) were performed using the *ranksum* function in MATLAB R2018b (Mathworks Inc., MA, USA) to determine the statistical significance (p<0.05) from the effect of strain rate and skin orientation with respect to the Langer's line on skin properties.

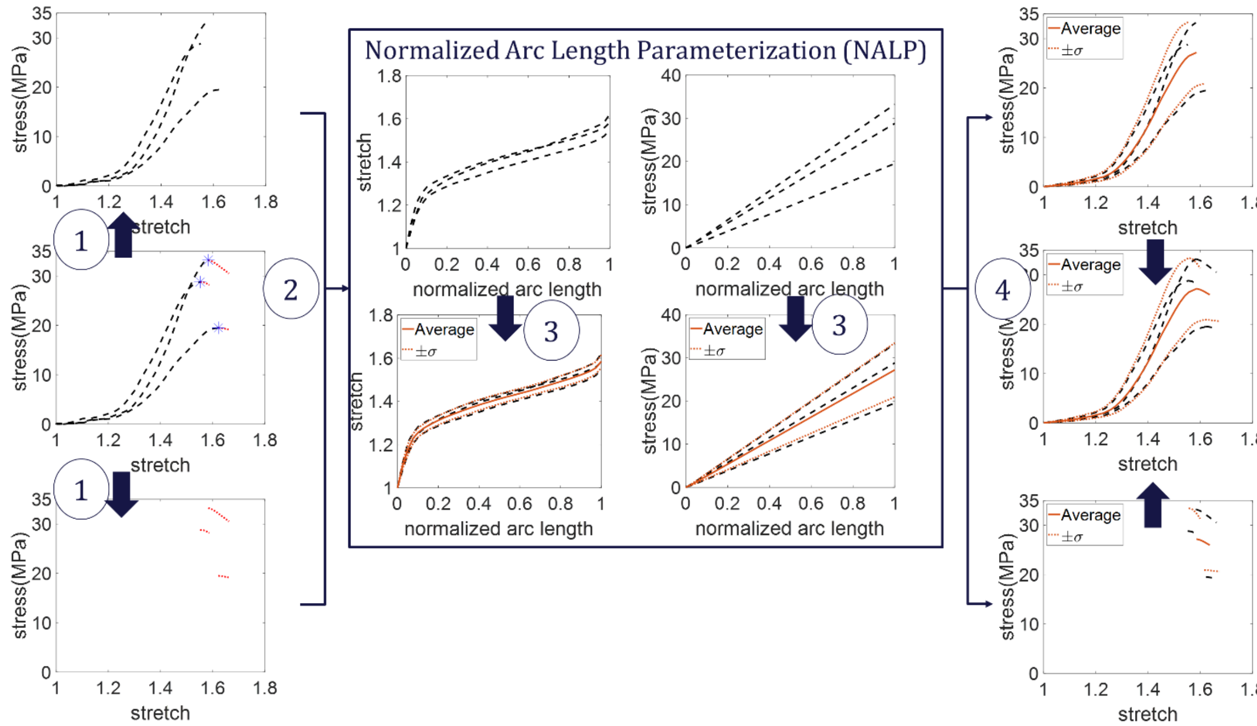

Figure 3-9: Workflow of average stress-stretch curve development.
Note: Only plots of pre-pivot curves in the normalized domain is illustrated in the NALP process.

3.3 Results

3.3.1 Uniaxial Tensile Tests

Table 4 summarizes the average mechanical properties of the skin samples and a visual interpretation of the results is also displayed in

Figure 3-10. Among the 48 skin samples, 6 samples (1x ST0, 3x ST90, 1x DT0, 1x DT90) slipped out of the test fixture and were permanently deformed during testing, therefore, these samples were excluded from the data analysis. Figure 3-11 illustrates a successful damage skin sample from the uniaxial tensile test.

Table 4: Average tensile properties of human skin.

Sample orientation	Strain rate (/s)	UTS (MPa)	Strain Energy (MPa)	E_1 (MPa)	E_2 (MPa)	λ_{UTS}	λ_f
Parallel	1 (n=11)	28.3±6.3	8.4±2.8	5.9±1.9	88.1±23.6	1.66±0.08	1.75±0.14
	75 (n=5)	20.5±7.8	5.3±2.5	10.0±6.6	73.2±27.0	1.52±0.09	1.59±0.13
	180 (n=6)	25.5±5.4	6.1±1.5	7.1±2.1	81.7±27.2	1.59±0.09	1.65±0.03
Perpendicular	1 (n=10)	22.0±4.5	7.1±1.2	3.5±0.9	46.2±14.8	1.95±0.15	1.99±0.15
	75 (n=5)	16.6±5.8	4.9±1.6	6.6±1.6	53.3±24.8	1.62±0.05	1.69±0.12
	180 (n=6)	20.4±4.7	5.9±1.3	7.3±1.9	62.9±20.4	1.61±0.05	1.67±0.10

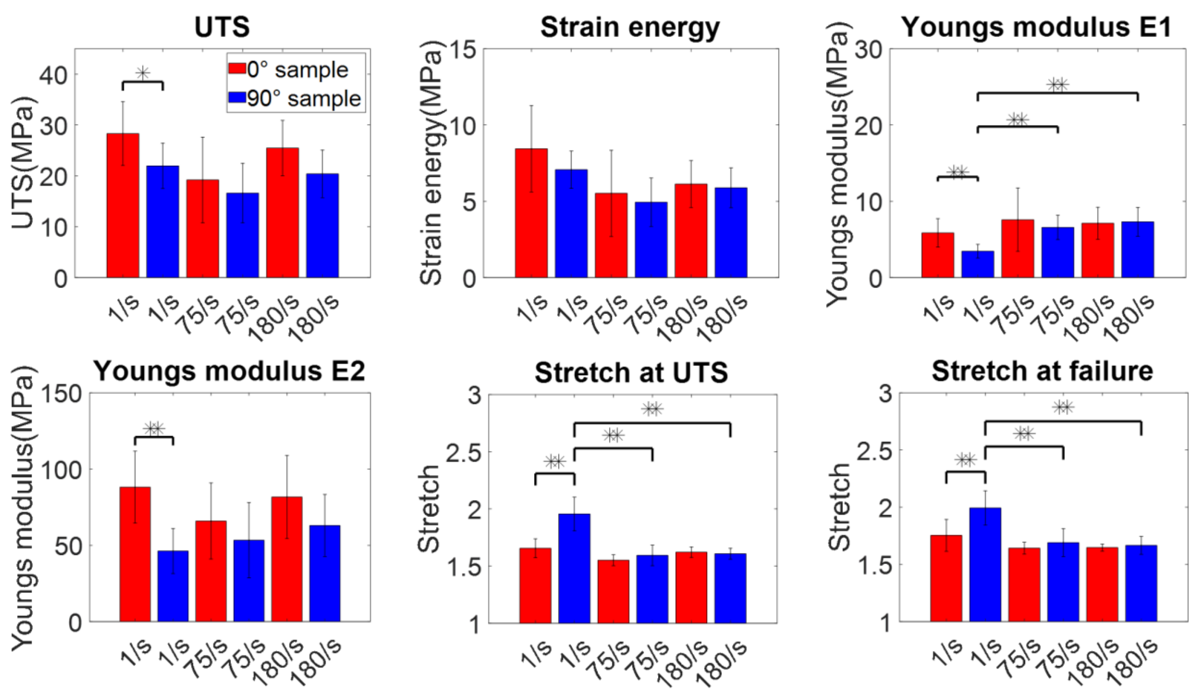

*Figure 3-10: Mann-Whitney U-test results (*p<0.05, **p<0.01).*
1. Effect of skin orientation with respect to Langer's line on skin response under the same loading rate.
2. Effect of loading rate on skin response under the same skin orientation.

Figure 3-11: Post-test photo of damaged skin sample from the tensile test.

For the skin samples tested at the same strain rate, the parallel and perpendicular samples were compared, and average, UB and LB responses for each test condition are illustrated at small strain (Figure 3-12) and full loading response including failure (Figure 3-13). Results from the statistical analysis show the skin response to be significantly different in terms of UTS (p=0.028), failure stretch (λ_f) (p=0.0024), initial Young's Modulus (E_1) (p=0.0039) and Young's Modulus (E_2) (p=0.0024) between the parallel and perpendicular samples at the static loading rate but no significant differences were found in both dynamic loading groups. The strain energy was found to be insignificantly different between the parallel and perpendicular samples under the three loading rate groups.

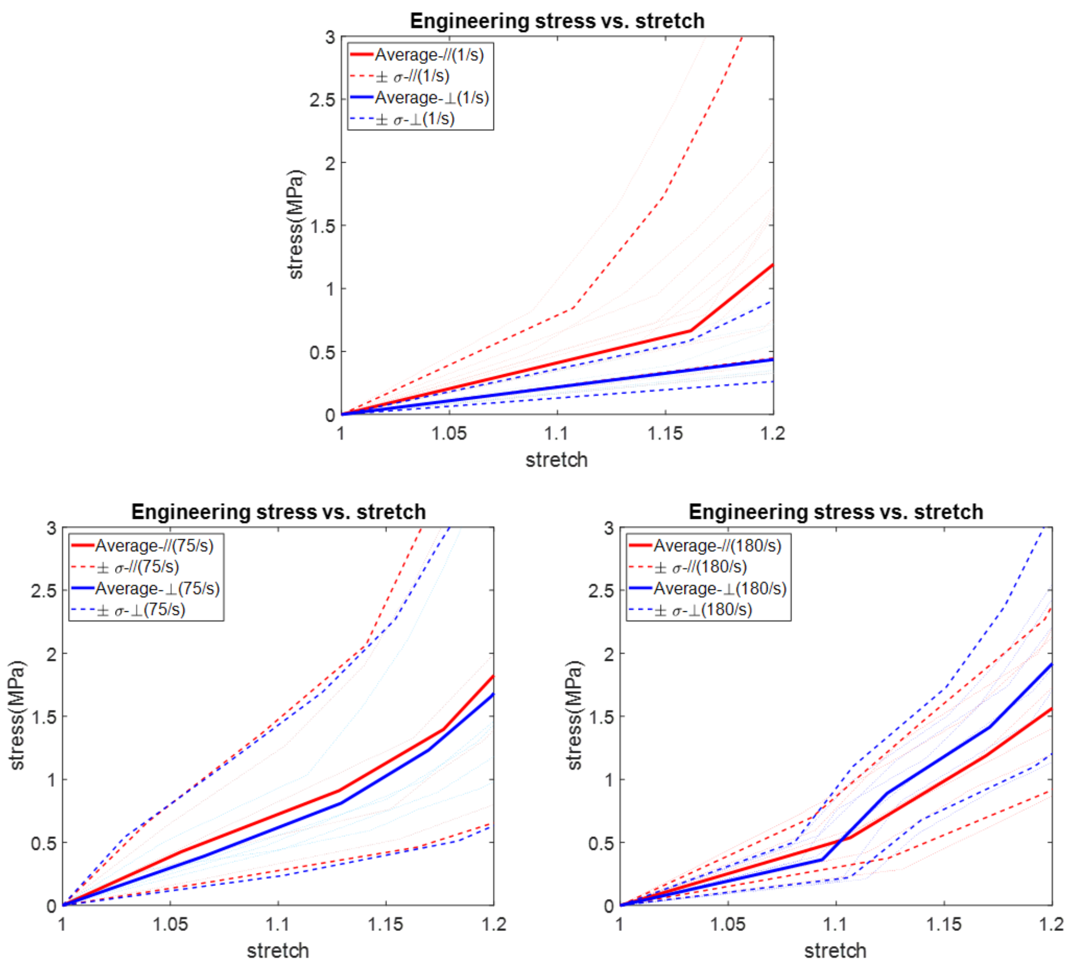

Figure 3-12: Comparison of skin sample initial loading response between different orientations (red-parallel, blue-perpendicular) under three loading rate groups (1/s (top), 75/s(bottom left), 180/s(bottom right)).

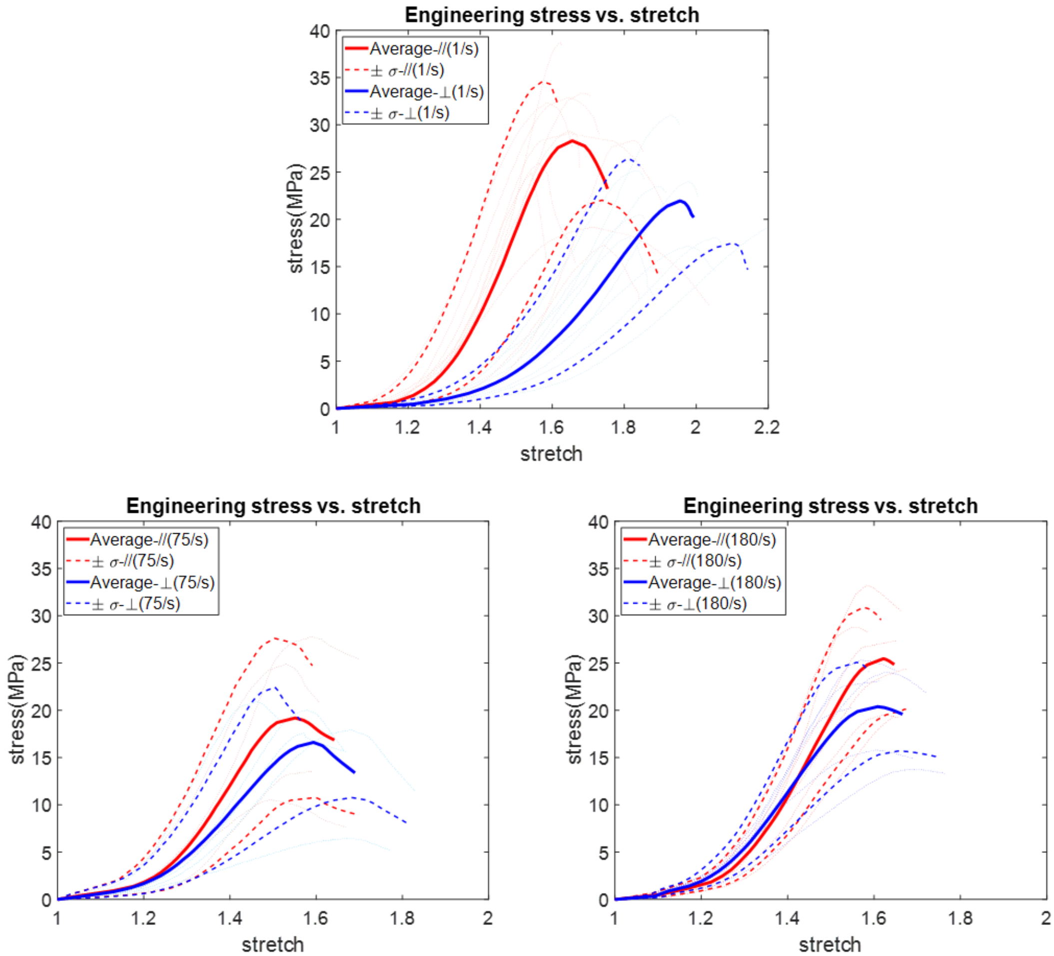

Figure 3-13: Comparison of skin sample full loading response between different orientations (red-parallel, blue-perpendicular) under three loading rate groups (1/s (top), 75/s(bottom left), 180/s(bottom right)).

To investigate the effect of strain rate on the skin response, the results were grouped between the parallel and perpendicular group (Figure 3-14). From the statistical analysis of the perpendicular samples, failure stretch (λ_f) and initial Young's modulus (E_1) were significantly different when comparing tests between 1/s and 75/s (p=9.9e-4). Similar results were also observed between 1/s and 180/s group on failure stretch (p=9.9e-4) and initial Young's modulus (E_1) (p=0.0016). However, the UTS, Young's modulus (E_2) and strain energy of the perpendicular samples were statistically similar. For the parallel samples, no statistical difference was found when compared between different loading rate groups.

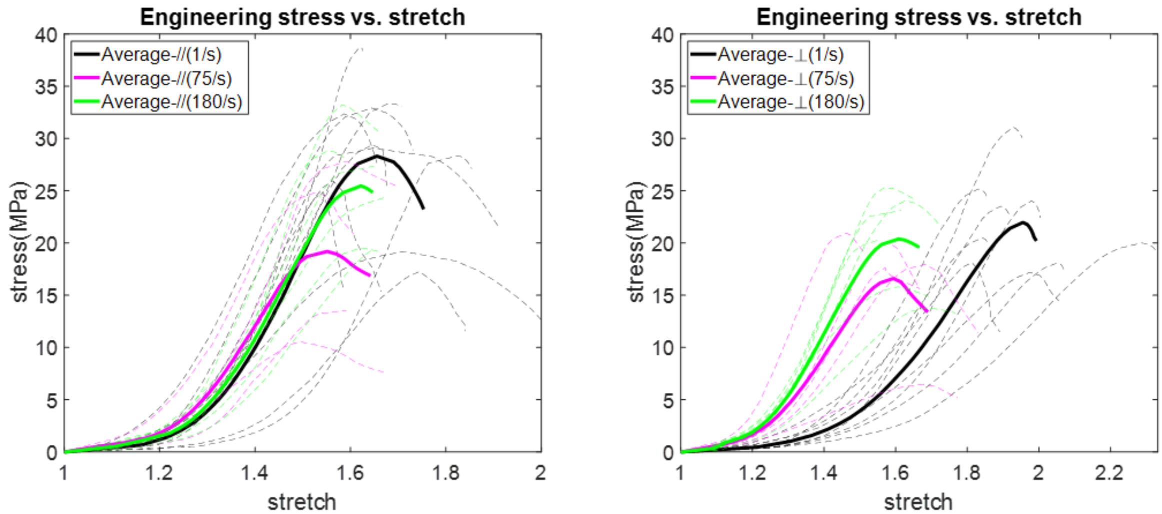

Figure 3-14: Comparison of skin sample response of two different skin orientations between different strain rates (parallel samples (left), perpendicular samples (right)).

3.3.2 Stress Relaxation Tests

All skin samples (n=24) were tested successfully without having slippage issues in the stress relaxation tests. Viscoelasticity was observed in both parallel and perpendicular samples with increasing peak stress at each ramp process followed by decaying of stress during the dwell period (Figure 3-15a). Although similar stretch profiles were prescribed, the average parallel samples exhibit higher peak stress than the average perpendicular samples, and a nonlinear stress-stretch relationship was observed on both sample types (Figure 3-15b) while the reduced relaxation time history (determined by normalizing stress decay response at each step with its corresponding peak stress) was independent of the skin orientation (Figure 3-16). Hence, for each step-hold, an average reduced relaxation time history (n=24, by combining the parallel and perpendicular samples) was computed and an overall reduced relaxation time history (n=120) taken from all step-hold regardless of the skin orientation was also determined along with responses within one standard deviation (Figure 3-15c).

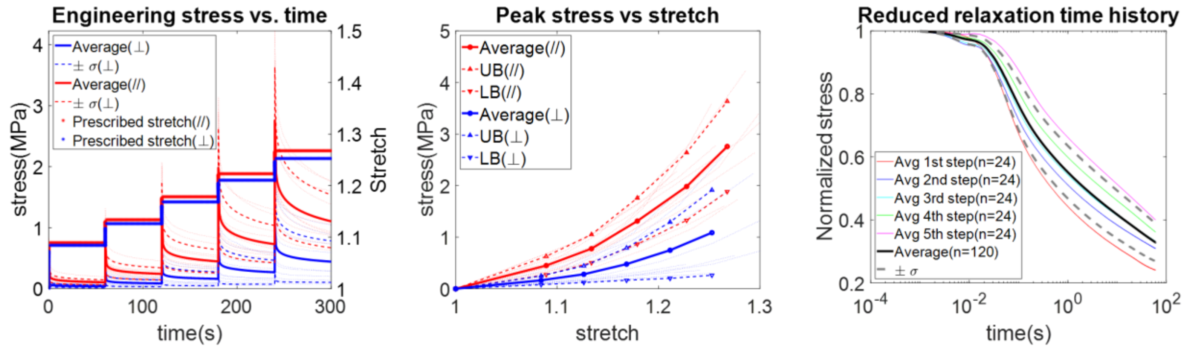

Figure 3-15: (a) Left: Average stress relaxation response of parallel (thick red) and perpendicular (thick blue) skin. (b) Middle: Average peak stress of parallel (thick red) and perpendicular (thick blue) skin at each step hold. (c) Right: Average reduced relaxation time history of individual step-hold profile.

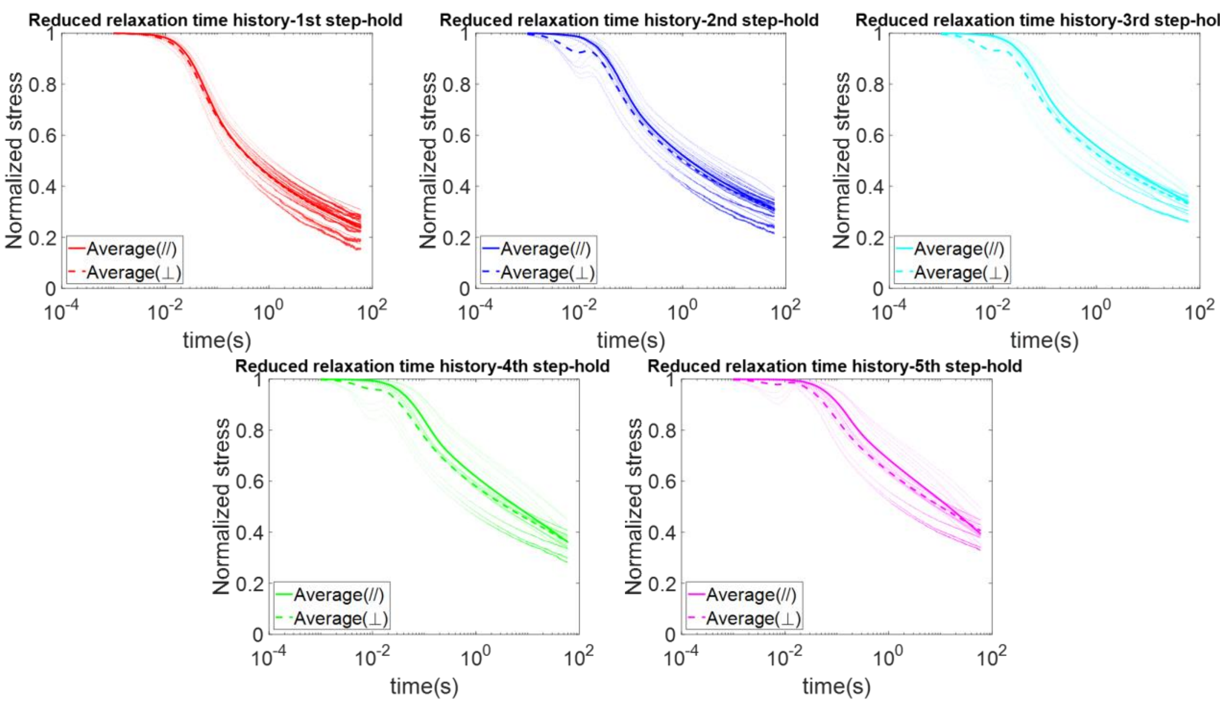

Figure 3-16: Comparison of stress relaxation response between parallel and perpendicular samples at each step-hold process.

3.3.3 Compression Tests

Figure 3-17 illustrates the average, UB, and LB compressive response of 18 human skin samples conducted at the quasi-static rate (0.01/s) where the skin's through-thickness property was measured. Similar to the skin tensile data, the skin under compression also exhibits the stress-stretch nonlinearity. The measured compressive stress is lower by two orders of magnitudes compared to the skin tensile properties due to the quasi-static loading rate.

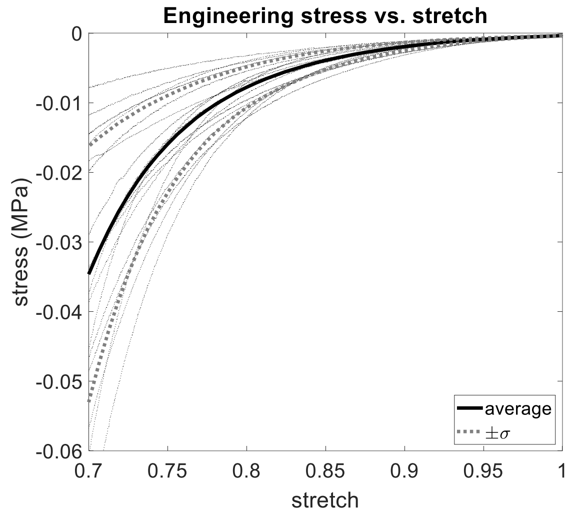

Figure 3-17: Average compressive stress-stretch response of human skin.

3.4 Discussion

A comprehensive test matrix including tensile, compression, and stress relaxation tests has been developed to strengthen the current human skin dataset for constitutive modeling by considering nonlinearity, anisotropy, viscoelasticity, damage, and inter-subject variability (six human subjects). In this chapter, the test matrix investigated skin data from a pool of a wide human population group aged between 42 and 74, producing average, UB and LB skin failure responses under tension at different strain rates and skin orientations. Moreover, identifying human skin's viscoelastic response using *ex vivo* stress relaxation test and compressive properties of human skin at the quasi-static rate were also determined for the first time.

To maximize the number of human skin samples for the test matrix, the mechanical properties of the human back region were treated as homogeneous, and the effect of location was not considered in this study. Although it has been examined, some of the mechanical properties of human skin appear differently across human back regions (Ní Annaidh et al. 2012) and it is believed the difference is due to the Langer's line distribution across body regions. Therefore, this study considered the spectrum of the skin properties at different body regions by characterizing two categories of skin orientation with respect to perceived Langer's line.

In the stress relaxation tests, the average of the parallel skin samples exhibits higher peak stress at each step hold process when compared to the perpendicular skin samples. The peak stress of both sample types increases in a nonlinear fashion as the stretch level increases. For the relaxation response, both parallel and perpendicular samples show very similar results regardless of stretch level. This indicates the fiber component in the parallel sample only contributes to the instantaneous elastic response and the relaxation response is mainly dominated by the ground substances of the skin. Overall, the stress relaxation test shows the skin elastic response is nonlinear and stretch dependent while its relaxation response is stretch independent where the reduced relaxation time history at each step-hold are all within 1 standard deviation corridor of the overall response. These results satisfy the requirement of the Quasi-Linear Viscoelastic (QLV) constitutive model as proposed by Fung (1972) which models the temporal response of biological tissues, and this can be coupled with various hyperelastic (isotropic or anisotropic) constitutive models. The selection of the QLV model was also consistent with other viscoelastic tests conducted on animal skins (Xu et al., 2008; Karimi et al., 2016; Liu et al., 2015; Wang et al., 2015)

By looking at the tensile failure properties, UTS and Young's modulus (E_2) of the perpendicular samples were statistically lower than the parallel samples and were only observed in the 1/s group. These partially agree with Ottenio et al. (2015) as the author reported the same trends are observed regardless of the strain rate. The disagreement between the current study and the literature data (Ottenio et al., 2015) was thought to be a different comparison approach as Ottenio et al. (2015) concluded the trend by grouping skin samples regardless of the loading rate while the current study isolated rate effect from the skin sample types, concluding the data trend just from the skin orientation perspective.

Human skin anisotropy was demonstrated in terms of UTS, initial Young's Modulus (E_1), and failure stretch (λ_f) at 1/s loading rate but the behavior becomes less distinct as loading rates increase (75/s and 180/s). The transition of skin's anisotropy at static strain rate to isotropic at dynamic strain rates was also found in porcine and human scalp tissues (Trotta & Ní Annaidh, 2019). A similar trend was also observed in pig skin under tension where the pig skins parallel to the spine was reported to be less rate-sensitive than the perpendicular skins, resulting in similar stiffness between skin samples in both directions under dynamic loading rate (Lim et al., 2011). To explain this phenomenon, it is believed that when loading the perpendicular skin samples, viscous ground substances was the main-loading component of skin, and by increasing loading rate, this stiffens up its mechanical properties and eventually reaching a similar mechanical response as the parallel sample. However, the stress stiffening effect was less pronounced in the parallel sample when the loading rate was increased. In the parallel skin samples, the collagen fibers were the main load-bearing component and it was shown from the stress relaxation test in this study that the fibers only contribute to the elastic response with a minimum viscous response (indicated by very similar relaxation responses between the two sample types). Rehorn et al. (2014) performed stress relaxation tests of muscle collagen fibers with various loading rates between 0.1/s and 10/s and found similar results where the fibers became rate insensitive after exceeding 3/s loading rate.

The strain rate effect on the perpendicular skin sample response takes place during the initial loading where the initial Young's modulus (E_1) increases as the strain rate increases. The initial stiffness history at the toe region might affect the extensibility of the skin sample and therefore, results in different failure stretch which was also reported to be statistically different and rate-dependent in the perpendicular samples. Overall, the amount of strain energy required to cause failure was not statistically different regardless of strain rate. This indicates the skin orientation with respect to the Langer's line only alters the extensibility and initial stiffness of the skin, but the overall energy required to cause skin failure was similar.

When comparing the tensile test results to previous literature data, the UTS and strain energy were similar and within a comparable range under similar loading rate conditions (Figure 3-18). However, there were differences observed when comparing with Ottenio et al. (2015) at the dynamic strain rate group (167-180/s) where a lower Young's modulus (E_2) was obtained in this study. Despite having similar loading rate conditions, the difference may be due to several reasons. First, only a single PMHS was tested in the previous study where inter-subject variation was not considered, and the result was drawn based on a single PMHS (90 years old). Elderly skin is generally believed to be stiffer and less extensible due to the straightening of collagen fibers as part of the aging process (Tonge et al., 2013). Second, a different testing protocol from the previous study where 2N preload was applied may have brought the skin samples to different stress state before testing. Furthermore, this is the only comparable study looking into the effect of loading rate and Langer line orientation simultaneously on human skin thus far and therefore brings difficulties to a conclusion.

In terms of failure stretch, the data obtained in this study were generally higher than other studies, which could also be due to the aging effect from the tested PMHS. The PMHS tested in previous studies lie between 77 and 90 years old while the tested PMHS in the current study lie between 42 and 74 years old. Besides, the definition of failure was not clearly defined across literature, hence, it was difficult to make a fair comparison of the failure stretch data. Only Ottenio et al. (2015) had defined the failure as a superficial tear visible on the epidermis layer determined from high-speed video and this definition was also used in the current study. Also, the failure stretch in the current study did not refer to complete separation of the skin sample which is difficult to determine through video tracking because the results are heavily dependent on the frame rate of the recorded video.

For the initial Young's modulus (E_1), only Ní Annaidh et al. (2012) reported the test data and this was not mentioned in other skin's destructive tensile tests. Ní Annaidh et al. (2012) reported an average range between 1.21 MPa and 1.95 MPa at the human middle and bottom back respectively for the parallel samples conducted at a quasi-static rate of 0.012 /s while a 0.91 MPa and 0.54 MPa for the perpendicular samples at the respective locations. These values were an order of magnitude lower than the reported values in the current study which is believed to be due to the large difference in loading rates (0.012/s vs. 1/s).

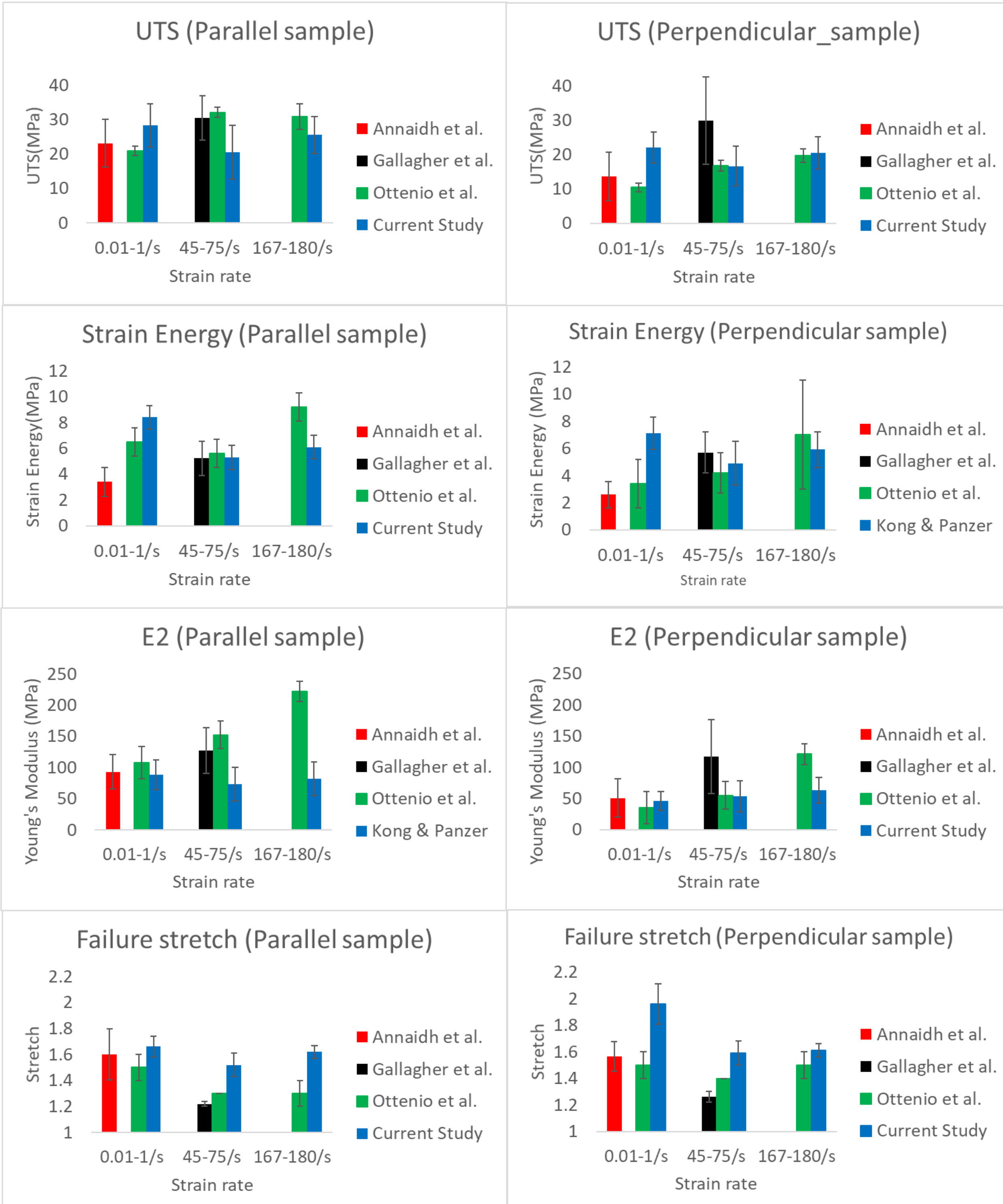

Figure 3-18: Comparison of ex vivo uniaxial tensile failure test results of human back skin.

3.5 Conclusion

In summary, the current study generates data corridors (average, UB, and LB) of human skin tensile failure with respect to different Langer's line and viscoelastic response. Major takeaways from this chapter are highlighted in the following statements:

1. An approximate strain rate ranged between 200 /s and 350 /s occurred as a result of the ballistic blunt impact from a less-lethal projectile based on simulations using the GHBMC (v5.0) HBM model.
2. Human skin exhibits strong anisotropy behavior (UTS, $E_{1,}$ and failure stretch) at a lower strain rate (1/s) and evolves to isotropic material as the strain rate increases.
3. Human skin loaded across (perpendicular) to the collagen fibers are rate dependent while the skin loaded along (parallel) to the collagen fibers are rate independent.
4. The relaxation response of human skin is independent of its orientation to the Langer's line.
5. Stress relaxation test informs the selection of the QLV analytical model to simulate human skin response.

The experimental data obtained in the current study can be used for developing the skin's constitutive model to capture its nonlinearity, viscoelasticity, and damage progress under ballistic impact. The QLV framework is shown to be appropriate for modeling the skin's response. By performing model optimization using the experimental data, the skin's material parameters can be identified which can be used for computational modeling.

CHAPTER 4 – Dynamic Indentation Failure Test of Human Skin

In Chapter 3, in preparation for developing a constitutive model of human skin, destructive uniaxial tensile tests, and viscoelastic tests of human skin were performed with simplified boundary conditions. However, to validate the model's capability in a more complex boundary condition, particularly under ballistic impact situations, a destructive dynamic indentation test series was proposed to capture human skin failure response under this condition. The indentation test results serve as a benchmark to validate the constitutive model of human skin. Hence, the goal of this chapter is to provide human skin failure properties under a dynamic indentation test.

4.1 Introduction

Skin is often characterized under simple loading conditions such as uniaxial tension or compression for constitutive model development to deduce material parameters. In reality, such simple loading conditions rarely exist. Many incidents such as skin piercing or mild to severe skin impacts from falling or sports-related impacts involve complex loading and may lead to open skin injury. To capture the complex stress state that develops within the skin, other mechanical testing such as suction (Grahame & Holt, 1969; Alexander & Cook, 1977; Barel, 1995; Jemec et al., 1996; Diridollou et al., 2000; Gniadecka & Serup, 2006), torsion (Sanders, 1973; Agache et al., 1980; Leveque et al., 1980; Grebeniuk & Uten'kin, 1994), bulge (Tonge et al., 2013), and indentation (Pailler-Mattei et al., 2008; Boyer et al., 2009; Groves, 2012; Ashrafi & Tönük, 2014) have been performed to determine the skin's stiffness, viscoelasticity, and anisotropy. Among these test methods, indentation was considered the most convenient test because no complicated test setups such as guard ring, optical or vacuum systems are required. Many of the indentation tests on human skin were conducted *in vivo*; hence, above physiological level, skin indentation response cannot be determined and with excessive indentation, the skin response cannot be isolated due to the presence of the underlying tissues. To perform destructive indentation tests, animal skins have been used to study skin piercing mechanisms by conducting *ex vivo* indentation tests on isolated porcine skins until failure (Kosoglu et al., 2010; Barnett et al., 2015). The obtained force-displacement results provide insights on isolated skin response indented by sharp microneedles in which the insertion speed were relatively slow (~1-80 mm/s) for surgical application purposes.

On the other hand, high rate indentation assessment on human skin such as ballistic blunt impact was investigated using PMHS, and skin failure criterion was established based on impactor energy density (Bir et al., 2005). Breeze and Clasper (2013) reviewed the velocity threshold required to cause skin penetration or perforation by standardized fragment simulating projectiles (metallic). The review included the relationship between skin failure velocity and sectional density on isolated human skin as well as gross body structure and animal skin. The high rate indentation studies are suitable for providing a general guideline on designing protective equipment, however, these results lack the mechanical response of skin in terms of force-displacement which can help to understand the underlying contribution of the skin during blunt impact. By quantifying the force-displacement response of human skin under high rate indentation, the information can be used to inform skin simulant as well as numerical skin model development.

To address the current research gap, the purpose of this chapter was to provide human skin failure response from a dynamic indentation test that can be used for skin model validation. *Ex vivo* indentation tests on isolated human skin were performed at constant impact velocity until failure occurred to generate a force-displacement corridor dataset. A contactless strain measurement system was used to create 3D skin deformation contours throughout the indentation process.

4.2 Methods

4.2.1 Test Fixture Design and Data Acquisition

The concept of the dynamic indentation (DI) test was to create isolated skin failure under indentation loading without having the influence of underlying tissues to obtain failure force and deformation contour under ballistic blunt impacts. To achieve this, a universal pneumatic linear impactor device mounted with a custom-made indenter along with a skin mounting rig was designed and used (Figure 4-1). The aluminum linear impactor weighed approximately 9 kg and different velocities can be achieved through variations in pneumatic pressure applied to the impactor. At the end of the impactor was a spherical-tipped aluminum indenter with a diameter of 12.7 mm. The skin mounting rig, on the other hand, consisted of a two-piece sandwiched plate assembly (Figure 4-2) and had a center hole with a 50.8 mm diameter for indentation, and a total of 22 holes were distributed on each plate to help secure skin samples in place. Both plates were also placed with additional 80-grit sandpaper to prevent skin samples from slipping during the test. The plate assembly was mounted to three 1000 lbf (4.4 kN) Honeywell model 31 piezoresistive one axis load cell (Honeywell, Charlotte, NC) in a triangular pattern that was attached to mounting brackets. The mounting brackets were bolted onto a scissor table lift. The pneumatic scissor table lift was adjusted vertically in height to make sure the indentation occurred at the center of the skin sample. To stop the impactor, two aluminum honeycombs (5" x 5" x 5") were placed towards the end of the impactor rail to absorb kinetic energy. The depth of the honeycombs was determined through pilot tests to make sure the skin sample was completely penetrated before deceleration took place. To measure the 3D displacement field of the skin samples, two Memrecam GX-1 high-speed cameras (NAC Image Technology, Simi Valley, CA) were placed at an equal angle with each other, facing towards the skin mounting rig to record the skin deformation process (Figure

4-3) and the Digital Image Correlation (DIC) technique was applied using a pattern recognition software, *ARAMIS* Professional 2017 (GOM GmbH, Braunschweig, Germany). For the data acquisition, a data sampling rate of 10,000 Hz was used on force data collection and all experimental videos of the skin indentation were also recorded at 10,000 fps using the two cameras. A spring-loaded trigger device placed underneath the rail of the impactor system was used to trigger data acquisition before the indenter had contact with the skin sample.

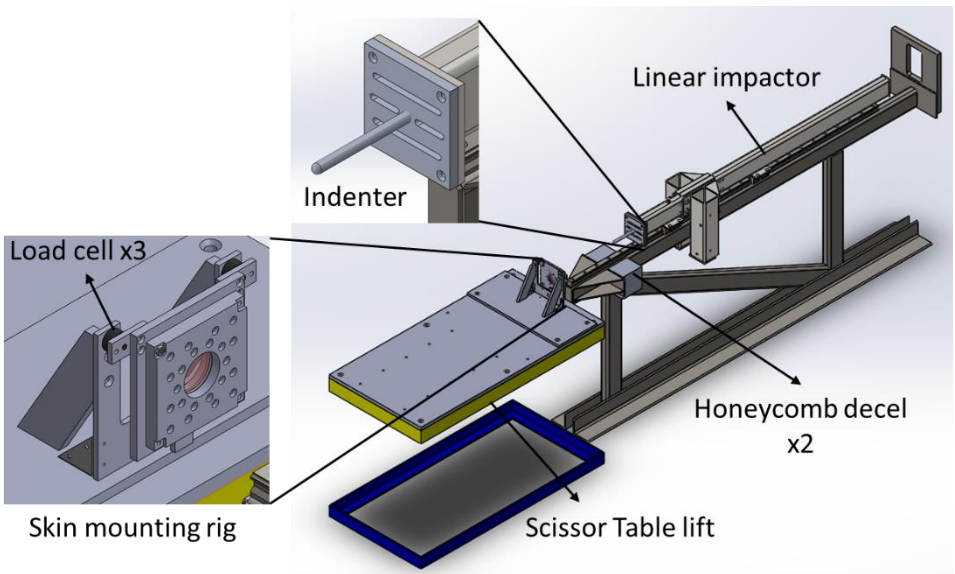

Figure 4-1: Overview of the dynamic indentation test setup. Note: The camera setup for DIC is not shown in the CAD assembly. The Scissor table lift model is also simplified for demonstration.

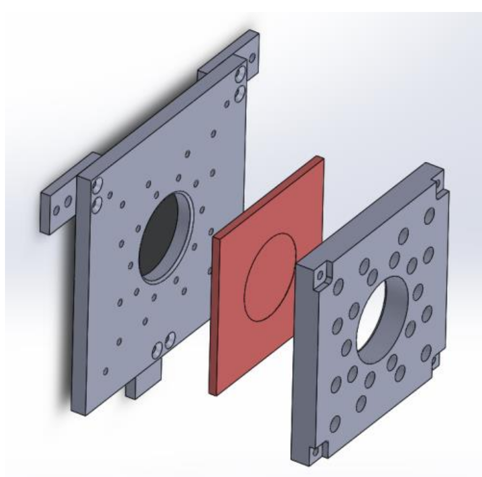

Figure 4-2: Exploded assembly view of skin mounting rig - skin is sandwiched between two aluminum plates.

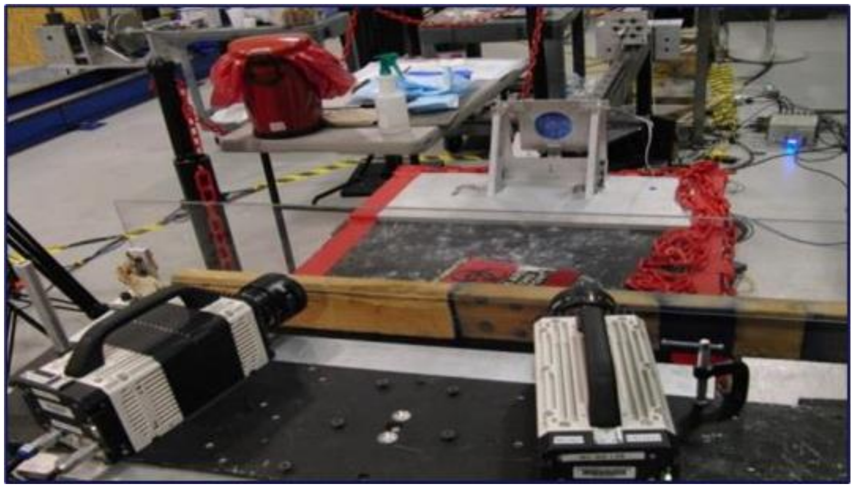

Figure 4-3: Camera setup for DIC.

The center hole with a 50.8 mm diameter was chosen based on preliminary results of FE simulations of the indentation tests that had developed minimum out of plane shear stress around the edge of the skin sample while maximizing the holding area of the skin to avoid skin slippage. Diameter sizes of 25.4 mm, 50.8 mm, and 101.6 mm were chosen and the GHBMC skin model was used for the preliminary indentation simulation by prescribing fully fixed constraints around the edge of the skin model (Figure 4-4).

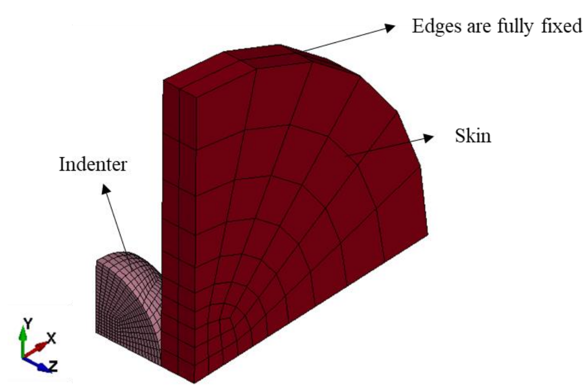

Figure 4-4: Preliminary DI simulation setup, model symmetry is assumed.

To simulate the skin failure in the simulation, a maximum principal strain threshold of 0.4762 (true strain) as reported in Chapter 3 was set in the *MAT_ADD_EROSION card. Shear stress (YZ stress) around the edges of the skin were used to investigate the effect of boundary size before the failure occurred in the simulation. A setup with a center hole of 101.6 mm in diameter provided the least and close to zero shear stress around the edge. However, after attempting pilot testing using the 101.6 mm test setup, skin samples could not be held in place but the 50.8 mm setup provided consistent test results without having skin slippage issues.

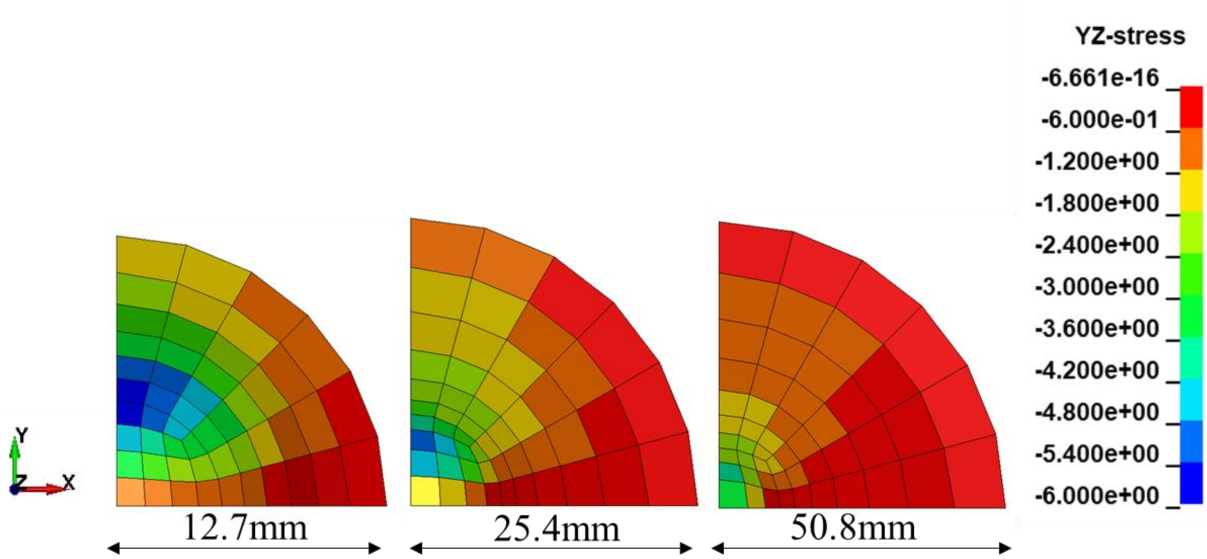

Figure 4-5: Effect of boundary size on out of plane shear stress. Results are taken from 1 frame before failure occurs.

4.2.2 Digital Image Correlation (DIC)

Digital Image Correlation (DIC) technique relies on the tracking of digitized images of deformable materials or objects to obtain 3D measurements. Each pixel in the digitized image has a grayness value between 0 and 255 and the fundamental idea is to trace each of these pixels throughout the deformation process. However, tracing individual pixels can be challenging since the gray value at the same location can vary and the same gray value can also be found in other pixel locations. To overcome this problem, one of the approaches is to create subpixel areas by creating random speckles over the target surface. Each subpixel area contains a portion of the image information and is registered to trace the object’s deformation, similar to the finite element discretization method where the object is being divided into smaller sections for calculations.

Within the subpixel area, the deformation is treated as homogenous and therefore size and distance between each subpixel area have an effect on obtaining local information. In *Aramis* software, these subpixel areas are called facets where their size and distance are input by the user when creating an object's 3D surface. To trace the facets, *Aramis* software uses an image correlation technique to maximize the rate of similarity of each facet through a correlation function. Information before and after deformation at each deformation state is related by the correlation function. With the facets being traced, 2D coordinates of the facet's center point are also tracked which can be used for computing strain. Each of these center points is used to form a triangular element in which the element strain is calculated. Based on the point coordinates, the *Aramis* software calculates the deformation gradient F via the least-squares method which can be decomposed into rotational tensor R and stretch tensor U. The stretch tensor U can be transformed into right stretch tensor C ($F^{T}F=U^{2}=C$) which contains the stretch value that can be converted into the strain.

To compute 3D coordinates of the point, *Aramis* software uses the principle of triangulation (Figure 4-7) where the depth of an object can be calculated when distance L between observer A and observer B as well as their respective observation angle is known. This information can be provided to the software during the camera calibration process. Before initiating the DI test, the cameras were calibrated with a 35 mm x 28 mm calibration panel which contains organized speckles with fixed distance (Figure 4-6). Both cameras were set to a resolution of 476 x 464 pixels, so the calibration panel was fully occupied in the window resolution. Different block orientations (e.g., direct facing, angled facing) were placed towards the two cameras and 13 pairs of monochrome images were taken according to *ARAMIS* User Manual v6. The monochrome images, along with the size of the calibration panel, camera lens (105 mm), and camera pixel size (4 μm) information were input for the software algorithm to generate a calibration file which contains overall measuring volume length (100 mm), width (100 mm), depth (75 mm) as well as camera angle (20°) between each other. The calibration file can be used to create a 3D surface of other speckled objects that have similar window resolutions.

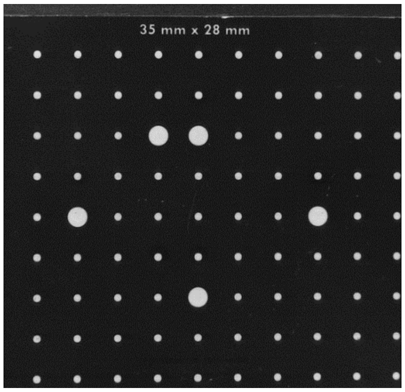

Figure 4-6: Standard speckles distribution for DIC calibration.

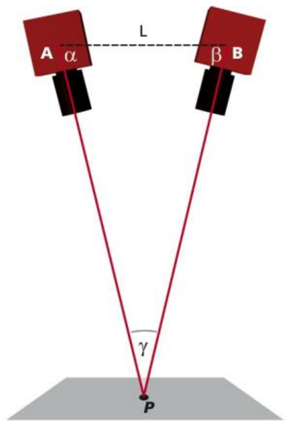

Figure 4-7: Principle of triangulation. (Source: GOM Testing Technical Documentation)

4.2.3 Skin Sample Preparation

The same skin excision and storage steps as described in Chapter 3 were adopted to obtain the dynamic indentation (DI) test skin samples. Before excision, a square stencil (5" x 5") with a 2" circular hole in the middle was used to draw out the contour of the skin's in-situ state. After the contours were drawn, three DI samples were excised from the right-back of each PMHS as used in Chapter 3 and an overall of 18 samples were obtained for testing. Skin thickness was measured using a digital caliper around its 4 corners and an overall average of 2.96±0.84 mm was obtained among the 18 samples.

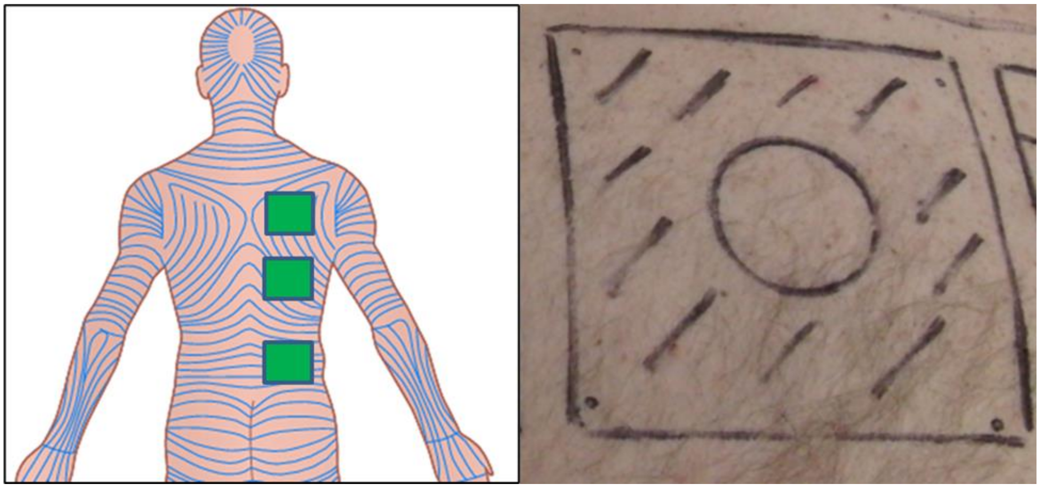

Figure 4-8: (a) Left: Locations of skin samples excised on the right side of the human. (b) Right: Marked in-vivo state of DI skin samples before excision (dashed marker lines indicate perceived Langer's line orientation).

On the day of testing, the skin sample was placed in between the skin mounting rig and stretched to its *in vivo* state using the circular mark as reference (Figure 4-9a). Both plates of the skin mounting rig were tightened by 22x 10-32 screws after the skin sample was stretched to its *in vivo* state. Once the skin sample was held in place, the skin mounting rig was flipped backward to begin the skin speckling process for the DIC. A layer of methylene blue solution (Kordon LLC, USA) was applied evenly by brushing the surface of the skin sample, followed by waiting for 1-2 minutes to allow the solution to dry out. Once the solution was dry, a random speckle pattern was applied on top of the solution layer by flicking a toothbrush head which was coated with white spray paint (Walmart ColorPlace, USA). The white paint along with the methylene blue creates a high color contrast (Figure 4-9b) which can be recognized by the *Aramis* software. A preliminary speckle check using the *Aramis* software was performed to ensure the applied speckles were recognizable (Figure 4-9c). Re-speckle was feasible by adding another layer of methylene blue and white speckles to cover the previous speckles if a bad or no speckle pattern was obtained. A facet size of 15 pixels with a facet distance of 8 mm was used to create a 3D surface of the skin sample. Due to shadows generated from the light source, edges of the skin samples were not recognized by the Aramis software and hence, resulted in a slightly smaller DIC surface (Figure 4-10).

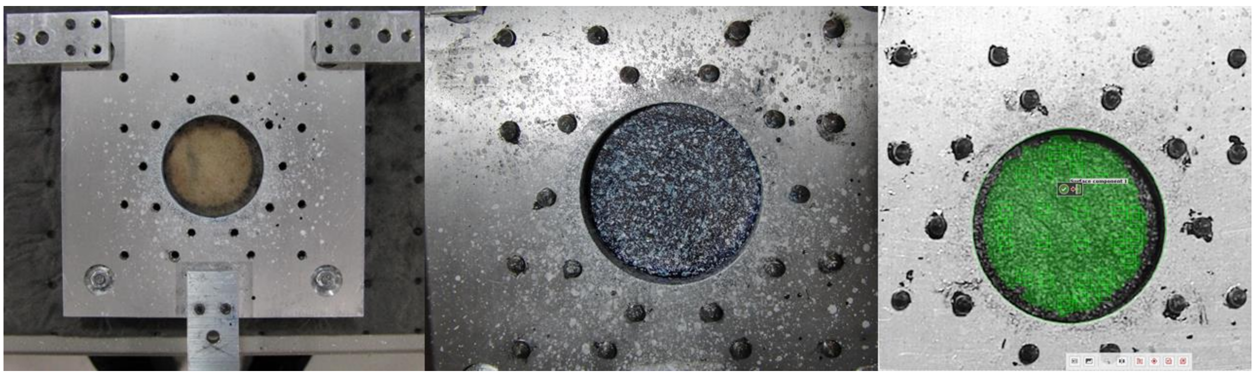

Figure 4-9:(a) Left: Skin placed in the in vivo state between the skin mounting rig. (b) Middle: Speckle pattern applied on the skin sample. (c) Right: Speckle pattern check using Aramis software, the green area indicates a recognized surface component.

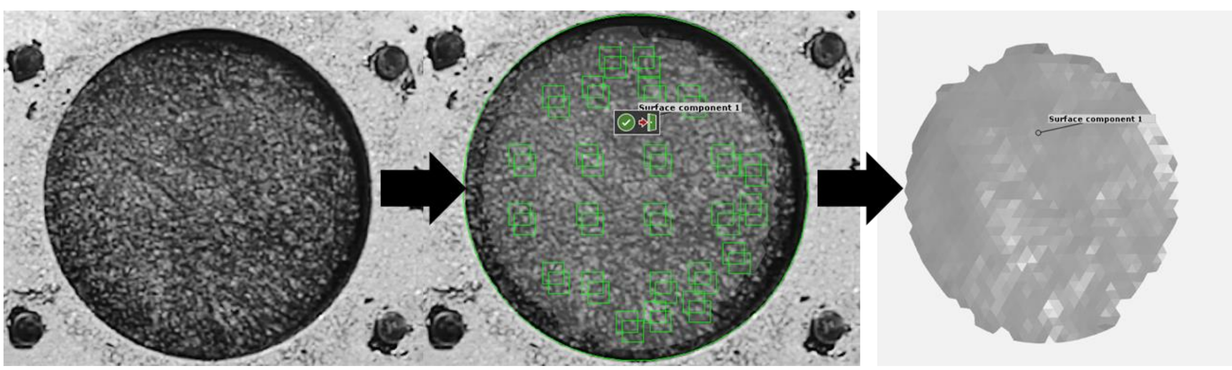

Figure 4-10: DIC surface generation process. (Left) Monochrome images supplied to Aramis software. (Middle) Facet generation by inputting facet size and distance. (Right) Generated DIC surface.

4.2.4 Test Matrix Development

To estimate the required travel velocity of the impactor to cause skin rupture, an experimental study conducted by Bir et al. (2005) reported an average energy density value between 33.14 J/cm^2 and 55.9 J/cm^2 created skin penetrating wounds. These values were obtained on PMHS where underlying tissues were also presented underneath the skin during the test. With an impact area of 2.45cm^2 (from a 12-gauge munition), the corresponding kinetic energy required to cause a skin wound was calculated to be between 81.19 J and 136.96 J. The linear impactor system in the current study weighs approximately 9 kg and therefore, a travel velocity between 4.25 m/s and 5.52 m/s was required to cause skin failure in the DI test. In addition to the required test velocity, pilot tests were carried out to assess the rate sensitivity of human skin under the indentation test. Three velocities (i.e. 4 m/s, 7 m/s, and 10 m/s) were chosen for the rate sensitivity tests and two metrics were chosen (i.e. displacement contour and normalized peak force) for analyzing the results. The displacement contour was the shape of the skin deformation subjected to indentation (Figure 4-11) and only the last frame of the displacement contour was chosen (before failure) for comparison between the three tests while the normalized force is defined as measured force per skin thickness. Skin samples of the pilot tests were excised from two additional PMHS (ID no. 903 and 904) and the results show similar displacement contour before failure (Figure 4-12, left). Although a smaller normalized force was measured at the 7 m/s impact, the peak normalized force between 4 m/s and 10 m/s impact was similar (Figure 4-12, right). To check the validity of the DIC results, the center point of the constructed surface from the *Aramis* software was used to generate a velocity-time profile and compared with the experimental velocity obtained from the velocity gates. The results (Figure 4-13) illustrated a similar velocity response between the *Aramis* software and the velocity gate.

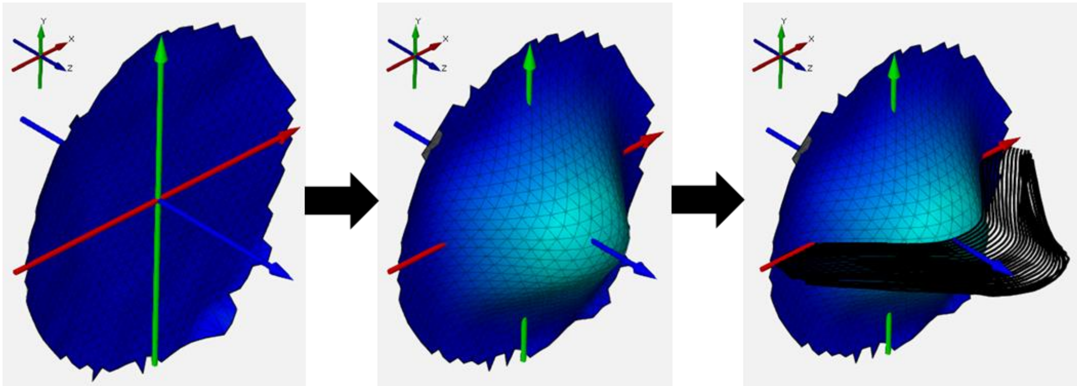

Figure 4-11: Skin deformation contour progression generated by Aramis software. Black lines indicate deformation trajectories with positive z-axis being the impact direction.

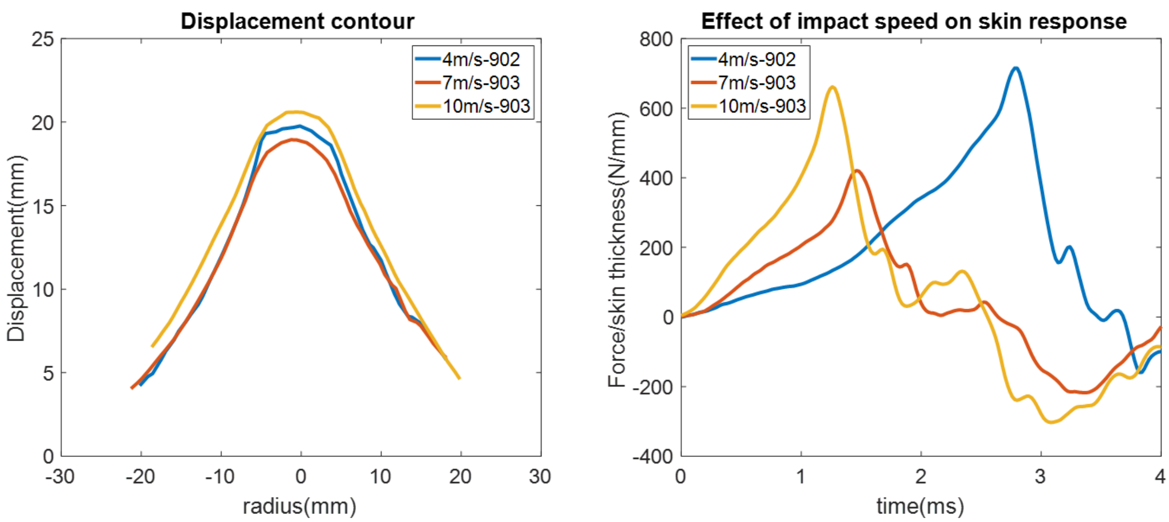

Figure 4-12: DI test results under 3 different impact velocities.

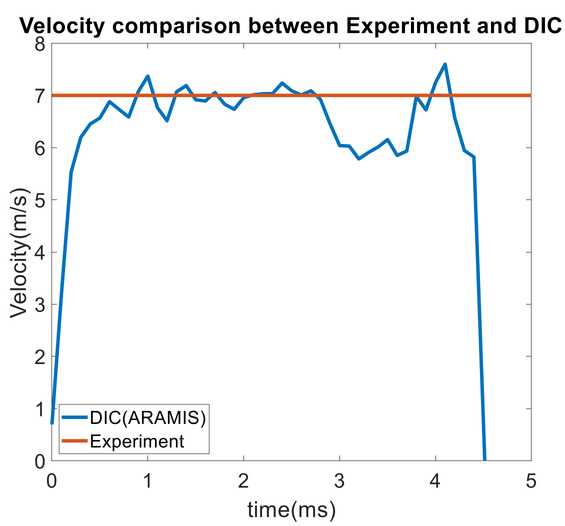

Figure 4-13: Velocity comparison between Aramis software and velocity gate.

Based on the rate in-sensitive results from the pilot study, it was decided to use only one travel velocity for DI tests, specifically 7 m/s as this was closest to the highest test speed (6 m/s) conducted at the DT tests in Chapter 3. As a result, a test matrix was determined to test three skin samples from each PMHS at 7 m/s. For the three skin samples, two of the samples were orientated with Langer's line aligned along the x-axis (parallel sample) and one other sample was orientated with Langer's line aligned along the y-axis (perpendicular sample) while the z-axis was the impact direction (Figure 4-11) to investigate the effect of collagen fibers orientation on skin indentation response.

4.3 Results

All the skin samples were tested successfully in the DI tests without slippage occurring and Figure 4-14 illustrates one of the ruptured skins. Since each skin sample failed at a different time and stretch level, the normalized arc length approach used in Chapter 3 was also employed to compute the average and corridor response. To capture the data range of interest, the starting time (t=0) was determined based on initial contact between the indenter and the skin sample. A center point was created in the middle of the DIC surface (where both x and y-axis cross) to create displacement and velocity-time profile. Based on these profiles, the initial starting point can be defined where both displacement and velocity start to ramp up. For the end of the data range, it was defined as one frame before skin failure takes place. By correlating the failure time in the *Aramis* software with the force-time data acquired from the load cell, the corresponding force values can be obtained. It should be noted although the 'failure' as illustrated in Figure 4-15 does not result in complete skin penetration, the DIC surface at this point could be disrupted due to the breaking of skin and therefore further 3D deformation field collection is prohibited.

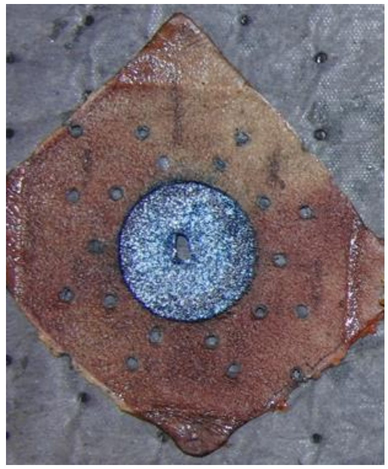

Figure 4-14: Ruptured skin from DI test.

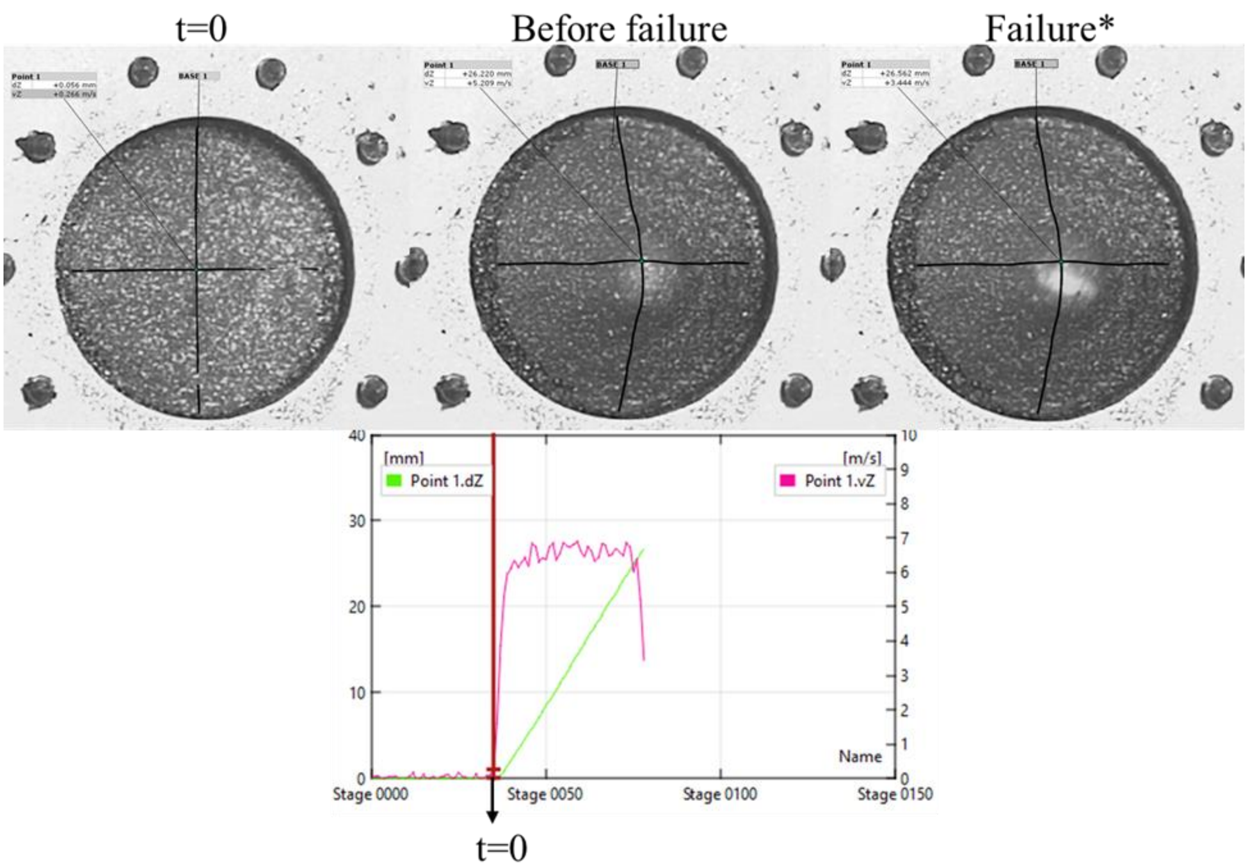

*Figure 4-15: Defining data range from Aramis software. *failure frame is excluded for data analysis.*

Figure 4-16 shows normalized force vs. displacement results of each skin sample from the DI tests as well as displacement contour obtained from the *Aramis* software using the DIC method. Each color group on the graph represents an individual PMHS where each marker type represents an individual tested sample. The x-axis of the force-displacement graph was obtained from the maximum displacement from the tip of the displacement contour at each time step during the test. It can be seen from both the force-displacement curve and displacement contour that very little intra-subject variability existed. All the samples obtained from the same PMHS (each color code represents each PMHS) had a very similar response with an exception to sample ID 757-RL-0 (Figure 4-16). By taking the average response of each PMHS, Figure 4-17 shows potential age-dependent inter-subject variation. To investigate the inter-subject variations, 4 metrics were chosen i.e. initial stiffness (slope measured at the initial 5% of the maximum failure force), final stiffness (slope measured between 30% and 70% of the maximum failure force), maximum normalized failure force and maximum failure displacement.

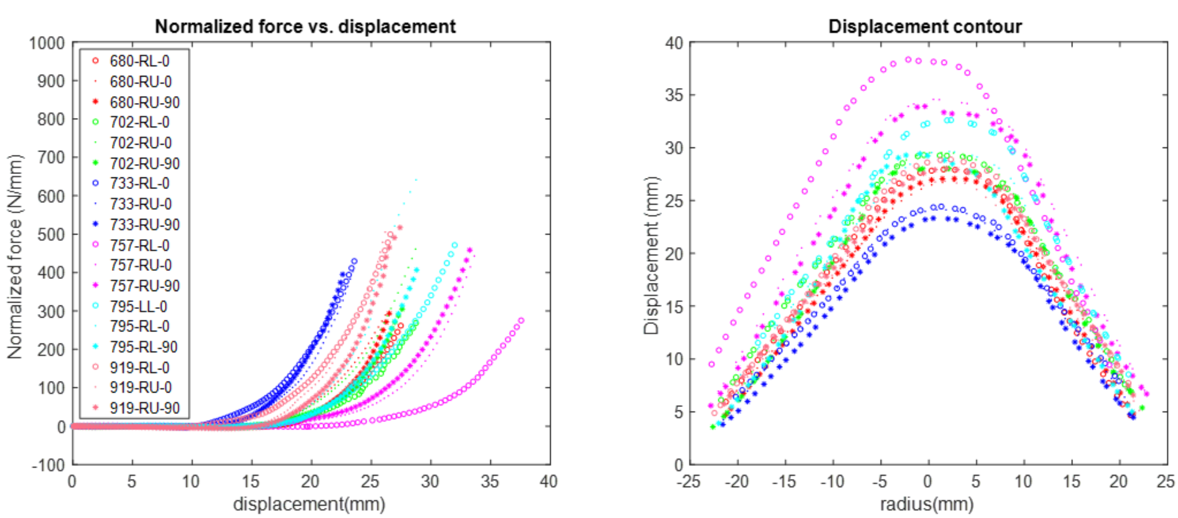

Figure 4-16: Inter-subject variation results of DI test.

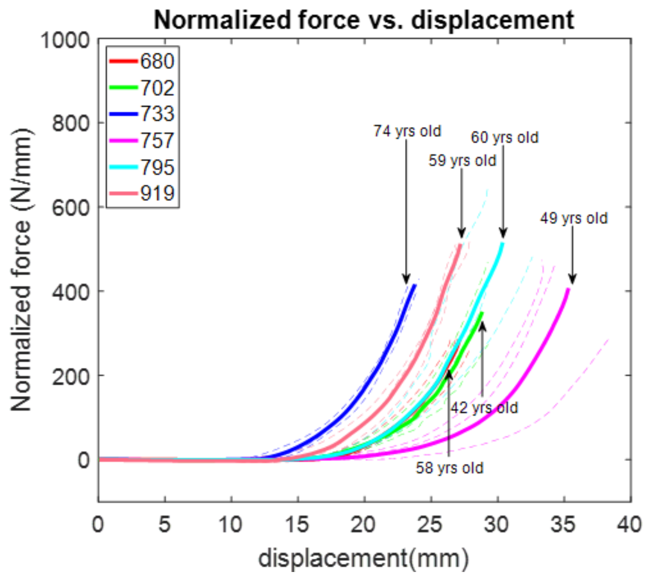

Figure 4-17: Average skin response of different aged PMHS.

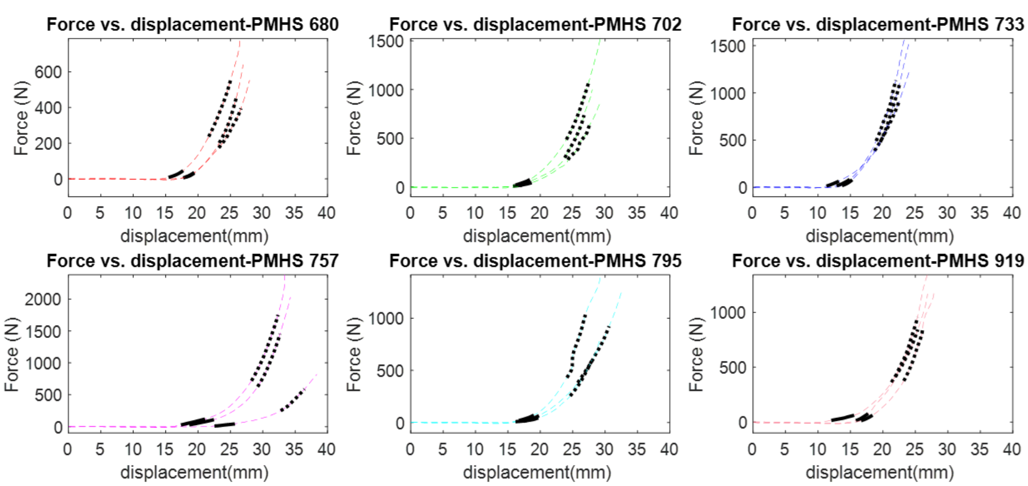

Figure 4-18: Force (denormalized)-displacement curve of the individual skin sample. Solid black lines indicate initial stiffness, dashed black lines indicate final stiffness.

The failure displacement of the skin sample under the DI test can potentially be age-dependent where the average response of 74 years old PMHS showed the lowest failure displacement while 49 years old PMHS had the highest failure displacement. Although no strong trend can be determined due to the small sample size (n=3 per PMHS), the failure displacement response of the 42, 58, 59, and 60-year old PMHS lies in between the other two specimens. A similar trend was also observed in initial stiffness where the 74 years old specimen tends to be stiffer than other young aged specimens. The final stiffness and failure force, however, showed similar results regardless of age (Figure 4-19). Overall, the failure force and failure displacement had an average value of 415(±107.42) N/mm and 28.77(±3.84) mm, respectively, and the force-displacement response and displacement contour of most of the samples lied within 1 standard deviation (Figure 4-20). In terms of the effect of Langer's line orientation, both sample groups showed very similar average responses (Figure 4-21).

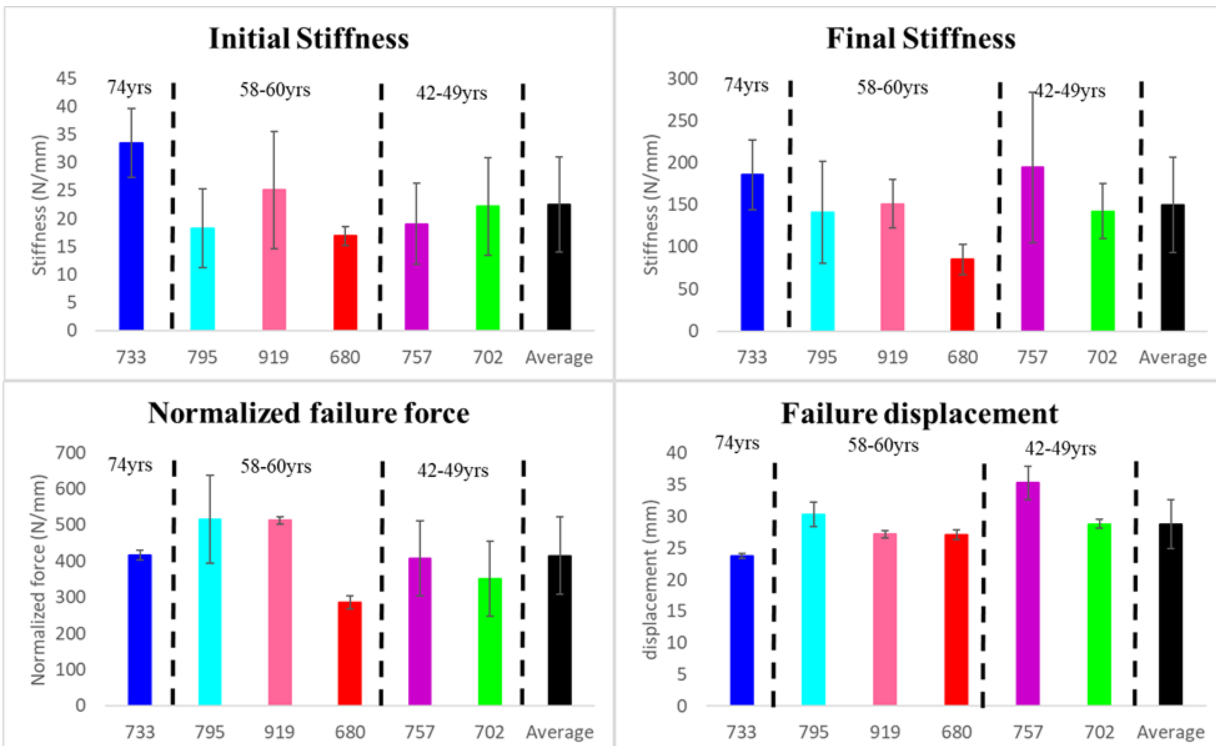

Figure 4-19: Bar plots of initial stiffness, final stiffness, failure force, and failure displacement between different age groups.

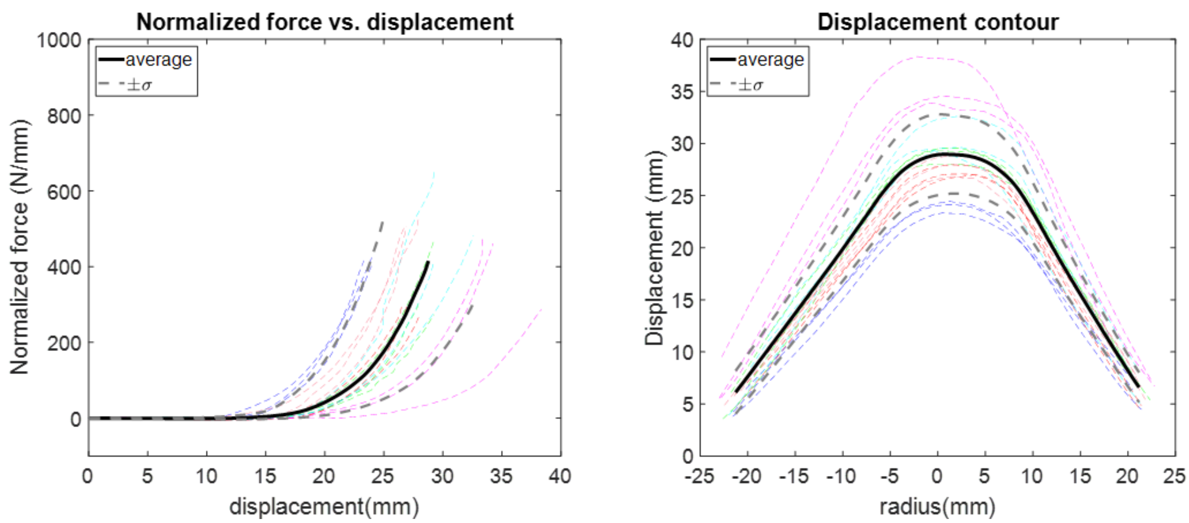

Figure 4-20: Average, UB, and LB skin response under DI tests.

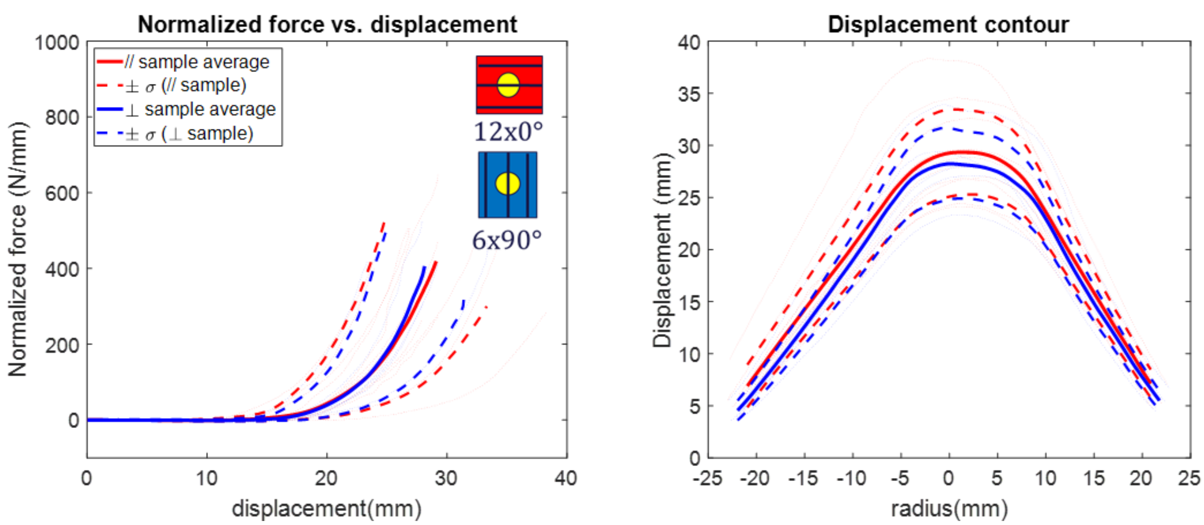

Figure 4-21: Average response comparison between parallel (red) and perpendicular (blue) samples. The yellow circle indicates out of plane impact direction.

4.4 Discussion

A dynamic indentation (DI) test methodology was developed to determine isolated human skin failure response subjected to dynamic impact. Digital Image Correlation (DIC), a contactless measurement technique was used to create 3D deformation contours of 18 human skin samples in the DI tests. Based on the 3D displacement field and the measured force, a data corridor consisting of average, UB, and LB force-displacement curves of isolated human skin was generated for the first time.

Fixed impact speed was used in the current study because the initial pilot test results indicate skin's rate-independent response was conflicting as the skin was reported to be viscoelastic in past studies. The impact velocities used in the pilot studies were within the same order of magnitude and therefore, it is believed the difference could not magnify the skin's rate dependency. The skin's rate dependency may be reflected if compared to lower impact velocities, but such impact speed could not result in skin failure with the spherical blunt indenter. No higher impact velocity was chosen because holding the skin sample in place at those impacts became difficult due to skin slippage and revision on the test fixture was needed. More importantly, the chosen impact velocity (i.e. 7 m/s) was sufficient to produce a similar strain-rate history as found in the ballistic blunt impact simulations shown in Chapter 3 (Figure 4-22 right) by having the large mass impactor system. The experimental strain rate was determined from the major strain component of the DIC results where true strain history at the center of the DIC surface was extracted and the average was taken from all the tested skin samples (Figure 4-22 left). The strain rate comparison addresses the effect of momentum, although impacting with a lower velocity. The high mass impactor system used in this study can achieve similar strain rate magnitudes as resulted from the 100 m/s impact of the rubber ball.

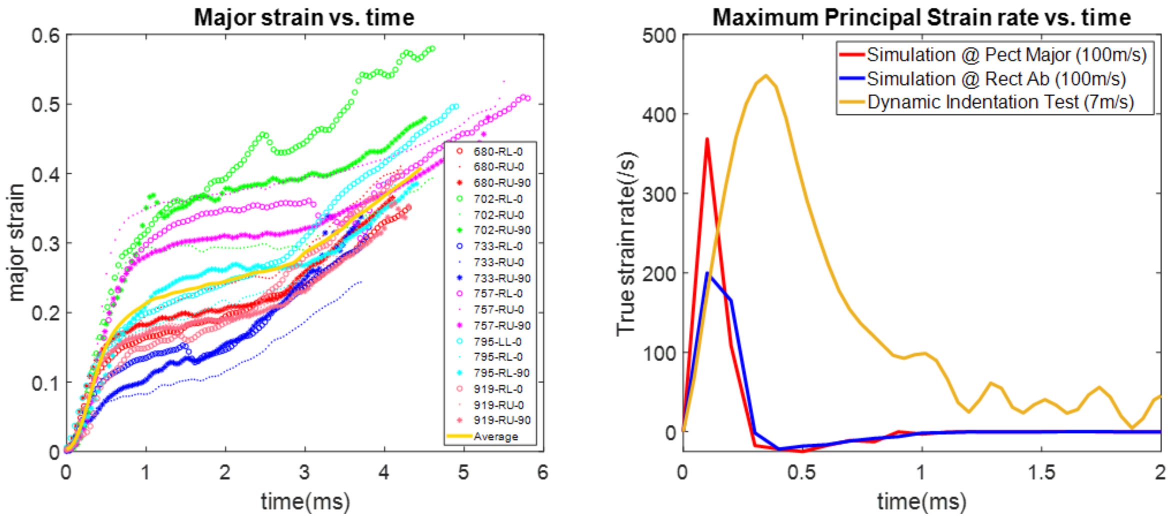

Figure 4-22: (Left) Maximum Principal Strain time history of DI test. (Right) Strain rate comparison between DI test in the current chapter and blunt impact simulations in Chapter 3.

The force-displacement response of the skin sample exhibits a plateau response at the beginning of indentation before expressing a stiffening effect where the force dramatically increases in a nonlinear fashion until failure occurs. As opposed to the uniaxial tensile test case, no obvious necking or material softening was observed from the force-displacement response. The stiffening effect is believed to occur when the skin sample was fully engaged with the edge. This means the presented force-displacement response was a result of the size of the circular boundary which is 50.8 mm in diameter in this study. Furthermore, the size of the indenter was also a contributing factor where a larger indenter diameter leads to early skin engagement with the edge and hence, results in a different plateau length. The boundary size was chosen to ensure out of plane shear stress around the edge was minimized. The skin failure progress is illustrated in Figure 4-23, showing a progressive skin failure as the skin sample was gradually torn with the initiation of an open crack (Figure 4-23b), followed by crack enlargement (Figure 4-23c & d) and finally resulted in complete failure as the indenter pushes through the skin sample (Figure 4-23e). Besides, no skin “plug” was observed separating from the skin sample during testing, indicating a tensile failure rather than a shear failure.

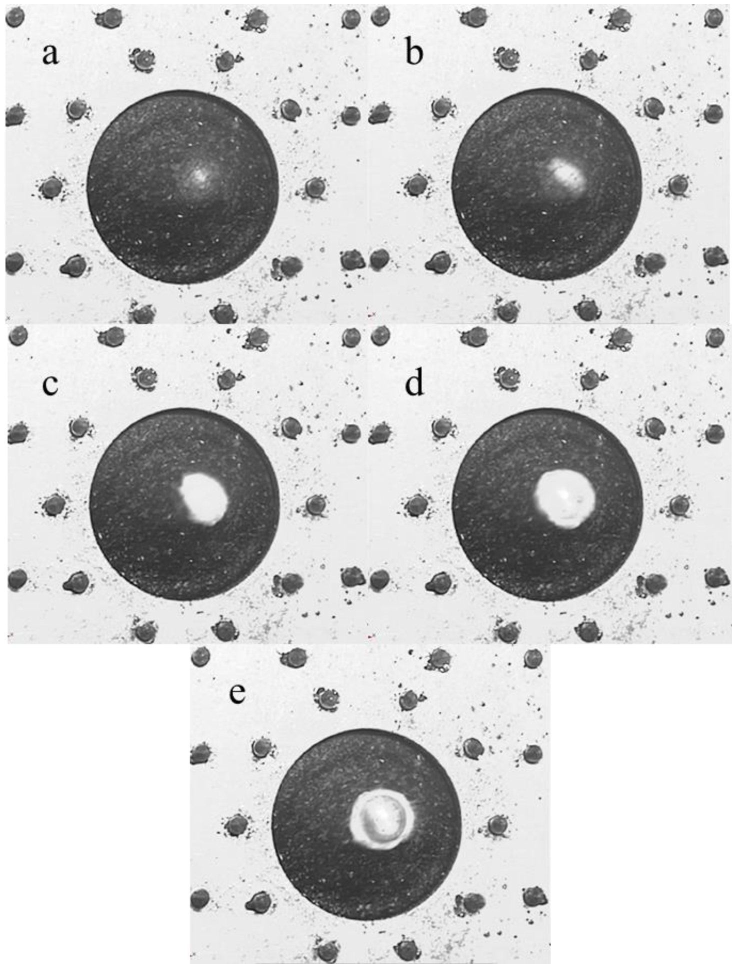

Figure 4-23: Skin indentation failure progress at 0.1 ms interval. a) Before failure; b) failure initiated with open crack; c) & d) crack enlarges; e) Complete failure with indenter pushes through

The indentation test results identify age-dependence of the initial stiffness and failure displacement where the eldest PMHS has the lowest failure displacement and highest initial stiffness. Although no failure displacement data can be used for comparison, the low failure displacement from the elder PMHS agrees with the trend reported by Escoffier et al. (1989) where skin's extensibility decreases with age. Similarly, higher initial stiffness found in the elder PMHS was also shown in previous studies (Grahame & Holt, 1969; Diridollou et al., 2000; Tonge et al., 2013; Dulińska-Molak et al., 2014). In terms of skin's anisotropy, this was not found in the current indentation test which was also observed in the dynamic tensile test cases in Chapter 3. This could be due to the effect of high rate loading where the stiffness of ground substances becomes the same as the collagen fibers as discussed in Chapter 3. However, this can also be caused by the use of the spherical indenter. Several indentation tests (Jeffrey E. Bischoff, 2004; Feng et al., 2013; Ashrafi & Tönük, 2014) have shown that in-plane anisotropy of soft tissues could not be observed if an axial symmetric indenter (e.g., circular indenter) was used unless using an axial asymmetric indenter (e.g., rectangular or ellipsoidal indenter). Therefore, the in-plane isotropy of the skin under high rate loading should be further evaluated with an axial asymmetric indenter. The current dataset is reasonable for model validation under blunt impact using less-lethal weapons which are mainly axisymmetric.

4.5. Conclusion

The current study provides a set of destructive force-displacement responses of isolated human skin under dynamic indentation tests at strain rate magnitudes similar to ballistic blunt impact. The current indentation setup in terms of boundary size and impactor diameter has resulted in skin tensile failure rather than shear failure which is important as this allows the strength of the skin to be fully characterized. Skin initial stiffness and failure displacement were observed to be age-dependent, where elderly skin was stiffer than the younger skin. The failure force and final stiffness, however, do not exhibit age-dependency. Besides, the skin’s in-plane anisotropy was not observed which could be because of the choice of impactor geometry or the effect of high rate impact. The generated dataset including average and corridor responses will be useful for validating skin numerical models, and evaluating, and developing biofidelic skin simulants for ballistic blunt impact applications.

CHAPTER 5 – Constitutive Damage Modeling of Human Skin

Based on the experimental data obtained from Chapter 3, constitutive damage models were developed to describe skin tensile failure response. A damage feature was incorporated into the constitutive model to capture skin failure. To include skin variations, 3 constitutive models were developed including average, upper bound (UB), and lower bound (LB) models which resulted in three sets of corresponding material parameters. The development of the constitutive models was divided into two stages, the first stage included pristine model fitting and the second stage included damage modeling induced by damage initiation of the skin. The goal of this chapter was to generate 3 sets of material and damage parameters that represent the variability of human skin tensile failure response.

5.1 Introduction

Constitutive models have been used extensively to describe the stress-strain relationship of skin subjected to mechanical loading which yields material parameters. These parameters can be used for comparison between different skins such as animal versus human to quantify the difference and to inform skin simulant development. The material parameters can generally be categorized into phenomenological and structural parameters depending on the type of constitutive model. The phenomenological parameters describe observed behavior through a combination of optimized numbers while the structural parameters contain underlying physical properties related to the material. Several constitutive models have been developed in the past decade for simulating the skin response at different experimental protocols including uniaxial tension, compression, indentation, and biaxial test. The complexity of the constitutive model is developed to suit the end application, therefore, modeling all the skin aspects is not necessary.

The simplest structural-based constitutive model is Hooke’s law or bi-linear elastic (extension of Hooke’s law) which relies on Young’s modulus to describe the skin’s linear and nonlinear relationship (Delalleau et al., 2008). To describe the continuity of skin’s nonlinear response, phenomenological hyperelastic models such as Mooney-Rivlin, Ogden, and Yeoh model which are based on strain energy density function have been used and showed promising results (Łagan & Liber-Kneć, 2017). A strain energy density function dedicated to the skin’s collagen fibers was added to the Veronda-Westmann hyperelastic model to simulate the skin’s anisotropy (Groves et al., 2013). The Gasser-Ogden-Holzapfel (GOH) model (Holzapfel & Gasser, 2001; Gasser et al., 2006) which uses both phenomenological and structural parameters is also capable of simulating the anisotropy of skin based on the fiber dispersion factor and orientation angle (Ní Annaidh et al., 2012). The Quasi-Linear Viscoelastic (QLV) framework (Fung, 1972) which considers the nonlinearity and viscoelasticity of skin has also been employed with success on pig and mouse skin (Liu et al., 2015; Wang et al., 2015). In terms of skin damage modeling, only Li and Luo (2016) developed such a model by modifying the GOH model to simulate the nonlinearity, anisotropy, and damage of the skin.

Although there are substantial constitutive models developed for skin, there is a lack of any constitutive models that describe the nonlinearity, viscoelasticity, and damage of skin simultaneously. Modeling of viscoelasticity is particularly important for the application of high rate impact and the ability to predict open skin injury as a result of the impact is also vital. Therefore, to address the current research gap, the purpose of this chapter was to develop a rate-sensitive skin damage model to determine the human skin’s material and damage parameters. The model development uses the destructive uniaxial tensile and stress relaxation dataset as performed in Chapter 3 to determine three sets of material parameters that represent the average, UB, and LB skin tensile failure response.

5.2 Methods

5.2.1 Finite Strain Theory

To describe human skin behavior, a continuum mechanics framework was employed where the human skin was assumed to be a continuous mass rather than discrete particles. The skin deformation was described using a Lagrangian description where the motion of a continuum body is defined by a mapping function χ which relates position vector X of a material point in the undeformed (reference) configuration at time $t = 0$ and position vector x in the deformed configuration at time t.

$$x = \chi(X, t)$$

By taking the partial derivative of the deformed vector x to its respective undeformed vector X, the deformation gradient F can be computed which contains 3D deformation information of a material that includes stretch tensor U and rotation tensor R. The rotation tensor R corresponds to the rigid body motion where only pure rotation is involved that does not result in material deformation while the right stretch tensor U (or left stretch tensor V) describes the material deformation.

$$F_{ij} = \frac{\partial x_i}{\partial X_j};\ F = RU = VR$$

Since the rotation tensor R does not contribute to material deformation, it can be excluded by multiplying F^T to the deformation gradient F and this gives a rotation independent deformation tensor, either right Cauchy-Green tensor C or left Cauchy-Green tensor B. The deformation tensor C can be used to evaluate Green-Lagrangian strain tensor E which was used to describe finite deformation.

$$F = RU \rightarrow F^T F = U^T R^T R U = U^2 = C$$

$$E = \frac{1}{2}(C - I)$$

5.2.2 Constitutive Equations

Hyperelastic constitutive models are used to describe material stress response under large deformation which is feasible for modeling the skin failure response. The hyperelastic law relates strain energy density function *W* of a material to its deformation gradient *F*. The strain energy density function *W* can be expressed as a function of different deformation tensors ($W = \breve{W}(F) = \widetilde{W}(C) = \widehat{W}(\lambda)$) which results in the calculation of different stresses. For example, the engineering stress or First Piola-Kirchhoff stress (1st PK stress) can be calculated by

$$1st\ PK\ stress = J^{-1} \frac{\partial W(F)}{\partial F}$$

where *J* refers to the Jacobian of the material which defines the ratio of a material's current volume to its reference volume. To describe material stress at every deformation step, Cauchy stress σ ('true stress') is more convenient and can be converted from Second Piola-Kirchhoff stress *S* (2nd PK stress) that is expressed as a function of right Cauchy-Green tensor *C*.

$$S = 2J^{-1} \frac{\partial \widetilde{W}(C)}{\partial C};\ \sigma = 2J^{-1} F \frac{\partial \widetilde{W}(C)}{\partial C} F^T$$

To describe the rotation independency of the deformation tensor *C*, invariants such as principal stretches λ are used and this yields a nonlinear stress calculation at large deformation.

$$\sigma = J^{-1} \lambda \frac{\partial \widehat{W}(\lambda)}{\partial \lambda}$$

In this dissertation, the Ogden strain energy density function $W(\lambda)$ was selected to evaluate the true stress response of the skin based on its successful performance in previous studies (Shergold et al., 2006b; Lapeer et al., 2010; Wang et al., 2015; Łagan & Liber-Kneć, 2017). In the equation, μ_i and α_i terms are material constants that are related to material's shear modulus *G*.

$$W(\lambda) = \sum_{j=1}^{n} \frac{\mu_j}{\alpha_j} \left(\lambda_1^{\alpha_j} + \lambda_2^{\alpha_j} + \lambda_3^{\alpha_j} - 3\right) + volumetric\ effect$$

$$G = \frac{1}{2} \sum_{j=1}^{n} \mu_j \alpha_j$$

Under uniaxial tensile loading, λ_1 is the primary loading stretch and λ_2 and λ_3 refers to the transverse and the through-thickness stretch. The resultant stress σ_1 is derived by taking the partial derivative of the Ogden strain energy density function with respect to λ_1 by assuming the material is fully incompressible and therefore the volumetric term is ignored.

$$\sigma_1 = \sum_{j=1}^{n} \mu_j \left[\left(\lambda_1^{\alpha_j} - \lambda_1^{-\frac{\alpha_j}{2}} \right) \right]$$

The hyperelastic models are capable of capturing material behavior subjected to large strain deformation without including material viscoelasticity (i.e., loading rate effect on the material response). To consider the viscoelasticity of human skin, Fung's Quasi-Linear Viscoelastic (QLV) framework (Fung, 1972) was employed along with the Ogden model to construct a nonlinear, rate-dependent constitutive model. The QLV model is expressed in the Generalized Maxwell configuration where a series of springs and dashpots are connected in parallel along with a single spring. Hence, the stress of the QLV model is mathematically expressed as

$$\sigma(t) = \int_0^t G(t-\tau, \lambda) \dot{\lambda}(\tau) d\tau$$

where $\dot{\lambda}(\tau)$ refers to loading stretch-time history which is the experimental input. It was assumed the relaxation function $G(t-\tau, \lambda)$ of the QLV model can be separated into an elastic response (stretch dependent) and a temporal response (time-dependent) where $G(t-\tau, \lambda) = \bar{G}(t-\tau) \frac{d\sigma_0(\lambda)}{d\lambda}$. The elastic response was modeled using the Ogden hyperelastic model to capture the skin's nonlinearity. For the temporal response, the term $\bar{G}(t-\tau)$ refers to reduced relaxation function which can be expressed in the form of a Prony series:

$$\bar{G}(t) = G_\infty + \sum_{i=1}^{n} G_i e^{-\left({t}/{\eta_i}\right)}$$

$$G_\infty + \sum_{i=1}^{n} G_i = 1$$

In the Prony series, G_i are the linear normalized coefficients bounded between 0 and 1 and ${1}/{\eta_i} = \beta_i$ are the nonlinear time constants. Each pair of G_i and β_i is responsible for the stress decaying rate at a specific time. G_∞ is the relaxation coefficient at the infinite time where the material is fully relaxed and no viscosity is presented. The use of reduced relaxation function yields maximum relaxation at time t = 0 and decays monotonically to G_∞ at time t = ∞.

As a result, the QLV stress can be written in terms of the Prony series as

$$\sigma(t) = \int_0^t \left(G_\infty + \sum_{i=1}^{n} G_i e^{-\left({(t-\tau)}/{\eta_i}\right)} \right) \frac{d\sigma_o}{d\tau} d\tau$$

$$= G_\infty \int_0^t \frac{d\sigma_o}{d\tau} d\tau + \sum_{i=1}^{n} \int_0^t G_i e^{-\left({(t-\tau)}/{\eta_i}\right)} \frac{d\sigma_o}{d\tau} d\tau$$

To calculate stress at each incremental time ($\sigma(t+\Delta t)$), the convolution integral containing the term G_i can be written in two Kernel functions.

$$\sigma_{G_i}(t+\Delta t) = \sigma_{1G_i}(t) + \sigma_{2G_i}(t+\Delta t)$$

$$= \int_0^t (Kernel\ 1) d\tau + \int_0^{t+\Delta t} (Kernel\ 2) d\tau$$

Kernel function 1:

$$\sigma_{1G_i}(t) = \int_0^t G_i e^{-\left({(t+\Delta t-\tau)}/{\eta_i}\right)} \frac{d\sigma_o}{d\tau} d\tau$$

$$= \int_0^t G_i e^{-\left(\Delta t/\eta_i\right)} e^{-\left(\mathrm{t}-\tau/\eta_i\right)} \frac{d\sigma_o}{d\tau} d\tau$$

$$= e^{-\left(\Delta t/\eta_i\right)} \int_0^t G_i e^{-\left(\mathrm{t}-\tau/\eta_i\right)} \frac{d\sigma_o}{d\tau} d\tau$$

$$= e^{-\left(\Delta t/\eta_i\right)} \sigma_i(t)$$

Kernel function 2:

$$\sigma_{2G_i}(t+\Delta t) = \int_t^{\mathrm{t}+\Delta t} G_i e^{-\left((t+\Delta t-\tau)/\eta_i\right)} \frac{d\sigma_o}{d\tau} d\tau$$

$$= \int_t^{\mathrm{t}+\Delta t} G_i e^{-\left((t+\Delta t-\tau)/\eta_i\right)} \left[\frac{\sigma_o(t+\Delta t) - \sigma_o(t)}{\Delta t}\right] d\tau$$

$$= e^{-\left(\Delta t/\eta_i\right)} \left[\frac{\sigma_o(t+\Delta t) - \sigma_o(t)}{\Delta t}\right] \int_t^{\mathrm{t}+\Delta t} G_i e^{-\left((t-\tau)/\eta_i\right)} d\tau$$

$$= e^{-\left(\Delta t/\eta_i\right)} \left[\frac{\sigma_o(t+\Delta t) - \sigma_o(t)}{\Delta t}\right] \left[\frac{G_i}{\beta_i} e^{-\left((t-\tau)/\eta_i\right)}\Big|_t^{\mathrm{t}+\Delta t}\right]$$

$$= G_i \eta_i \left(1 - e^{-\left(\Delta t/\eta_i\right)}\right) \left[\frac{\sigma_o(t+\Delta t) - \sigma_o(t)}{\Delta t}\right]$$

By combining the two kernel functions, the total stress of the term G_i at an incremental time is

$$\sigma_{G_i}(t+\Delta t) = e^{-\left(\Delta t/\eta_i\right)} \sigma_i(t) + G_i \eta_i \left(1 - e^{-\left(\Delta t/\eta_i\right)}\right) \left[\frac{\sigma_o(t+\Delta t) - \sigma_o(t)}{\Delta t}\right]$$

Similarly, for the convolutional integral terms containing G_∞.

$$\sigma_{G_\infty}(t+\Delta t) = \sigma_\infty(t) + G_\infty \left[\frac{\sigma_o(t+\Delta t) - \sigma_o(t)}{\Delta t}\right] \int_t^{\mathrm{t}+\Delta t} d\tau$$

$$= \sigma_\infty(t) + G_\infty [\sigma_o(t+\Delta t) - \sigma_o(t)]$$

Hence, the total stress at $t + \Delta t$ can be written by combining the temporal and infinite stress terms.

$$\sigma(t+\Delta t) = \sigma_\infty(t) + G_\infty[\sigma_o(t+\Delta t) - \sigma_o(t)] + \sum_{i=1}^{n} e^{-\left(\Delta t/\eta_i\right)}\sigma_i(t) + G_i\eta_i\left(1 - e^{-\left(\Delta t/\eta_i\right)}\right)\left[\frac{\sigma_o(t+\Delta t) - \sigma_o(t)}{\Delta t}\right]$$

5.2.3 Constitutive Model Development

The QLV model is suitable to model skin response as observed in Chapter 3. Experimental data of human skin including destructive tensile and stress relaxation test data obtained in Chapter 3 were used along with the QLV framework to generate the human skin material parameters. It has been shown in Chapter 3 that skin behaves as an isotropic material at a high loading rate and exhibits anisotropy at a low loading rate where only the ground substances exhibit viscoelasticity while the collagen fibers remain rate independent. This phenomenon creates a contradiction to model the skin as a single material by using the QLV framework as it is mathematically formulated to express rate effect on material stress response where higher loading rates result in a stiffer material response. Because high-rate deformation response was the application target, an isotropic hyper-viscoelastic constitutive model was necessary by using the high rate data (i.e. 180/s DT test data) for developing the model and validating against the average 75/s DT and the average 1/s ST test group. The average 1/s ST test result was obtained by taking the average of all the sample response without considering the anisotropy factor that was observed in the 1/s group.

The central idea of the constitutive damage model development consists of two stages (Figure 5-1). First, the QLV constitutive model was used to simulate the pristine behavior of the skin sample where no damage was presented. The model fit was performed up to damage initiation stretch (λ_*), defined as the inflection point where the material softening was identified (i.e. stiffness decreases). Second, a damage function was incorporated into the pristine constitutive model to alter the stress response during the material softening process.

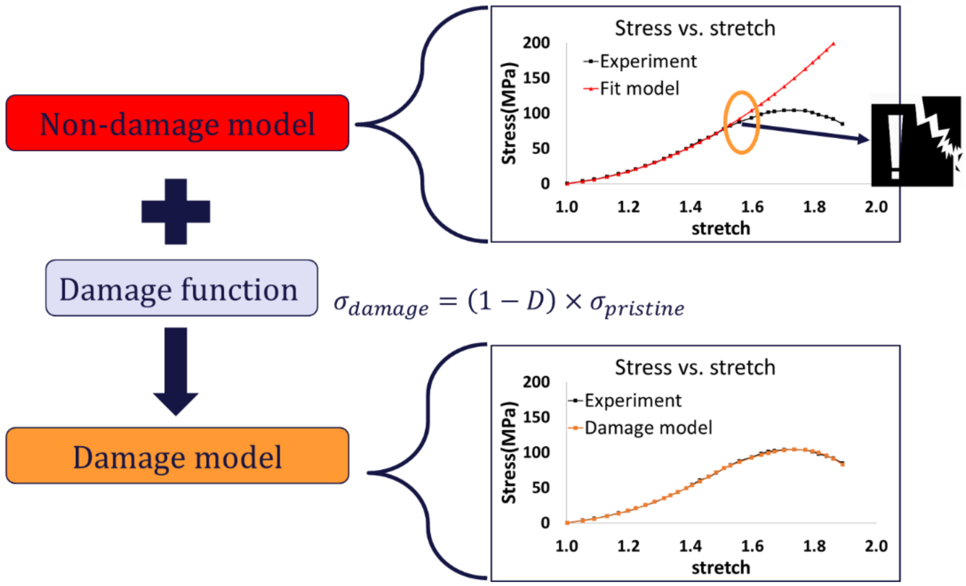

Figure 5-1: Central idea of constitutive damage model development.

5.2.3.1 Pristine Modeling (QLV)

In the first stage, all the experimental data obtained in Chapter 3 were converted from engineering stress to true stress by multiplying the engineering stress with the corresponding stretch value. An average true stress-stretch DT curve along with the UB and LB response of the skin samples conducted in the 180/s case was also constructed (Figure 5-2, right). The true stress conversion for the DT data was carried out up to the UTS point as the conversion would not be valid once necking occurred after the UTS. From the true stress-stretch curves, the stiffness of the skin sample was calculated by taking the derivative of true stress to the respective stretch at each time step. As a result, damage initiation stretch at maximum stiffness of each skin sample conducted at 180/s was identified (Figure 5-3), resulting in an average value of 1.47±0.056. The stretch was chosen as damage driven metric as it has been reported to be the best parameter for capturing skin failure (Li & Luo, 2016). Similarly, the stress relaxation was also converted to true stress response for model fitting (Figure 5-2, left). The first stage of the constitutive model fitting was performed up to the damage initiation stretch which resulted in 3 sets of materials parameters that represent the average, UB, and LB human skin pristine response.

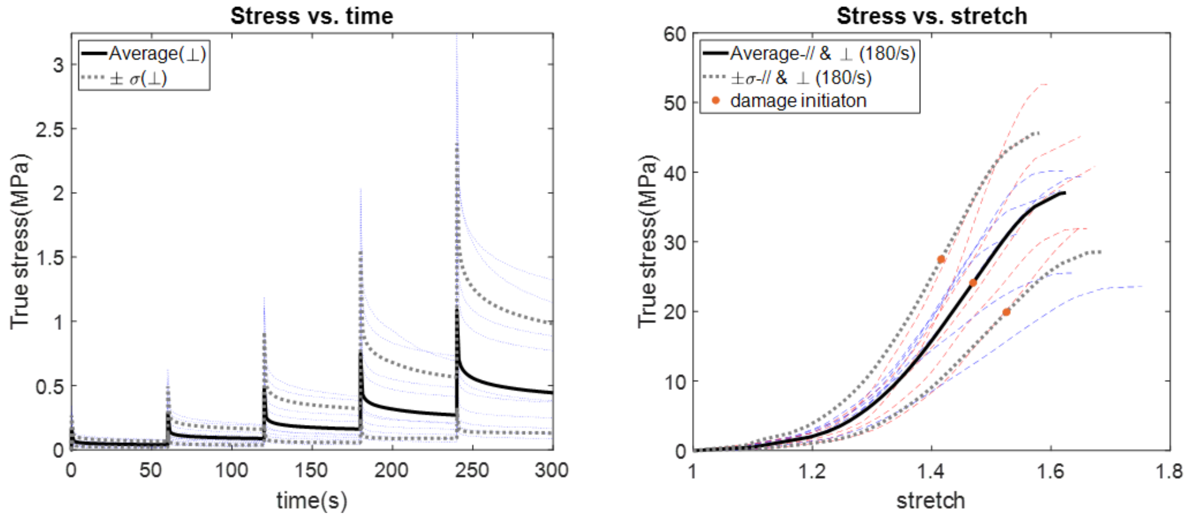

Figure 5-2: Skin's average stress relaxation response (left) and average tensile response under 180/s loading rate (right).

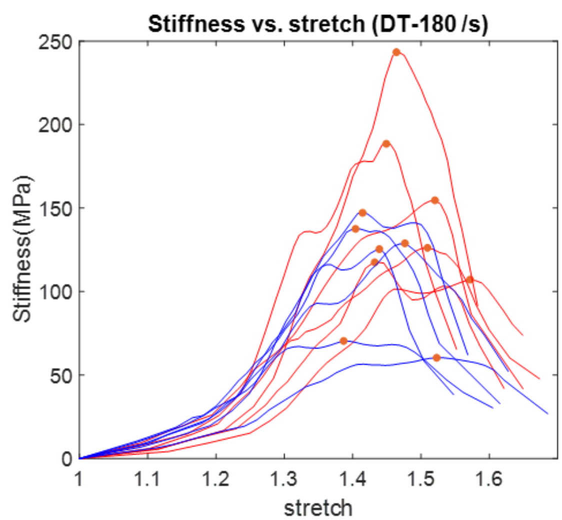

Figure 5-3: Stiffness vs. stretch of skin samples at the DT test (180/s). Orange dots indicate initiation of stiffness drop. Red curves represent parallel samples; Blue curves represent perpendicular samples.

To determine the required number of elastic parameters to capture the tensile response, initial parameter fittings were performed only using the DT test curves by minimizing the sum of squared errors (SSE) between the model response and the experimental response for each data group (average, UB, LB). The 3 terms Ogden model was selected initially by having 5 different sign combinations (Table 5) on the elastic parameters to investigate the sign effect on model response and find the optimal number of terms needed for capturing the skin tensile response.

$$SSE(\alpha_1, \alpha_2, \alpha_3, \mu_1, \mu_2, \mu_3) = \sum_{i=1}^{n} \left(\sigma_{DTexp} - \sigma_{DTmodel}\right)^2$$

Table 5: Sign constraints applied to the elastic parameters.
(PN = positive & negative value. P = positive value only. N = negative value only.)

Parameter	μ_1	α_1	μ_2	α_2	μ_3	α_3
Constraint 1			N/A			
Constraint 2	P	PN	P	PN	P	PN
Constraint 3	PN	P	PN	P	PN	P
Constraint 4	P	P	P	P	P	P
Constraint 5	N	N	N	N	N	N

Upon determining the required number of elastic parameters, 6 QLV models with different numbers of Prony series terms were investigated to determine the number of terms that have optimal performance capturing both SR and DT test responses. An initial time constant of 0.01 s^{-1} was used for the 1-term Prony Series as this represents the longest time interval obtained in the SR tests (60 s step-hold). An overall objective function ($SSE_{overall}$) for each pair of data groups (e.g. SSE of average SR and average DT) was minimized for each QLV model with different numbers of Prony series terms. To ensure fair treatment on the optimization process and remove bias on the different number of data points between test types, a normalized weight factor ω was assigned to each data group. The normalized weight factor considers a maximum sum of experimental stress found between test types and normalized by the individual sum of stress.

$$SSE_{overall} = \sum_{i=1}^{n} \left[\omega_{SR}\left(\sigma_{SRexp} - \sigma_{SRmodel}\right)\right]^2 + \sum_{i=1}^{n} \left[\omega_{DT}\left(\sigma_{DTexp} - \sigma_{DTmodel}\right)\right]^2$$

$$\omega_{SR} = \frac{\max(sum(\sigma_{SR}), sum(\sigma_{DT}))}{sum(\sigma_{SR})};\ \omega_{DT} = \frac{\max(sum(\sigma_{SR}), sum(\sigma_{DT}))}{sum(\sigma_{DT})}$$

A script was written using *fmincon* function embedded in MATLAB using interior-point algorithm to perform the optimization by having the following constraints:

1. The sum of the multiplication of the elastic constants (μ_i, α_i) should be positive to ensure a positive shear modulus is obtained.
2. The sum of the relaxation coefficients G_i's and G_∞ should be equal to 1 and all the coefficients are bounded between 0 and 1.
3. Time constants are input and fixed where β_1 is 0.01 s^{-1} with one order of magnitude increment from β_2 to β_5 to ensure the uniqueness of fit.

To evaluate the model fitted response, root mean squared error normalized by the mean experimental response (N-RMSE) was used where the difference between the experimental data and the model data is measured as

$$\epsilon = \frac{1}{\sigma_{exp\_mean}} \sqrt{\frac{\sum_{i=1}^{n} \left(\sigma_{exp} - \sigma_{model}\right)^2}{number\ of\ data\ points}}$$

5.2.3.2 Damage Modeling (Damage-QLV)

The second stage of model development is to introduce a damage function to the QLV model to alter the remaining stress response using a continuous damage mechanics approach (Lemaitre, 1985).

$$\sigma_D = \sigma_{QLV}(1 - D),\ D = \begin{cases} 0,\ \lambda < \lambda_* \\ 0 < D < 1,\ \lambda > \lambda_* \end{cases}$$

σ_D is the damage stress which equals to σ_{QLV} before damage initiates where D = 0, σ_{QLV} is the pristine stress calculated using the QLV framework in the first stage and λ_* refers to the damage initiation stretch. To guess the mathematical form of the damage function, a theoretical damage factor was determined from the equation where $D_{theory} = 1 - \frac{\sigma_D}{\sigma_{QLV}}$ between damage initiation stretch and final stretch. Since the true stress conversion from the engineering stress was only applied up to the UTS, the stretch at UTS (λ_{UTS}) was used as the final stretch rather than the failure stretch. The choice of using the stretch at UTS as the final stretch can be sufficient since it was not significantly different from the failure stretch as reported in Chapter 3. By constructing the relationship between theoretical damage factor and stretch value, a second-order polynomial function which consists of two damage coefficients (D_1 and D_2) were determined. The damage parameters D_1 and D_2 were determined through the least-squares method.

$$D = D_1(\lambda - \lambda_*) + D_2(\lambda - \lambda_*)^2$$

$$SSE(D_1, D_2) = \sum_{i=1}^{N} \left(D_{theory} - D\right)^2$$

Similarly, three sets of damage coefficients were also obtained from the average, UB, and LB curves and this completed the constitutive damage model development of human skin.

5.3 Results

5.3.1 Sensitivity Analysis of Ogden (Tensile) Parameters

Under the constraint of having a positive shear modulus (i.e. $\frac{\sum \mu_i \alpha_i}{2} > 0$), the fitted shear moduli of the average, UB, and LB model as a result of different sign constraints applied on the elastic parameters are shown in Table 6. The first 3 constraints generally result in a lower RMSE percentage value compared to Constraint 4 and 5. However, the order of magnitude of resultant shear moduli of the average, UB, and LB model was deemed to be extremely low compared to the shear modulus of 0.11 MPa obtained by Shergold and Fleck (2005) using human skin quasi-static tensile data conducted by Jansen and Rottier (1958). In contrast, Constraints 4 and 5 yielded higher shear moduli by an order of magnitude but this makes physical sense as this was due to the dynamic loading rate used in the experiment. Overall, Constraint 4 provides the best model performance by having the lowest RMSE. Hence, by using Constraint 4, preliminary results (Table 7) showed only 1 pair of the elastic parameter was sufficient to describe the skin's average, UB, and LB tensile response.

Table 6: Fitted shear modulus from parameter fitting on the Ogden model.

Parameter	Shear Modulus (MPa)					
	Average	RMSE (%)	UB	RMSE (%)	LB	RMSE (%)
Constraint 1	0.001	1.43	0.030	1.55	2.43e-5	4.19
Constraint 2	5.17e-4	3.01	0.003	1.70	5.35e-5	4.52
Constraint 3	0.001	2.69	0.041	1.57	2.23e-4	2.94
Constraint 4	2.36	4.81	3.80	3.56	1.48	6.14
Constraint 5	4.52	5.12	6.99	3.98	2.85	6.37

Table 7: Preliminary elastic parameters of the Ogden model under Constraint 4 for skin DT test response.

Parameter	μ_1	α_1	μ_2	α_2	μ_3	α_3
Average	0.003	0.006	**0.452**	**10.462**	4.946e-6	4.645
UB	0.003	0.005	**0.695**	**10.687**	0.002	0.008
LB	**0.291**	**10.149**	5.222e-6	1.367	1.395	0.00

5.3.2 Sensitivity Analysis of Prony Series

By selecting 1 term Prony series as a start, a time constant β_1 ($^1/_{\eta_i} = \beta_i$) of 0.01 s^{-1} was used and time constants with one higher order of magnitude were added for each additional Prony series term (i.e. β_2 = 0.1 s^{-1} β_3 = 1 s^{-1}, β_4 = 10 s^{-1}, β_5 = 100 s^{-1} and β_6 = 1000 s^{-1}). Figure 5-4 illustrates the decrement of N-RMSE from 64.12% to 20.9% on average SR prediction, 71.49% to 23.48% on UB SR prediction and 74.06% to 14.74% on LB SR prediction as the number of Prony series term increases from 1 to 6. Similar error decrements were also found on the DT test prediction of the average (17.27% to 4.99%), UB (16.2% to 3.66%), and LB (32.21% to 7.09%) data. Overall, a 5 Prony series term starts to show saturation on the data fitting process, starting from a 1-term model with a time constant of 0.01 s^{-1}.

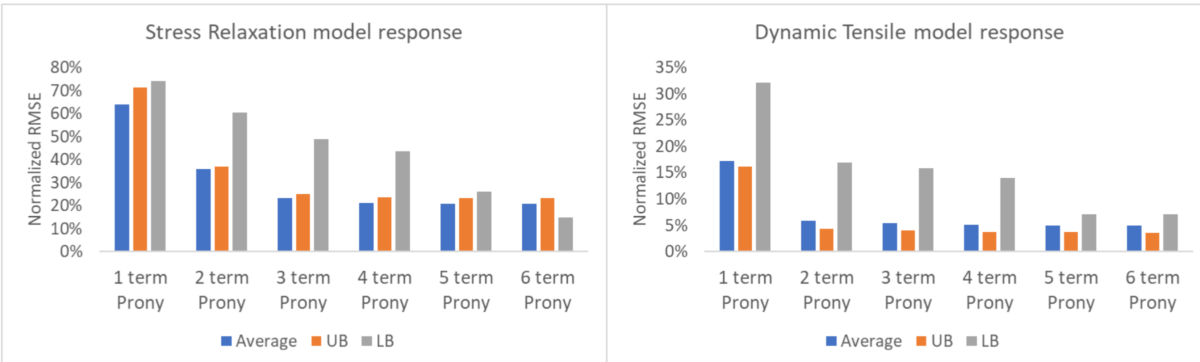

Figure 5-4: Effect of the number of Prony series on QLV model performance on the SR test (left) and DT test (right).

From the 6-term models (Table 8), no relaxation occurred at the 0.01 s^{-1} time interval for the average, UB, and LB data. For the average model, the majority (~77%) of the relaxation occurred at 1, 10, and 100 s^{-1} time constants and little relaxation window at 0.1 s^{-1} (~5%) and 1000 s^{-1} (6%). In the UB model, a similar relaxation portion (~84%) happened at 1, 10 and 1000 s^{-1} time constants instead with approximately 3% relaxation happened at 0.1 s^{-1} time constant. In the LB model, 100 and 1000 s^{-1} time constants account for 89% of the relaxation and a total of 8% at 0.1 and 1 s^{-1} time constant. As a result, time constants between 0.1 – 1000 s^{-1} were deemed appropriate for the 5 term QLV model to simulate the average, UB and LB stress relaxation and tensile data.

Table 8: Relaxation distribution of the QLV models.

Time constant (s^{-1})	Relaxation constant	Model	1-term	2-term	3-term	4-term	5-term	6-term
		Avg	1.000	0.000	0.000	0.000	0.000	0.000
0.01	G_1	UB	1.000	0.000	0.000	0.000	0.000	0.000
		LB	1.000	0.051	0.125	0.126	0.025	0.005
		Avg		0.892	0.072	0.085	0.046	0.045
0.1	G_2	UB		0.882	0.051	0.080	0.037	0.029
		LB		0.949	0.071	0.000	0.046	0.040
		Avg			0.800	0.000	0.303	0.282
1	G_3	UB			0.807	0.001	0.329	0.292
		LB			0.804	0.000	0.000	0.039
		Avg				0.785	0.269	0.290
10	G_4	UB	N/A			0.775	0.315	0.339
		LB		N/A		0.874	0.000	0.000
		Avg					0.253	0.198
100	G_5	UB			N/A		0.174	0.000
		LB				N/A	0.895	0.471
		Avg						0.059
1000	G_6	UB					N/A	0.208
		LB						0.416

5.3.3 Pristine Model Fitting

Results of SR and DT fitting using the QLV (1-term hyperelastic, 5-term viscoelastic) model are illustrated in Figure 5-5 with the material parameters summarized in Table 9. The N-RMSE expressed in percentage were calculated as 20.90%, 23.48%, and 23.74% for the average, UB, and LB stress relaxation response. For the DT tests, the N-RMSE was calculated as 4.99%, 3.66%, and 6.61% for the three data groups. The N-RMSE shown in Figure 5-5 of the DT test were calculated within the pristine region.

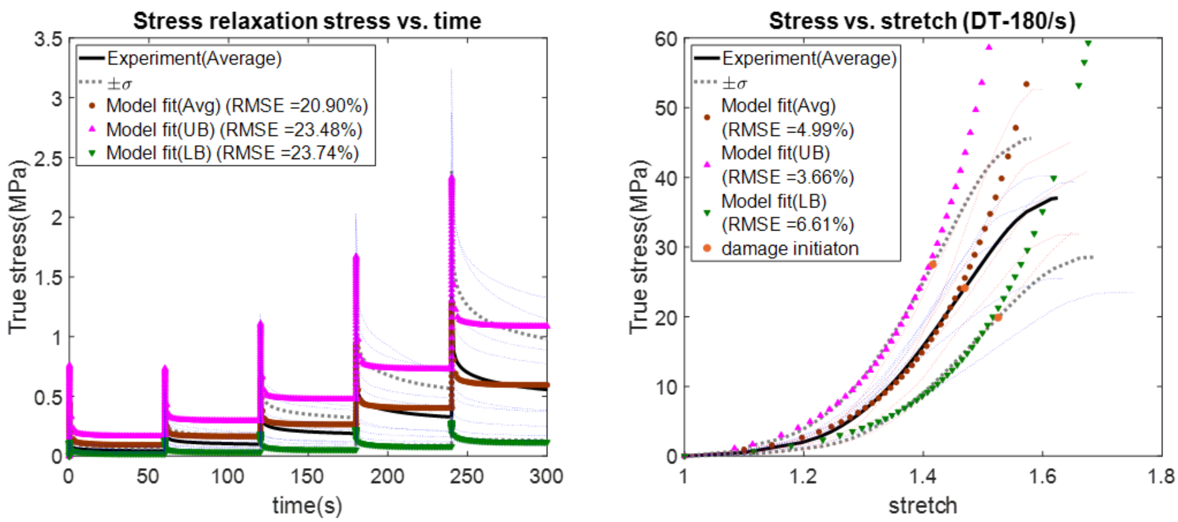

Figure 5-5: QLV model simultaneous fitted results of SR tests (left) and DT tests (right).

5.3.4 Damage Model Fitting

A relationship between theoretical damage factor D and stretch was constructed and a second-order polynomial function fit was performed to obtain the damage coefficients (D_1 and D_2) (Figure 5-6). The fitted damage coefficients are presented in Table 9. By multiplying the damage factors to the pristine QLV stress, DT response prediction with N-RMSE of 3.08%, 2%, and 3.96% was obtained using the average, UB, and LB QLV damage model respectively (Figure 5-7).

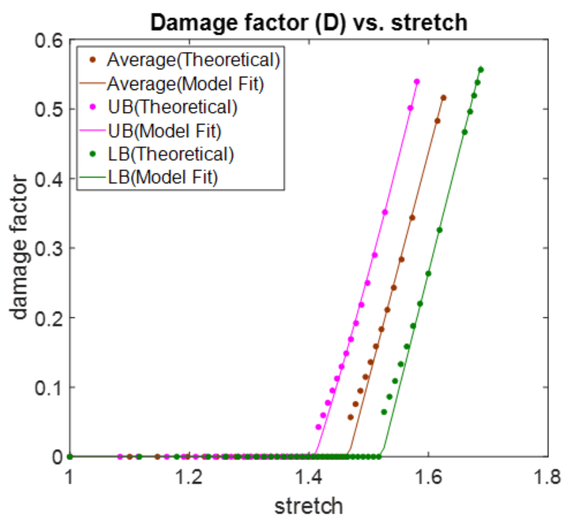

Figure 5-6: Damage factor evolution vs. stretch - Theoretical vs. Model Fit.

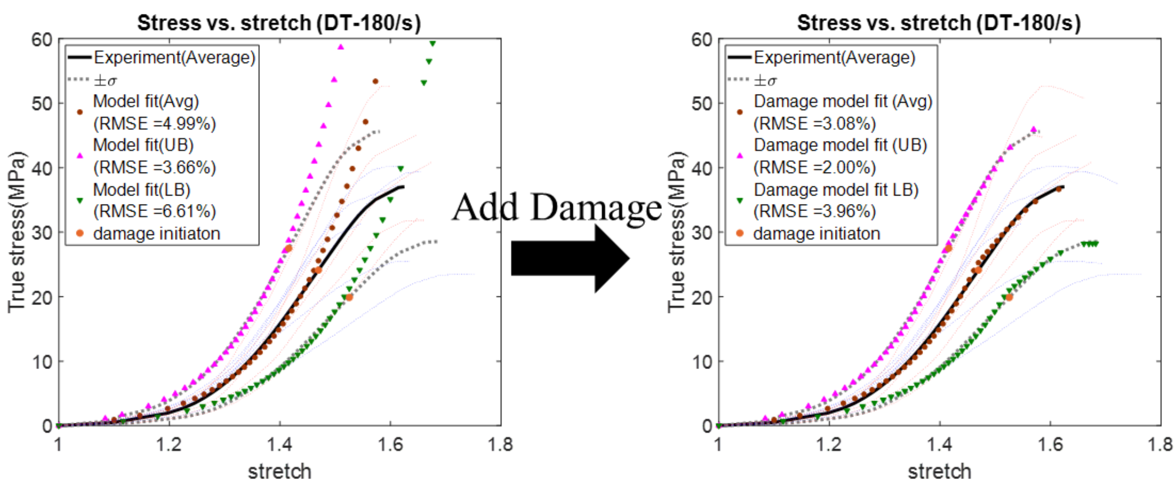

Figure 5-7: QLV damage model fitted results.

5.3.5 QLV Model Validation

To demonstrate the capability of the QLV framework to predict strain rate effect on the skin response, the optimized material parameters based on the 180/s dynamic tensile test and the stress relaxation test (Table 9) were used to generate model responses using the experimental loading rate at 1/s and 75/s (Figure 5-8). N-RMSE between the average experimental data and the average QLV model was calculated as 5.72% at the 75/s test group and 34.41% at the 1/s test group. Although high N-RMSE was obtained in the 1/s test case, the average model prediction still lied within the data pool. Model predictions of UB and LB data also lied within the data pool, however, the UB model performed the worst at 1/s test case with an N-RMSE of 48.33%. Hence, the average, UB, and LB data of the three strain rates were investigated and the results (Figure 5-9) showed no loading rate dependency was found in the UB data group. This explained the high N-RMSE obtained by the UB model prediction since the QLV framework was designed to respond to different strain rates. In contrast, both average and LB data groups showed rate dependency in which the QLV model provided better predictions.

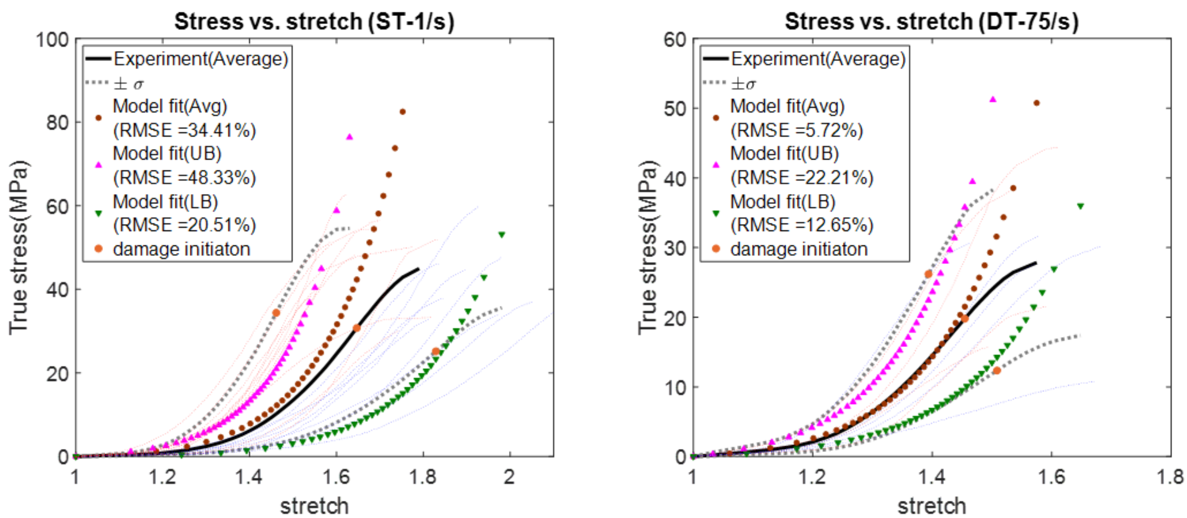

Figure 5-8: QLV model prediction vs. experimental tensile data at 1/s (left) and 75/s (right).

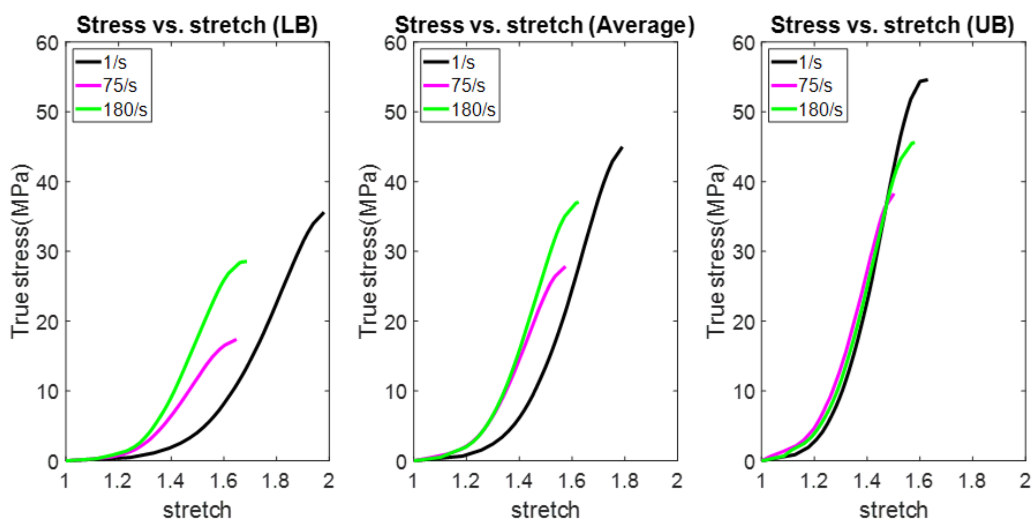

Figure 5-9: LB, Average, and UB skin experimental data. The skin's UB response does not show loading rate dependency.

By adding the optimized damage coefficients, the damage responses at 1/s and 75/s predicted by the QLV model are illustrated (Figure 5-10). Similar to the pristine prediction, the damage coefficients capture the skin-softening response with an N-RMSE of 4.32% and 32.79% from the average model and 11.93% and 18.52% from the LB model at 75/s and 1/s, respectively. Due to the poor UB pristine model fitting, the UB damage model continued to result in high N-RMSE, particularly in the 1/s test group. Despite giving high N-RMSE, the UB model still yielded the stiffest response that was within the data corridor across the three strain rates.

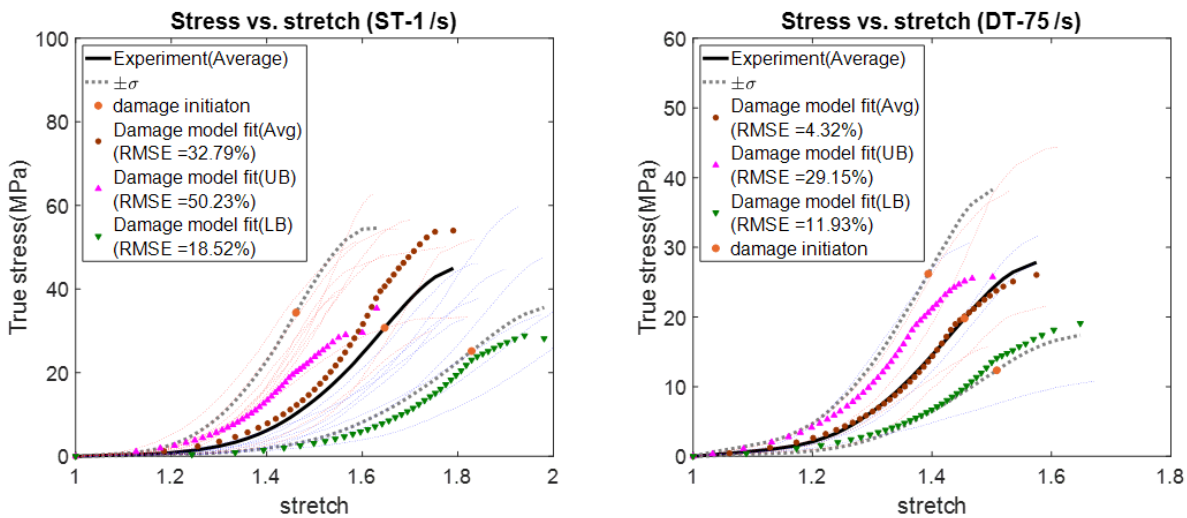

Figure 5-10: QLV damage model prediction vs. experimental tensile data at 1/s(left) and 75/s (right).

Table 9: Summary of QLV damage model material parameters of human skin

	Parameter	Average	Upper Bound (UB)	Lower Bound (LB)
Hyperelastic	μ_1(MPa)	0.431	0.699	0.362
	α_1	10.700	11.073	10.447
	Shear modulus (MPa)	2.303	3.872	1.892
Viscoelastic	G_1	0.043	0.028	0.046
	G_2	0.314	0.295	0.033
	G_3	0.240	0.334	0.000
	G_4	0.277	0.000	0.489
	G_5	0.000	0.211	0.401
	G_∞	0.127	0.132	0.031
	β_1 (s^{-1})		0.1	
	β_2 (s^{-1})		1	
	β_3 (s^{-1})		10	
	β_4 (s^{-1})		100	
	β_5 (s^{-1})		1000	
Damage	D_1	3.189	2.719	3.389
	D_2	0.001	2.482	9.198e-4
	λ_*	1.47	1.41	1.52
	λ_{UTS}	1.61	1.57	1.66

5.4 Discussion

A continuum damage mechanics approach coupled with the isotropic QLV framework was used in the current study to model skin tensile failure responses at three distinct loading rates (1/s, 75/s, and 180/s) using stress relaxation and destructive uniaxial tensile test data. As a result, three sets of material parameters including damage coefficients were generated to represent the average, UB, and LB skin tensile failure response.

The three QLV model predictions on stress relaxation response resulted in an overall error below 25% when fitting both SR and DT test data simultaneously. First, the SR tests were only performed up to 25% strain level while the DT test had the skin sample tested until failure where the stretch level was higher (~60% strain). Hence, only limited viscoelastic information was obtained and used for higher loading strain when fitting the DT test data. The human skin relaxation response was shown to be strain independent up to 25% strain level, however, the independency remained uncertain as strain level increased in the DT test. The hyperelastic stress at higher strain levels also remains unknown. Therefore, the range of applicability of the viscoelastic information obtained in the stress relaxation test was limited to the extent of the skin deformation. In an ideal situation, a high strain level would be applied to cover the entire relaxation spectrum of the skin during the stress relaxation test, but this was impossible because the skin sample could be damaged when subjected to extreme deformation. Furthermore, a fully nonlinear viscoelastic model would also be necessary to replace the QLV framework as the relaxation response may no longer be strain independent as loading strain increases. Nevertheless, the SR test data provide fundamental rate sensitivity information that can be reflected using the QLV model. To demonstrate the effect of strain level, an identical model fitting process was performed on the three QLV models only up to 25% strain on the DT tests, and the SR tests. This yields better results compared to full DT data fitting where less than 3% and 15% N-RMSE were obtained for the DT and the SR predictions, respectively (Figure 5-11).

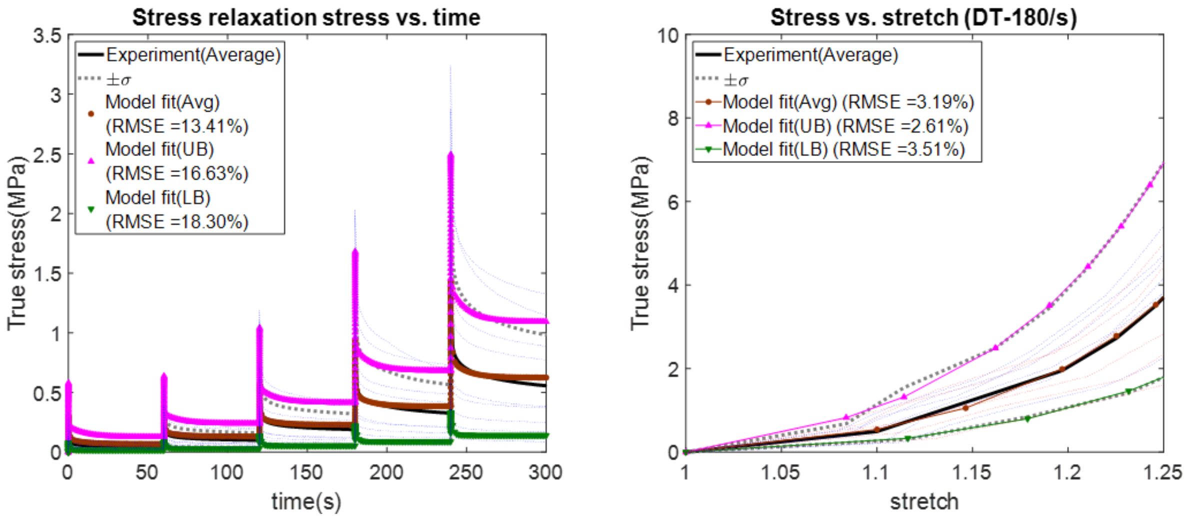

Figure 5-11: QLV model simultaneous fitted results of SR tests (left) and DT tests (right) up to 25% strain.

Second, the rate of loading was also a factor contributing to the viscoelasticity of the skin. In theory, the viscoelastic response resulting from a 2/s (SR) and a 180/s (DT) loading rate would be different where the higher the loading rate, the more the elastic and viscous component of the skin could be separated under the SR test. Since a lower loading rate was applied in the SR tests, skin's relaxation may have occurred during the ramp-up period and therefore resulting in different skin stiffness and relaxation response compared to the DT tests. By performing model fitting using stress relaxation and dynamic tensile test data simultaneously, the model optimization process would compromise the stiffness difference from both data types and therefore, resulting in poorer N-RMSE as opposed to fitting only to the SR data.

The one-term Ogden parameters (μ_1 =0.431 MPa; α_1 = 10.700) was sufficient to capture the skin tensile response which was also found by Shergold and Fleck (2005) who performed parameter fitting using human umbilical skin *ex vivo* tensile data conducted at 0.01/s by Jansen and Rottier (1958). The difference between the shear modulus (2.3 MPa vs. 0.11 MPa) could be due to the different loading rates used in the current study compared to the literature data. However, the exponential term α is similar (10.7 vs. 9) which is deemed to be strain rate-independent (180/s vs. 0.01/s). The strain independency of the exponential term was also found in *ex vivo* uniaxial tensile (0.005 /s - 3500 /s) and compression (0.004 /s - 4000 /s) tests conducted using pig skin (Shergold et al., 2006; Lim et al., 2011) where consistent α values of 11 (tension) and 12 (compression) were found in these tests while the μ term increased with increasing strain rate. From the LB and UB models, a consistent exponential term (~10) was also observed while the material constant μ was positively correlated with the model stiffness. The same positive correlation was also observed in shear modulus where the highest shear modulus of 3.872 MPa was obtained in the UB model, followed by the average model and the lowest shear modulus in the LB model.

For the damage modeling, all the theoretical damage factors were found to be around 0.5 rather than 1, this was because the damage was only modeled up to UTS and no sudden stress drop was presented in the stress-stretch curve (zero stress value). This brings convenience to the damage fitting process because capturing the sudden stress drop would be difficult using the polynomial function. The damage accumulation deduced from the pristine stress as a function of tensile stretch exhibited a linear relationship for the average and LB model where the quadratic term was negligible. This was not found in the UB model where a higher-order damage term was required. With stiffer skin, the damage initiation stretch was lower since the collagen fibers were more aligned which results in a shorter amount of pristine model fitting (early J turn captured by the model). Hence, the damage function would require higher-order terms to better fit the damage response.

The material parameters generated using the QLV damage framework were capable of capturing the skin’s average and LB tensile failure response at different loading rates. Although the UB model underpredicts the failure response, particularly at low strain rates (1/s), the relevant response still lies within the data. The QLV damage model developed in the current study neglects skin's anisotropy which was apparent at low loading rates limits its application and anisotropy implementation should be accounted for in future work.

5.6 Conclusion

A rate-sensitive skin damage model that coupled the isotropic Quasi-Linear Viscoelastic (QLV) framework with the continuum damage mechanics approach using a second-order polynomial function was developed in the current study. The sensitivity analysis showed that an all positive one term Ogden model along with 5 term Prony series in the QLV framework was sufficient to model the skin's pristine tensile response. The model distinguishes the pristine and damage phases of the skin based on damage initiation stretch which was determined from the inflection point of the stiffness history during the loading process. It was observed that the skin damage factor exhibits a linear relationship with the loading stretch while a higher-order polynomial term was required when simulating damage of stiffer skin. The rate-sensitive skin material and damage parameters were inversely determined based on stress relaxation and destructive uniaxial tensile test data which were designed at the rate of ballistic blunt impact. Three sets of material parameters that represent the average, UB, and LB skin were generated in the current chapter and will serve as input for numerical skin model development.

CHAPTER 6 – Finite Element Material Model Development of Human Skin

The constitutive damage model of human skin has been developed in the previous chapter using the QLV framework incorporated with the Lemaitre damage approach. The outcomes provide three sets of rate-dependent material and damage parameters for average, UB, and LB human skin subjected to tensile loading. In this chapter, finite element (FE) material models with damage prediction of human skin were developed by using the parameters obtained in Chapter 5. The user-defined material (UMAT) card of the constitutive damage model was compiled and implemented into a FE solver (LS-DYNA). The UMATs were verified and validated using the experimental data of human skin as conducted in Chapter 3 and Chapter 4. The goal of this chapter is to develop a validated human skin FE material model that can simulate skin progressive failure under high-speed ballistic impact.

6.1 Introduction

The ability to describe skin's mechanics has been extensively studied, especially on constitutive model development as mentioned in the previous chapter. To transfer scientific knowledge to engineering applications, the Finite Element (FE) method is one of the commonly used approaches which simulates the object response by solving complex numerical equations to inform the application consequences. By implementing the human skin's constitutive model in the FE solver, the numerical model can be used as a surrogate to provide opportunities to potential users to conduct skin research in the engineering, medical, and cosmetic industries. A validated FE model can also be used repetitively for sensitivity analysis to inform future research. However, the transition from the analytical model to the numerical implementation of human skin is very scarce. Most of the human skin FE models are treated as a singular component, i.e. the epidermis and the dermis are modeled with identical material properties (Flynn et al., 2011; Groves et al.,

2013) while Flynn & McCormack, (2008) have developed a three-layer skin model. Different skin properties such as nonlinearity, viscoelasticity, and anisotropy have been implemented in these FE models. These FE models are particularly useful to study skin mechanics within the human physiological level. However, there are limitations to studying skin injury since the models are not built with damage prediction capability. For modeling skin injury, there is only one study investigating skin failure under stab penetration using FE analysis (Ní Annaidh et al., 2013). The FE model was validated against a quasi-static penetration dataset using a hyperelastic model while the failure was modeled using the element erosion feature when exceeding the designated failure strain and no material softening was considered. Furthermore, Chanda and Upchurch (2018) have also developed a FE skin failure model but focused on post-injury development where the FE model was constructed with a hollow 'wound'. One of the commonly used skin FE models in the field of injury biomechanics today is found on the Global Human Body Model Consortium (GHBMC) human body models. The GHBMC skin model uses a linear viscoelastic formulation with a single time constant and a failure criterion is not included.

The performance of the GHBMC skin model on the application of ballistic impact remains questionable and has not been investigated. Based on the existence of the current skin FE damage model which used the hyperelastic constitutive model (Ní Annaidh et al., 2013), there is a lack of viscoelastic damage FE models of human skin. Therefore, the purpose of this chapter is to develop a FE skin damage model that can be used to study skin failure under the ballistic blunt impact. The viscoelastic damage constitutive model developed in the previous chapter was implemented in a FE solver as a user-defined material (UMAT) and was numerically verified and validated against the previously determined tensile and indentation data. Moreover, the GHMBC skin was used and compared with the UMAT to evaluate its performance.

6.2 Methods

6.2.1 User-Defined Material (UMAT)

The QLV-damage coupled constitutive model as demonstrated in Chapter 5 was implemented into LS-DYNA software as a user-defined material (UMAT) to simulate skin tensile failure. Hydrostatic pressure ($\sum_{j=1}^{n}\left(\frac{1}{m}(J^{-m\alpha_j}-1)\right)$) which corresponds to the volumetric deformation was added to the Ogden strain energy density function (Ogden, 1972; Hill, 1979). This term provides flexibility on material compressibility by adjusting parameter m which is related to the Poisson's ratio as part of the user input (Storåkers, 1986). The Jacobian J is calculated from the determinant of deformation gradient F, which is solved numerically depending on the deformation of the element.

$$W(\lambda) = \sum_{j=1}^{n}\frac{\mu_j}{\alpha_j}\left(\lambda_1^{\alpha_j}+\lambda_2^{\alpha_j}+\lambda_3^{\alpha_j}-3\right)+\sum_{j=1}^{n}\left(\frac{1}{m}(J^{-m\alpha_j}-1)\right)$$

$$m = \frac{\nu}{1-2\nu}$$

$$J = det\begin{bmatrix} F_{11} & F_{12} & F_{13} \\ F_{21} & F_{22} & F_{23} \\ F_{31} & F_{32} & F_{33} \end{bmatrix}$$

As a result, the principal Cauchy stress of this compressible material is reduced to the following equation

$$\sigma_j = \sum_{j=1}^{n}\frac{\mu_j}{J}\left[\left(\lambda_1^{\alpha_j}-J^{-m\alpha_j}\right)\right]$$

To find the principal stretches in the FE model, left Cauchy-Green deformation tensor B was first calculated ($B = FF^T$). Next, the principal stretches were determined by taking square roots of eigenvalues of the tensor B where this process was performed numerically using TRED2 and TQLI subroutine files (Press et al., 1996).

$$B = {\lambda_1}^2 b^{(1)} \otimes b^{(1)} + {\lambda_2}^2 b^{(2)} \otimes b^{(2)} + {\lambda_3}^2 b^{(3)} \otimes b^{(3)}$$

With the Jacobian and the principal stretches being determined, a 3 dimensional instantaneous stress σ_{ij} tensor of the material in each direction can be calculated.

$$\sigma_{ij} = \frac{1}{J}\left(\sum_{j=1}^{n} \mu_j\left[\left(\lambda_1^{\alpha_j} - J^{-m\alpha_j}\right)\right] \times {b_i}^{(1)}{b_j}^{(1)} + \sum_{j=1}^{n} \mu_j\left[\left(\lambda_2^{\alpha_j} - J^{-m\alpha_j}\right)\right] \times {b_i}^{(2)}{b_j}^{(2)} + \sum_{j=1}^{n} \mu_j\left[\left(\lambda_3^{\alpha_j} - J^{-m\alpha_j}\right)\right] \times {b_i}^{(3)}{b_j}^{(3)}\right)$$

The viscoelastic stress calculated using the QLV framework was based on the hyperelastic parameters and the reduced relaxation constants as presented in Chapter 5. An overall view of the UMAT card in LS-DYNA is illustrated in Figure 6-1. A maximum of 4 terms Ogden (*mu* and *alpha*) and 5 terms Prony series (*G* and *beta*) can be supplied to the UMAT card to calculate the viscoelastic stress. The viscoelastic feature can be disabled by setting the *ve* term to zero in the UMAT which results in only hyperelastic stress calculations. The optimized damage coefficients can be supplied under the *D1* and *D2* terms while the *h_initial* and *h_fail* allow the user to decide damage initiation and failure (i.e. element erosion) threshold in terms of stretch ratio. The damage coefficients are ignored if the *dsw* term is set to zero and element erosion will only occur if the *ifail* term is set to one. Lastly, a bulk modulus *K* and shear modulus *G* were given to the UMAT for transmitting boundaries, contact interfaces, and time step calculations to initiate the simulation process. The *nu* term refers to the material Poisson's ratio that dictates the material's compressibility. All simulations and UMAT compilation were conducted using the shared memory parallel (SMP), double precision processing capability of LS-DYNA (v971, R10.1.0, LSTC, Livermore).

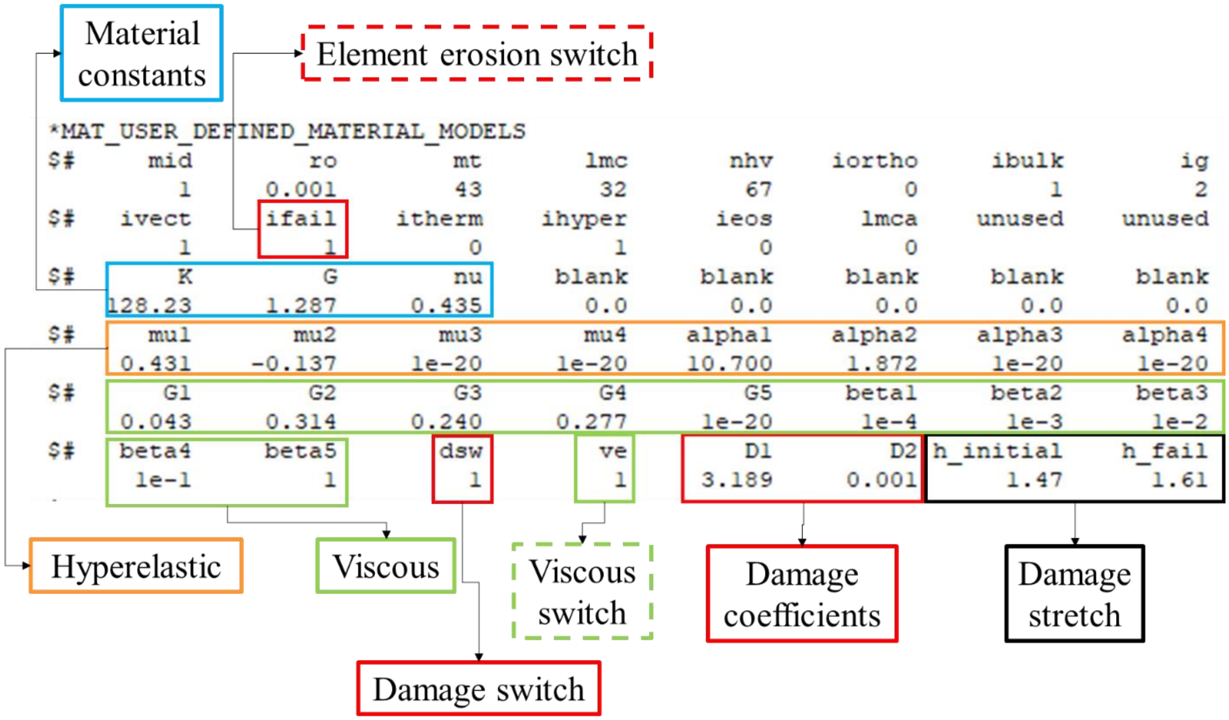

Figure 6-1: UMAT example of the QLV damage model developed in LS-DYNA.

6.2.2 UMAT Code Verification and Dynamic Tensile Test Verification

Details including methods and results of the verification of the implemented UMAT were documented in Appendix A. These include code verification using a single solid element to demonstrate unrecoverable damage and viscoelastic modeling. Besides, the DT test simulations of the dogbone specimen were also performed to verify the UMAT.

6.2.3 Indentation Test Validation

The verified UMAT based on the uniaxial tensile loading case was validated against the indentation test using the DI test data presented in Chapter 4. A successful UMAT validation under the DI test will demonstrate the material capability to simulate skin tensile failure under ballistic blunt impacts. Three sample-specific models which have the closest data response to the average, UB and LB DI force-displacement data were chosen from the 18 tested samples to validate the UMAT. To do this, three 4th order polynomial functions were fitted separately to the average, UB, and LB DI force-displacement data, and these provided polynomial coefficients that were used to compute the RMSE between the individual sample and the models to select the closest similar curves with minimum RMSE.

The boundary and initial conditions of the model of the DI test were investigated since it was observed in the experiments that the skin was not always loaded perfectly. Three model setups were investigated (Figure 6-2). The first model included the taut skin without edge slip where the edge of the skin was fully fixed (Figure 6-3, bottom left). The second model included the taut skin with edge slip, sandwiched in between two restraining plates. No constraint was applied around the skin edge while the rest of the nodes were free to slide against the restraining plates with some being fully fixed at screw locations (Figure 6-3, bottom right). Finally, for the third model, the same sandwiched model was setup but instead a curved skin was used since it was observed from the DIC surface that the DI skin samples do not show complete flatness before impact (Figure 6-4). The amount of curvature was determined from the generated DIC surface by measuring out of the plane distance (z-direction) between the origin and center point of the surface. Symmetry was assumed on the skin and quarter models were built to save simulation time with 2 mm mesh size served as the baseline model, having the same hourglass control as used in the tensile test verification step. A mesh sensitivity study was also performed using 1 mm and 0.5 mm element size. The indenter was modeled as a rigid body (*MAT_RIGID), assigned with aluminum material properties as it is relatively tougher than the skin and the *PART_INERTIA keyword was used to define its mass, initial velocity, and inertial properties. *CONTACT_AUTOMATIC_SURFACE_TO_SURFACE keyword with a segment based contact (SOFT = 2) was used to create contact between the indenter and the skin as well as skin-plate interaction. The effect of friction of coefficients for both contacts on the force-displacement response was also performed as part of the FE model sensitivity analysis. Force was measured from the contact force (*DATABASE_RCFORC) between the skin and the indenter and multiplied by 4 to obtain total force due to model symmetry while indentation displacement was measured using the center node of the skin model. In addition to the force-displacement response, displacement contour before failure was also used as a validation metric. To obtain the displacement contour, x, and z coordinates of each node along the radius of the skin model were measured where the x-coordinate represents the position of skin radius and the z-coordinate represents indented skin displacement (Figure 6-2).

The GHBMC skin material was used to compare with the UMAT skin. Skin failure on the GHBMC skin was simulated using the *MAT_ADD_EROSION keyword by assigning the same maximum principal strain value used by the average UMAT as the failure threshold.

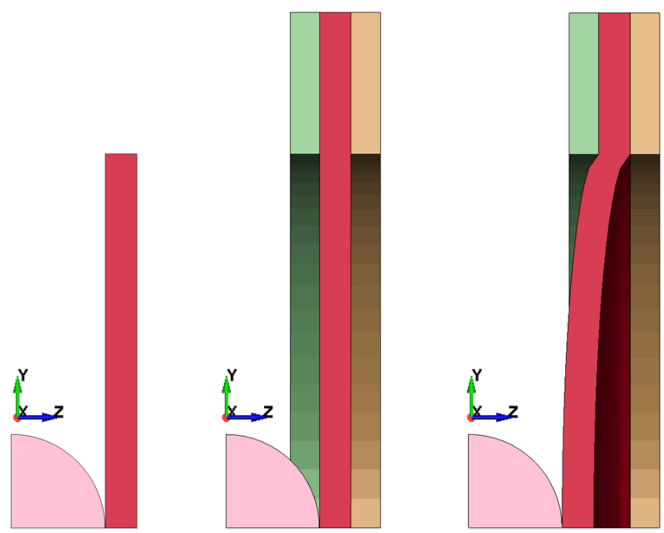

Figure 6-2: Side view of DI test FE model setup. Taut skin (left). Taut skin sandwiched in between two restraining plates (middle). Curved skin sandwiched in between two restraining plates (right).

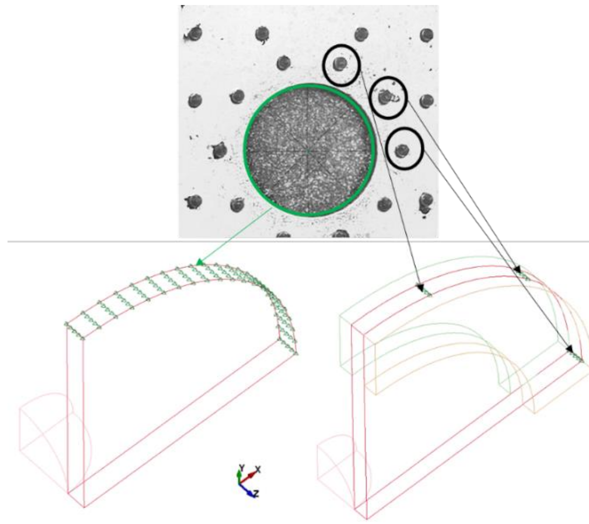

Figure 6-3: Physical DI test setup (Top middle). Fully constrained boundary condition around the skin edge on taut skin setup(bottom left). Partial constrained at screw locations on taut skin sandwiched in between restraining plates setup (bottom right).

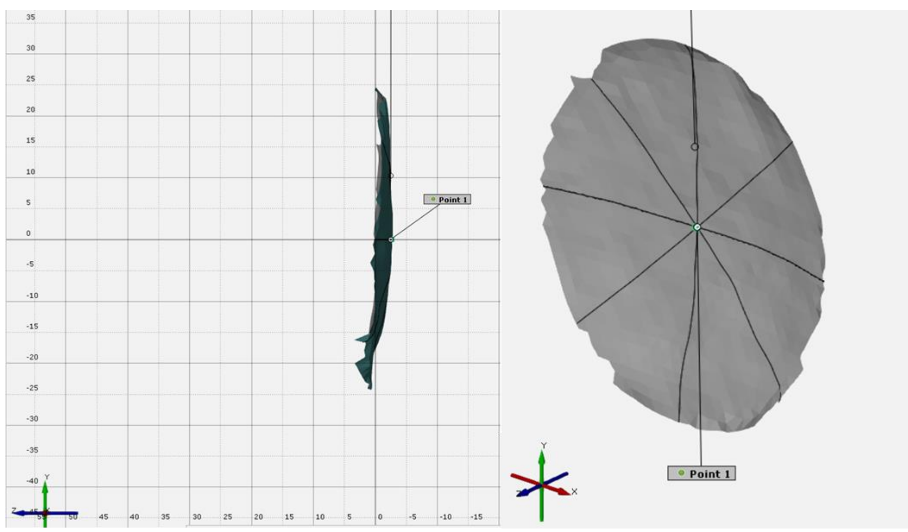

Figure 6-4: Curved skin sample before impact observed from DIC surface (left). The Center point (Point 1) shows the amount of curvature from the origin. An isometric view of the curved sample is shown (right).

6.3 Results

6.3.1 Dynamic Indentation Test Simulation

The DI FE model sensitivity was investigated from three different perspectives including physical effect, numerical effect, and effect of material parameters to obtain the optimum FE simulation result possible. Three skin samples that have the closest force-displacement response to the average, UB, and LB experimental data were chosen (Figure 6-5). The skin sample (702-

RU-0) which represents the average response was used to construct a sample-specific FE model for the model sensitivity analysis.

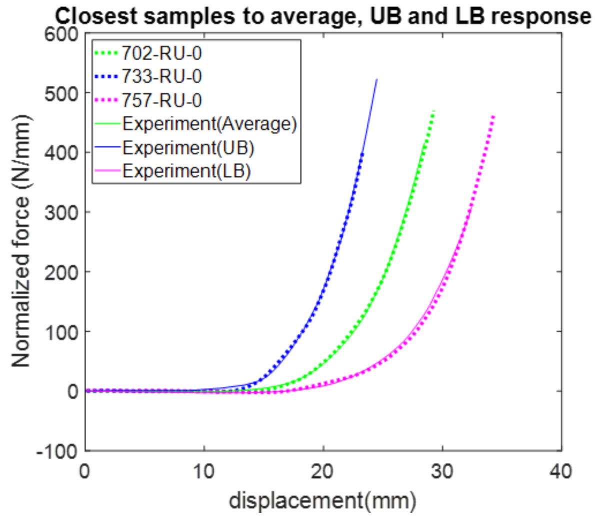

Figure 6-5: Closest samples (dotted color lines) to average, UB, and LB experimental responses (solid color lines).

6.3.1.1 Physical Effect - Model Setup and Contact Friction

Three different model setups were compared to assess the effect of boundary conditions on the model's force-displacement response. Overall, all three models had a similar force-displacement response but stiffen at different indentation displacement. By assuming no sliding and having the skin edge fully constrained, the taut skin model stiffened at the earliest displacement when being indented at about 10 mm. There was only a slight improvement when modeled the taut skin sandwiched in between the restraining plates where the skin edge was not constrained. Lastly, by considering the curved, non-taut initial geometry of skin, the timing of the model response was the closest to the average experimental data (Figure 6-6). This study demonstrated that the initial skin curvature had a larger effect than the boundary condition in dictating force-displacement response.

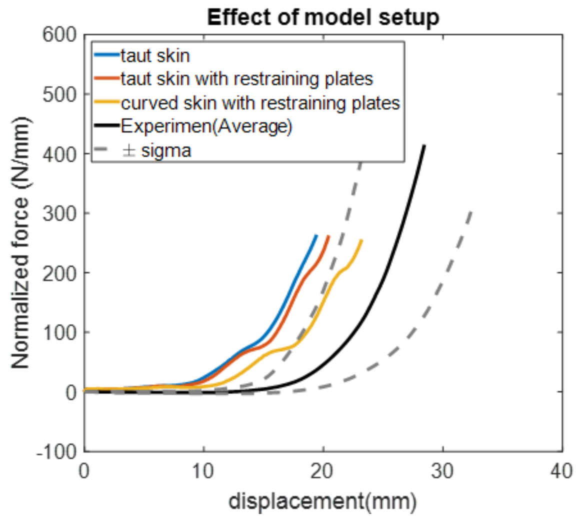

Figure 6-6: Effect of model setup on the DI force-displacement response.

Next, both skin-indenter friction and skin-plate friction effects were investigated. Both static and dynamic friction coefficients of 0.1, 0.5, 1.0, 1.5, and 1.9 were studied for the skin-plate interaction. A range that included a high friction coefficient was considered because a sandpaper interface was used between the skin and the restraining plate in the experimental setup. The results (Figure 6-7, left) demonstrate that friction coefficient had a minimal effect on the skin force-displacement response. For the skin-indenter interaction, friction coefficients from 0.1 to 0.6 at 0.1 intervals were investigated since literature has shown friction coefficient between human skin and unlubricated aluminum lies within 0.4 and 0.6 (Zhang & Mak, 1999; Seo & Armstrong, 2009). Similar to the skin-plate friction study, friction between the indenter and the skin had a negligible effect on the force-displacement response (Figure 6-7, right) except for the maximum failure force. A higher friction coefficient resulted in a higher failure force with a maximum difference of 36.6 N (~12%) between 0.1 and 0.6. As the dynamic friction coefficient was known to decay with an increasing velocity between two objects, friction of 0.1 between the skin and the indenter was decided.

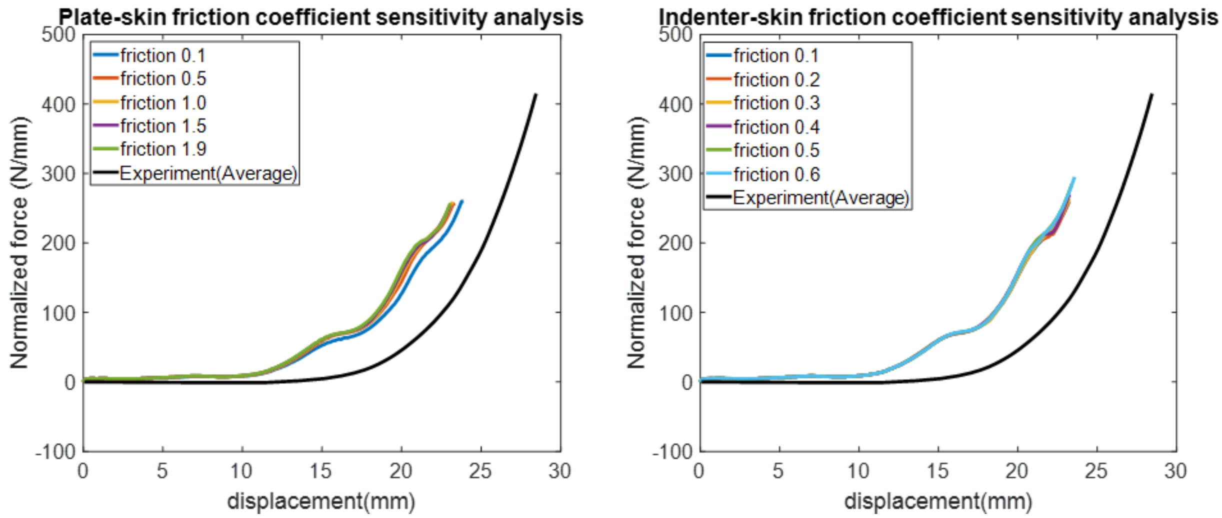

Figure 6-7: Effect of plate-skin friction (left) and indenter-skin friction (right) on the DI force-displacement response.

6.3.1.2 Numerical Effect – Mesh Size and Hourglass Control

Three different mesh sizes (2 mm, 1 mm, and 0.5 mm) were chosen to investigate model response sensitivity to mesh size. The results demonstrated that mesh size did not affect the model's force-displacement response (Figure 6-8), but it was a factor that causes early failure with a smaller mesh size similar to the DT test simulation (Appendix A).

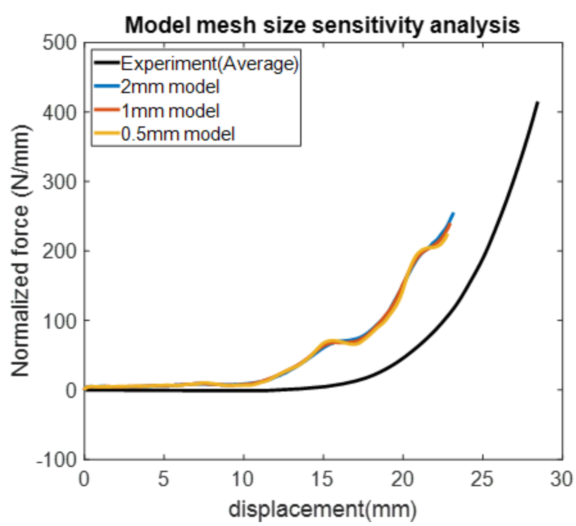

Figure 6-8: Effect of mesh size on the DI force-displacement response.

Different hourglass controls in LS-DYNA including viscous form (type 3), stiffness form (type 5) with exact volume integration, and type 6 were also investigated. The analysis showed type 5 and type 6 hourglass control had a poor performance where large element distortion was observed (Figure 6-9) while default type 1 and type 3 did not have similar simulation results.

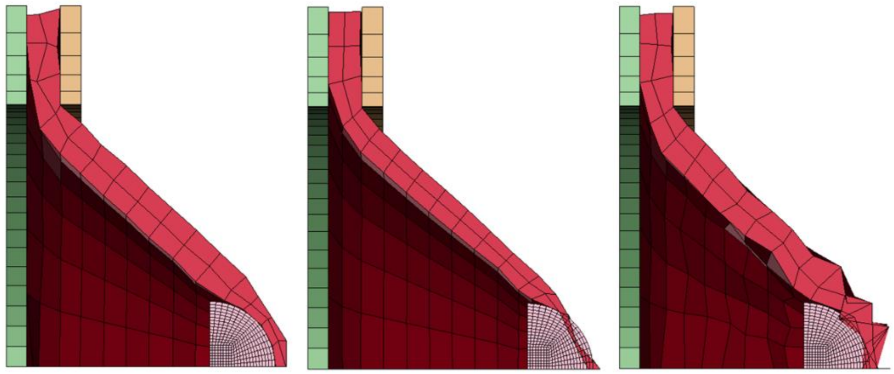

Figure 6-9: Effect of hourglass control type in LS-DYNA. Left: IHQ 1&3. Middle: IHQ 5. Right: IHQ 6.

By using a time scale factor of 0.1 (determined from DT simulation in Appendix A), with a curved initial skin geometry, a boundary condition represented by the retaining plates, a 2 mm mesh size, type 3 hourglass control for the skin model, coefficient friction of 1.0 between the skin and the retaining plate, and friction coefficient of 0.1 for the skin-indenter interaction was chosen for simulating the DI test. However, the initial DI test simulation result shows early stiffening, lower failure force, and shorter failure displacement than the experimental data. The following section investigated potential material parameters to understand the reason for the differences.

6.3.1.3 Material Parameters Effect – Poisson's ratio and Compression Material Parameters

The first parameter to investigate was the Poisson's ratio of the skin material. Four different Poisson's ratios (0.495, 0.435, 0.3, and 0.1) were investigated for the skin UMAT. The simulation results indicated that the effect of the Poisson's ratio was minimal, although there was a trend that the skin was more compliant as the Poisson's ratio was decreased (Figure 6-10).

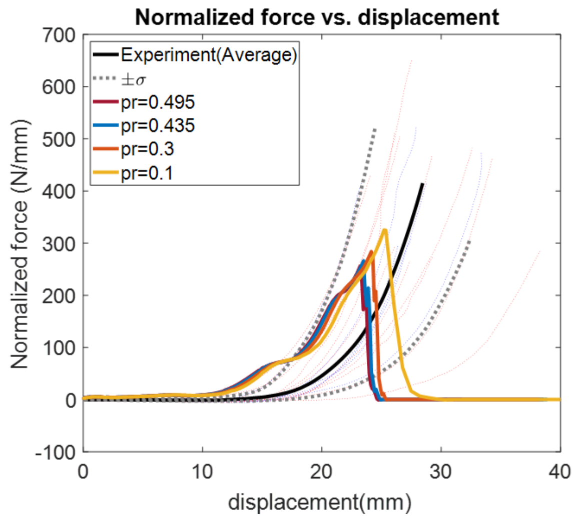

Figure 6-10: Effect of Poisson's ratio (pr) on DI force-displacement response.

Therefore, it was believed that the current material parameters developed from uniaxial tension data overpredicted the material response when it was loaded in a combined tension/compression mode around the indenter tip. This was demonstrated in Figure 6-11, (left) where the current QLV model (baseline model) was compared with the quasi-static compression data of human skin as obtained in Chapter 3.

To improve the model compressive response, an additional Ogden term (i.e. μ_2 and α_2) was added to the current QLV model. These values were determined through the SSE minimization between the compression data and the model response while maintaining the original tensile behavior. The fitted result ($\mu_2 = -1.089$ and $\alpha_2 = 1.872$) is indicated by the orange line (Updated Model) in Figure 6-11 (left). The addition of the elastic constants slightly improves the model compressive response, and this is reflected in the DI simulation where the model stiffening response was delayed (Figure 6-10, right). This shows the incorporation of the compressive response to the QLV model improved the overall indentation model result.

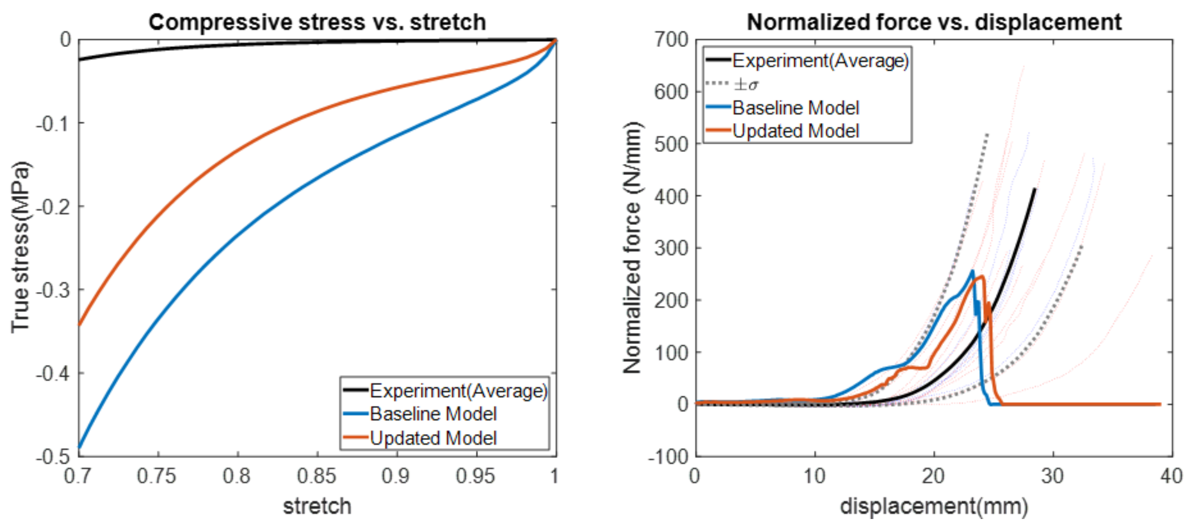

Figure 6-11:Model compressive performance (left) and indentation performance (right).

The delay of the model stiffening was also reflected in the maximum principal strain (MPS) response (Figure 6-12, right). The experimental MPS data was collected from the center of the DIC surface and the FE result was taken from the middle front element of the skin model. For demonstration purposes, Figure 6-12 illustrated the DI response when the material model was solely fitted to the quasi-static compression dataset (Compression Model). By fully capturing the compressive response, stress stiffening occurred at a higher displacement, although the peak stress decreased which was because the tensile properties were compromised to fit the compression data. Hence, the model prediction on the DI force-displacement response can be improved with higher failure displacement and force if both tension and compression were captured correctly.

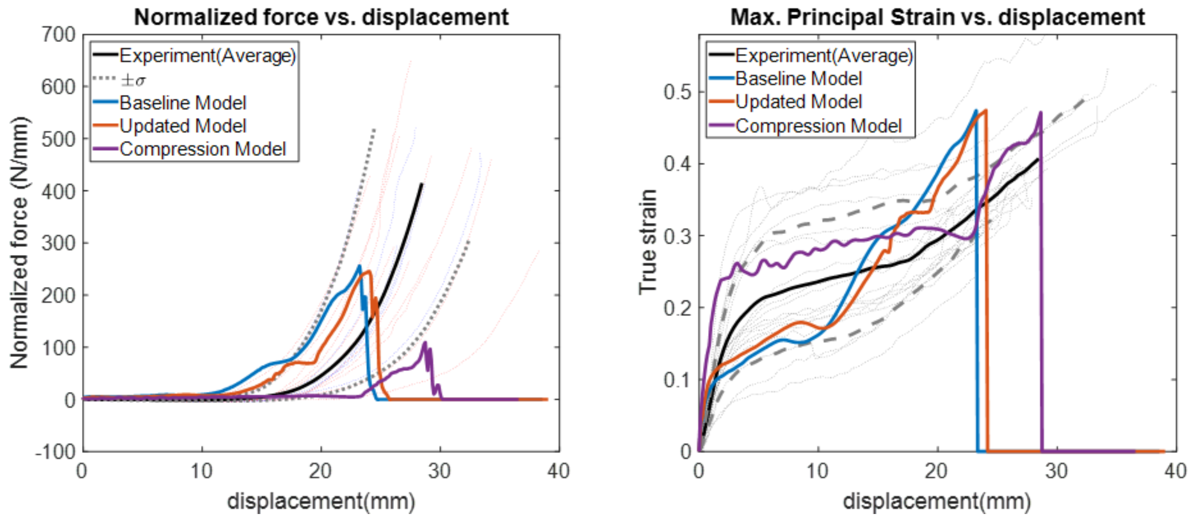

Figure 6-12: Compression model performance compared to the Baseline and Updated model.

Introducing additional Ogden terms to decrease the compressive stiffness improved DI simulation results, however, it also introduced model instability where hourglass energy exceeded the material's internal energy (Figure 6-13). To solve the model instability due to compression parameters, the UMAT's Poisson's ratio was investigated by decreasing from 0.495 at 0.01 intervals until the model was stabilized. As a result, the final obtained Poisson's ratio was 0.435 and the skin's hourglass energy was smaller than the internal energy before failure (Figure 6-13).

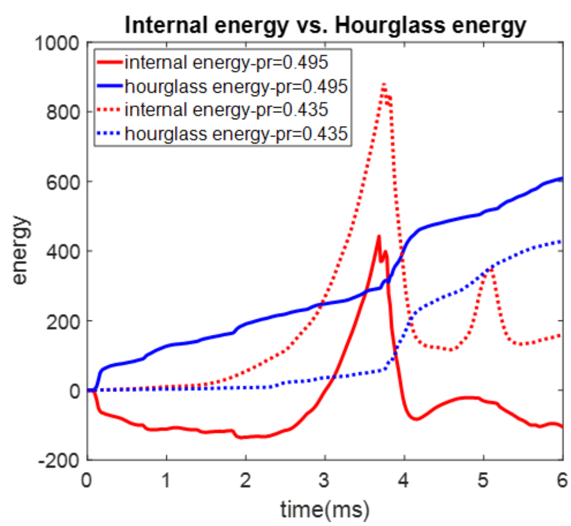

Figure 6-13: Effect of Poisson's ratios (pr) on the skin's internal energy vs. hourglass energy.

In summary, compression elastic constants were added to the current QLV model by minimizing the SSE between the compression data and the model response while fixing the previously determined tensile elastic and viscoelastic constants. Three sets of compression constants were determined for the average, UB, and LB responses (Table 10). The simulated force-displacement response and the displacement contour of the skin model in the DI test are illustrated in Figure 6-14. For the force-displacement response, the UB and LB models followed the data corridor while the average model behaved slightly stiffer than the average experimental response. All three models had lower failure force and failure displacement than the corresponding experimental data. In comparison to the GHBMC skin, all the three UMAT cards improved the skin performance by achieving a closer experimental response (Figure 6-15).

Table 10: Best fitted compression elastic constants.

Model	μ_2	α_2
Average	-1.089	1.872
UB	-1.431	2.913
LB	-0.995	1.685

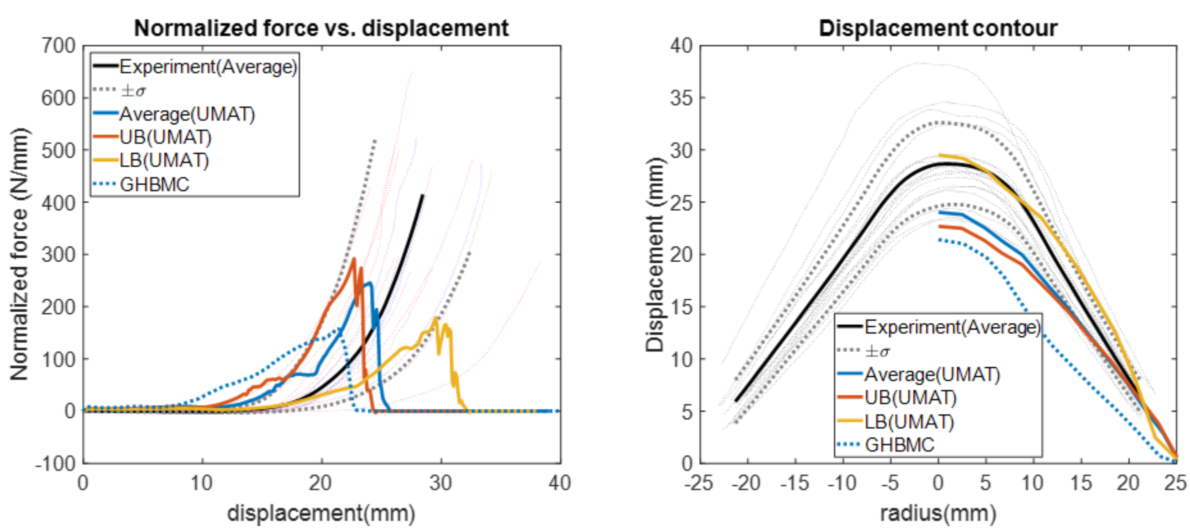

Figure 6-14: DI simulation results with average, UB, and LB UMAT skin in comparison with the GHBMC skin.

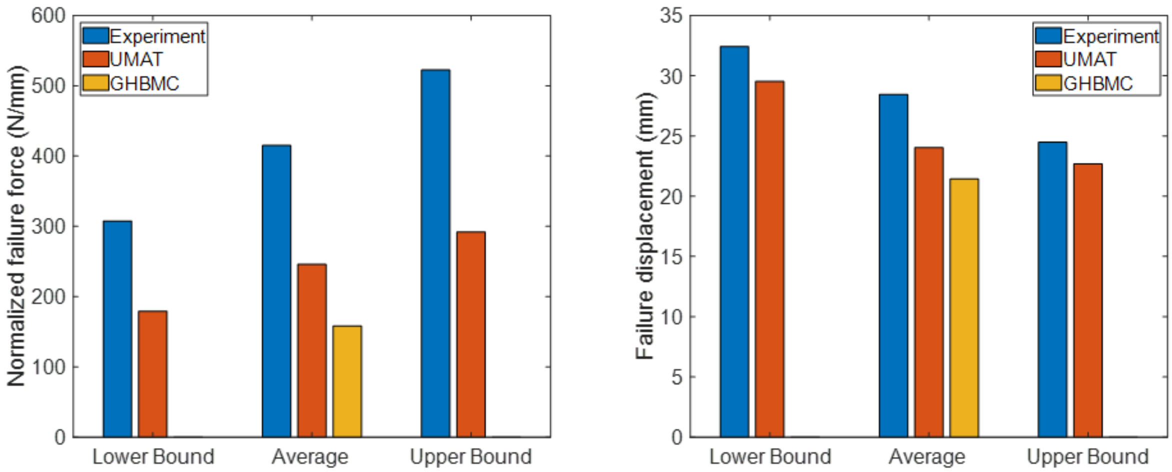

Figure 6-15: Bar plot overview between experiment, UMAT, and GHBMC skin: Normalized failure force (left) and failure displacement (right).

6.4 Discussion

Skin FE material model with the capability to simulate gradual tensile failure (material softening) under ballistic impact was developed in this chapter. By incorporating Lemaitre damage modeling in the material model, this allows users to tailor ductile damage progress rather than defining a single threshold to activate element erosion for failure modeling. The skin FE material model was implemented in LS-DYNA solver as a user-defined material (UMAT) using the QLV framework. Three skin FE models that represent the average, UB, and LB human skin were verified and validated under the uniaxial tensile and indentation test respectively, showing improvement in comparison with the current GHBMC skin material model. The DI simulation using a solid skin model revealed the compression parameters were important in capturing the skin's initial response subjected to blunt ballistic impact, and tensile parameters were responsible for the strength after stress stiffening was initiated.

The UMAT skin model can simulate the nonlinearity of skin under uniaxial tensile loading which was not observed in the GHBMC skin model. When simulating the dynamic indentation test, the UMAT skin shows improvement compared to the current GHMBC skin. The UMAT skin response to dynamic indentation was shown to lie within the data corridor, although it failed at lower peak force and shorter displacement than the average response The current reason for this is not clear, and it may necessitate a more complicated damage metric than maximum principal strain to account for the delay in failure during biaxial tension. Besides, another reason could be due to the current isotropic model incapability to capture the skin's through-thickness compressive response where the DI model was shown to result in higher failure displacement when the skin compression properties were fully captured. The unaltered damage model, based on experimental data, can be beneficial when used for designing protective equipment against skin impact as it creates a factor of safety.

Several factors were identified that could affect or improve the force-displacement response. First, the current model setup with curvature skin was shown to be better than the taut skin setup by delaying the timing of stress stiffening. This initial geometry effect was observed in the experiments. The curvature degree simulated in this validation study was determined from the coordinate of the center point of the DIC surface and an elliptical profile was assumed. Ideally, the FE skin geometry could be constructed by taking the stereolithography (STL) file from the DIC surface, however, due to shadows created around the skin sample in the experiment, full skin surface construction was not feasible. Second, the initial isotropic QLV model overpredicted the quasi-static compressive response which leads to early stress stiffening in the force-displacement response. The early stress stiffening likely allowed an early failure threshold to be achieved and hence resulted in a lower failure force. It was shown that the stress stiffening response can be delayed and the failure displacement can be increased when compression data was included in the model fit. Hence, the current material parameters were identified by performing a model fit to the stress relaxation (tension), tensile, and compression data simultaneously. Due to the nature of the skin which can only be subjected to in-plane tension, and out of plane compression loading mode, it is believed the current model's inability to capture both tension and compression data is due to the lack of model anisotropy, not tension-compression asymmetry.

6.5 Conclusion

In this chapter, three FE viscoelastic damage material models that represent an average, UB, and LB human skin response were developed by compiling a user-defined material (UMAT) in LS-DYNA, verified and validated against dynamic tensile and indentation test data, respectively. The current GHBMC skin material model cannot simulate the skin's nonlinearity and behaves stiffer than the UMAT skin. Although failed at lower force and displacement, the UMAT skin model showed improvement when compared to the GHBMC skin. The indentation simulation process showed skin compression properties are dominant in the initial impact before stress stiffening occurs where the skin's tensile properties take over to achieve appropriate failure force. The current isotropic material model was not able to capture both through-thickness compression and tension properties of the skin simultaneously. Therefore, an anisotropic based constitutive model is recommended for future skin model implementation for the high rate impact application.

CHAPTER 7 – Development of a Skin-Adipose-Muscle Sub-System Model for Ballistic Blunt Impact

A FE skin material model for simulating skin failure was developed in the previous chapter where the model was verified and validated based on uniaxial and indentation experimental test data. In this chapter, the FE skin material model was used to construct a sub-system model that consists of skin, adipose, and muscle tissue layers. The sub-system model was calibrated and validated against stress relaxation and blunt impact test data. The material properties of the underlying tissues were determined via material parameter optimization from literature and in-house data. The goal of this chapter was to develop a sub-system model that can serve as a computational surrogate to replace the full human body model for open skin injury research subjected to ballistic blunt impact.

7.1 Introduction

Human skin surrogates, including physical skin simulants and computational FE models, have been developed as a tool to investigate the response of the tissue for severe impact scenarios. These tools help to evaluate the efficacy of protective equipment, where human volunteer testing is not feasible or there is limited access to PMHS. Physical skin simulants, such as chamois skins, have been used with success along with gelatin content to construct sub-system models to evaluate skin failure thresholds subjected to ballistic blunt impacts (Bir et al., 2012; Papy et al., 2012). The sub-system surrogates consist of a laceration assessment layer (LAL) and a penetration assessment layer (PAL) which represent the skin and underlying tissues respectively and are a valuable assessment tool for skin injury research. Nonetheless, the use of chamois skin has been challenging due to its inconsistent skin thickness which prevents result reproducibility. In the computational world, the development of the individual skin FE model has been performed and discussed in the previous chapter. However, the individual tissue model alone is not sufficient to describe complex tissue interactions that exist in the human body system. Hence, the human body models (HBMs) are used to better represent the anatomical and biomechanical response of human skin because it is designed to combine different tissue layers. The downside of using the HBM is that it becomes computationally expensive if only a localized region of the human body is being studied. For instance, in the case of needle injections or light-weight blunt impacts, the response of the body is highly localized to the skin, flesh, and surrounding area, and modeling the response of the rest of the human body is unnecessary and expensive. To reduce the computational cost, it is common to employ sub-system models to simulate areas of interest. Some examples of sub-system modeling include simulating the brain for traumatic brain injury (TBI) research (Alshareef, 2019; Wu, 2019), the pelvis for underbody blast (UBB) research (Greenhalgh, 2019), and the lower extremities for sports injury research (O'Cain, 2020). All these sub-system models were extracted from the full HBMs to save computational time, and detailed simulations were performed to gain an in-depth understanding of the mechanics of the local body region. To date, there is only one computational sub-system model that consists of skin, adipose, and muscle (SAM) tissue, and that was developed to mimic the human upper arm subjected to a quasi-static indentation loading condition (Pilarczyk, 2019) where the injury was not a focus of the model. Besides, the material properties used in the SAM model were obtained from quasi-static rate experiments, and the model is unsuitable for impact analysis. Thus, there is a lack of existing computational surrogates that can be used to conduct skin injury research, especially in the ballistic blunt impacts.

To address this need and provide a cost-effective computational surrogate for skin injury research, the UMAT skin developed in the previous chapter was used with adipose and muscle tissue to create a simplified sub-system model. First, the material parameters of the underlying tissues were extracted via parameter optimization using high rate literature data and calibrated using stress relaxation test data of skin-adipose-muscle tissues. Second, the calibrated material parameters were validated by simulating blunt impacts on the sub-system model against a set of PMHS blunt impact test data.

7.2 Methods

7.2.1 Sub-System Model Material Properties

To determine appropriate material parameters for each soft tissue i.e. skin, adipose, and muscle in the sub-system model, a simulation matrix (Table 11) consists of five simulations using different material parameters were designed. These material parameters were evaluated in FE simulations of the stress-relaxation test of skin-adipose-muscle tissues in the next section (7.2.2). The investigated soft tissue material parameters were obtained from a combination of the HBM (GHBMC v5.0), the UMAT skin, literature, and unpublished internal UVA experimental data.

Material properties of the adipose tissue were obtained from recent literature data (Sun et al. 2020, unpublished internal UVA data) in which human adipose tissue was extensively characterized under compression and shear at large strain (50%) and high loading rates (50/s). This test protocol was reported to be the highest loading rate ever conducted on human adipose tissue in terms of compression and shear. The author also presented a set of average material parameters that were best fitted at 3/s, 13/s, and 50/s loading rate simultaneously using the QLV-Ogden constitutive model. In addition to the Sun’s data, the adipose tissue material from the HBM (GHBMC v5.0) was also used to evaluate the sub-system model performance.

For the muscle tissue, a QLV material model was also desired and this was done through material optimization using both literature and unpublished UVA data. Researchers have shown most of the muscle constitutive models were based on experimental data performed either with relative slow loading rates (quasi-static to 3/s) or with animal muscles (Bosboom et al., 2001; Van Loocke et al., 2006; Böl et al., 2012; Takaza et al., 2013; Calvo et al., 2014; Rehorn et al., 2014). Only Balaraman et al. (2006) have performed uniaxial compression tests on human extremity muscles at a comparable high loading rate between 136/s and 262/s where the data was later used to produce a linear viscoelastic material model (Chawla et al., 2009). Therefore, the high rate compression data was used as a reference for the hyperelastic part of the muscle QLV model.

With viscoelastic constants of skin and adipose tissues being determined, viscoelastic constants of the muscle tissues were determined using stress relaxation test data conducted on skin-adipose-muscle tissues of 4 PMHS specimens (Panzer et al. 2020, unpublished internal UVA data) In this stress relaxation test, the skin-adipose-muscle was excised as a single unit and subjected to high-speed step-hold under indentation to approximately 50% (±10%) of the tissue thickness at approximately 200/s strain rate using a drop tower setup. The resultant relaxation response obtained from the test was used as part of the muscle material calibration to determine the muscle viscoelastic (relaxation) response. It was assumed the relaxation response of the sub-tissue is similar to the muscle tissue.

The QLV parameters of the muscle tissue were deduced by minimizing SSE of elastic and viscoelastic data from both experiments simultaneously (Figure 7-1). According to Balaraman et al. (2006), human muscles exhibited around 0.06MPa of true stress when compressed to 50% strain at 183/s. This stress is relatively low compared to the peak of the stress relaxation test where around 0.9MPa was calculated when the skin-adipose-muscle tissues were indented at roughly the same strain level and loading rate. It should be noted the 0.9MPa is calculated by dividing the indented peak force (~500N) by the contact area (7.62mm radius indenter) between the indenter and the sub-tissue where a multi-stress state was involved including tension on the tissue surface, compression underneath the sub-tissue and shear along with the depth of the sub-tissue. To calibrate the muscle material, a sample that had the closest response to the experimental average curve (Panzer et al. 2020, unpublished internal UVA data) was chosen. The displacement per sub-tissue thickness ratio that occurred on the sample was found to be 66% while the compression level of the muscle tissues from Balaraman et al. (2006) was 50%. Therefore, the muscle QLV model was optimized to capture the Balaraman et al. (2006) elastic response and increase the model's stiffness at a higher compressive strain (above 50% strain) to account for the much higher stress level in the stress relaxation test from Panzer et al. 2020 (unpublished internal UVA data). Similarly, the muscle model from the HBM (GHBMC v5.0) was also used to investigate the sub-system model performance.

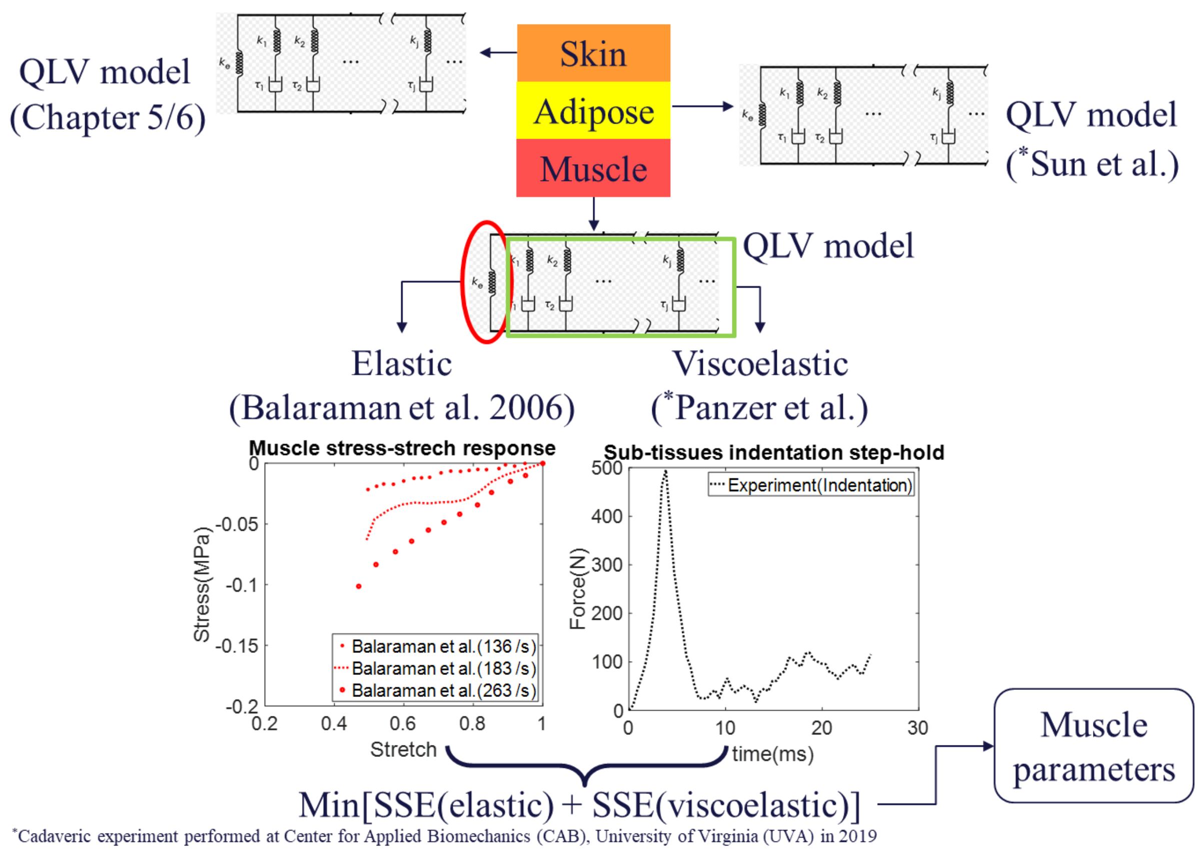

Figure 7-1: Resources of QLV parameters of individual sub-tissue.

Table 11: Stress relaxation simulation matrix based on different material models.

Tissue	Simulation 1	Simulation 2	Simulation 3	Simulation 4	Simulation 5
Skin(S)	GHBMC	UMAT	UMAT	UMAT	GHBMC
Adipose(A)	GHBMC	GHBMC	Sun	Sun	Sun
Muscle(M)	GHBMC	GHBMC	GHBMC	Material Calibration	Material Calibration

7.2.2 Verification of Sub-System Material Properties

To verify the material parameters as described in the previous section, a quarter FE sub-system model which consists of skin, adipose, and muscle were constructed along with the experimental setup where the tissue was placed within a 38.1mm inner radius acrylic tube on top of a drop tower platform and compressed by a 7.625mm radius aluminum indenter (Figure 7-2). In the FE setup, both aluminum indenter and acrylic tube were modeled as a rigid body. The displacement-time profile was prescribed to the indenter via *BOUNDARY_PRESCRIBED_MOTION_RIGID to simulate the indenter movement. Two contacts (*CONTACT_AUTOMATIC_SURFACE_TO_SURFACE) were defined with one in between the indenter and the skin-adipose-muscle tissues and another one between the skin-adipose-muscle tissues and the acrylic tube. Friction coefficients of the two contacts were adjusted between 0.1 and 1.9 to investigate model sensitivity. The contact force between the indenter and the skin was extracted via *DATABASE_RCFORC to compare with the experimental force.

The tissue thicknesses of the sub-system model were obtained from Panzer et al. 2020 (unpublished internal UVA data) where the skin and adipose tissue thicknesses were measured from human volunteers using shear-wave elastography (SWE). By assuming similar skin and adipose thicknesses in the PMHS, the muscle tissue thickness was deduced by subtracting the PMHS excised skin-adipose-muscle tissue thickness from the volunteers' skin and the adipose tissue thickness. The sample which had the closest experimental response by having the least SSE to the average force-time data was chosen as a candidate for the FE sub-system model construction (Figure 7-2). As a result, the selected sample had a total tissue thickness of 20.5mm with 2.3 mm of skin tissue, 4.61mm of adipose tissue, and 13.56mm of muscle tissue. All three tissues were modeled as viscoelastic material using the Ogden-QLV model where the skin was modeled using the UMAT developed in Chapter 6 and the rest were modeled using *MAT_OGDEN_RUBBER (*MAT_077_O) with the viscoelastic formulation in LS-DYNA. For the compressibility of the new adipose and muscle material, sensitivity analysis on the Poisson's ratio was investigated including 0.49, 0.499, 0.4999, and 0.49999.

With the 2.33mm skin, 1mm element mesh size was selected on the soft tissue so that a minimum of 2 elements could be modeled through the skin tissue thickness. The mesh size was believed to be sufficient because an element size of 2mm was also recommended when a similar FE indentation simulation of gluteal tissue (55mm in radius and 44mm thick in total) was performed where element mesh size between 3.8mm and 0.5mm was investigated (Greenhalgh, 2019).

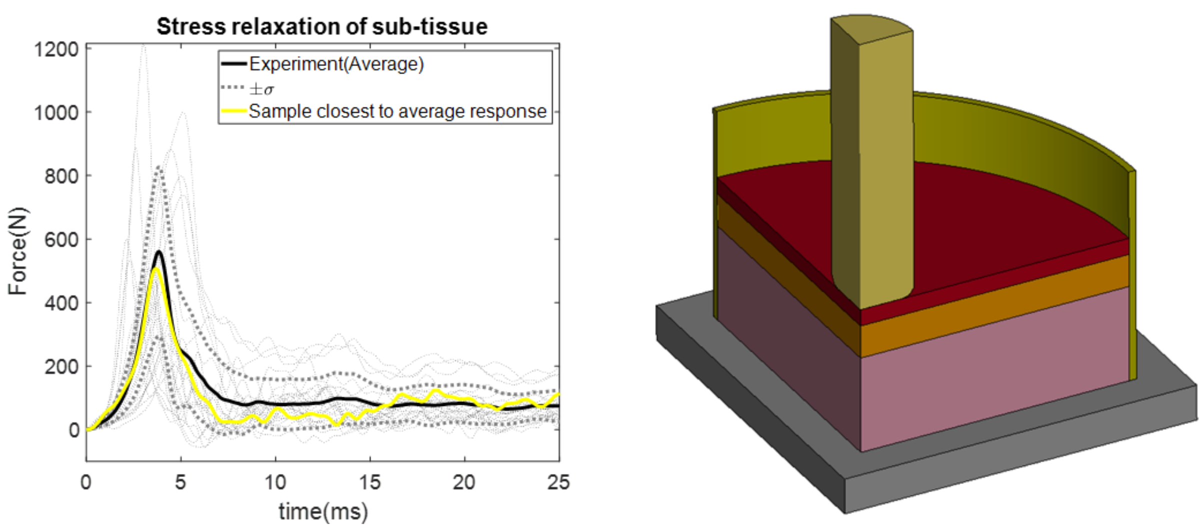

Figure 7-2: Skin-adipose-muscle tissues stress relaxation average data vs. sample closest to average response (left). FE model of stress relaxation test (right).

7.2.3 Validation of Sub-System Material Properties

The verified material models of the three tissues under the stress relaxation test were validated using an additional set of impact test data performed by Panzer et al. 2020 (unpublished internal UVA data). The impact tests refer to approximately 5m/s and 11m/s blunt impacts of a custom made cylindrical impactor onto different anatomical locations of the 4 PMHS specimens under different postures. The impactor was 3D printed with plastic infused with chopped carbon fibers, measured 40mm in diameter, and weighed 40 grams. Rather than using a full human body model for FE analysis, a portion of the impact area was constructed which had 3 times the impactor radius (60mm) to exclude boundary effect upon impact. The effect of the model size on the model response by constructing 4 models with different radii was also investigated (Figure 7-3).

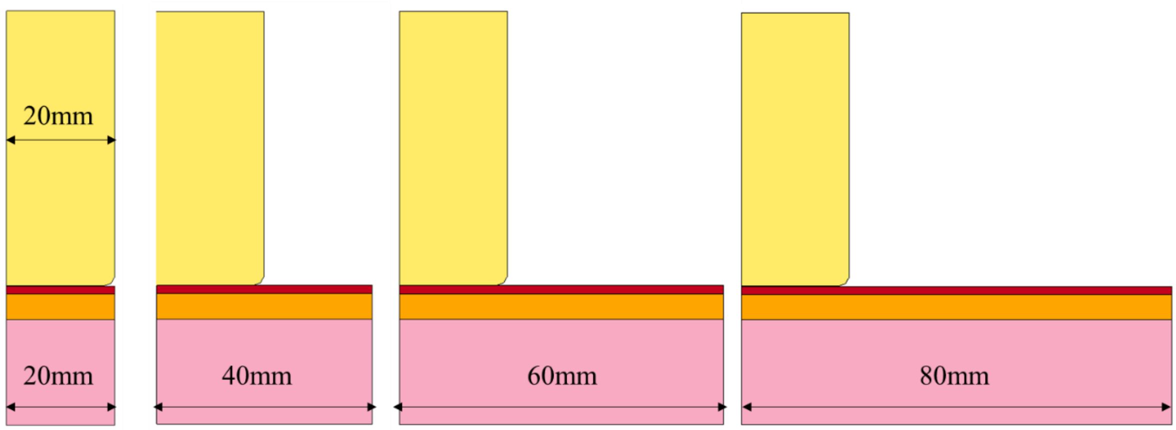

Figure 7-3: Four model sizes were simulated to investigate the sub-system model response.

Upon deciding a model size with minimum boundary effect, the flexibility around the edge of the model was also investigated by adding constraints in all six degrees of freedom (Figure 7-4, left). Since the skin surface was not always flat in the experiment especially when the impactor gun was put flat on the body of the PMHS, a dome shape of the skin was likely to happen due to the pressure while holding the impactor gun, therefore, a curved skin model was also developed (Figure 7-4, right). The skin's curvature was assumed to be elliptical with a minor radius similar to the skin's thickness i.e. 2mm.

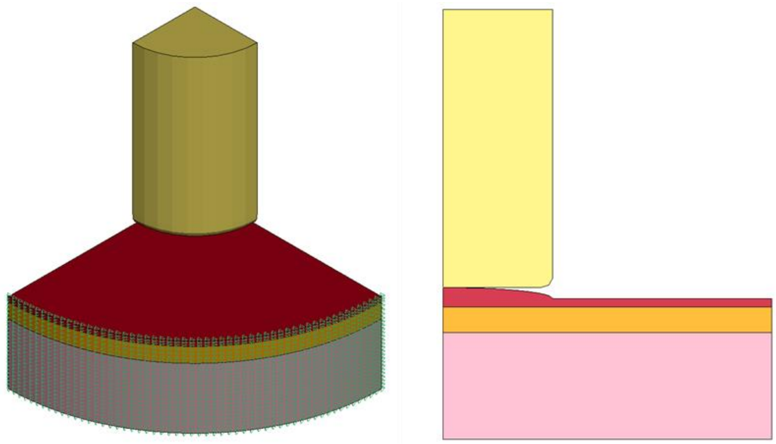

Figure 7-4: Sub-system model edge constraint (highlighted in green) to investigate the edge effect on the sub-system model response (left). Curved skin model to investigate tissue curvature on the sub-system model response (right).

Two sub-system models, both consist of skin, adipose, and muscle tissues were constructed based on the sample that had the least SSE compared to the average experimental data at 5m/s and 11m/s, respectively for model validation. As a result, the two samples were found to be at the abdominal (5m/s) and pectoral (11m/s) location of the human body (Figure 7-5).

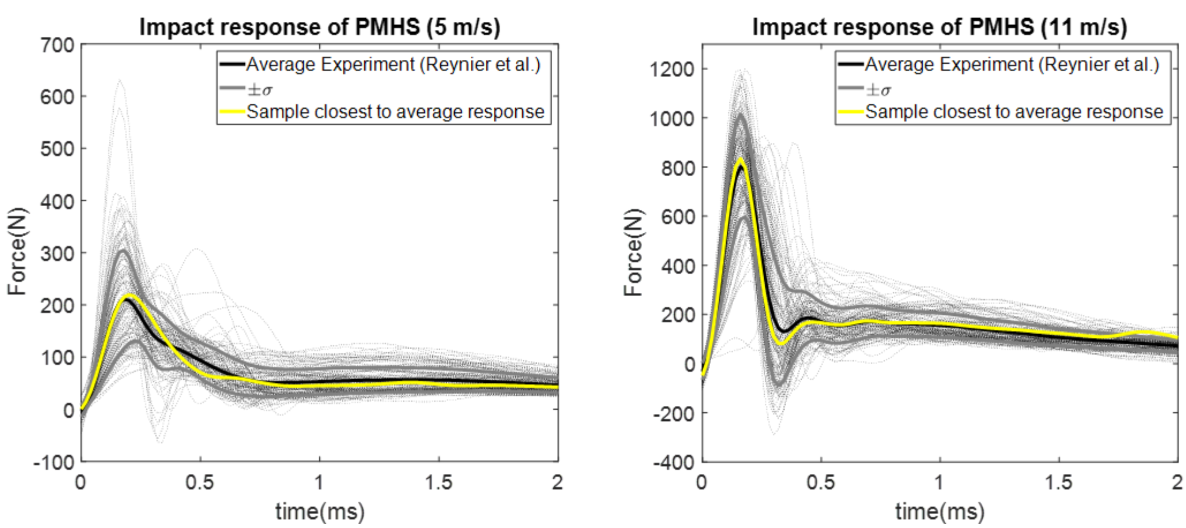

Figure 7-5: Sub-system impact response at 5 m/s (left) and 11 m/s (right).

Individual tissue thickness of the models was determined using the same thickness measurement approach as described in the previous section. For the pectoral sub-system model, the base of the model was constrained to move vertically but allowed to move in-plane to mimic muscle-bone interaction while the base of the abdominal model was free to move since there were soft organs underneath the muscle. For the impactor, it was modeled as a rigid body and constrained to move along impact direction using *MAT_RIGID with plastic material properties (Young's modulus = 1400MPa, density = 0.0012g/mm^3 and Poisson's ratio = 0.35) while using *PART_INERTIA to define the part's mass, inertia, and initial travel velocity. Simulation force was calculated by multiplying the acceleration and mass of the impactor which was also used in the experiment. The acceleration-time history was obtained from the node located at the back of the impactor and filtered using a 4th order Butterworth low pass filter at 4000Hz, the same filtering technique used in the experiment data. A friction coefficient between 0.1 and 1.9 for the skin-impactor interaction was also investigated.

7.3 Results

7.3.1 Sub-System Material Verification

The optimization results of the muscle material are illustrated in Figure 7-6. The QLV model fit to the muscle compressive response (Balaraman et al., 2006) was fairly well (Figure 7-6, left). A sudden stress increment was observed when the compressive strain reached beyond 50% to accommodate the higher stress level observed in the stress relaxation data (Panzer et al. 2020, unpublished internal UVA data) (Figure 7-6, right).

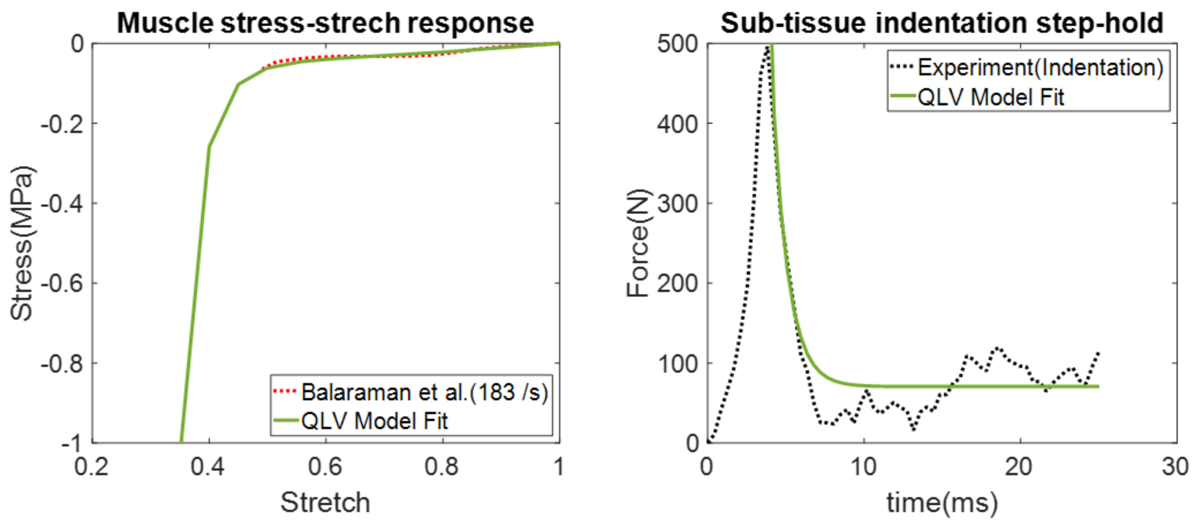

Figure 7-6: Simultaneous fitted model results of human muscle compressive response (left) and skin-adipose-muscle relaxation response (right).

Figure 7-7 illustrates the difference between FE models with soft tissue materials obtained from different resources (Table 11, Skin = S, Adipose = A, Muscle = M). The baseline model (GHBMC (S, A, M)) which uses all the soft tissues obtained from the GHBMC v5.0 had very good agreement with the experimental data in the beginning but failed to reach peak force. A similar result was also achieved when the GHBMC skin was replaced by the UMAT skin (UMAT(S)+GHBMC (A, M)), with a slightly less stiff response and lower peak force. The change from GHBMC adipose material to 'Sun adipose' material did not change the overall force-time response (UMAT(S)+Sun(A)+GHBMC(M)).

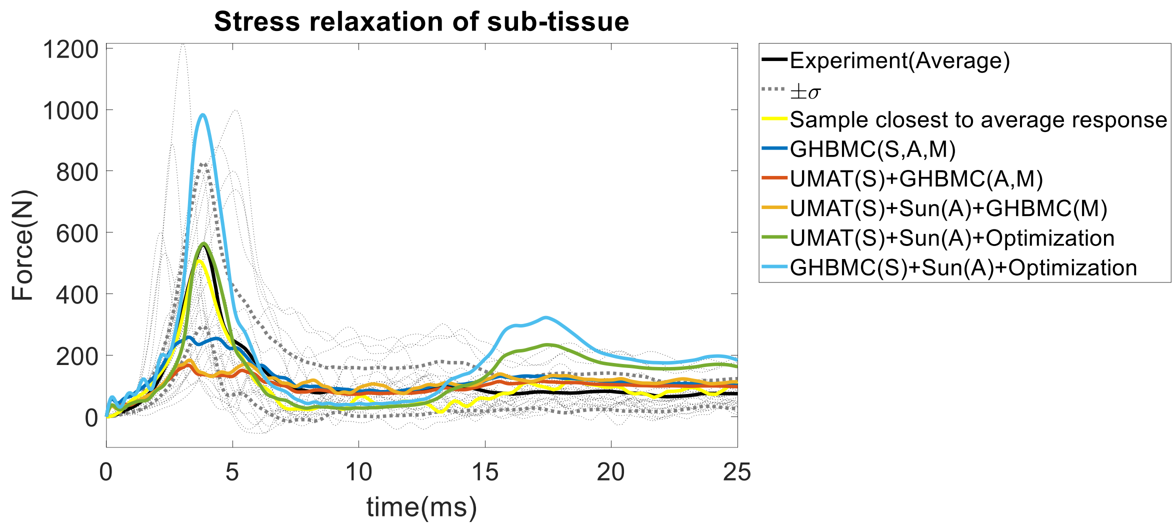

Figure 7-7: Sub-system FE model response.

For the next model (UMAT(S)+Sun(A)+Optimization(M)), where the muscle tissue was developed through material optimization using the compression test (Balaraman et al., 2006) and the stress relaxation test (Panzer et al. 2020, unpublished internal UVA data) showed a very good agreement with the experimental curve in the first 15ms which covers both loading and relaxation response. Besides, the Poisson's ratio of the muscle tissue also played an important role in the model response. By changing the Poisson ratio from 0.49 to 0.49999, the peak force nearly doubled from 293.7N to 564.2N (Figure 7-8, right). On the other hand, the Poisson's ratio of the adipose tissue was insignificant on the sub-system's response (Figure 7-8, left). With the same adipose and muscle material used in the previous model (UMAT(S)+Sun(A)+Optimization(M)), the GHBMC skin was used again for the stress relaxation simulation (GHBMC(S)+Sun(A)+ Optimization(M)) and the resultant peak force was higher than the UMAT skin, the same phenomena observed between the baseline model (GHBMC(S, A, M)) and the UMAT(S)+GHBMC(A, M) model. To compare the five simulation results with the average experimental data, the correlation analysis (CORA) was used (Figure 7-9). Only the data at the first 10ms were compared as this covered the loading and relaxation response of the skin-adipose-muscle tissues. In conclusion, the material parameters used in the UMAT(S)+Sun(A)+Optimization(M) model, yielded the best correlation rating at 0.952.

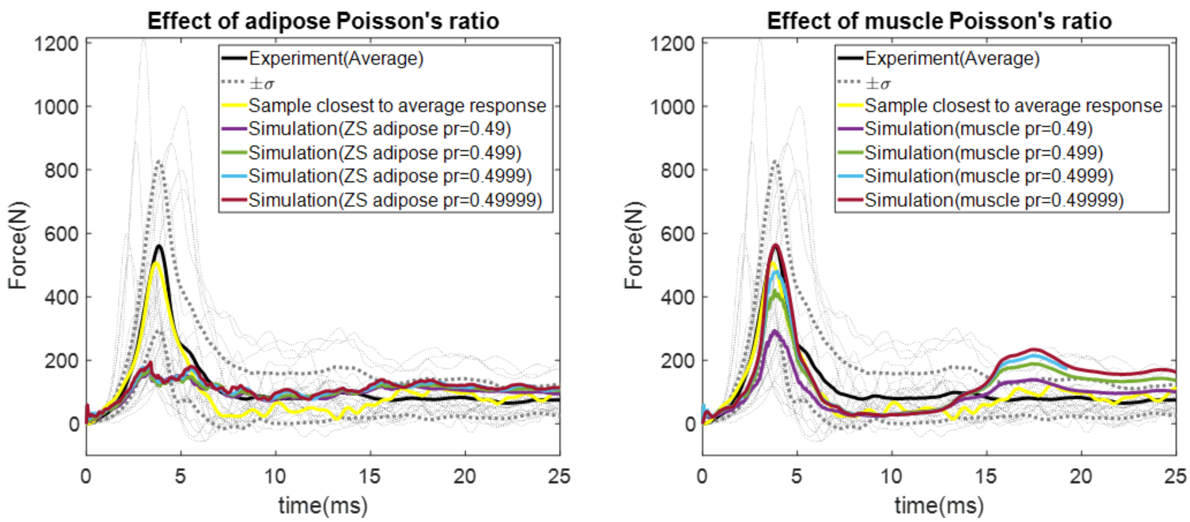

Figure 7-8: Effect of Poisson ratio (pr) of adipose (left) and muscle (right) tissue on the sub-system model.

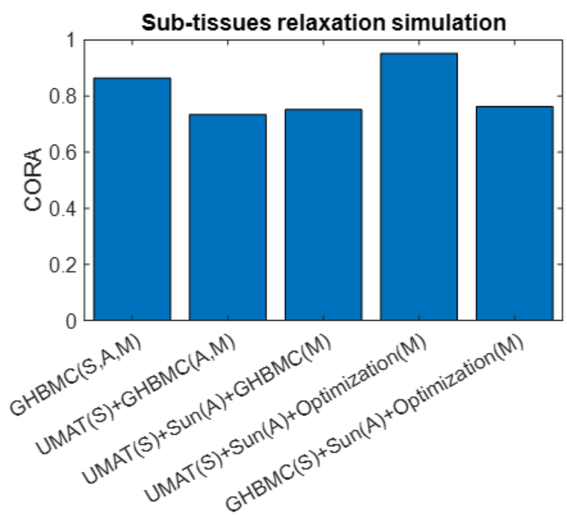

Figure 7-9: CORA comparison between the five simulations.

Friction analyses on the tissues-tube and the tissues-indenter contacts are also presented (Figure 7-10). The friction coefficient between the sub-system model and the tube had a negligible effect while the friction between the sub-system model and the indenter changed the simulated peak force from 564.2N to 714.2N when increasing the friction coefficient from 0.1 to 1.9. A friction coefficient of 0.1 was best for capturing the experimental response.

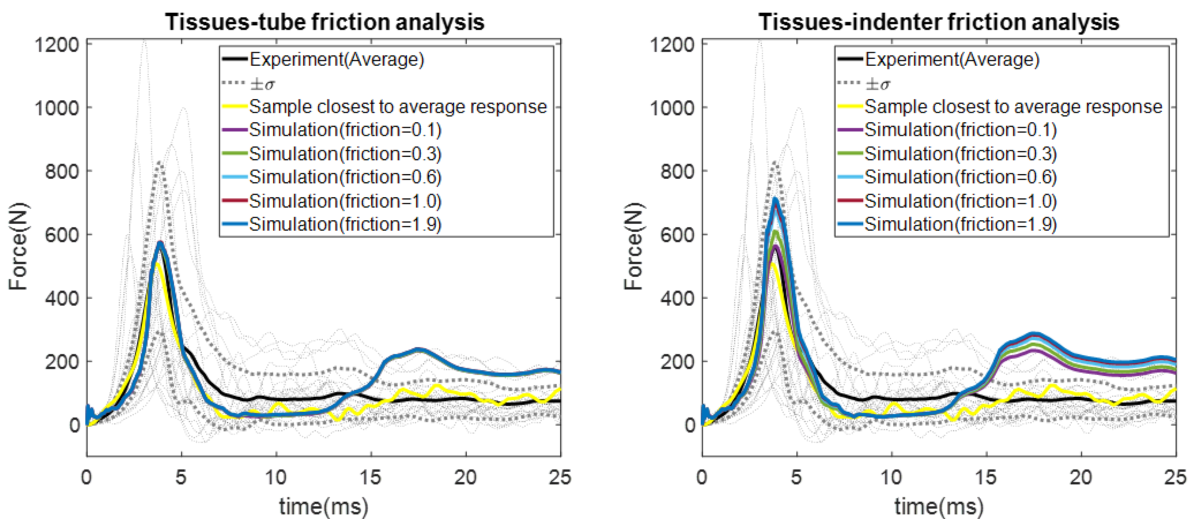

Figure 7-10: Effect of friction coefficient on tissues-tube (left) and tissues-indenter (right) interaction.

7.3.2 Sub-System Material Validation

Sensitivity studies on the model response of the impact simulations are presented in Figure 7-11. The results showed at least a 40mm radius model was required to exclude boundary effect when subjected to a 20mm radius impactor (Figure 7-11, top left). The smaller model size (i.e. 20 mm) resulted in a smaller peak force followed by a second loading at a later time (~1.8 ms) which was not observed in the experimental data. By having the 60mm radius model, the choice of fully constraining the tissue edges became negligible (Figure 7-11, top right). As observed in previous impact simulations, the effect of contact friction between the skin and the indenter dominated the peak force value (Figure 7-11, bottom left). There was about a 13% increment of peak force when increasing the friction coefficient from 0.1 to 1.9. As the friction decreased with increasing impact velocity, the friction coefficient of 0.1 was selected for the simulation. In terms of skin geometry, the curved skin affected the model response (Figure 7-11, bottom right) by delaying the force response resulting in a lower peak force compared to the flat skin model. Since the degree of curvature was unknown and the model performance was worse than the flat skin model, it was decided to use the flat skin model.

By studying and excluding possible parameters that could affect the impact simulation results, the final simulation results for the 5m/s and 11m/s impacts are illustrated in Figure 7-12. The sub-system model response at the two impact velocities showed fairly good agreement with the average experimental response. The skin model from GHBMC v5.0 was also used for simulation to compare with the UMAT skin model. For the 5m/s impact, both skin materials exhibited identical force-time response while at 11m/s impact, the GHBMC skin exhibited a slightly higher peak force response than the UMAT skin model.

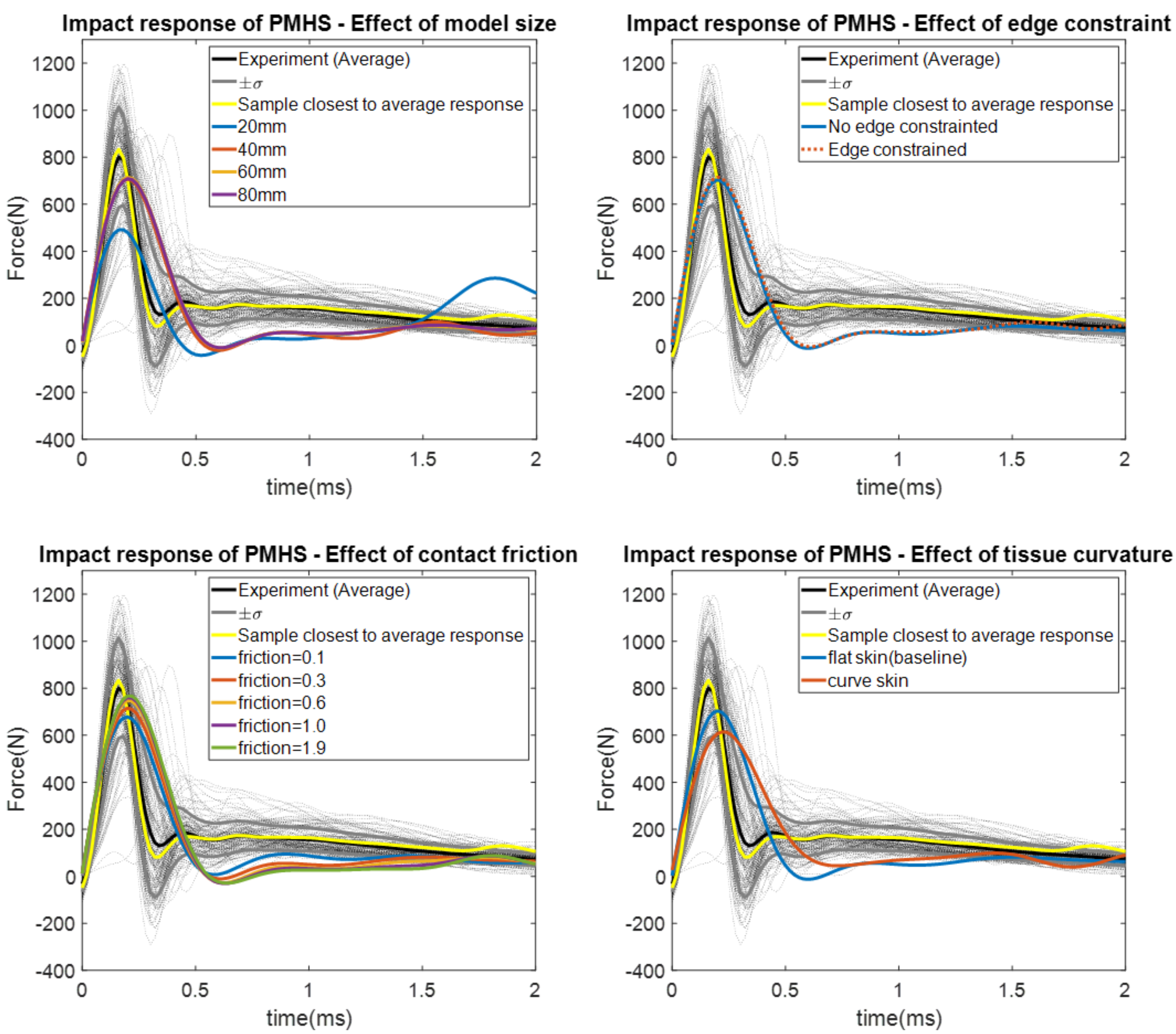

Figure 7-11: Tissues' edge constraint effect (top left), model size effect (top right), contact friction effect (bottom left) and tissue curvature effect (bottom right) on model response.

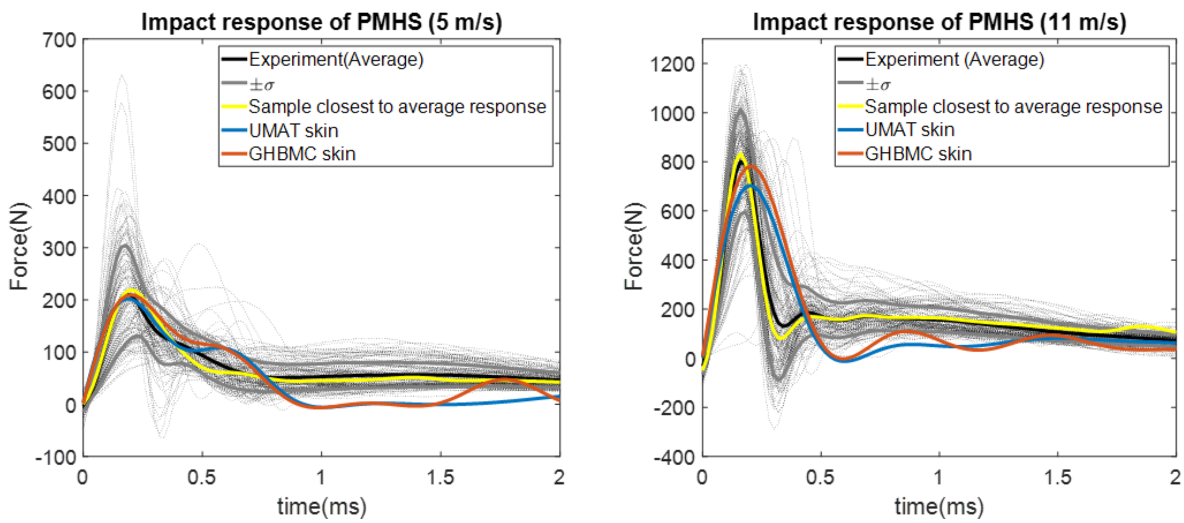

Figure 7-12: Sub-system FE model impact response using UMAT skin and GHBMC skin at 5m/s (left) and 11m/s (right).

7.4 Discussion

A sub-system FE model which consists of skin, adipose, and muscle tissues was developed for ballistic blunt impact through verification and validation against two types of experimental data including stress relaxation test and blunt impact test. Both current skin and GHBMC skin models were used in the sub-system FE model to compare and results showed the current skin model consistently demonstrated better correlation with the experimental data, especially under high energy impact situations. The contribution of the adipose tissue within the sub-system during the blunt impact was deemed negligible while both skin and muscle tissue affected the force response of the sub-system.

7.4.1 GHBMC Skin vs. UMAT Skin Model

The usage of the UMAT skin model developed in Chapter 6 showed little difference compared to the GHBMC skin model when simulating the sub-system impact response. However, this was not the case in the stress relaxation simulation where the GHBMC skin demonstrated a much higher force. Although similar impact speed was used in the stress relaxation test (i.e. approximately 4.5m/s), the mass of the impactor was 780 grams while the mass of the impactor used in the impact tests was only 40 grams. The difference was the kinetic energy imposed on the sub-system upon impact. The stress relaxation case had approximately 7.9 J while the impact cases had around 0.5J (5m/s) and 2.42J (11m/s) of kinetic energy. It was reported in Chapter 6 that the GHMBC skin and the UMAT skin behaved similarly during the initial impact and deviated where the GHBMC skin exhibited a stiffer response than the UMAT skin in the dynamic indentation (DI) simulations. The higher energy impact at the stress relaxation test caused severe skin deformation (more than 20% maximum principal strain at peak force, Figure 7-13, top row) while for the low energy impact cases at 11m/s, a maximum principal strain at the center of impact was reported to be less than 2% at peak force. The smaller strain that occurred at the low energy impact cases explained the similar force-time response achieved by the two skin models (GHBMC and UMAT). As the impact energy increased, the difference in force-time response between the two skin models became obvious. Overall, the UMAT skin model showed better results in both low and high energy impact cases than the GHBMC skin.

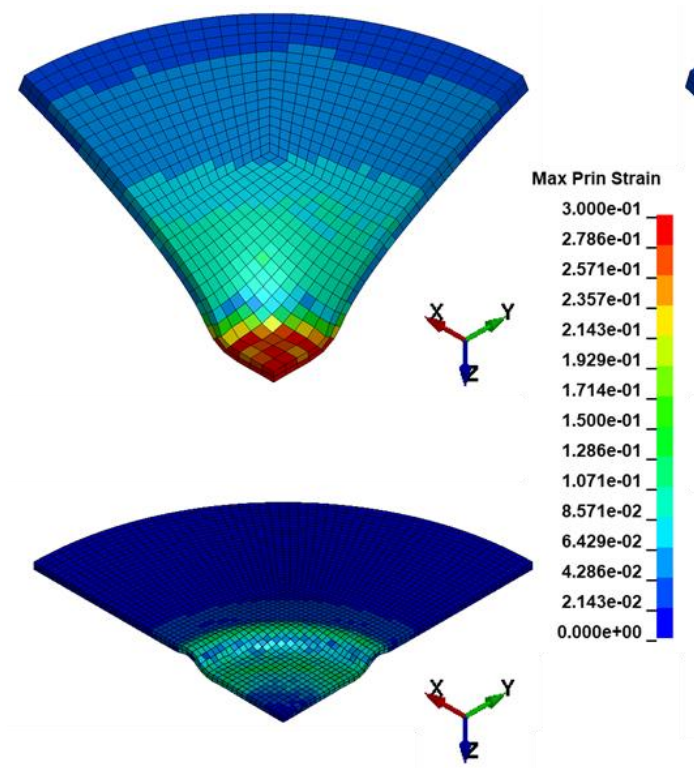

Figure 7-13: Max. Principal Strain (True strain) distribution on the skin model at peak force in the stress relaxation simulation (top row) and impact simulation (bottom row). Left column: GHBMC skin. Right column: UMAT skin.

7.4.2 Effect of Individual Sub-Tissue

The sub-system material properties, specifically the muscle material have been tuned to match the stress relaxation test data, the muscle material properties may have been overpredicted by increasing the muscle stiffness when being compressed over 50% strain level. However, the material calibration yielded fairly good FE simulation results compared to other material configurations. Although the sub-tissues were indented to approximately half of its thickness (50% strain), the actual compression level on the muscle was unknown and could be higher than the prescribed indented level which may also lead to a higher stress level. Besides, increasing the muscle stiffness at a higher compression level also helps to overcome the numerical instability issue. Furthermore, the nature of the stress relaxation test conducted by Panzer et al. 2020 (unpublished internal UVA data) was considered to be a rapid indentation test (7.62 mm radius indenter compressing a 38.1 mm radius tissues) where compression, tension, and shear existed concurrently in the sub-tissue. The increment of the stiffness for the muscle material model considered the multi-stress state involved in the indentation step-hold test and its compressive response. Further material development of the muscle tissue is necessary but this falls outside the scope of the current research. Although the muscle material may not be an ideal representation, the muscle material parameters obtained in the current study demonstrate its validity on ballistic blunt impact response and should be used with care for other applications.

Overall, the muscle tissue was deemed a significant contributor to the sub-system model response for the types of impacts investigated, while the skin tissue had a minor effect, and the adipose tissue had a negligible effect. Apart from the QLV parameters, the Poisson's ratio of the muscle tissue was specifically important to provide a realistic model response where a two times force difference can be achieved between 0.49 and 0.49999 Poisson's ratio. Skin's contribution to the model impact response has been discussed in the previous section by comparing the UMAT and the GHBMC skin model where an approximate 35% peak force difference was observed in a high energy impact situation. The investigation of the skin's Poisson's ratio was not performed as the current skin Poisson's ratio has been proven to provide model stability to account for the skin failure modeling. For the adipose, it did not have a significant effect on the sub-system impact response. This was investigated in two aspects, replacing the GHMBC adipose with a newly developed adipose tissue (Sun et al. 2020, unpublished internal UVA data) and performing the material's compressibility check by changing its Poisson's ratio (0.49-0.49999).

7.4.3 Sub-System Model

The sub-system model developed in the current study aims to represent a portion of the human body region to save simulation time in which several assumptions are made and investigated. One of the unknowns in the impact tests is the boundary condition where the degree of "tissue pulling" outside of the impact area is unclear and this was mainly based on the condition and region of the sub-system on the PMHS. The current sub-system model assumes the effect of surrounding tissues outside of the impactor was minor when the sub-system model diameter was two times larger than the impactor diameter. From the experimental data, this seems to be the case as no second loading is observed after the initial loading, indicating the "tissue pulling" effect was negligible. It should be noted the current model size was sufficient for the low energy impact (i.e. 5 m/s and 11 m/s impact velocity of a 40 grams impactor) to exclude the boundary effect. The model size should be reevaluated if modeling severe impact situations. Second, the curvature of the soft tissues varied across different human body regions. The effect of the tissue's curvature played an important role as it affected the contact area between the impactor and the skin which resulted in different loading responses, and this was briefly demonstrated in the current study. This raises other research questions, including what are the variations of the skin curvature at different human body regions and how is this correlated to the impact response? The current study demonstrated the sub-system model, built with flat skin geometry was sufficient to model direct impact responses, but its validity on oblique impacts is uncertain. Lastly, the adipose and muscle constitutive models were not developed with failure features. It may be possible for the adipose or the muscle to be injured or damaged before the skin is injured in the case of a contusion or muscle strain, and this was not accounted for in the current sub-system model. The sub-system model can only simulate laceration injury where the skin is injured and torn when subjected to impact before the impactor reaches further to the adipose and the muscle tissues.

7.5 Conclusion

The current chapter developed a simplified sub-system FE model which consists of skin, adipose, and muscle tissue layer that is verified and validated against stress relaxation and ballistic blunt impact test data. It was found the muscle tissue was the main contributor for loading and stress relaxation within the sub-system model upon impact, followed by the skin tissue, and the contribution from the adipose tissue was nearly negligible. For low energy impact where tissue deformation was not severe, the current GHBMC skin model was no different than the UMAT skin model. The deviation threshold in terms of impact energy between the two skin models is yet to be determined. For the sub-system model, a model size of two times the impactor size in terms of diameter was required to exclude the boundary effect. This result assumes the surrounding tissues outside of the impact area are flexible to move and does not affect the impact response. This is suitable for wide impact locations such as thoracic, abdominal, or back area but could be inadequate for tight impact locations such as the elbow. The sub-system model can be used as an engineering tool to investigate the skin failure threshold from different perspectives such as evaluating the safety of munition and the effectiveness of protective armor. Furthermore, the sub-system model can also be used for skin material sensitivity studies by including stiffer/compliant skin and could examine the effect of underlying tissue properties and soft tissue thicknesses at different anatomical regions.

CHAPTER 8 – Investigate Human Skin Failure under Ballistic Blunt Impact: A Finite Element Simulation Study

The goal of this chapter was to answer the hypothesis stated at the beginning of the dissertation. Sub-system FE models of human flesh, as developed in Chapter 7, were used to evaluate the human skin failure threshold subjected to a series of ballistic blunt impacts. The investigation used a range of impactor masses and velocities based on the current less-lethal weapons available on the market. Different impactor geometry (spherical vs. cylindrical), skin properties (average, UB, and LB), and underlying tissues thicknesses ratios (i.e. three anatomical locations were chosen to represent areas with least to most skin, adipose, and muscle ratio) were investigated to examine the effects on skin failure threshold. As part of the analysis, damage factors and failure displacement were extracted from the simulation results to examine skin damage and failure dependency based on impactor mass and impact velocity. Empirical equations were also established to determine skin injury level for a given impactor mass, velocity, and cross-sectional area.

8.1 Introduction

Ballistic blunt trauma results from the use of kinetic energy-based impactors such as less-lethal munitions, recreational paintball, and baseball. Hubbs and Klinger (2004) studied 373 incident cases involved with 969 less-lethal projectiles fired between 1985 and 2000. The study showed injuries such as broken ribs and lung piercing occurred from the impact of the less-lethal projectiles, making the safety of less-lethal weapons remains questionable. Besides, minor skin injuries such as bruising or cuts are common in paintball activities. Therefore, it is important to understand the human skin's tolerance to ballistic blunt impact as it acts as the first protective layer to the human body.

Ballistic impact experiments were performed to determine human skin failure threshold, in terms of impact velocity, mostly at the thigh region using metallic impactors (Journee, 1907; Mattoo et al., 1974; Tausch et al., 1978; DiMaio, 1981; DiMaio et al., 1982; Missliwetz, 1987). Bir et al. (2005) performed skin failure assessments at different body regions including the thorax, abdomen, back, and thigh using a rubber impactor on PMHS and identified a range of failure energy densities. This raises a question about the root cause of the difference in the skin failure threshold: Is it caused by certain skin properties or the skin's underlying tissues being present at different body regions? Breeze and Clasper (2013) reviewed the effect of impactor geometry between the cylinder and spherical on the skin failure threshold and found no correlation. However, the data was from the impacts of isolated skin. Will this still hold when underlying tissues are present? The effect of impactor geometry, skin properties, and the presence of underlying tissues at different body regions on skin failure threshold remain uncertain. Therefore, the goal of the current chapter was to employ sub-system FE models as developed in the previous chapter to assess the three effects on skin failure threshold. Understanding each effect can inform designs of less-lethal impactors, identify vulnerable body regions, and develop region specific protective systems.

As mentioned, skin penetration assessments were performed to determine the failure threshold of the skin but little is known about skin damage or failure kinematics. In general, skin failure is believed to be the result of the breaking of collagen fibers which depends on the applied stretch. With different possible impact velocities and impactor sectional densities which can induce various stretch levels on the skin, this raises a question: Is there a skin damage or failure dependency based on the impactor mass or velocity? Knowing the correlation between the impactor characteristics and the skin damage/failure will help the design of the impactor to avoid skin injury. The current less-lethal impactor design criterion is based on Blunt Criterion (BC) (Sturdivan, 1976) which considers impactor mass, velocity, cross-sectional area, target mass, and target thickness to determine the Abbreviated Injury Scale (AIS) under the blunt impact. BC values have been determined that relate to a 50% probability of AIS 2-3 on human thoracic (Bir & Viano, 2004) and abdominal (Bir & Eck, 2005) areas. However, a recent study found conflicting results when applying the BC on less-lethal impactors available on the market and claimed the criterion underpredicts the skin penetration velocity using a physical skin penetration surrogate (Bir et al., 2012; Kapeles & Bir, 2019). Nevertheless, the underpredicted velocity was likely to develop close skin injury such as a bruise which cannot be observed using the skin surrogate. Although the developed sub-system FE model in this dissertation can model skin injury by modeling specific impact scenarios, for the ease of end-user access, it would be beneficial to be able to provide an engineering tool (e.g., empirical equation) to determine the level of skin damage upon blunt impact. Hence, the second part of this chapter investigated skin damage and failure dependency and developed empirical equations relating to skin injury level for a given impactor mass, impact velocity, and impactor cross-sectional area.

8.2 Methods

An overview of the skin failure study under the ballistic blunt impact, which was mainly divided into two sections is illustrated (Figure 8-1). The first section studied skin failure from three different perspectives (i.e., the external system, internal system, and skin tissue properties). The external system refers to the effect of the impactor geometry while the internal system refers to the effect of the ratio of the underlying tissues. A total of six FE models (Table 12) were developed for the investigations, detailed descriptions of each perspective are introduced in section 8.2.2, 8.2.3, and 8.2.4. Impact velocity was considered as a failure velocity whenever a single skin element was eroded in the FE simulation. The FE simulation was also terminated whenever the erosion occurred by using the keyword *TERMINATION_DELETED_SOLIDS to avoid model instability that leads to error termination. Three failure metrics including failure velocity, failure kinetic energy, and failure momentum were chosen, and relationships between the metrics and the impactor sectional density were established. The sectional density refers to the impactor mass normalized by its cross-sectional area.

Table 12: Six FE models used to investigate the effect of impactor geometry, skin properties, and underlying tissues on the skin failure threshold. (Avg = Average, UB = Upper Bound, LB = Lower Bound, PM = Pectoralis Major, EO = External Oblique, RA = Rectus Abdominis)

Model	Impactor	Skin	Underlying tissue	Note
Baseline(PM)	Sphere	Avg	PM	Baseline model
Cylinder	Cylinder	Avg	PM	Effect of impactor geometry
Skin_UB	Sphere	UB	PM	Effect of skin properties
Skin_LB	Sphere	LB	PM	
EO	Sphere	Avg	EO	Effect of underlying tissues
RA	Sphere	Avg	RA	

In the second section, skin damage dependency and failure dependency were investigated. Damage factor was used to assess the skin damage dependency between impactor mass and impact velocity using the contour plot graphical technique. The skin's failure displacement under different impactor mass was plotted against velocity, kinetic energy, and momentum to investigate failure transition and dependency (2a). By collecting the damage factor from the simulation matrix, empirical equations were established to determine the skin injury level for a given impactor mass, velocity, and cross-sectional area using a Weibull cumulative distribution function (2b).

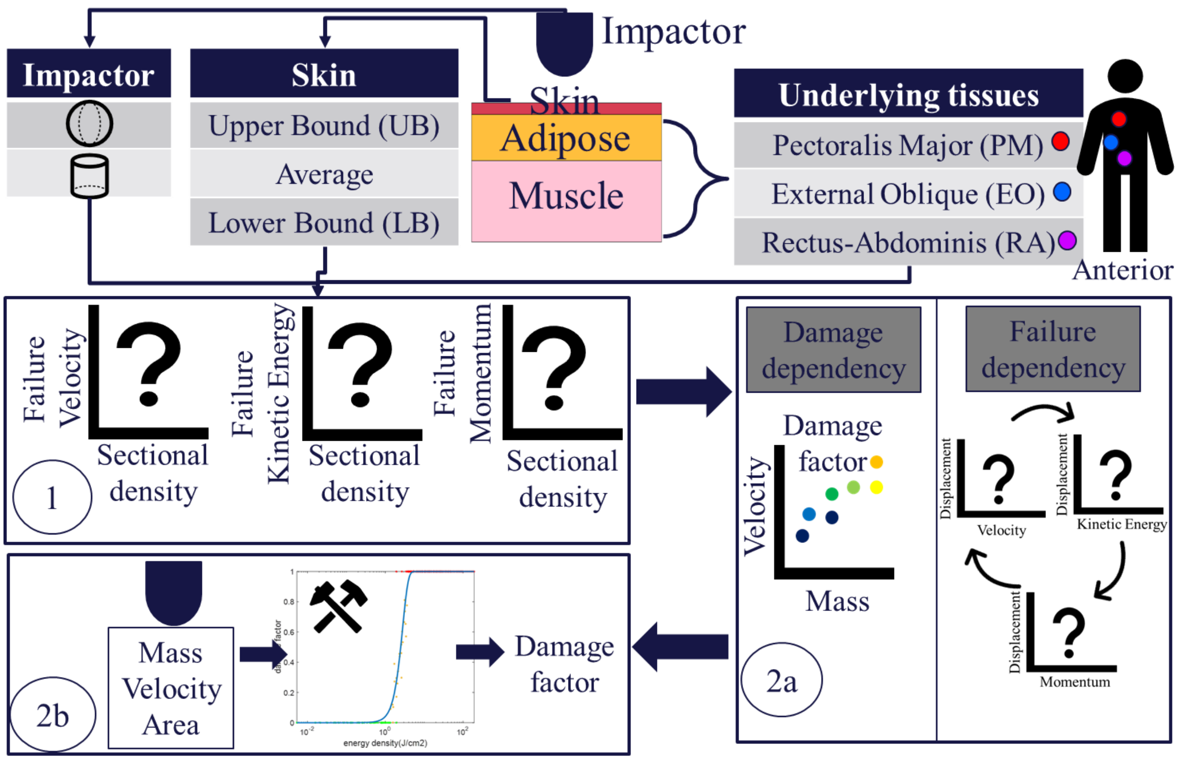

Figure 8-1: Overview of investigation of skin failure under ballistic blunt impacts.

8.2.1 Less-lethal Weapons Munitions

A range of commonly used kinetic based less-lethal weapons (LLWs) was identified (Table 13) based on the US government guidelines and commercial products (National Security Research, Inc., 2002; Defense Technology. https://www.defense-technology.com/). Paintball was also included in the table for comparison due to it being used commonly in recreational activities. Most of the LLWs are made of rubber but are also available in other materials such as foam, wood, and beanbag. In terms of geometry, spherical and cylindrical are the two most common shapes. The LLWs weigh approximately between 1 and 30 grams with muzzle velocity mostly at 100m/s except for the 12-gauge fin-stabilized round at 150m/s. The paintball, on the other hand, has a slightly lower muzzle velocity at about 86m/s.

Table 13: Less-lethal Weapons (LLWs).

Name	Material*	Radius* (mm)	Weight* (g)	Muzzle Velocity* (m/s)
a) 12-gauge fin stabilized round**	rubber	9.25	5.8	152
b) 0.32/0.60 caliber rubber ball**	rubber	4.1-7.5	0.3-2.5	91-99
c) Sponge round	foam	20	26	99
d) Baton round	rubber***	17.75	11.2-30.8	99-79
e) 0.68 caliber paintballs	polyethylene glycol	8.636	3	86

*** Available in foam and wood.
** National Security Research, Inc, 2002.
*Defense Technology (https://www.defense-technology.com/).

8.2.2 Impactor Geometry (External System)

To study the effect of impactor geometry on the skin failure threshold, a spherical and a cylindrical impactor shape were chosen to simulate blunt impacts on the sub-tissues model (Figure 8-2). A sub-system model was constructed based on the pectoralis major location where the thickness of each soft tissue layer was determined from volunteers and PMHS measurements (Panzer et al. 2020, unpublished internal UVA data). For the impactor, a fixed radius (8.636 mm) identical to a 0.68 caliber paintball was chosen and it was modeled as a rigid body in the FE model. A FE simulation matrix consisting of a spectrum of impactor masses and impact velocities were designed which covers 6 different impactor masses between 1 and 40 grams and 30 different impact velocities between 5m/s and 150m/s (Figure 8-3, left). The impactor mass was also converted to sectional density to compare munitions with different mass and cross-sectional area (Figure 8-3, right).

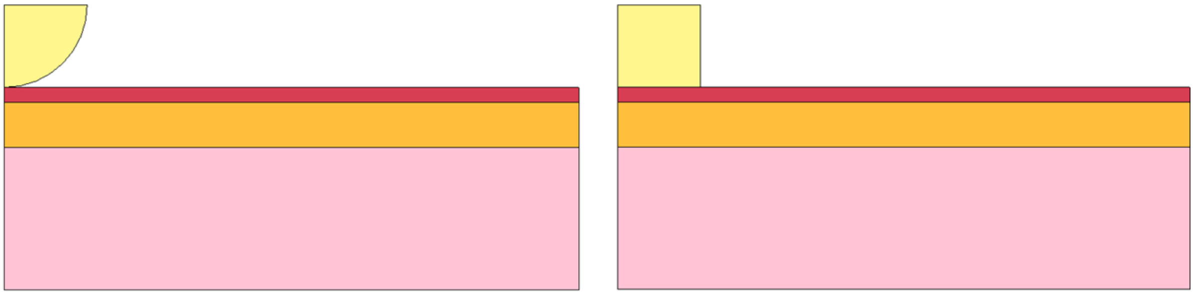

Figure 8-2: Spherical (left) vs. cylindrical (right) impactor on the pectoralis major (PM) sub-system model.

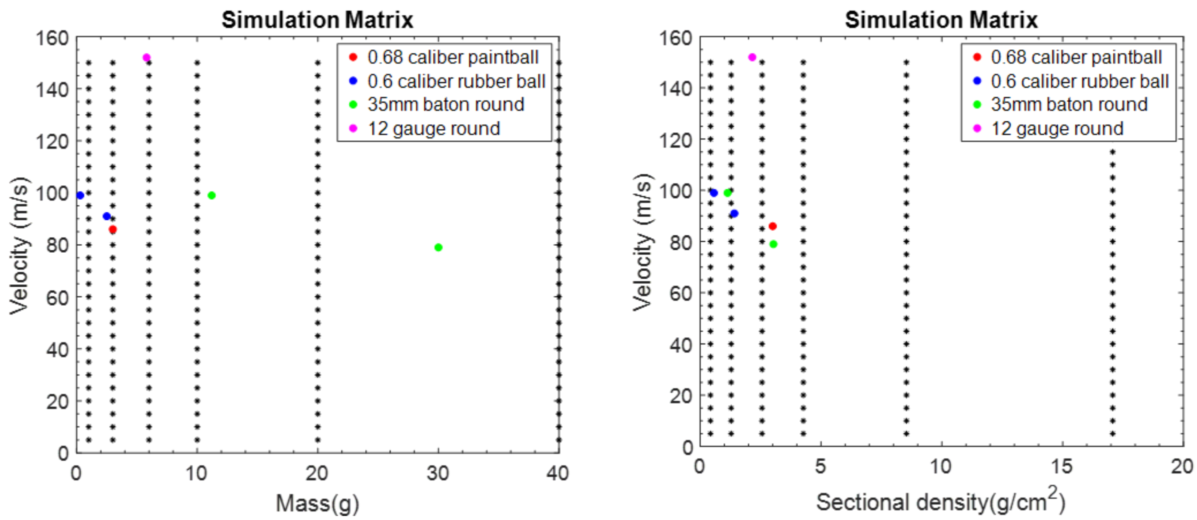

Figure 8-3: FE simulation matrix (black points) and the available LLWs (color points).

8.2.3 Underlying Tissues (Internal System)

For the underlying tissues, three anatomical locations including pectoralis major (PA), external oblique (EO), and rectus abdominis (RA) were chosen to investigate the skin failure threshold. The three locations represent human body regions with a relatively higher skin-adipose-muscle (PM) to a lower skin-adipose-muscle ratio (RA). Furthermore, the boundary condition of these body regions was also different. The bottom of the PM and EO model were constrained but allowing in-plane deformation to mimic the muscle-bone interaction while no constraint was applied to the bottom of the RA model since other soft organs are underneath the muscle tissue. Similarly, the three sub-system FE models were constructed using the same tissue thickness data obtained from Panzer et al. 2020, (unpublished internal UVA data). The average individual tissue thickness is shown in Table 14 where the skin thicknesses were similar across the three body regions. The spherical impactor was used for the three sub-system FE models. Each of the sub-system models was simulated using the same impact simulation matrix as illustrated in Figure 8-3. The material properties of the adipose and muscle tissues were obtained from the validated material model in Chapter 7 where no failure criteria were built in both materials.

Table 14: Average tissue thickness in various regions of the human body.

Location	Skin (mm)	Adipose (mm)	Muscle (mm)	Total (mm)
Pectoralis Major (PM)	1.52	4.72	14.94	21.19
External Oblique (EO)	1.91	7.85	13.83	23.59
Rectus Abdominis (RA)	2.12	14.5	17.59	34.22

As discussed in Chapter 7, the model size dictates the FE model impact response. Therefore, it was desired to exclude and minimize the edge effect from the simulation to fairly compare the FE results. All the FE simulation results were ignored after the impactor reached zero velocity. To make sure minimal boundary effects before reaching zero velocity for the impactor, the following approach was taken to determine an appropriate model size for the three-body regions (Figure 8-4). Since the total thickness of the PM and EO models were roughly 20mm and because the bottom side of the model was constrained, it was assumed the maximum tissue displacement could only be 20mm. Hence, by allowing a maximum 5% stretch (i.e. stretch ratio of 1.05) from the edge, the model radius was calculated to be approximately 60mm with the assumption of the Pythagoras theorem. For the RA model (~35mm thick), since the model was thicker and the bottom was not constrained, a maximum displacement of 40mm was assumed, and by using the same theorem, the radius of the RA model was determined to be roughly 125mm. The three sub-system FE models are illustrated in Figure 8-5, showing different underlying tissues ratio and model sizes.

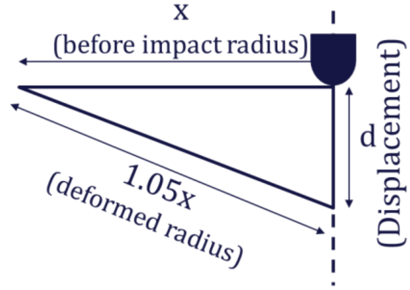

Figure 8-4: Sub-tissue deformation from blunt impact to calculate FE model radius x.

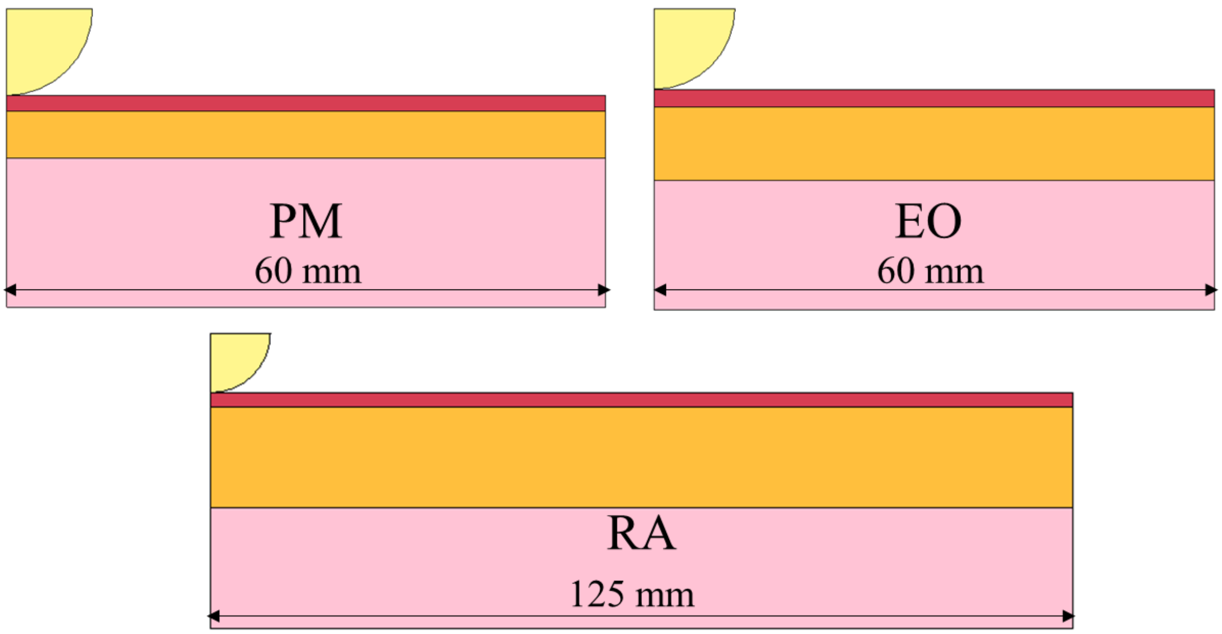

Figure 8-5: Three sub-tissues FE models - Pectoralis Major (PM) at the top left, External Oblique (EO) at top right, and Rectus Abdominis (RA) at the bottom.

8.2.4 Skin Properties

To investigate the effect of skin properties on the skin failure threshold, as developed in Chapter 6, three skin FE models which represent the average, upper bound (UB), and lower bound (LB) skin were used. The sub-system model (i.e. PM model) and the impactor geometry (i.e. spherical impactor) was fixed for this investigation. The same simulation matrix (Figure 8-3) was also used to identify the failure threshold using the three skin models. The sensitivity of skin tissue thickness was not evaluated since the thickness variation across the three body regions is minimal.

8.3 Results

Ballistic impact data from literature were compiled from different sources which looked into human skin failure using various types of impactors experimentally (Journee, 1907; Mattoo et al., 1974; Tausch et al., 1978; DiMaio, 1981; DiMaio et al., 1982; Missliwetz, 1987; Bir et al., 2005; Jussila et al., 2005; Breeze & Clasper, 2013). From these experiments, skin failure was referred to as either skin penetration or skin perforation which were not consistent and sometimes not described in the literature and therefore were grouped to provide an overview of skin injury data. According to Breeze et al. (2013) and Breeze and Clasper (2013), skin penetration was described as skin that was partially penetrated, while skin perforation was defined as skin that was entirely damaged with an obvious hole. Apart from the failure velocity, failure energy density and failure momentum density were also selected as response variables by dividing the kinetic energy and momentum by the impactor's cross-section area, respectively. As a result (Figure 8-6), the general trend observed from the experimental data was the failure velocity decreased exponentially with increasing impactor sectional density. There was no obvious trend observed in terms of failure energy density apart from the results obtained from Bir et al. (2005), which was significantly higher than the rest of the experimental data. This could be due to the use of the rubber impactor, which is more compliant than the metallic impactor and results in a higher skin failure threshold. Lastly, the momentum density exhibited an inverse exponential growth with the impactor sectional density. It should be noted the skin failure data presented in Figure 8-6 includes both skin penetration (e.g. skin abrasion) which is indicated by filled markers and unfilled markers for the skin perforation. All the data was referred to skin failure threshold, however, some of these data were deemed to be right-censored data (Tausch et al., 1978; Missliwetz, 1987) since only the perforation velocities were reported and therefore the skin failure threshold could be exaggerated.

Standard deviation and average values of Bir's data are also illustrated. Although stated as "non-skin penetration" in Bir et al. (2005), this also includes slight skin tearing.

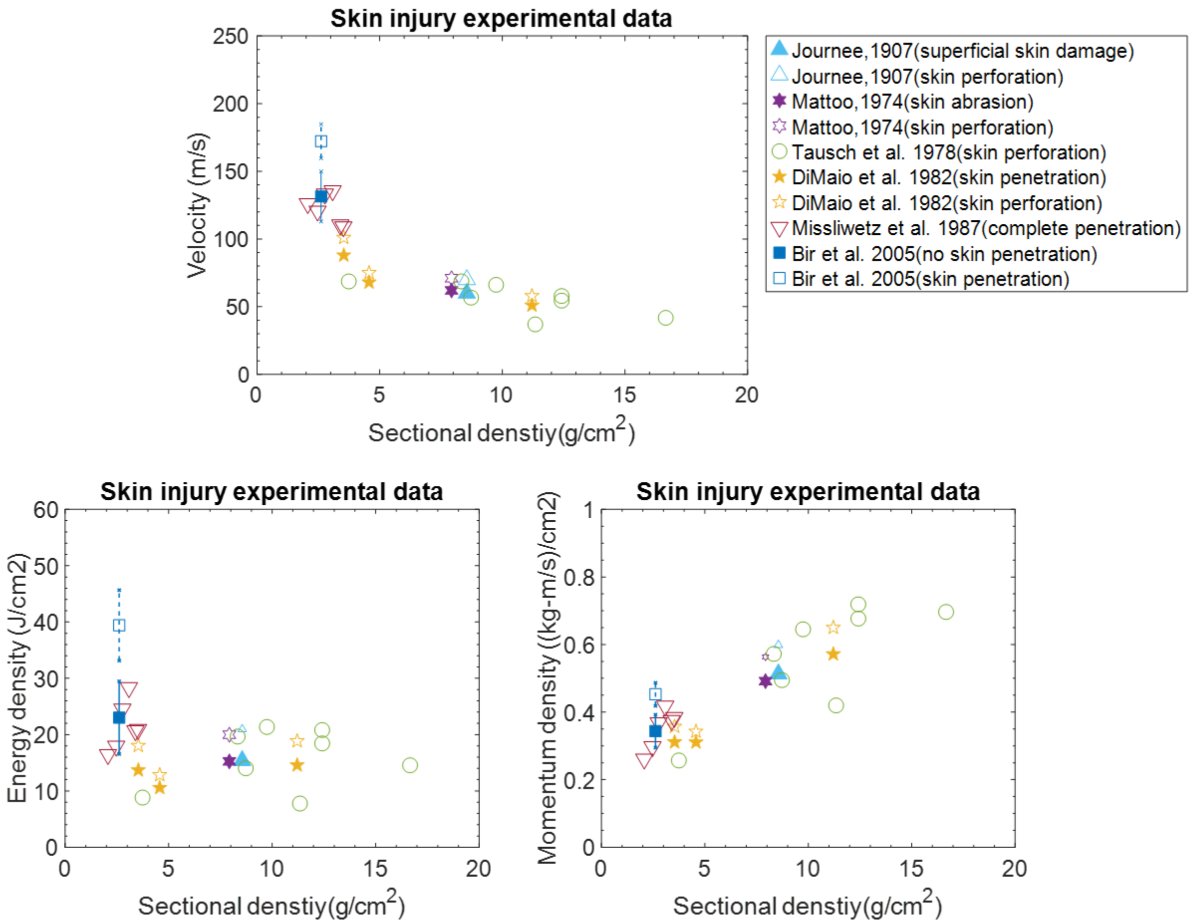

Figure 8-6: Ballistic impact failure data on human skin.

8.3.1 Effect of Impactor Geometry (External System)

The FE results exhibited a similar trend as observed in the experimental data but with lower predicted values. Between the spherical and cylindrical impactor, the FE simulation using the spherical impactor had a slightly lower failure threshold than the case using the cylindrical impactor. Nevertheless, the effect of using different impactor geometry was deemed negligible especially at higher impactor sectional density above 5 g/cm^2.

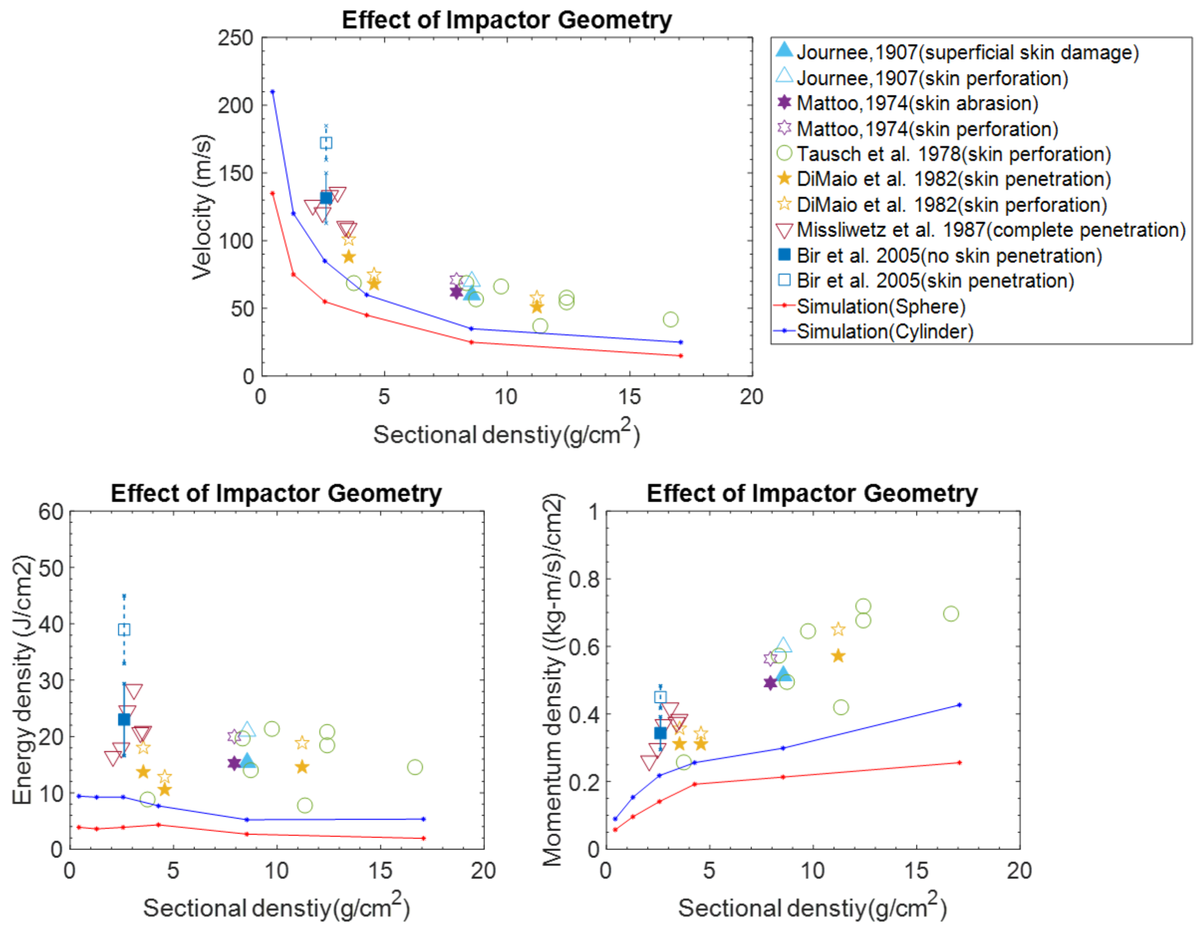

Figure 8-7: Effect of impactor geometry on the skin failure threshold under ballistic blunt impacts.

8.3.2 Effect of Skin Properties

By changing the skin properties from "soft" to "stiff" skin using the LB and UB skin respectively, this did not change the skin's failure threshold as illustrated in Figure 8-8. The overall FE results were underpredicted than the experimental data while showing a similar trend as the experimental data.

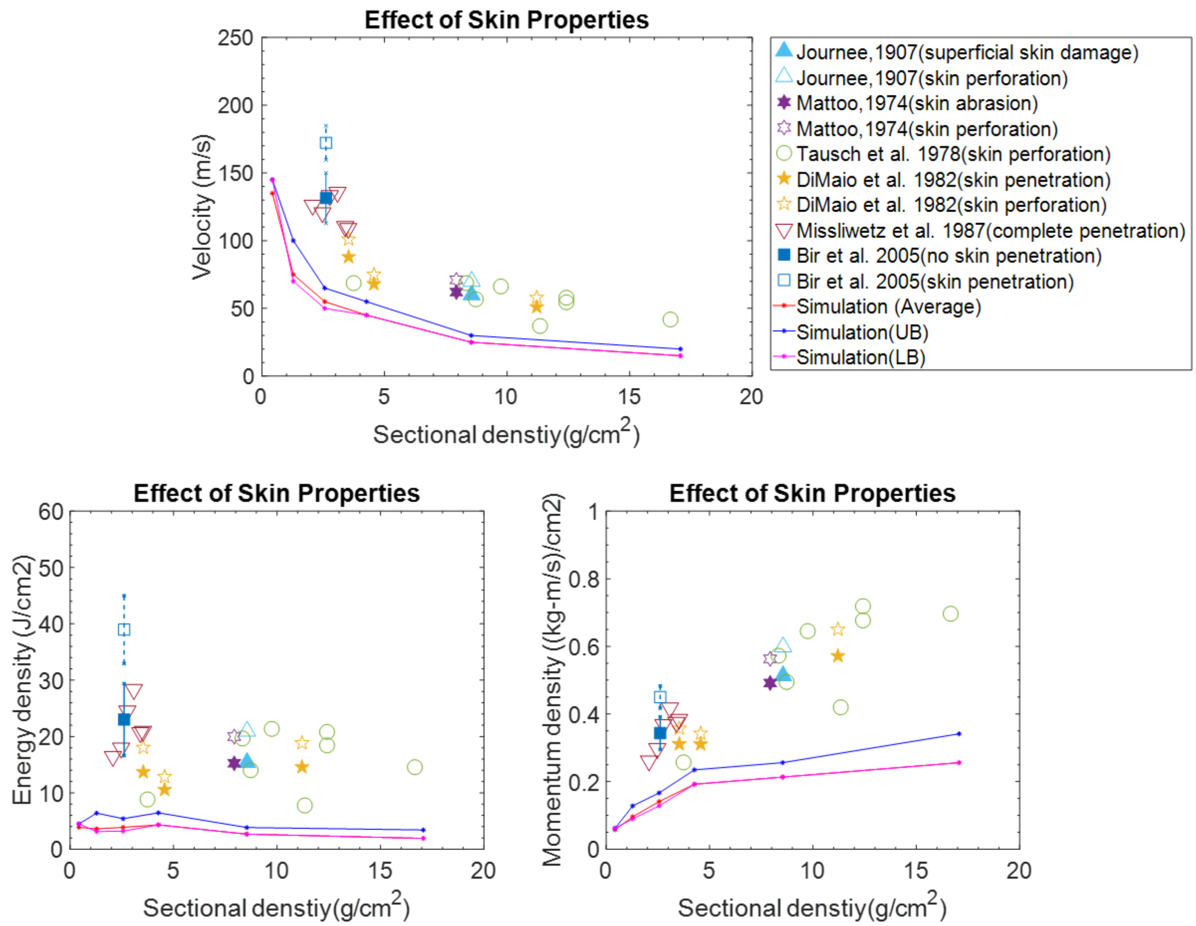

Figure 8-8: Effect of skin properties on the skin failure threshold under ballistic blunt impacts.

8.3.3 Effect of Underlying Tissues (Internal System)

Similar to the previous sections, the FE results of the PM, EO, and RA models showed lower predicted values than the experimental data. By comparing the three models, the models' responses were similar at low impactor sectional density but only the RA model started to deviate as the impactor sectional density increased. The PM and EO models behaved similarly regardless of the impactor sectional density while the RA model had the closest response to the experimental data when having the impactor sectional density above 5 g/cm^2. Hence, it is believed the underlying tissue thickness ratio and the boundary condition has an effect on the skin failure threshold when exceeding a certain impactor sectional density.

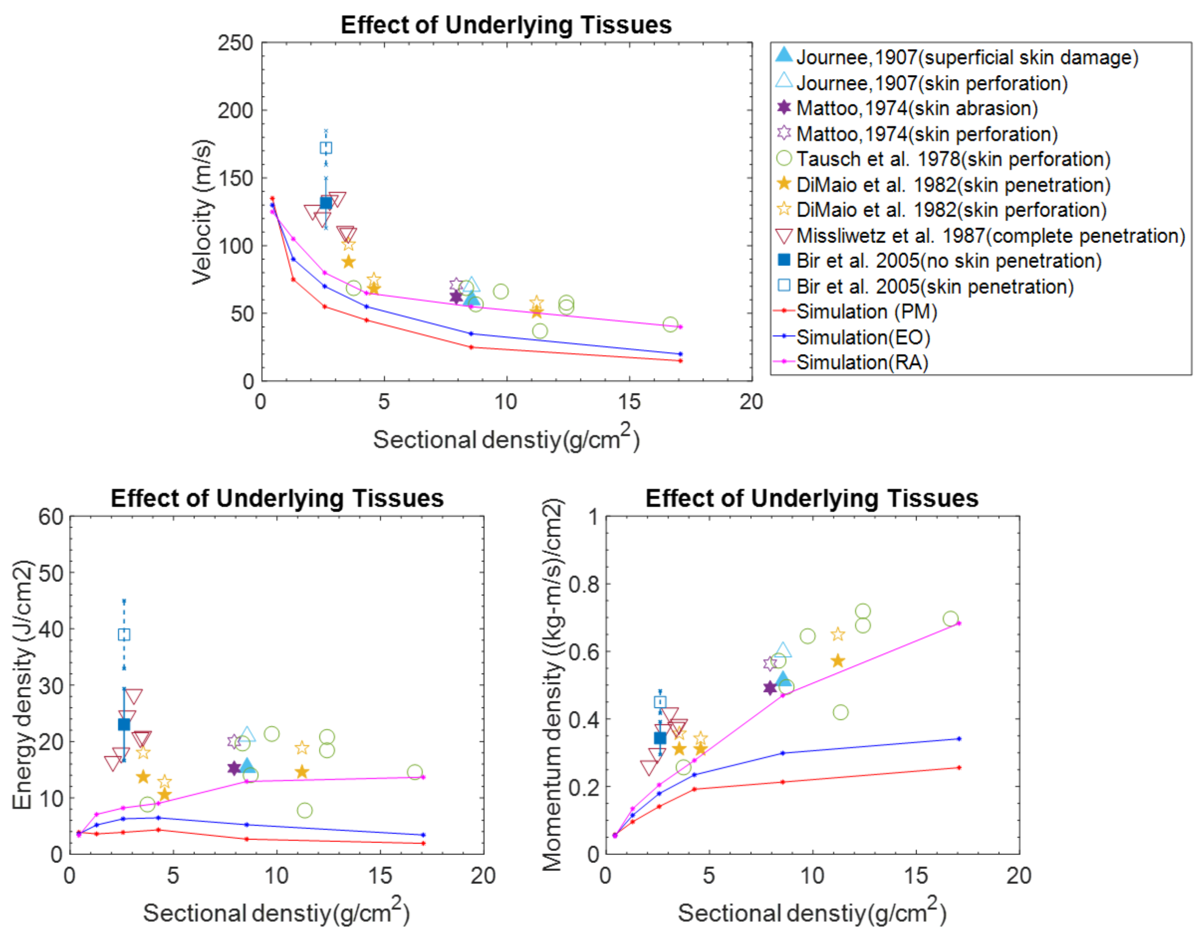

Figure 8-9: Effect of underlying tissues on the skin failure threshold under ballistic blunt impacts.

In terms of model size effect, the stretch ratio at the edges of the six FE models was also demonstrated to be less than 5% from most of the impact cases except for a few cases where the stretch ratio reached 1.07 (7%) (Figure 8-10). Nevertheless, this ensured a fair comparison between models subjected to different impact conditions by having a minimum boundary effect.

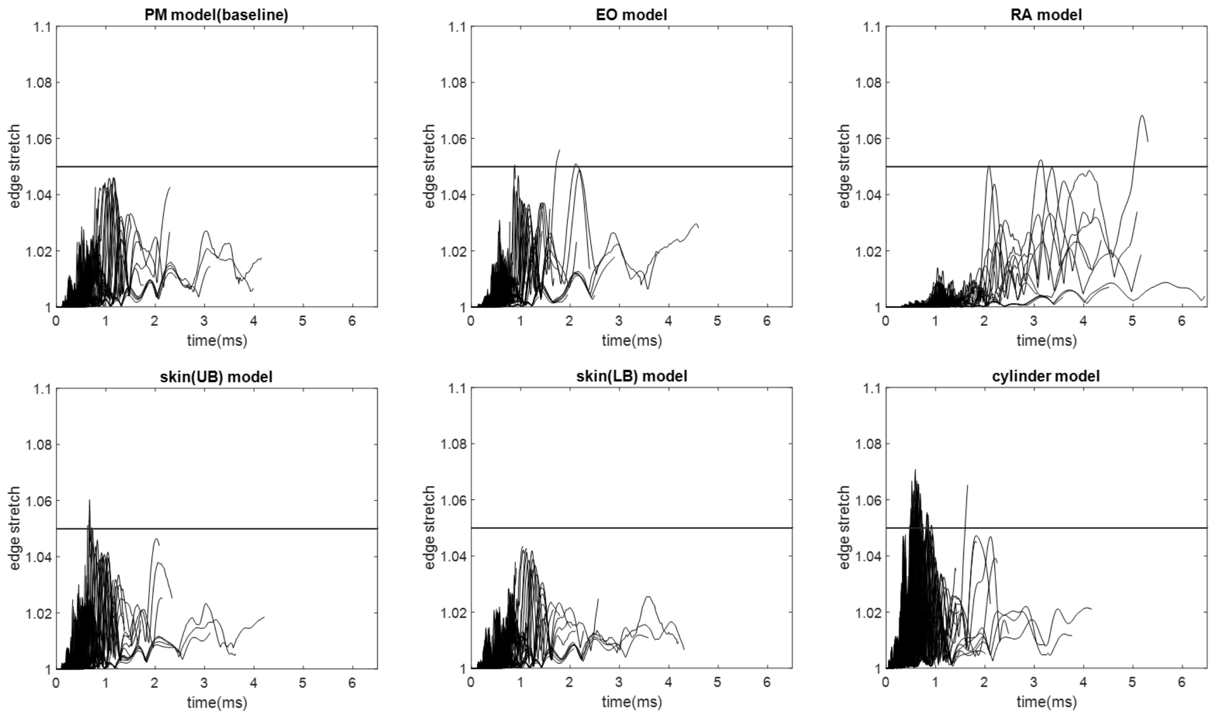

Figure 8-10: Stretch ratios at the edges of the six FE models under different impact configurations. 180 impact configurations with different combinations of impactor mass and velocity were simulated for each model.

8.3.4 Damage and Failure Dependency

In the QLV-damage model, the damage factor was assigned to model the skin's softening as part of the damage progress. A maximum damage factor of approximately 0.5 was determined which caused complete skin failure on an average skin model. The effect of impactor geometry, skin properties, and underlying tissue on the skin failure threshold was illustrated in the first part of this chapter (section 8.3.1, 8.3.2, 8.3.3). However, the mechanics of the damage progress subject to blunt impact remains unknown. Does the evolution of the damage factor depend on the impactor mass or impact velocity? Is there a dependency transition of skin failure? To answer these questions, an example of a contour plot of damage factors against impact velocity and impactor sectional density was demonstrated (Figure 8-11). It can be seen the growth of damage factor varies under different combinations of impactor sectional density and impact velocity. In region I which has small impactor sectional density and high impact velocity, the damage growth was mainly dependent on the impactor sectional density. This transits to velocity-dependent in region III with large impactor sectional density and low impact velocity. Region II which lies between region I and region III represented the transition region where the damage evolution depended on both impact velocity and impactor sectional density. Muzzle velocity of the current less-lethal munitions including recreational paintball was also plotted where most appear within region I.

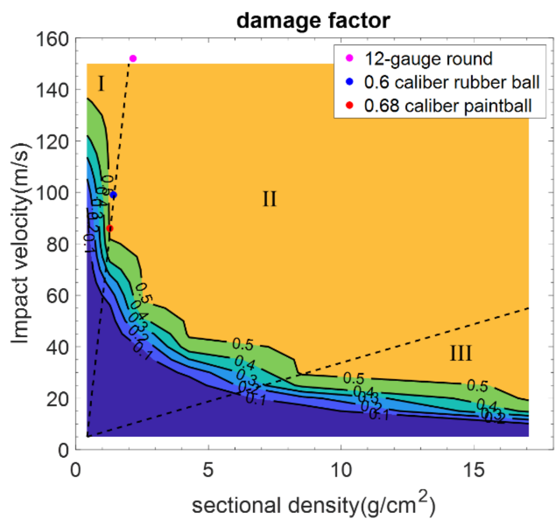

Figure 8-11: Contour plot of skin damage factor using the baseline sub-system model.

To better visualize the damage dependency and transition, the same information was plotted in floating bars (Figure 8-12, left) where the bottom end of the bar represents impact velocity required to achieve a damage factor larger than 0 (damage initiates) and the top end of the bar represents impact velocity required to achieve a damage factor of 0.5 (failure). Next, for each skin condition (damage initiates or failure), the velocity was normalized against its highest velocity to compare the trend between different models. As a result, Figure 8-12, (right) illustrated a strong sectional density dependency and transits towards velocity dependency of the damage factor as the section density increased in the PM model. With softer tissue backed body region, the sectional density dependency became weaker (i.e. RA model). Furthermore, the damage dependency and transition did not change between the damage initiation and the failure (indicated by the solid and dashed line in Figure 8-12, right).

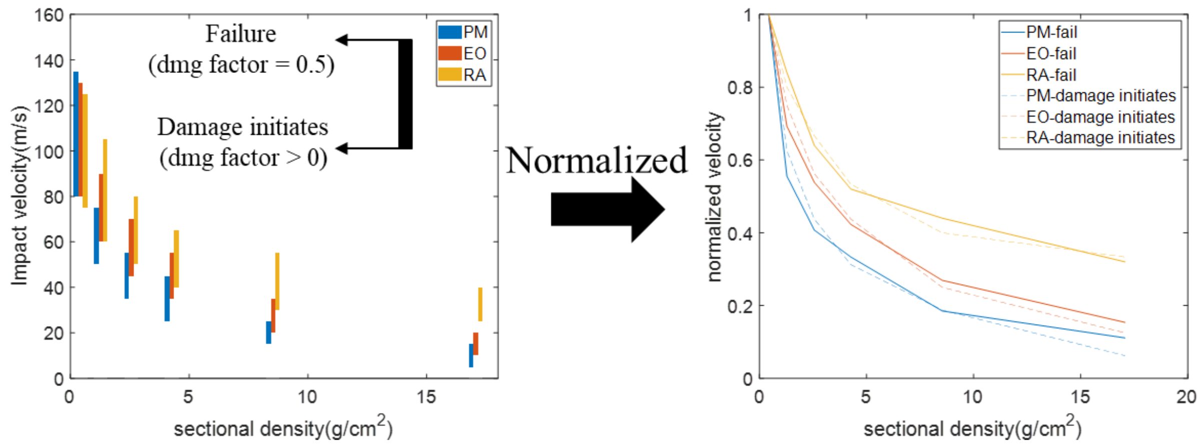

Figure 8-12: Impact velocity required to cause damage initiation (damage factor > 0) and failure (damage factor ≈ 0.5) of the three sub-system models (left). Damage and failure dependency comparison of the three models. (right).

The growth of the damage factor was demonstrated to be related to the impactor sectional density and impact velocity and the damage transition was also observed. To investigate the skin failure, the skin's maximum displacements upon impact by the six different impactor masses were plotted against impact velocity, kinetic energy, and momentum (Figure 8-13) using the baseline model. Figure 8-13 shows the skin's maximum displacement when the impactor came to rest (i.e. 0 velocities) or when the skin failure took place (denoted with color markers). The figure is an exemplar of using the baseline model. Under a fixed impactor mass, the displacement increased in an inverse exponential way with increasing impact velocity. On the other hand, it increased exponentially with increasing resultant kinetic energy and momentum (Note: the x-axis is in the logarithmic scale in the kinetic energy and momentum plot). With larger impactor mass, the rate of the displacement increment became higher (stiffer slope).

For the skin failure, the failure displacement remained plateau when approaching larger impactor mass and decreased with smaller impactor mass in the displacement-velocity plot. From the displacement-momentum plot, the failure displacement was positively correlated with the failure momentum and remained constant with constant momentum. On the other hand, the kinetic energy remained constant as the failure displacement increased and started decreasing as the failure displacement reached the plateau region. This shows that skin failure is driven by impactor momentum and has no correlation with impactor kinetic energy. The fact that the failure displacement increased and remained plateau also showed two different failure regions (i.e. local failure and global failure) exist by changing the impactor sectional density. The transition point between the local and global failure was 10 grams or an equivalent sectional density of 4.27 g/cm^2.

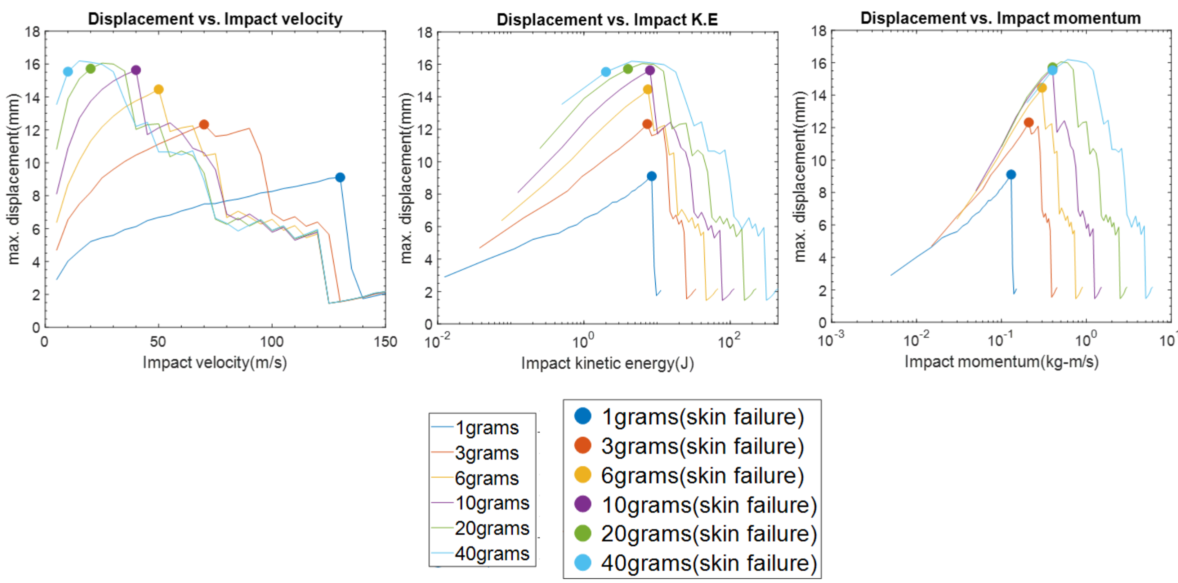

Figure 8-13: Skin's maximum displacement vs. impact velocity (left), kinetic energy (middle), and momentum (right). The dotted color points refer to the skin failure displacements under impacts from six different impactor masses.

Figure 8-14 extracted the failure displacement of the PM, EO, and RA models. All the models showed a similar trend as described (Figure 8-14, Figure 8-15, Figure 8-16) except for the RA model.

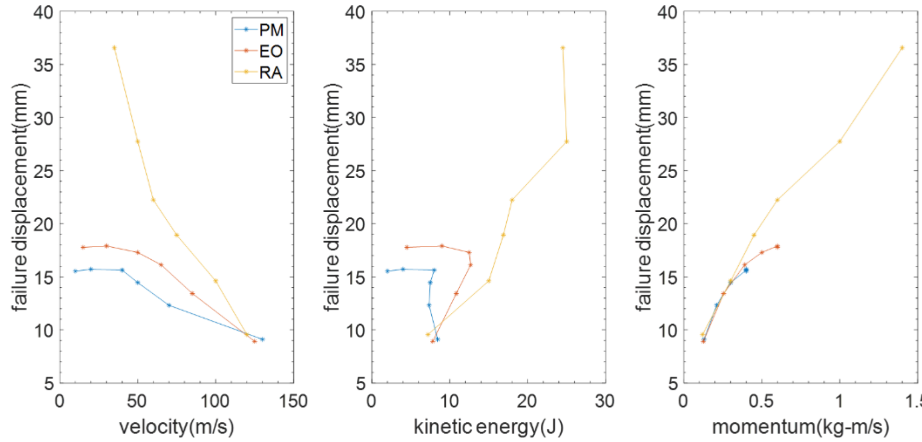

Figure 8-14: Failure displacement vs. velocity (left), kinetic energy (middle), and momentum (right) for the three underlying tissue configurations.

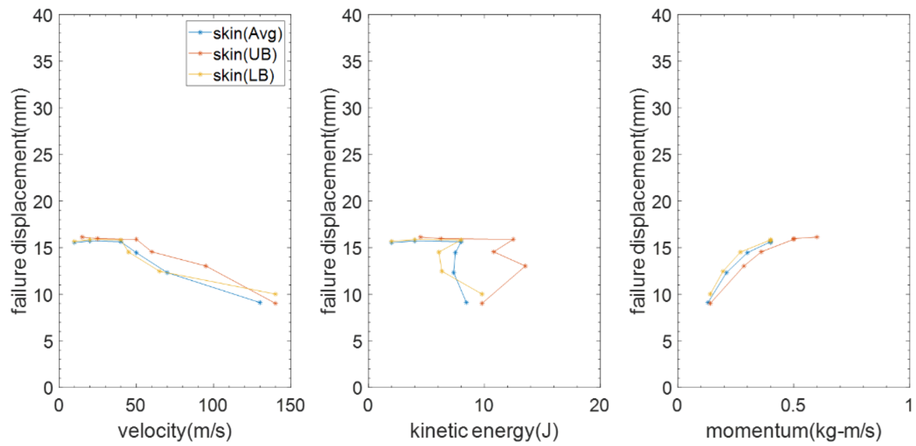

Figure 8-15: Failure displacement vs. velocity (left), kinetic energy (middle), and momentum (right) for the three skin properties configurations.

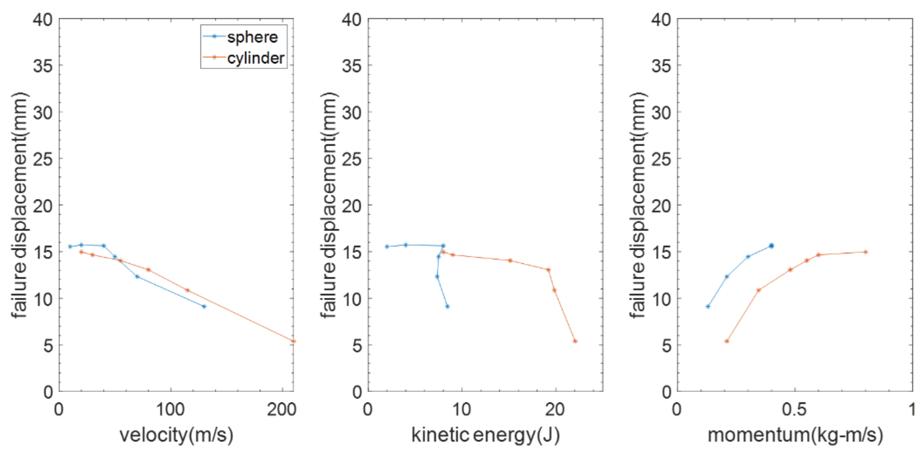

Figure 8-16: Failure displacement vs. velocity (left), kinetic energy (middle), and momentum (right) for the two impactor geometries configurations.

8.3.5 Relationship between Impactor and Skin Damage Level

To determine the skin damage level based on a given impactor mass, velocity, and cross-sectional area, skin damage factors from each simulation (180 cases) of the baseline model were plotted against impactor energy density (Figure 8-17, left). The damage factors were normalized, resulting in between 0 and 1 where 0 refers to no skin damage (green points) and 1 refers to skin failure (red points). The Weibull cumulative distribution function ($f(x;k,\lambda) = 1 - e^{-(x/\lambda)^k}$) was used to establish the relationship between the impactor energy density and the skin damage factor by optimizing the scale (λ) and shape (k) factor. The optimized Weibull parameters of the six model configurations are shown in Table 15. The six model curves are also illustrated along with the experimental skin failure energy density (Figure 8-18).

Table 15: Model parameters of each model configuration.

Configuration / Parameter	Baseline	EO	RA	Skin UB	Skin LB	Cylinder
λ	2.806	3.704	5.632	3.634	2.882	6.780
k	3.073	2.835	1.746	2.611	3.397	2.763

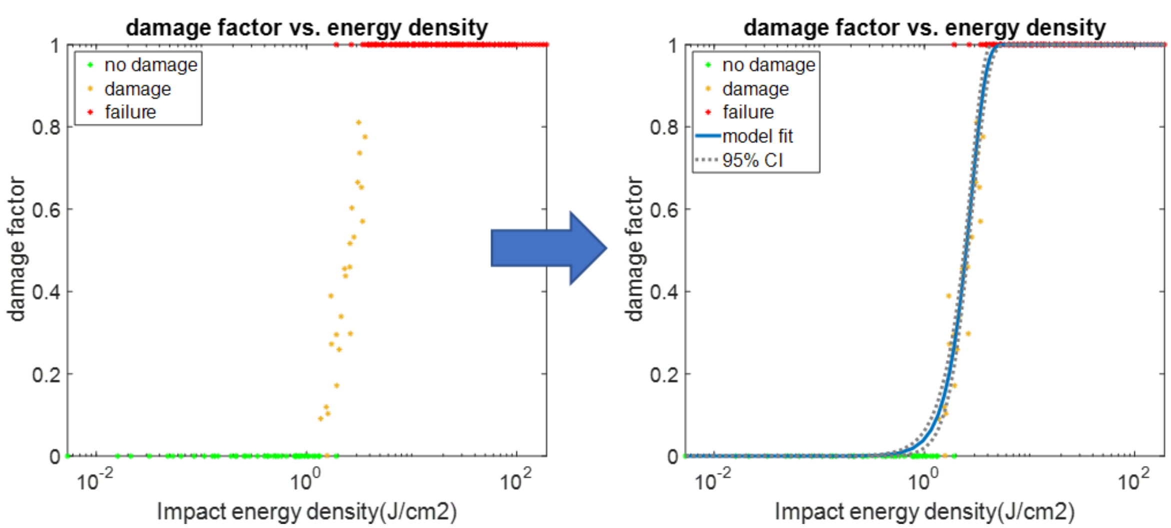

Figure 8-17: Normalized skin factors vs. impactor energy density of the baseline model (left). Weibull model (right).

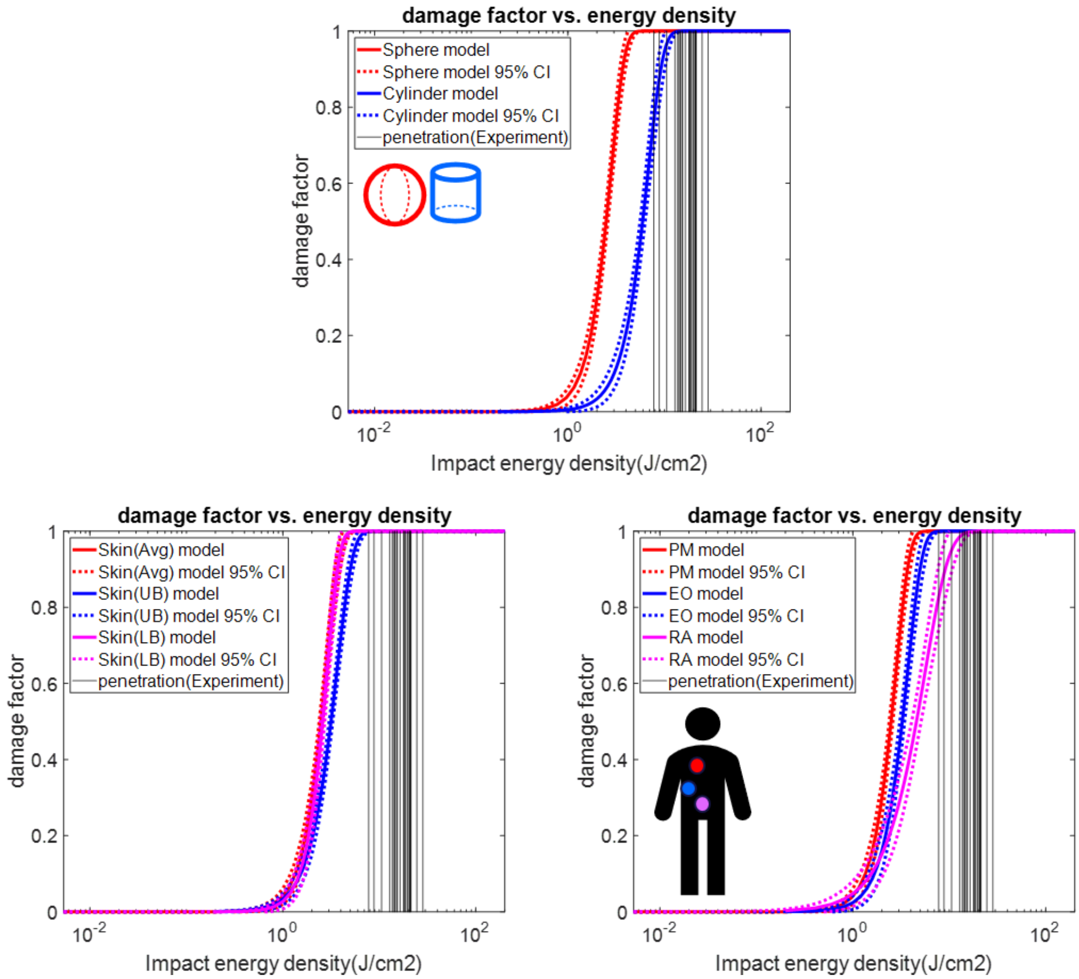

Figure 8-18:Six skin injury response function vs. experimental skin failure data. Model prediction of different impactor geometry(top). Model prediction of different skin properties (bottom left). Model prediction of different body regions. (bottom right).

8.4 Discussion

Six different sub-system FE models were developed to investigate the effect of impactor geometry, skin properties, and underlying tissues on the skin failure subjected to ballistic blunt impacts. A simulation matrix consisting of impactor sectional density and impact velocities that cover the range of current less-lethal munitions were used. The simulation results showed the effect of skin properties on skin failure threshold was negligible. The impactor geometry affects the skin failure threshold with lower impactor sectional density while the underlying tissue ratio and boundary condition caused different skin failure thresholds with higher impactor section density.

The damage growth was dependent on both impactor sectional density and impact velocity. In terms of skin failure, impactor momentum was observed to be a driven factor rather than the impactor kinetic energy. A local to global skin failure transition was also observed where the skin failure displacement reached a saturated value after reaching a certain impactor sectional density. These were found to be only applicable to hard tissue backed body regions.

Overall, the sub-system FE model underpredicted the skin failure threshold compared to the experimental data. One of the possible reasons was that the skin model developed in Chapter 6 had a lower failure force and failure displacement due to the inability to capture the skin's through-thickness compressive response (see Chapter 6 for discussion) during the impact process. Furthermore, most of the experimental data were collected on human thighs while the current simulations simulated the human upper torso region. The region effect which leads to different boundary conditions and tissue ratio could be a contributing factor especially after investigating the effect of underlying tissues on the skin failure threshold. Lastly, the difference in skin failure definition between the simulation and the experiment should also be discussed. The single element erosion criterion was used for the simulation, but this is complicated for the physical experiments. Due to the nature of testing, only a limited number of impacts can be performed on the same impact location and therefore could potentially lead to right-censored data. Therefore, the simulation results provide a bottom-line threshold for skin failure.

Among the six FE sub-system models, the RA model has the closest response to the experimental data which may be due to the following reasons. First, the presence of adipose and muscle is relatively abundant in the thigh region which is believed to be similar to the abdominal region as opposed to the thoracic region. Second, the abundant presence of underlying tissues makes different physical boundary conditions. However, the RA model only performs well after exceeding certain impactor sectional density which is believed to be due to the failure mode transition. Local failure (lower failure displacement) was observed when having a lower impactor sectional density and vice versa for the higher impactor sectional density. This explains the underprediction coming from the RA model when using low impactor sectional density because local failure was difficult to observe in the experimental tests.

A similar phenomenon (local failure) also existed in the PM and EO model when using low impactor sectional density, the reason behind the deviation between the PM/EO, and the RA model when reaching a high impactor sectional density is the boundary conditions of the models. When subjected to low impactor sectional density, the effect of bottom constraint was not obvious as the skin deformation was not severe (Figure 8-19, top row). With increasing sectional density, this brought severe skin deformation, and with the bottom being constrained in the PM/EO model, this yielded high strain concentration at the bottom area which resulted in earlier failure compared to the RA model where no strain concentration was found (Figure 8-19, bottom row). The flexibility of the RA model yielded less severe skin deformation under the same amount of impact momentum or kinetic energy and therefore resulted in a higher failure threshold compared to the PM and EO model. The difference was also observed in Bir's study (Bir et al., 2005) where a relatively lower energy density was required to cause skin failure in hard tissue backed regions such as the scapula versus soft tissue backed regions such as the abdomen.

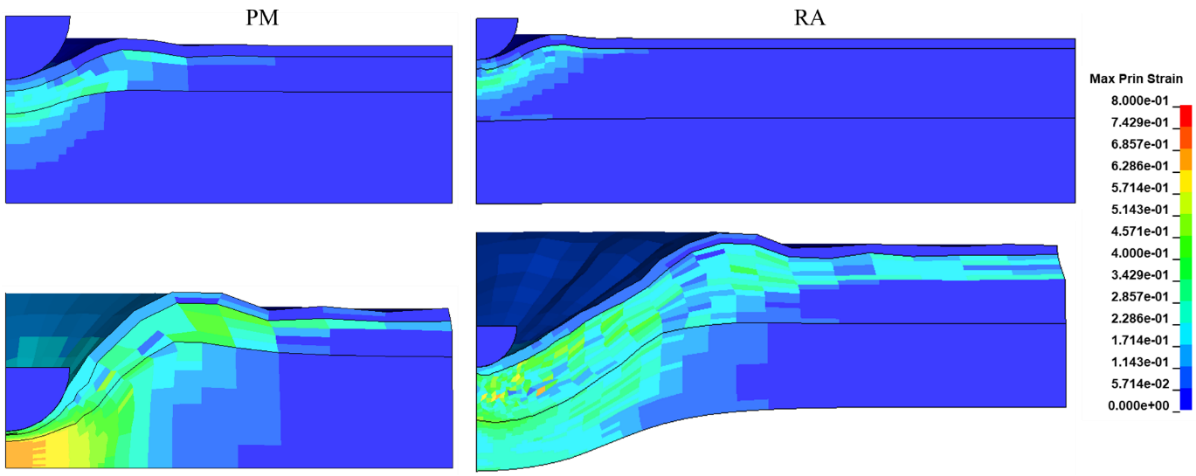

Figure 8-19: Strain distribution comparison of the sub-system models (PM vs RA) under the same impact velocity (15 m/s) between low mass and high mass impacts. The PM model is on the left column and the RA model is on the right column. The top row refers to the low mass impact (1 gram) and the bottom row refers to the high mass impact (40 grams). The screenshots are taken when the impactor reaches zero velocity.

The effect of impactor geometry was almost negligible (Figure 8-20) and this was also observed in the study reviewed by Breeze and Clasper, (2013) where the experimental data collected only covered the isolated skin. However, in the FE results, impacts using cylindrical impactor resulted in higher failure velocity thresholds than spherical impactor, especially in the smaller impactor sectional density region were observed. In general, the cylindrical impactor had a larger impact area than the spherical impactor and therefore yielded less stress concentration on the skin upon impact. The small stress concentration resulted in mild skin deformation and therefore required a higher failure threshold. Assuming a full contact area coverage between the impactor and the skin was 1 and no contact area was 0, the cylindrical impactor had a constant area coverage of 1 but this varied for the spherical impactor throughout the deformation process, increasing from close to 0 towards 1. For a small sectional density of a spherical impactor, its contact area coverage will be smaller than a cylindrical impactor due to a lower impact momentum. Conversely, the contact area coverage of a spherical impactor with high impactor sectional density is allowed to increase due to high impact momentum that causes a more severe skin deformation. By having similar contact area coverage between the two impactor geometries at large impactor sectional density, the difference of the skin failure threshold becomes smaller. Hence, this explains the negligible effect of the impactor geometry towards high impactor sectional density.

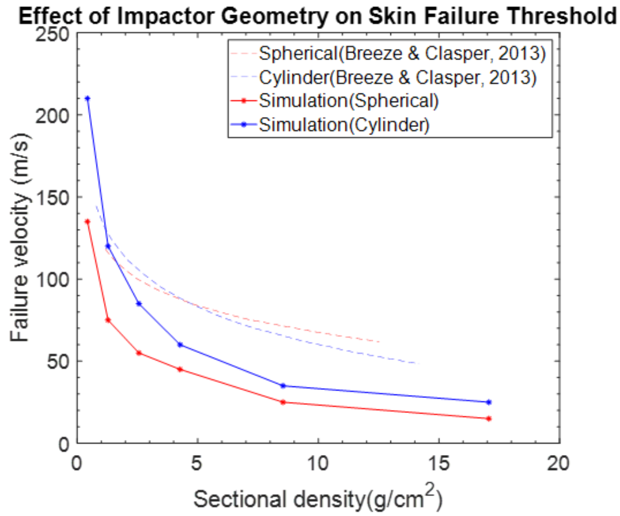

Figure 8-20: Impactor geometry on skin failure velocity (dashed lines from Breeze and Clasper, 2013).

In terms of skin damage, three regions were defined based on the contour lines to show the damage factor dependency. The sectional density dependency of the damage factor became weaker/invalid in the RA model could be due to the model boundary condition which gives more flexibility on skin deformation upon impact. Besides, the ratio of the underlying tissue could be another factor. Given the same boundary condition between the PM and EO models, the PM model had a skin-adipose-muscle ratio of 1:3:10 while the EO model had a ratio of 1:4:7. As a result, the EO model has less mass dependency (less vertical contour line) compared to the PM model. In comparison, the RA model had a ratio of 1:7:8 which resulted in the least mass dependency from the contour plot. This means the more adipose tissue underneath the skin, the more flexible the skin deformation becomes and results in less mass dependency for the damage factor. The mass dependency agreed with previous observations (Tausch et al., 1978; DiMaio et al., 1982) where the studies state the impactor mass had an effect on penetration power on the skin.

In the current study, the skin damage progress or "injury severity" was based on the damage factor which does not have physical interpretation and purely a mathematical operator to simulate skin injury until failure occurs. The simulated damage factor between 0 and 1 indicates some level of injury (damage) but without resulting skin failure (open skin injury). The damage could refer to close skin injury such as contusion but the definition is yet to be determined which requires input from experiment or field data. The Weibull function models demonstrated in the current study provided an initial opportunity for the impactor design to determine if skin failure occurred. However, the model does not consider parameters from impact location as the Blunt Criterion (BC) does and therefore the six fitted models are presented to provide a range based on impact condition. Merging of the six models by incorporating parameters such as impactor geometry and impact locations to provide a new design criterion is recommended for future study. To assess the skin injury response function in a comparable term with the experimental data (i.e. rigid spherical impactor on soft tissue backed location), only the RA model (pink curve in Figure 8-18, bottom right) should be focused on. The RA model showed promising results in capturing the experimental skin penetration data.

8.5 Conclusion

The current chapter utilizes sub-system FE models to evaluate the effect of impactor geometry (external system), underlying tissues (internal system), and skin properties on the skin failure threshold in terms of impact velocity, kinetic energy density, and momentum density. It was found that the effect of skin properties was negligible. The same conclusion was made for the impactor geometry, except when using small impactor sectional density. The body region effect was obvious in the area with an abundant soft tissue (abdominal area) under the impacts of large impactor sectional density where skin deformation was more severe. Besides, the damage factor which controls the skin damage progress was found to be dependent on both mass and impact velocity. The damage factor was found to be solely mass-dependent when using “small mass high velocity” munition and transits to solely velocity-dependent in “high mass low velocity” munition. Skin failure was mainly driven by impactor momentum rather than kinetic energy for hard tissue backed body region such as the chest area. A local to global skin failure transition was observed when reaching a certain impactor sectional density (4.27 g/cm^2). The skin damage transition and failure dependency were only applicable at the PM and EO region where underlying tissue movement was restricted by bone structures as opposed to the RA region where soft organs were presented underneath the skin’s underlying tissues.

CHAPTER 9 – Conclusions

Open skin injuries as a result of skin rubs or punctures lead to underlying tissue exposure that can cause disability and fatality through soft tissue infection or severe blood loss. Understanding human skin tolerance is crucial to preventing open skin injury, and research efforts such as skin simulant development and impact experiments have been performed to advance skin injury research. However, the current skin injury research has its limitations: There is a lack of rate-sensitive skin constitutive models with damage (material softening) and failure prediction capabilities. Moreover, integrating the constitutive model to construct a Finite Element (FE) model which can be used as an engineering tool to study skin injury would also be beneficial. Furthermore, understating the effect of impactor, skin and underlying tissues on the skin tolerance is important and this can be evaluated through the use of the FE models.

Hence, the goal of this dissertation was to develop a skin FE damage model that could simulate skin failure to investigate the skin failure threshold. To achieve the goal, comprehensive material level testing using cadaveric skin was performed to inform constitutive model development and a user-defined material (UMAT) card was also complied to integrate the constitutive model to the FE environment. The skin FE model was verified and validated using different skin impact data. Finally, the skin FE model was combined with adipose and muscle tissue to produce a sub-tissue FE model to investigate the skin failure threshold under a series of ballistic blunt impact conditions.

9.1 Major Contributions & Findings

1. *Rate sensitive skin FE damage models.*

Three viscoelastic skin FE damage material models (UMAT) that cover the average, upper bound (stiff), and lower bound (soft) skin properties were developed for blunt impact application.

The model considers the nonlinearity and viscoelasticity of skin; although skin's anisotropy was found in low rate loading (i.e. 1/s), this was not the case in high rate loading (> 75/s) and therefore only skin's isotropy was considered for high rate impact. Skin damage and failure were modeled using the damage factor which controls the material softening process after damage initiates, eventually leading to failure. This progressive damage approach results in a more realistic injury simulation and was unique to modeling skin injury compared to other approaches that have relied on a specific failure threshold. The improvement was demonstrated when comparing to the skin model used in the current human body model (GHBMC, v5.0) under blunt impact situations.

2. *Sub-system (Skin-Adipose-Muscle) FE model development for ballistic blunt impact.*

Sub-system FE model which consists of newly developed skin (UMAT skin), adipose, and muscle tissues was developed for use as a tool to investigate skin injury threshold under the ballistic blunt impact. The sub-system FE model was verified and validated using stress relaxation and impact test data. It was found the GHMBC skin only performed well under low energy impact where skin deformation was not severe but the UMAT skin performed satisfactorily in both low and high energy impact. On the other hand, the contribution of adipose tissue was deemed negligible and both skin and muscle tissue are contributors to the sub-tissues impact response.

By investigating the skin failure threshold, the sub-system FE model (abdominal region) predicted the experimental data (thigh region) fairly well given the same impactor geometry and similar anatomical location/boundary condition. The damage factors were found to be dependent on both impactor sectional density and velocity. The impactor sectional density dependency of the damage factor was stronger in 'low mass high speed' munition and transited to velocity-dependent in 'high mass low speed' munition. The dependency transition was obvious when impact occurred at hard tissue backed region such as the thorax and vice versa in soft tissue backed region such as the abdomen. In terms of skin failure, the global and local failure mode was observed where the skin's failure displacement increased (local failure) as the impactor sectional density increased and remained plateau (global failure) after reaching approximately 4.27 g/cm^2 of sectional density. The skin failure was observed to be driven by the impactor momentum instead of the impactor kinetic energy. The failure transition and dependency were only observed in hard tissue backed body region such as the chest area. The local failure mode was difficult to observe in the experiment and that caused the model to underestimate the experimental data within the small impactor sectional density range. Apart from the regional effect, skin properties did not affect the skin failure threshold. This holds similar to the impactor geometry when comparing between cylindrical and spherical impactors except for a smaller impactor sectional density (<5 g/cm^2).

3. *Experimental dataset for computational/physical skin model development.*

A comprehensive human skin dataset to examine the skin's nonlinearity, viscoelasticity, anisotropy, and failure response simultaneously based on six PMHS was constructed. This dataset includes average and corridor response of human skin loaded under tension at loading rates between 1/s and 180/s which were aimed for the ballistic impact application. Furthermore, stress relaxation tests of human skin under tension to characterize its viscoelasticity were performed for the first time. The step-hold tests, along with the tensile test results provide a platform for developing a visco-hyperelastic skin material model. Apart from the material testing, isolated skin testing under dynamic indentation using Digital Image Correlation (DIC) was also performed for the first time to characterize skin deformation contour subjected to blunt impact. As a result, the force-displacement response of the isolated skin was generated and can be served as a validation dataset for skin model development. This has been used as part of the skin FE model development in this dissertation but can also be used for physical skin simulant development in the future.

9.2 Assumptions, Limitations, and Applicability

1. *Skin's Langer line distribution.*

The skin's anisotropy in this dissertation was defined based on a theoretical Langer line distribution used by clinical surgeons. It has been reported the Langer line orientation evolves with age and is different across sexes (Cox, 1941). However, identifying collagen fiber orientation before removing the skin tissue was not possible, and it was infeasible to assess this in the samples that were eventually tested. While the "parallel" and "perpendicular" skin samples used in the experiment were orthogonal to each other and taken from the same region of the body, they may not be completely aligned with, or across, the underlying collagen fibers. Furthermore, the through-thickness fiber distribution was unclear and this could also evolve throughout with the skin thickness. Nevertheless, the aim was to provide an effective skin property versus a multilayered skin property, and the current approach was deemed sufficient. To determine the skin's Langer line, histological analysis on skin samples taken adjacent to the test sample can be performed. However, it is not clear if going to these additional lengths would improve the outcome of the study, especially when the high-rate mechanical response is considered and the effect of orientation becomes negligible.

2. *Skin's regional properties.*

The skin samples used in the experiments were all collected from the human back. This region of the body permitted a large number of samples to be collected that were fairly homogenous in composition, and away from joints, so that material data from different test series could be combined. The difference in skin failure properties across body regions has yet to be explored. The skin properties in other body regions are likely to be different than the back skin, but opportunities for collecting a lot of viable tissue from other regions is limited. Therefore, future studies should test limited samples from different regions of the body in dynamic tension rather than the full set of tests performed in this study, and then assess how consistent the mechanical properties are relative to the more comprehensive back skin database.

3. Skin's constitutive model.

Although the skin was observed to be anisotropic in low loading rate (1/s), the isotropic skin material model was sufficient to simulate the ballistic blunt impact rate. Therefore, the material parameters generated in this dissertation should be used with care especially at a low loading rate. The transition threshold from anisotropy to isotropy on the skin is yet to be determined and it lies between 1/s and 75/s according to the experimental results in this dissertation. The through-thickness compression properties of the skin material are not well captured and the investigation from this dissertation shows this causes early stress stiffening of the skin upon blunt impact.

4. Skin FE model applicability.

The viscoelastic skin material model was quantified and validated on a material level between 1/s and 180/s (engineering strain rate) which was designed for ballistic blunt impact. The model performance is uncertain when subjected to higher strain rate loading (if higher impact velocity is of interest). However, the model validation using a dynamic indentation dataset which has an average of 450 /s strain rate shows the loading rate within the same order of magnitude does not deteriorate the model performance.

For the sub-system FE model, both the adipose and muscle tissues were not built with a damage/failure feature and it is possible the underlying tissues could get damaged before the skin failure occurs. The muscle material model was optimized to match with the sub-tissue experimental test and should be used with care for other applications. The sub-system model was simulated using impactor between 1 gram (0.427 g/cm^2) and 40 grams (17.07 g/cm^2) at impact velocity between 5 m/s and 150 m/s and the model prediction (i.e. RA model) was fairly good with the experimental data. Results using impactor sectional density and impact velocity higher than the simulated range should be investigated further.

The skin failure mechanism simulated in this dissertation was assumed to be on a tensile basis, where the skin was stretched during deformation of the blunt impactor and failed when reaching the designated maximum principal stretch. With the same impactor, the degree of skin deformation was mainly controlled by the underlying tissues and this can potentially change the failure mechanism. For example, an impact on soft tissue backed location such as the abdomen allows a high degree of skin deformation and vice versa on hard tissue backed locations including the sternum or forehead region. As long as the skin deformation follows the above process, the model failure prediction should be valid regardless of the impact location on the human body. From the impact simulation, the skin was considered a failure (open skin injury) when a skin element was eroded. This could cause different observations when compared between the model and the physical experimental results, especially in local failure.

5. *Skin injury and other aspects.*

The skin injury investigated in this dissertation was most aligned with penetrating injury types where skin deforms through the perforation. Other open skin injuries such as abrasions and incisions were not considered due to different loading mechanisms (i.e. shear or surface friction). Closed skin injuries such as contusion and hematoma, which involves localized bleeding and clotting outside of blood vessels within the adipose tissues were also beyond the scope of this dissertation. Results of skin failure threshold investigation in this dissertation were based on a rigid impactor and direct impact. More sophisticated scenarios involved oblique impact and the use of deformable impactors were not studied in this dissertation.

9.3 Future Work

1. *Improvement of the UMAT skin FE model.*

The UMAT skin model developed in this dissertation failed at lower force and lower displacement. This can be improved by incorporating a transversely isotropic material model where both through-thickness compression and tensile properties of the skin can be captured simultaneously. A high rate compression test on the skin can also be added to validate the skin viscoelasticity under compression. An anisotropy to in-plane isotropy transition feature can also be added to the current model to consider a relatively low loading rate application such as automotive crash incidents. To do this, skin testing in between 1/s and 75/s should be performed to determine the transition threshold. Besides, a shell element version of the UMAT skin should be developed to be integrated with the current human body model (GHBMC, v5.0) for more potential users.

2. *Ballistic blunt impact dataset on skin injury assessment.*

There is a very limited ballistic blunt impact experiment dataset focusing on skin injury assessment that can be used for the FE model validation, especially for different body locations. Most of the dataset presented in this dissertation was conducted between the 1970s and 1980s and only focused on one body region. The latest skin injury assessment as a result of blunt impact was performed in 2005 (Bir et al., 2005) where the skin in multiple body locations was assessed. One of the biggest challenges for developing a skin injury response function is the complication of right-censored data, where the measured value of failure is higher than the actual failure threshold. This is a challenge due to the limited number of impacts that can be performed on cadaveric specimens. The sub-system FE model developed in this dissertation can be used to inform and design a preliminary impact test matrix. Furthermore, a consistent definition of open skin injury in the experiment should also be established.

3. *Skin injury response function development.*

Apart from the FE model that can be used for investigating skin failure threshold, skin injury response function using damage factor as a function of impactor energy density was also established. Six skin injury response functions were established under different impact configurations such as target location and impactor geometry. It would be convenient by merging these factors to produce a single injury response function in the future. The current skin injury response function indicated no skin damage at a damage factor of 0 and open skin injury at a damage factor of 1. Damage factors between 0 and 1 are believed to result in closed skin injury such as contusion. Hence, future experiments such as mild skin impact using living animal subjects to create contusion or sports injury data would be beneficial to inform the interpretation of the damage factor between 0 and 1.

9.4 Summary

Skin which acts as the first barrier of protection against the external environment is important and any open skin injuries can potentially lead to other injuries through infection. To prevent open skin injuries, it is crucial to understand the skin tolerance and determine the skin failure threshold. As the skin can be injured under various conditions, it is essential to develop a computational tool that can be used consistently and systematically to determine the skin failure threshold. This dissertation has developed a skin FE damage model that can simulate damage initiation, skin softening, and skin failure under different loading rates. The skin model was developed based on experimental data acquired from material and impact testing. The model was combined with adipose and muscle tissue to create a sub-system FE model to investigate skin failure threshold under different impact configurations that were within the range of current less-lethal munitions in terms of impactor mass and impact velocity. As part of the analysis, the skin injury response function was established to provide damage factor value (0 = no injury, 1 = skin failure) given the impactor energy density. Skin injury research, particularly in the area of high rate impact, is necessary to assess the safety of less-lethal munitions and design better protective equipment. This dissertation began by developing a skin computational tool and a sub-system FE model for the ease of potential skin injury research under ballistic blunt impacts. The simulation results of this dissertation could be used as a design guideline. However, before conclusive guidelines can be established, more research is needed that includes improvement of the skin model, deformable impactor, oblique impact, addition of ballistic blunt impacts to the dataset, and advancement of the skin injury response function by considering both impactor and impact location characteristics.

REFERENCES

Agache, P. G., Monneur, C., Leveque, J. L., & De Rigal, J. (1980). Mechanical properties and Young's modulus of human skin in vivo. *Archives of Dermatological Research*, *269*(3), 221–232. https://doi.org/10.1007/BF00406415

Alexander, H., & Cook, T. H. (1977). ACCOUNTING FOR NATURAL TENSION IN THE MECHANICAL TESTING OF HUMAN SKIN. *Journal of Investigative Dermatology*, *69*(3), 310–314. https://doi.org/10.1111/1523-1747.ep12507731

Arnout, N., Myncke, J., Vanlauwe, J., Labey, L., Lismont, D., & Bellemans, J. (2013). *The influence of freezing on the tensile strength of tendon grafts: A biomechanical study—PubMed*. https://pubmed.ncbi.nlm.nih.gov/24205775/

Ashrafi, P., & Tönük, E. (2014). *Indentation and Observation of Anisotropic Soft Tissues Using an Indenter Device*.

Aziz, J., Shezali, H., Radzi, Z., Yahya, N. A., Kassim, N. H. A., Czernuszka, J., & Rahman, M. T. (2016). Molecular Mechanisms of Stress-Responsive Changes in Collagen and Elastin Networks in Skin. *Skin Pharmacology and Physiology*, *29*(4), 190–203. https://doi.org/10.1159/000447017

Balaraman, K., Mukherjee, S., Chawla, A., & Malhotra, R. (2006). *Inverse Finite Element Characterization of Soft Tissues Using Impact Experiments and Taguchi Methods*. 2006-01–0252. https://doi.org/10.4271/2006-01-0252

Barel, A. (1995). Suction method for measurement of skin mechanical properties: The cutometer. *Handbook of Non-Invasive Methods and the Skin*. https://ci.nii.ac.jp/naid/10019105009

Barnett, A. C., Jones, J. A., Lee, Y.-S., & Moore, J. Z. (2016). Compliant Needle Vibration Cutting of Soft Tissue. *Journal of Manufacturing Science and Engineering*, *138*(11). https://doi.org/10.1115/1.4033690

Barnett, A. C., Lee, Y.-S., & Moore, J. Z. (2015). Fracture Mechanics Model of Needle Cutting Tissue. *Journal of Manufacturing Science and Engineering*, *138*(1), 011005. https://doi.org/10.1115/1.4030374

Basler, R. S. W., Garcia, M. A., Gooding, K. S., & Roberts, W. O. (2001). Immediate Steps for Treating Abrasions. *The Physician and Sportsmedicine*, *29*(4), 69–70. https://doi.org/10.3810/psm.2001.04.744

Bir, C. A., Resslar, M., & Stewart, S. (2012). Skin penetration surrogate for the evaluation of less lethal kinetic energy munitions. *Forensic Science International*, *220*(1–3), 126–129. https://doi.org/10.1016/j.forsciint.2012.02.008

Bir, C. A., Stewart, S. J., & Wilhelm, M. (2005). Skin Penetration Assessment of Less Lethal Kinetic Energy Munitions. *Journal of Forensic Sciences*, *50*(6), 1–4. https://doi.org/10.1520/JFS2004551

Bir, C., & Eck, J. (2005). Preliminary Analysis of Blunt Ballistic Impacts to the Abdomen. In M. D. Gilchrist (Ed.), *IUTAM Symposium on Impact Biomechanics: From Fundamental Insights to Applications* (Vol. 124, pp. 25–32). Springer-Verlag. https://doi.org/10.1007/1-4020-3796-1_3

Bir, C., & Viano, D. C. (2004). Design and Injury Assessment Criteria for Blunt Ballistic Impacts: *The Journal of Trauma: Injury, Infection, and Critical Care*, *57*(6), 1218–1224. https://doi.org/10.1097/01.TA.0000114066.77967.DE

Bischoff, J. E., Arruda, E. M., & Grosh, K. (2002). Orthotropic Hyperelasticity in Terms of an Arbitrary Molecular Chain Model. *Journal of Applied Mechanics*, *69*(2), 198–201. https://doi.org/10.1115/1.1432664

Bischoff, Jeffrey E. (2004). Static Indentation of Anisotropic Biomaterials Using Axially Asymmetric Indenters—A Computational Study. *Journal of Biomechanical Engineering*, *126*(4), 498–505. https://doi.org/10.1115/1.1785808

Böl, M., Kruse, R., Ehret, A. E., Leichsenring, K., & Siebert, T. (2012). Compressive properties of passive skeletal muscle—The impact of precise sample geometry on parameter identification in inverse finite element analysis. *Journal of Biomechanics*, *45*(15), 2673–2679. https://doi.org/10.1016/j.jbiomech.2012.08.023

Bosboom, E. M. H., Hesselink, M. K. C., Oomens, C. W. J., Bouten, C. V. C., Drost, M. R., & Baaijens, F. P. T. (2001). Passive transverse mechanical properties of skeletal muscle under in vivo compression. *Journal of Biomechanics*, *34*(10), 1365–1368. https://doi.org/10.1016/S0021-9290(01)00083-5

Boyer, G., Laquièze, L., Bot, A. L., Laquièze, S., & Zahouani, H. (2009). Dynamic indentation on human skin in vivo: Ageing effects. *Skin Research and Technology*, *15*(1), 55–67. https://doi.org/10.1111/j.1600-0846.2008.00324.x

Breeze, John, & Clasper, J. (2013). Determining the velocity required for skin perforation by fragment simulating projectiles: A systematic review. *Journal of the Royal Army Medical Corps*, *159*(4), 265–270. https://doi.org/10.1136/jramc-2013-000070

Breeze, Johno, James, G. R., & Hepper, A. E. (2013). Perforation of fragment simulating projectiles into goat skin and muscle. *Journal of the Royal Army Medical Corps*, *159*(2), 84–89. https://doi.org/10.1136/jramc-2013-000065

Calvo, B., Sierra, M., Grasa, J., Muñoz, M. J., & Peña, E. (2014). Determination of passive viscoelastic response of the abdominal muscle and related constitutive modeling: Stress-relaxation behavior. *Journal of the Mechanical Behavior of Biomedical Materials*, *36*, 47–58. https://doi.org/10.1016/j.jmbbm.2014.04.006

Chanda, A., & Upchurch, W. (2018). Biomechanical Modeling of Wounded Skin. *Journal of Composites Science*, *2*(4), 69. https://doi.org/10.3390/jcs2040069

Chawla, A., Mukherjee, S., & Karthikeyan, B. (2009). Characterization of human passive muscles for impact loads using genetic algorithm and inverse finite element methods. *Biomechanics and Modeling in Mechanobiology*, *8*(1), 67–76. https://doi.org/10.1007/s10237-008-0121-6

Clavert, P., Kempf, J.-F., Bonnomet, F., Boutemy, P., Marcelin, L., & Kahn, J.-L. (2001). Effects of freezing/thawing on the biomechanical properties of human tendons. *Surgical and Radiologic Anatomy*, *23*(4), 259–262. https://doi.org/10.1007/s00276-001-0259-8

Cox, H. T. (1941). The cleavage lines of the skin. *BJS*, *29*(114), 234–240. https://doi.org/10.1002/bjs.18002911408

Crichton, M. L., Donose, B. C., Chen, X., Raphael, A. P., Huang, H., & Kendall, M. A. F. (2011). The viscoelastic, hyperelastic and scale dependent behaviour of freshly excised individual skin layers. *Biomaterials*, *32*(20), 4670–4681. https://doi.org/10.1016/j.biomaterials.2011.03.012

Delalleau, A., Josse, G., Lagarde, J.-M., Zahouani, H., & Bergheau, J.-M. (2008). A nonlinear elastic behavior to identify the mechanical parameters of human skin in vivo. *Skin Research and Technology*, *14*(2), 152–164. https://doi.org/10.1111/j.1600-0846.2007.00269.x

DiMaio, V. J. M., Copeland, A. R., Besant-Matthews, P. E., Fletcher, L. A., & Jones, A. (1982). Minimal Velocities Necessary for Perforation of Skin by Air Gun Pellets and Bullets. *Journal of Forensic Sciences*, *27*(4), 12207J. https://doi.org/10.1520/JFS12207J

DiMaio, Vincent J. M. (1981). Penetration and perforation of skin by bullets and missiles, A review of the literature: *The American Journal of Forensic Medicine and Pathology*, *2*(2), 107–110. https://doi.org/10.1097/00000433-198106000-00003

Diridollou, S., Patat, F., Gens, F., Vaillant, L., Black, D., Lagarde, J. M., Gall, Y., & Berson, M. (2000). In vivo model of the mechanical properties of the human skin under suction. *Skin Research and Technology*, *6*(4), 214–221. https://doi.org/10.1034/j.1600-0846.2000.006004214.x

Dulińska-Molak, I., Pasikowska, M., Pogoda, K., Lewandowska, M., Eris, I., & Lekka, M. (2014). Age-Related Changes in the Mechanical Properties of Human Fibroblasts and Its Prospective Reversal After Anti-Wrinkle Tripeptide Treatment. *International Journal of Peptide Research and Therapeutics*, *20*(1), 77–85. https://doi.org/10.1007/s10989-013-9370-z

Escoffier, C., de Rigal, J., Rochefort, A., Vasselet, R., Léveˆque, J.-L., & Agache, P. G. (1989). Age-related mechanical properties of human skin: An in vivo study. *Journal of Investigative Dermatology*, *93*(3), 353–357. https://doi.org/10.1016/0022-202X(89)90058-4

Feng, Y., Okamoto, R. J., Namani, R., Genin, G. M., & Bayly, P. V. (2013). Measurements of mechanical anisotropy in brain tissue and implications for transversely isotropic material models of white matter. *Journal of the Mechanical Behavior of Biomedical Materials*, *23*, 117–132. https://doi.org/10.1016/j.jmbbm.2013.04.007

Ferruzzi, J., Sun, M., Gkousioudi, A., Pilvar, A., Roblyer, D., Zhang, Y., & Zaman, M. H. (2019). Compressive Remodeling Alters Fluid Transport Properties of Collagen Networks – Implications for Tumor Growth. *Scientific Reports*, *9*. https://doi.org/10.1038/s41598-019-50268-z

Flynn, C., & McCormack, B. A. O. (2008). Finite element modelling of forearm skin wrinkling. *Skin Research and Technology*, *14*(3), 261–269. https://doi.org/10.1111/j.1600-0846.2008.00289.x

Flynn, C., Taberner, A., & Nielsen, P. (2011). Mechanical characterisation of in vivo human skin using a 3D force-sensitive micro-robot and finite element analysis. *Biomechanics and Modeling in Mechanobiology*, *10*(1), 27–38. https://doi.org/10.1007/s10237-010-0216-8

Frykberg, R. G., & Banks, J. (2015). Challenges in the Treatment of Chronic Wounds. *Advances in Wound Care*, *4*(9), 560–582. https://doi.org/10.1089/wound.2015.0635

Fung, YCB. (1972). Stress-strain-history relations of soft tissues in simple elongation. *Biomechanics Its Foundations and Objectives*, 181–208.

Gallagher, A. J., Ní Anniadh, A., Bruyere, K., Otténio, M., Xie, H., & Gilchrist, M. D. (2012). *Dynamic tensile properties of human skin*. Proceedings of the 2012 International IRCOBI Conference on the Biomechanics of Injury. http://wbldb.lievers.net/10077915.html

Gallo, R. L. (2017). Human Skin Is the Largest Epithelial Surface for Interaction with Microbes. *The Journal of Investigative Dermatology*, *137*(6), 1213–1214. https://doi.org/10.1016/j.jid.2016.11.045

Gasser, T. C., Ogden, R. W., & Holzapfel, G. A. (2006). Hyperelastic modelling of arterial layers with distributed collagen fibre orientations. *Journal of The Royal Society Interface*, *3*(6), 15–35. https://doi.org/10.1098/rsif.2005.0073

Giannini, S., Buda, R., Di Caprio, F., Agati, P., Bigi, A., De Pasquale, V., & Ruggeri, A. (2008). Effects of freezing on the biomechanical and structural properties of human posterior tibial tendons. *International Orthopaedics*, *32*(2), 145–151. https://doi.org/10.1007/s00264-006-0297-2

Gniadecka, M., & Serup, J. (2006). Suction Chamber Method for Measuring Skin Mechanical Properties: The Dermaflex®. In J. Serup, G. Jemec, & G. Grove (Eds.), *Handbook of Non-Invasive Methods and the Skin, Second Edition* (pp. 571–577). CRC Press. https://doi.org/10.3109/9781420003307-78

Grahame, R., & Holt, P. J. L. (1969). The Influence of Ageing on the in vivo Elasticity of Human Skin. *Gerontology*, *15*(2–3), 121–139. https://doi.org/10.1159/000211681

Grebeniuk, L. A., & Uten'kin, A. A. (1994). [The mechanical properties of human skin. I]. *Fiziologiia Cheloveka*, *20*(2), 157–162.

Groves, Rachel B., Coulman, S. A., Birchall, J. C., & Evans, S. L. (2013). An anisotropic, hyperelastic model for skin: Experimental measurements, finite element modelling and identification of parameters for human and murine skin. *Journal of the Mechanical Behavior of Biomedical Materials*, *18*, 167–180. https://doi.org/10.1016/j.jmbbm.2012.10.021

Groves, Rachel Beth, & Eng, B. (n.d.). *QUANTIFYING THE MECHANICAL PROPERTIES OF SKIN IN VIVO AND EX VIVO TO OPTIMISE MICRONEEDLE DEVICE DESIGN*. 253.

Hill, R. (1979). Aspects of Invariance in Solid Mechanics. In *Advances in Applied Mechanics* (Vol. 18, pp. 1–75). Elsevier. https://doi.org/10.1016/S0065-2156(08)70264-3

Holzapfel, G. A., & Gasser, T. C. (2001). A viscoelastic model for fiber-reinforced composites at finite strains: Continuum basis, computational aspects and applications. *Computer Methods in Applied Mechanics and Engineering*, *190*(34), 4379–4403. https://doi.org/10.1016/S0045-7825(00)00323-6

Huang, H., Zhang, J., Sun, K., Zhang, X., & Tian, S. (2011). *Effects of repetitive multiple freeze–thaw cycles on the biomechanical properties of human flexor digitorum superficialis and flexor pollicis longus tendons | Elsevier Enhanced Reader*. https://doi.org/10.1016/j.clinbiomech.2010.12.006

Hubbs, K., & Klinger, D. (n.d.). *Impact Munitions Use: Types, Targets, Effects*. 16.

Humphrey, J. D., & Yin, F. C. P. (1987). On Constitutive Relations and Finite Deformations of Passive Cardiac Tissue: I. A Pseudostrain-Energy Function. *Journal of Biomechanical Engineering*, *109*(4), 298–304. https://doi.org/10.1115/1.3138684

Ito, M., Pramudita, J. A., Watanabe, R., Shimizu, Y., & Tanabe, Y. (2017). INVESTIGATION OF SKIN LACERATION THRESHOLD UNDER A SPECIFIC CONDITION: BLADE PENETRATION TEST ON PORCINE SKIN. *Journal of Mechanics in Medicine and Biology*, *17*(08), 1750114. https://doi.org/10.1142/S0219519417501147

Jacquemoud, C., Bruyere-Garnier, K., & Coret, M. (2007). Methodology to determine failure characteristics of planar soft tissues using a dynamic tensile test. *Journal of Biomechanics*, *40*(2), 468–475. https://doi.org/10.1016/j.jbiomech.2005.12.010

Jansen, L. H., & Rottier, P. B. (1958). Some Mechanical Properties of Human Abdominal Skin Measured on Excised Strips. *Dermatology*, *117*(2), 65–83. https://doi.org/10.1159/000255569

Jemec, G. B. E., Gniadecka, M., & Jemec, B. (1996). Measurement of skin mechanics. *Skin Research and Technology*, *2*(4), 164–166. https://doi.org/10.1111/j.1600-0846.1996.tb00144.x

Johnson, K. L. (1985, May). *Contact Mechanics*. Cambridge Core; Cambridge University Press. https://doi.org/10.1017/CBO9781139171731

Jones, R. E., Foster, D. S., & Longaker, M. T. (2018). Management of Chronic Wounds—2018. *JAMA*, *320*(14), 1481–1482. https://doi.org/10.1001/jama.2018.12426

Joodaki, H., & Panzer, M. B. (2018). Skin mechanical properties and modeling: A review. *Proceedings of the Institution of Mechanical Engineers, Part H: Journal of Engineering in Medicine*, *232*(4), 323–343. https://doi.org/10.1177/0954411918759801

Jung, H.-J., Vangipuram, G., Fisher, M. B., Yang, G., Hsu, S., Bianchi, J., Ronholdt, C., & Woo, S. L.-Y. (2011). The effects of multiple freeze–thaw cycles on the biomechanical properties of the human bone-patellar tendon-bone allograft. *Journal of Orthopaedic Research*, *29*(8), 1193–1198. https://doi.org/10.1002/jor.21373

Jussila, J., Leppäniemi, A., Paronen, M., & Kulomäki, E. (2005). Ballistic skin simulant. *Forensic Science International*, *150*(1), 63–71. https://doi.org/10.1016/j.forsciint.2004.06.039

Kalra, A., Lowe, A., & Al-Jumaily, A. (2016). Mechanical Behaviour of Skin: A Review. *Journal of Material Science & Engineering*, *5*(4). https://doi.org/10.4172/2169-0022.1000254

Kapeles, J. A., & Bir, C. A. (2019a). Human Effects Assessment of 40-mm Nonlethal Impact Munitions. *Human Factors and Mechanical Engineering for Defense and Safety*, *3*(1), 2. https://doi.org/10.1007/s41314-019-0017-5

Kapeles, J. A., & Bir, C. A. (2019b). Human Effects Assessment of 40-mm Nonlethal Impact Munitions. *Human Factors and Mechanical Engineering for Defense and Safety*, *3*(1), 2. https://doi.org/10.1007/s41314-019-0017-5

Karimi, A., Haghighatnama, M., Shojaei, A., Navidbakhsh, M., Motevalli Haghi, A., & Adnani Sadati, S. J. (2016). Measurement of the viscoelastic mechanical properties of the skin tissue under uniaxial loading. *Proceedings of the Institution of Mechanical Engineers, Part L: Journal of Materials: Design and Applications*, *230*(2), 418–425. https://doi.org/10.1177/1464420715575169

Khadem, M., Rossa, C., Sloboda, R. S., Usmani, N., & Tavakoli, M. (2016). Mechanics of Tissue Cutting During Needle Insertion in Biological Tissue. *IEEE Robotics and Automation Letters*, *1*(2), 800–807. https://doi.org/10.1109/LRA.2016.2528301

Khatyr, F., Imberdis, C., Vescovo, P., Varchon, D., & Lagarde, J.-M. (2004). Model of the viscoelastic behaviour of skin in vivo and study of anisotropy. *Skin Research and Technology*, *10*(2), 96–103. https://doi.org/10.1111/j.1600-0846.2004.00057.x

Kosoglu, M. A., Hood, R. L., Chen, Y., Xu, Y., Rylander, M. N., & Rylander, C. G. (2010). Fiber Optic Microneedles for Transdermal Light Delivery: Ex Vivo Porcine Skin Penetration Experiments. *Journal of Biomechanical Engineering*, *132*(9), 091014. https://doi.org/10.1115/1.4002192

Kostadinova-Petrova, I., Mitevska, E., & Janeska, B. (2017). Histological Characteristics of Bruises with Different Age. *Open Access Macedonian Journal of Medical Sciences*, *5*(7), 813–817. https://doi.org/10.3889/oamjms.2017.207

Łagan, S. D., & Liber-Kneć, A. (2017). Experimental testing and constitutive modeling of the mechanical properties of the swine skin tissue. *Acta of Bioengineering & Biomechanics*, *19*(2), 93–102. https://doi.org/10.5277/ABB-00755-2016-02

Langlois, N. E. I. (2007). The science behind the quest to determine the age of bruises—A review of the English language literature. *Forensic Science, Medicine, and Pathology*, *3*(4), 241–251. https://doi.org/10.1007/s12024-007-9019-3

Lanir, Y., & Fung, Y. C. (1974). Two-dimensional mechanical properties of rabbit skin—II. Experimental results. *Journal of Biomechanics*, *7*(2), 171–182. https://doi.org/10.1016/0021-9290(74)90058-X

Lapeer, R. J., Gasson, P. D., & Karri, V. (2010). Simulating plastic surgery: From human skin tensile tests, through hyperelastic finite element models to real-time haptics. *Progress in Biophysics and Molecular Biology*, *103*(2–3), 208–216. https://doi.org/10.1016/j.pbiomolbio.2010.09.013

Laurent, A., Mistretta, F., Bottigioli, D., Dahel, K., Goujon, C., Nicolas, J. F., Hennino, A., & Laurent, P. E. (2007). Echographic measurement of skin thickness in adults by high frequency ultrasound to assess the appropriate microneedle length for intradermal delivery of vaccines. *Vaccine*, *25*(34), 6423–6430. https://doi.org/10.1016/j.vaccine.2007.05.046

Lee, E. H., & Radok, J. R. M. (1960). The Contact Problem for Viscoelastic Bodies. *Journal of Applied Mechanics*, *27*(3), 438–444. https://doi.org/10.1115/1.3644020

Lemaitre, J. (1985). A Continuous Damage Mechanics Model for Ductile Fracture. *Journal of Engineering Materials and Technology*, *107*(1), 83–89. https://doi.org/10.1115/1.3225775

Lemperle, G., Knapp, D., & Tenenhaus, M. (2019). Minimal Scar Formation After Orthopaedic Skin Incisions Along Main Folding Lines. *JBJS*, *101*(5), 392–399. https://doi.org/10.2106/JBJS.18.00331

Leveque, J. L., de Rigal, J., Agache, P. G., & Monneur, C. (1980). Influence of ageing on the in vivo extensibility of human skin at a low stress. *Archives of Dermatological Research*, *269*(2), 127–135. https://doi.org/10.1007/BF00406532

Li, W., & Luo, X. Y. (2016). An Invariant-Based Damage Model for Human and Animal Skins. *Annals of Biomedical Engineering*, *44*(10), 3109–3122. https://doi.org/10.1007/s10439-016-1603-9

Lim, J., Hong, J., Chen, W. W., & Weerasooriya, T. (2011). Mechanical response of pig skin under dynamic tensile loading. *International Journal of Impact Engineering*, *38*(2–3), 130–135. https://doi.org/10.1016/j.ijimpeng.2010.09.003

Lim, K. H., Chew, C. M., Chen, P. C. Y., Jeyapalina, S., Ho, H. N., Rappel, J. K., & Lim, B. H. (2008). New extensometer to measure in vivo uniaxial mechanical properties of human skin. *Journal of Biomechanics*, *41*(5), 931–936. https://doi.org/10.1016/j.jbiomech.2008.01.004

Lin, D. C., Shreiber, D. I., Dimitriadis, E. K., & Horkay, F. (2009). Spherical indentation of soft matter beyond the Hertzian regime: Numerical and experimental validation of hyperelastic models. *Biomechanics and Modeling in Mechanobiology*, *8*(5), 345–358. https://doi.org/10.1007/s10237-008-0139-9

Liu, F., Li, C., Liu, S., Genin, G. M., Huang, G., Lu, T., & Xu, F. (2015). Effect of viscoelasticity on skin pain sensation. *Theoretical and Applied Mechanics Letters*, *5*(6), 222–226. https://doi.org/10.1016/j.taml.2015.11.002

Liu, Z., & Yeung, K. (2008). *The Preconditioning and Stress Relaxation of Skin Tissue*. 7.

Manschot, J. F. M., & Brakkee, A. J. M. (1986). The measurement and modelling of the mechanical properties of human skin in vivo—I. The measurement. *Journal of Biomechanics*, *19*(7), 511–515. https://doi.org/10.1016/0021-9290(86)90124-7

Martins, J. A. C., Pires, E. B., Salvado, R., & Dinis, P. B. (1998). A numerical model of passive and active behavior of skeletal muscles. *Computer Methods in Applied Mechanics and Engineering*, *151*(3), 419–433. https://doi.org/10.1016/S0045-7825(97)00162-X

Martins, P. a. L. S., Jorge, R. M. N., & Ferreira, A. J. M. (2006). A Comparative Study of Several Material Models for Prediction of Hyperelastic Properties: Application to Silicone-Rubber and Soft Tissues. *Strain*, *42*(3), 135–147. https://doi.org/10.1111/j.1475-1305.2006.00257.x

Mattice, J. M., Lau, A. G., Oyen, M. L., & Kent, R. W. (2006). Spherical indentation load-relaxation of soft biological tissues. *Journal of Materials Research*, *21*(8), 2003–2010. https://doi.org/10.1557/jmr.2006.0243

Mattoo, B. N., Wani, A. K., & Asgekar, M. D. (1974). Casualty Criteria for Wounds from Firearms with Special Reference to Shot Penetration—Part II. *Journal of Forensic Sciences*, *19*(3), 10215J. https://doi.org/10.1520/JFS10215J

Meliga, S. C., Coffey, J. W., Crichton, M. L., Flaim, C., Veidt, M., & Kendall, M. A. F. (2017). The hyperelastic and failure behaviors of skin in relation to the dynamic application of microscopic penetrators in a murine model. *Acta Biomaterialia*, *48*, 341–356. https://doi.org/10.1016/j.actbio.2016.10.021

Meyer, A. L. M., Berger, E., Monteiro Jr., O., Alonso, P. A., Stavale, J. N., & Gonçalves, M. P. S. (2007). Quantitative and qualitative analysis of collagen types in the fascia transversalis of inguinal hernia patients. *Arquivos de Gastroenterologia*, *44*(3), 230–234. https://doi.org/10.1590/S0004-28032007000300010

Missliwetz, J. (1987). *[Critical velocity in skin (an experimental ballistic study with firearms of 4 mm and 4.5 mm calibers)]*. Beitrage Zur Gerichtlichen Medizin; Beitr Gerichtl Med. https://pubmed.ncbi.nlm.nih.gov/3663077/

Mooney, M. (1940). A Theory of Large Elastic Deformation. *Journal of Applied Physics*, *11*(9), 582–592. https://doi.org/10.1063/1.1712836

Ng, B.-H., & Chou, S.-M. (2003). The effect of freeze storage on the tensile properties of tendons. *Journal of Mechanics in Medicine and Biology*, *03*(03n04), 299–308. https://doi.org/10.1142/S0219519403000818

Ní Annaidh, A., Bruyère, K., Destrade, M., Gilchrist, M. D., Maurini, C., Otténio, M., & Saccomandi, G. (2012). Automated Estimation of Collagen Fibre Dispersion in the Dermis and its Contribution to the Anisotropic Behaviour of Skin. *Annals of Biomedical Engineering*, *40*(8), 1666–1678. https://doi.org/10.1007/s10439-012-0542-3

Ní Annaidh, A., Bruyère, K., Destrade, M., Gilchrist, M. D., & Otténio, M. (2012a). Characterization of the anisotropic mechanical properties of excised human skin. *Journal of the Mechanical Behavior of Biomedical Materials*, *5*(1), 139–148. https://doi.org/10.1016/j.jmbbm.2011.08.016

Ní Annaidh, A., Bruyère, K., Destrade, M., Gilchrist, M. D., & Otténio, M. (2012b). Characterization of the anisotropic mechanical properties of excised human skin. *Journal of the Mechanical Behavior of Biomedical Materials*, *5*(1), 139–148. https://doi.org/10.1016/j.jmbbm.2011.08.016

Ní Annaidh, A., Cassidy, M., Curtis, M., Destrade, M., & Gilchrist, M. D. (2013). A combined experimental and numerical study of stab-penetration forces. *Forensic Science International*, *233*(1), 7–13. https://doi.org/10.1016/j.forsciint.2013.08.011

Nussbaum, S. R., Carter, M. J., Fife, C. E., DaVanzo, J., Haught, R., Nusgart, M., & Cartwright, D. (2018). An Economic Evaluation of the Impact, Cost, and Medicare Policy Implications of Chronic Nonhealing Wounds. *Value in Health*, *21*(1), 27–32. https://doi.org/10.1016/j.jval.2017.07.007

Ogden, R. W., & Hill, R. (1972). Large deformation isotropic elasticity – on the correlation of theory and experiment for incompressible rubberlike solids. *Proceedings of the Royal Society of London. A. Mathematical and Physical Sciences*, *326*(1567), 565–584. https://doi.org/10.1098/rspa.1972.0026

Oltulu, P., Ince, B., Kokbudak, N., Findik, S., & Kilinc, F. (2018). Measurement of epidermis, dermis, and total skin thicknesses from six different body regions with a new ethical histometric technique. *Turkish Journal of Plastic Surgery*, *26*(2), 56. https://doi.org/10.4103/tjps.TJPS_2_17

Ottenio, M., Tran, D., Ní Annaidh, A., Gilchrist, M. D., & Bruyère, K. (2015). Strain rate and anisotropy effects on the tensile failure characteristics of human skin. *Journal of the Mechanical Behavior of Biomedical Materials*, *41*, 241–250. https://doi.org/10.1016/j.jmbbm.2014.10.006

Oxlund, H., Manschot, J., & Viidik, A. (1988). The role of elastin in the mechanical properties of skin. *Journal of Biomechanics*, *21*(3), 213–218. https://doi.org/10.1016/0021-9290(88)90172-8

Pailler-Mattei, C., Bec, S., & Zahouani, H. (2008). In vivo measurements of the elastic mechanical properties of human skin by indentation tests. *Medical Engineering & Physics*, *30*(5), 599–606. https://doi.org/10.1016/j.medengphy.2007.06.011

Papy, A., Robbe, C., Nsiampa, N., Oukara, A., & Goffin, J. (2012). *Definition of a standardized skin penetration surrogate for blunt impacts*. 8.

Piérard, G. E., Piérard, S., Delvenne, P., & Piérard-Franchimont, C. (2013). In Vivo Evaluation of the Skin Tensile Strength by the Suction Method: Pilot Study Coping with Hysteresis and Creep Extension. *ISRN Dermatology*, *2013*, 1–7. https://doi.org/10.1155/2013/841217

Press, W. H., Teukolsky, S. A., Vetterling, W. T., & Flannery, B. P. (1996). *FORTRAN numerical recipes* (2nd ed). Cambridge University Press.

Rajesh, A., Wise, L., & Hibma, M. (2019). The role of Langerhans cells in pathologies of the skin. *Immunology & Cell Biology*, *97*(8), 700–713. https://doi.org/10.1111/imcb.12253

Rehorn, M. R., Schroer, A. K., & Blemker, S. S. (2014). THE PASSIVE PROPERTIES OF MUSCLE FIBERS ARE VELOCITY DEPENDENT. *Journal of Biomechanics*, *47*(3), 687–693. https://doi.org/10.1016/j.jbiomech.2013.11.044

Ren, D., Sun, K., Tian, S., Yang, X., Zhang, C., Wang, W., Huang, H., Zhang, J., & Deng, Y. (2012). Effects of gamma irradiation and repetitive freeze–thaw cycles on the biomechanical properties of human flexor digitorum superficialis tendons. *Journal of Biomechanics*, *45*(2), 252–256. https://doi.org/10.1016/j.jbiomech.2011.10.035

Sanders, R. (1973). Torsional elasticity of human skin in vivo. *Pfl�gers Archiv European Journal of Physiology*, *342*(3), 255–260. https://doi.org/10.1007/BF00591373

Seo, N. J., & Armstrong, T. J. (2009). Friction coefficients in a longitudinal direction between the finger pad and selected materials for different normal forces and curvatures. *Ergonomics*, *52*(5), 609–616. https://doi.org/10.1080/00140130802471595

Shergold, O. A., & Fleck, N. A. (2004). Mechanisms of deep penetration of soft solids, with application to the injection and wounding of skin. *Proceedings of the Royal Society of London. Series A: Mathematical, Physical and Engineering Sciences*, *460*(2050), 3037–3058. https://doi.org/10.1098/rspa.2004.1315

Shergold, O. A., & Fleck, N. A. (2005). Experimental Investigation Into the Deep Penetration of Soft Solids by Sharp and Blunt Punches, With Application to the Piercing of Skin. *Journal of Biomechanical Engineering*, *127*(5), 838. https://doi.org/10.1115/1.1992528

Shergold, O. A., Fleck, N. A., & Radford, D. (2006a). The uniaxial stress versus strain response of pig skin and silicone rubber at low and high strain rates. *International Journal of Impact Engineering*, *32*(9), 1384–1402. https://doi.org/10.1016/j.ijimpeng.2004.11.010

Shergold, O. A., Fleck, N. A., & Radford, D. (2006b). The uniaxial stress versus strain response of pig skin and silicone rubber at low and high strain rates. *International Journal of Impact Engineering*, *32*(9), 1384–1402. https://doi.org/10.1016/j.ijimpeng.2004.11.010

Sherratt, M. J. (2013). Age-Related Tissue Stiffening: Cause and Effect. *Advances in Wound Care*, *2*(1), 11–17. https://doi.org/10.1089/wound.2011.0328

Storåkers, B. (1986). On material representation and constitutive branching in finite compressible elasticity. *Journal of the Mechanics and Physics of Solids*, *34*(2), 125–145. https://doi.org/10.1016/0022-5096(86)90033-5

Takaza, M., Moerman, K. M., & Simms, C. K. (2013). Passive skeletal muscle response to impact loading: Experimental testing and inverse modelling. *Journal of the Mechanical Behavior of Biomedical Materials*, *27*, 214–225. https://doi.org/10.1016/j.jmbbm.2013.04.016

Tausch, D., Sattler, W., Wehrfritz, K., Wehrfritz, G., & Wagner, H.-J. (1978). Experiments on the penetration power of various bullets into skin and muscle tissue. *Zeitschrift Für Rechtsmedizin*, *81*(4), 309–328. https://doi.org/10.1007/BF02096436

Tonge, T. K., Atlan, L. S., Voo, L. M., & Nguyen, T. D. (2013). Full-field bulge test for planar anisotropic tissues: Part I – Experimental methods applied to human skin tissue. *Acta Biomaterialia*, *9*(4), 5913–5925. https://doi.org/10.1016/j.actbio.2012.11.035

Trotta, A., & Ní Annaidh, A. (2019). Mechanical characterisation of human and porcine scalp tissue at dynamic strain rates. *Journal of the Mechanical Behavior of Biomedical Materials*, *100*, 103381. https://doi.org/10.1016/j.jmbbm.2019.103381

Van den Berg, F. (2012). 4.3—Extracellular matrix. In R. Schleip, T. W. Findley, L. Chaitow, & P. A. Huijing (Eds.), *Fascia: The Tensional Network of the Human Body* (pp. 165–170). Churchill Livingstone. https://doi.org/10.1016/B978-0-7020-3425-1.00058-1

van den Eijnde, W. A. J., Peppelman, M., Lamers, E. A. D., van de Kerkhof, P. C. M., & van Erp, P. E. J. (2014). Understanding the Acute Skin Injury Mechanism Caused by Player-Surface Contact During Soccer: A Survey and Systematic Review. *Orthopaedic Journal of Sports Medicine*, *2*(5), 232596711453348. https://doi.org/10.1177/2325967114533482

van Kuilenburg, J., Masen, M. A., & van der Heide, E. (2013). Contact modelling of human skin: What value to use for the modulus of elasticity? *Proceedings of the Institution of Mechanical Engineers, Part J: Journal of Engineering Tribology*, *227*(4), 349–361. https://doi.org/10.1177/1350650112463307

Van Loocke, M., Lyons, C. G., & Simms, C. K. (2006). A validated model of passive muscle in compression. *Journal of Biomechanics*, *39*(16), 2999–3009. https://doi.org/10.1016/j.jbiomech.2005.10.016

Veronda, D. R., & Westmann, R. A. (1970). Mechanical characterization of skin—Finite deformations. *Journal of Biomechanics*, *3*(1), 111–124. https://doi.org/10.1016/0021-9290(70)90055-2

Wan Abas, W. A. B., & Barbenel, J. C. (1982). Uniaxial tension test of human skin in vivo. *Journal of Biomedical Engineering*, *4*(1), 65–71. https://doi.org/10.1016/0141-5425(82)90029-2

Wang, Y., Marshall, K. L., Baba, Y., Lumpkin, E. A., & Gerling, G. J. (2015). Compressive Viscoelasticity of Freshly Excised Mouse Skin Is Dependent on Specimen Thickness, Strain Level and Rate. *PLOS ONE*, *10*(3), e0120897. https://doi.org/10.1371/journal.pone.0120897

Weiss, J. A., Maker, B. N., & Govindjee, S. (1996). Finite element implementation of incompressible, transversely isotropic hyperelasticity. *Computer Methods in Applied Mechanics and Engineering*, *135*(1), 107–128. https://doi.org/10.1016/0045-7825(96)01035-3

Xu, F., Seffen, K., & Lu, T. (n.d.). *A Quasi-Linear Viscoelastic Model for Skin Tissue*. 8.

Yang, W., Sherman, V. R., Gludovatz, B., Schaible, E., Stewart, P., Ritchie, R. O., & Meyers, M. A. (2015). On the tear resistance of skin. *Nature Communications, 6*, 6649. https://doi.org/10.1038/ncomms7649

Yeoh, O. H. (1993). Some Forms of the Strain Energy Function for Rubber. *Rubber Chemistry and Technology*, *66*(5), 754–771. https://doi.org/10.5254/1.3538343

Yousef, H., Alhajj, M., & Sharma, S. (2020). Anatomy, Skin (Integument), Epidermis. In *StatPearls*. StatPearls Publishing. http://www.ncbi.nlm.nih.gov/books/NBK470464/

Zhang, M., & Mak, A. F. T. (1999). *In vivo* friction properties of human skin. *Prosthetics and Orthotics International*, *23*(2), 135–141. https://doi.org/10.3109/03093649909071625

APPENDIX A: UMAT Verification

To verify the code of the implemented UMAT, a single hexahedral element model (1x1x1 unit volume, (Figure A1) was used to simulate the DT tests at 180/s. The true stress response of the element was calculated using total force measured by the 4 nodes at the bottom using *DATABASE_NODAL_FORCE_GROUP Keyword and divided by the cross-section area at each time step. The stretch ratio was computed from the ratio between the element length at each time step and the original length. Three sets of UMAT parameters were input for simulation and compared with the average, UB, and LB DT stress-stretch curves respectively for UMAT verification. The bulk modulus K was calculated using the Lamé relationship ($K = \frac{2G(1+\upsilon)}{3(1-2\upsilon)}$) while the shear modulus G was determined from the Ogden elastic constants ($G = \frac{1}{2}\sum_{i=1}^{n} \mu_i \alpha_i$) and a Poisson's ratio of 0.495 was used. Furthermore, the hexahedral element was also subjected to a virtual loading and unloading profile within the pristine region to investigate its hysteresis loop and compared it with an analytical solution to demonstrate the model viscoelasticity. Lastly, a loading and unloading profile beyond the damage initiation stretch was also performed to demonstrate the damage is unrecoverable once initiates. No damage was allowed once the material was unloaded and only resumed when surpassing the previous damage stretch ratio.

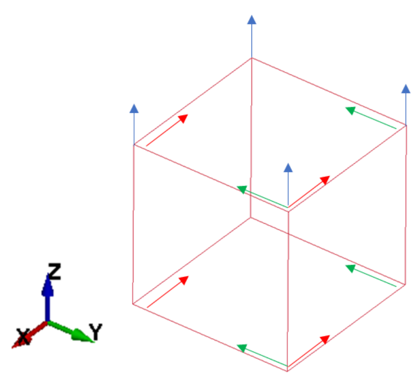

Figure A1: Constraints applied on a single hexahedral element subjected to tension for verifying UMAT implementation. Colored arrows indicate the degree of freedom of each node in x(red), y(green), and z(blue) direction.

Single Solid Element (UMAT Code Verification)

By inputting the average, UB, and LB material parameters into the UMAT card, the DT strain profile at 180/s as conducted in the experiment was simulated on a single hexahedral element and the stress-stretch simulation results are illustrated in Figure A2. The simulation results match with the corresponding analytical model and the element is deleted (element erosion) upon reaching the failure stretch which results in a sudden stress drop in the stress-stretch plot. This process verifies the implemented UMAT card which was able to perform the same calculation as with the QLV-damage analytical model. The UMAT card was also compiled to output some of the desired parameters such as damage factor *D* to show individual element damage progress. Damage initiates after passing the damage initiation stretch was shown to be unrecoverable when the element is being unloaded. The damage continues to accumulate once passing over the previous highest stretch value until failure occurs (Figure A3, left). Furthermore, hysteresis was also observed when simulating a loading-unloading cycle to the single hexahedral element and the simulation result also matched well with the analytical solution (Figure A3, right).

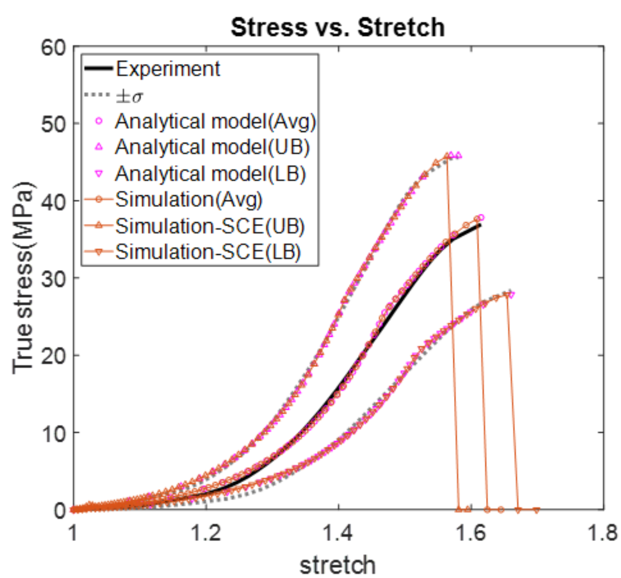

Figure A2: Stress-stretch response of single hexahedral element using average, UB, and LB UMAT.

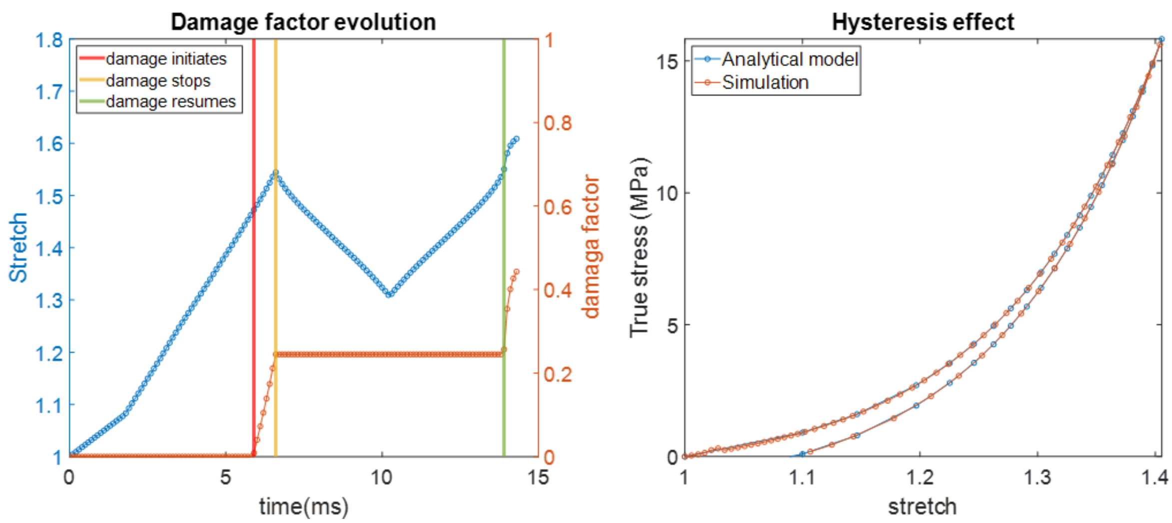

Figure A3: Damage factor vs. stretch value (left). Hysteresis developed from the loading-unloading cycle (right).

Tensile Test Verification

After verifying the code of the UMAT card, the UMAT was applied to a skin FE model as used in the DT test to simulate the uniaxial tensile failure process. The skin FE model was built with a dogbone shape (Figure A4), having the same dimensions as the dogbone cutter used in the experiment with an average thickness of 3.669mm, obtained from the sample group performed at 180/s. One end of the FE model was fixed and the other end was constrained to travel only in the vertical direction at a prescribed average experimental velocity-time profile via *BOUNDARY_PRESCRIBED_MOTION keyword while the remaining section was free of constraints. To calculate the true stress from the model, the total force was obtained from the nodes at the fixed end and divided by the cross-section area at the gauge section at every time step. The stretch ratio was computed by measuring the distance between the two end nodes along the gauge length. The baseline FE model was built with an element size of 3mm with 124 hexahedral elements in total. The 3mm mesh size was chosen because the gauge width of the skin sample is 6.35 mm, and the 3mm mesh size allows a minimum number of two elements across the gauge width. Model sensitivity analysis on element density was also investigated using 2mm, 1mm, and 0.5mm mesh size which corresponds to the total element number of 282, 1602, and 17017, respectively. Default viscous form hourglass control (type 1 in LS-DYNA) with default hourglass coefficient (QM = 0.1) was used to prevent the model's internal energy exceeded by the hourglass energy. After determining the optimum mesh size, the average, UB, and LB material parameters were used to simulate the DT test and were compared with the experimental results.

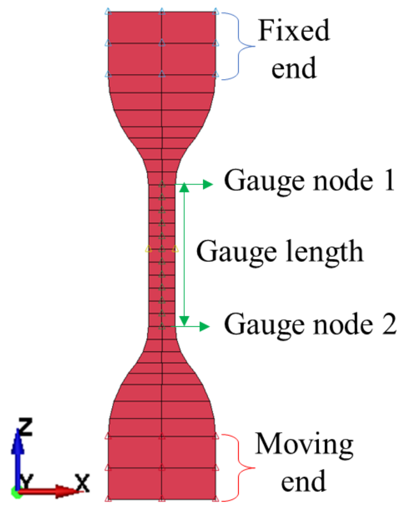

Figure A4: Dogbone skin FE baseline model (3mm element size).

FE simulation of the DT test on the dogbone skin model ran normally until tensile failure occurred which led to a negative volume of the remaining element and caused error termination. This was solved by setting a lower time scale factor (0.1) for calculating the simulation time step. Model mesh size sensitivity analysis using 3mm, 2mm, 1mm and 0.5mm mesh size were performed and the resultant stress-stretch response shows little difference (Figure A5). It should be noted that the simulation results are plotted up to the point before failure occurs. Although all the models show similar stress-stretch paths compared to the average experimental data, it was observed that models with more refined meshes induce earlier failure, especially in the 1mm and 0.5mm model. The 3mm and 2mm model both have a similar failure stretch at 1.59 compared to the designated failure stretch of 1.61 while the two finest models failed at a stretch ratio of 1.56

since local deformation is better simulated. By considering the closest response to the average experimental results and maintaining the finest model resolution at the same time, the 2mm model was chosen.

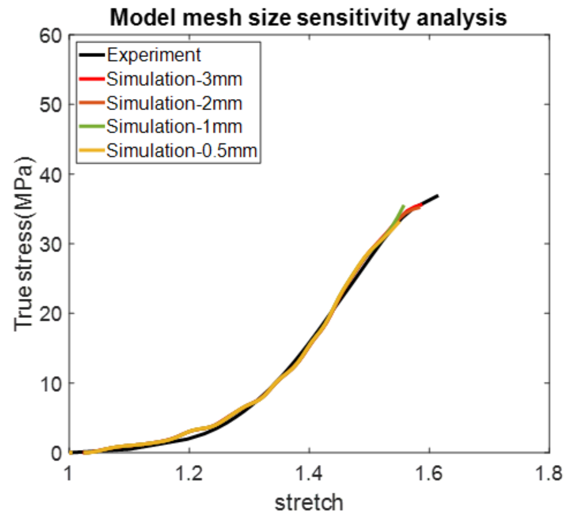

Figure A5: Model mesh size sensitivity analysis of dynamic tensile test simulation.

Three UMAT cards with average, UB, and LB material parameters were used to simulate the DT test (Figure A6). The UMATs capture the skin's nonlinear and failure response successfully. A screenshot of the FE model, demonstrating the FE skin model failure was compared with the experimental skin (Figure A7).

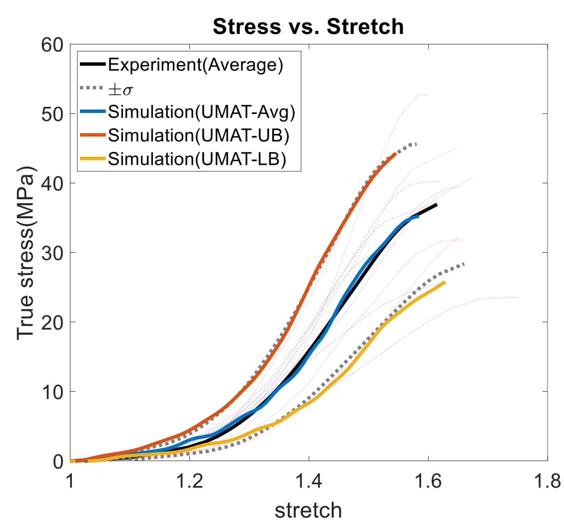

Figure A6: Stress-stretch response of the UMAT skin model.

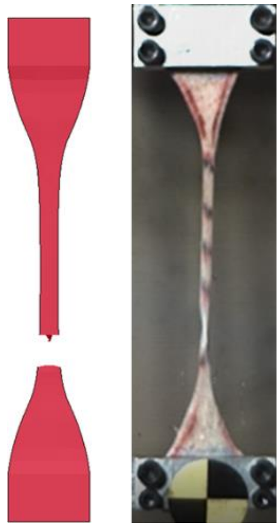

Figure A7: Simulated skin failure (left) and experiment (right).